Vol. 283, No. 3, December 15, 1993
Completing Volume 283

ISSN 0003-2670

Special Issue

SOLID STATE NMR

ANALYTICA CHIMICA ACTA

An international journal devoted to all branches of analytical chemistry

ELSEVIER

ANALYTICA CHIMICA ACTA

Scope. *Analytica Chimica Acta* publishes original papers, preliminary communications and reviews dealing with every aspect of modern analytical chemistry. Reviews are normally written by invitation of the editors, who welcome suggestions for subjects. Preliminary communications of important urgent work can be printed within four months of submission, if the authors are prepared to forego proofs.

Submission of Papers

Americas

Prof. Harry L. Pardue
Department of Chemistry
1393 BRWN Bldg, Purdue University
West Lafayette, IN 47907-1393
USA

Tel:(+1-317) 494 5320
Fax:(+1-317) 496 1200

Computer Techniques

Prof. J.T. Clerc
Universität Bern
Pharmazeutisches Institut
Baltzerstrasse 5, CH-3012 Bern
Switzerland

Tel:(+41-31) 654171
Fax:(+41-31) 654198

Prof. Sarah C. Rutan
Department of Chemistry
Virginia Commonwealth University
P.O. Box 2006
Richmond, VA 23284-2006
USA
Tel:(+1-804) 367 1298
Fax:(+1-804) 367 8599

Other Papers

Prof. Alan Townshend
Department of Chemistry
The University
Hull HU6 7RX
Great Britain

Tel:(+44-482) 465027
Fax:(+44-482) 466410

Prof. Willem E. van der Linden
Laboratory for Chemical Analysis
Department of Chemical Technology
Twente University of Technology
P.O. Box 217, 7500 AE Enschede
The Netherlands
Tel:(+31-53) 892629
Fax:(+31-53) 356024

Prof. Paul Worsfold
Dept. of Environmental Sciences
University of Plymouth
Plymouth PL4 8AA
Great Britain

Tel:(+44-752) 233006
Fax:(+44-752) 233009

Submission of an article is understood to imply that the article is original and unpublished and is not being considered for publication elsewhere. *Anal. Chim. Acta* accepts papers in English only. There are no page charges. Manuscripts should conform in layout and style to the papers published in this issue. See inside back cover for "Information for Authors".

Publication. *Analytica Chimica Acta* appears in 16 volumes in 1994 (Vols. 281–296). *Vibrational Spectroscopy* appears in 2 volumes in 1994 (Vols. 6 and 7). Subscriptions are accepted on a prepaid basis only, unless different terms have been previously agreed upon. It is possible to order a combined subscription (*Anal. Chim. Acta* **and** *Vib. Spectrosc.*).
Our p.p.h. (postage, packing and handling) charge includes surface delivery of all issues, except to subscribers in the U.S.A., Canada, Australia, New Zealand, China, India, Israel, South Africa, Malaysia, Thailand, Singapore, South Korea, Taiwan, Pakistan, Hong Kong, Brazil, Argentina and Mexico, who receive all issues by air delivery (S.A.L.–Surface Air Lifted) at no extra cost. For Japan, air delivery requires 25% additional charge of the normal postage and handling charge; for all other countries airmail and S.A.L. charges are available upon request.

Subscription orders. Subscription prices are available upon request from the publisher. Subscription orders can be entered only by calendar year and should be sent to: Elsevier Science Publishers B.V., Journals Department, P.O. Box 211, 1000 AE Amsterdam, The Netherlands. Tel: (+31-20) 5803 642, Telex: 18582, Telefax: (+31-20) 5803598, to which requests for sample copies can also be sent. Claims for issues not received should be made within six months of publication of the issues. If not they cannot be honoured free of charge. Readers in the U.S.A. and Canada can contact the following address: Elsevier Science Publishing Co. Inc., Journal Information Center, 655 Avenue of the Americas, New York, NY 10010, U.S.A. Tel: (+1-212) 6333750, Telefax: (+1-212) 6333990, for further information, or a free sample copy of this or any other Elsevier Science Publishers journal.

US mailing notice – Analytica Chimica Acta (ISSN 0003-2670) is published biweekly by Elsevier Science Publishers (Molenwerf 1, Postbus 211, 1000 AE Amsterdam). Annual subscription price in the USA US$ 3035.75 (valid in North, Central and South America), including air speed delivery. Second class postage paid at Jamaica, NY 11431. *USA Postmasters*: Send address changes to Anal. Chim. Acta, Publications Expediting, Inc., 200 Meacham Av., Elmont, NY 11003. Airfreight and mailing in the USA by Publication Expediting.

ANALYTICA CHIMICA ACTA

An international journal devoted to all branches of analytical chemistry

(Full texts are incorporated in CJELSEVIER, a file in the Chemical Journals Online database available on STN International; Abstracted, indexed in: Aluminum Abstracts; Anal. Abstr.; Biol. Abstr.; BIOSIS; Chem. Abstr.; Curr. Contents Phys. Chem. Earth Sci.; Engineered Materials Abstracts; Excerpta Medica; Index Med.; Life Sci.; Mass Spectrom. Bull.; Material Business Alerts; Metals Abstracts; Sci. Citation Index)

VOL. 283 NO. 3 CONTENTS DECEMBER 15, 1993

Special issue on Solid State NMR

Foreword
(*by W.S. Veeman*) 927

Applications of solid-state NMR for the study of molecular sieves. Review
J. Klinowski (Cambridge, UK) 929
Multinuclear solid state NMR of host–guest systems with TO_2 (T = Si, Al) host-frameworks. A case study on sodalites
G. Engelhardt (Stuttgart, Germany), P. Sieger and J. Felsche (Konstanz, Germany) 967
Quantitative evaluation of gallium phosphide samples prepared from rapid solid state metathesis. Solid state ^{31}P and ^{69}Ga magic angle spinning NMR strategies
D. Franke, H. Eckert (Santa Barbara, CA, USA), R.B. Kaner and R.E. Treece (Los Angeles, CA, USA) 987
Applications of nuclear magnetic resonance spectrometry to solid polymers. Review
R.L. Silvestri and J.L. Koenig (Cleveland, OH, USA) 997
Analysis of polymer stabilizers by means of solid state NMR: some case studies
W. Barendswaard, J. Moonen and M. Neilen (Geleen, Netherlands) 1007
Improving selectivity by using a multipurpose cross polarization magic angle spinning NMR pulse sequence. Characterization of π-conjugated compounds
I. Hoogmartens, P. Adriaensens, D. Vanderzande and J. Gelan (Diepenbeek, Belgium) 1025
Quantification of ^{13}C in solids using CPMAS-DD-NMR spectroscopy
D.G. Rethwisch (Iowa City, IA, USA), M.A. Jacintha and C.R. Dybowski (Newark, DE, USA) 1033
Non-linear least squares procedure for the extraction of NMR parameters from multi-tensor solid state line shapes
J.M. Koons, E. Hughes and P.D. Ellis (Columbia, SC, USA) 1045
Determination of proton densities on silica gel catalyst supports by *n*-quantum coherence in NMR
B.C. Gerstein, M. Pruski and S.-J. Hwang (Ames, IA, USA) 1059
Nuclear magnetic resonance methods for measuring dipolar couplings in rotating solids
J.M. Griffiths and R.G. Griffin (Cambridge, MA, USA) 1081
^{129}Xe NMR spectroscopy in microporous solids: the effect of bulk properties
J.A. Ripmeester and C.I. Ratcliffe (Ottawa, Canada) 1103

Author Index 1113

SPECIAL ISSUE

SOLID STATE NMR

Analytica Chimica Acta, 283 (1993) 927
Elsevier Science Publishers B.V., Amsterdam

FOREWORD

Everyone will agree that NMR spectroscopy is an important analytical tool for chemists. In the early days of NMR many experiments were performed on solid samples, but when it became clear that the NMR spectra of compounds in a solution displayed a much higher resolution, the interest of chemists in high-resolution liquid state NMR increased rapidly while low-resolution solid state NMR mainly remained of interest to physicists.

About 25 years ago this slowly started to change, thanks to the efforts of mainly Professor John Waugh and his co-workers at MIT. Techniques were developed which were capable to narrow the broad solid state NMR lines to such a degree that chemists started to recognize the possibilities of such techniques for the study of compounds and materials that are either hard to dissolve or for which it is important to gain knowledge in the solid state.

It soon became clear that, from a chemists point of view, the solid state NMR techniques which relied on the observation of nuclei with a relatively low abundance, like ^{13}C, ^{29}Si and many others, were easier to perform and gave more direct information than high-resolution proton NMR. Techniques like cross-polarization and magic angle spinning are nowadays routinely performed in many laboratories (academic and industrial) around the world with high quality, commercially manufactured instruments.

This thematic issue of *Analytica Chimica Acta* intends to show how far solid state NMR has proceeded. As in other fields where NMR plays a key role (high-resolution liquid state NMR, NMR imaging, NMR of biological systems) it is surprising that so many variations on a basic experimental technique exist.

The contributions in this issue show the application of solid state NMR to organic systems, smaller molecules and polymers, and to inorganic systems, especially catalysts. Also quantitative aspects of solid state NMR are discussed. In two papers, two of the many directions in which the development of solid state NMR progresses, are described.

In spite of this variation, many applications of solid state NMR could not be covered in this issue. To make up for this, an application of an NMR technique that is strictly speaking not a solid state NMR technique, ^{129}Xe NMR, is included to show that for NMR investigations of solid materials also other possibilities exist.

I like to thank all the authors and the referees for their crucial contribution to this thematic issue!

Wiebren S. Veeman

Analytica Chimica Acta, 283 (1993) 929–965
Elsevier Science Publishers B.V., Amsterdam

Review

Applications of solid-state NMR for the study of molecular sieves

Jacek Klinowski

Department of Chemistry, University of Cambridge, Lensfield Road, Cambridge CB2 1EW (UK)

(Received 10th December 1992; revised manuscript received 10th April 1993)

Abstract

Nuclear magnetic resonance (NMR) provides important new insights into the structure and function of zeolitic and aluminophosphate ($AlPO_4$) molecular sieves. The Si/Al ratio of the zeolitic framework can be calculated from ^{29}Si magic angle spinning (MAS) spectra, and the distribution of Si and Al atoms in the structure, which has important catalytic consequences, can be determined. The chemical shift of ^{29}Si NMR resonances is related to the magnitude of the average Si–O–Si angle, and subtle local rearrangements of atoms in the structure can be monitored. ^{27}Al NMR quantitatively distinguishes between 4-, 5- and 6-coordinated aluminium in zeolites and $AlPO_4$ materials. In particular, quadrupole nutation ^{27}Al NMR provides important information on the chemical status of aluminium.

In situ ^{13}C MAS NMR studies of catalytic reactions identify many different organic species in the adsorbed phase and monitor their fate as a function of time and temperature; demonstrate the reality of product shape selectivity; observe a new type of shape selectivity and unequivocally distinguish between mobile and attached species. ^{1}H MAS NMR allows the Brønsted acid sites to be directly studied. Two-dimensional NMR techniques have been usefully applied to the study of molecular sieves, and a number of other promising methods are briefly described.

High-resolution solid-state NMR spectra of molecular sieves have been measured since 1979, and approximately 1300 research papers, books and reviews on the subject have now appeared. It is clearly impossible to discuss such extensive body of work in an article in a learned journal. However, the principal areas in which NMR is of use to the study of zeolites and $AlPO_4$s can be outlined. I have therefore decided to highlight the main achievements and potentialities of NMR and place special emphasis on the *analytical* applications of the technique. Our research group has been involved in the various areas of solid-state NMR of molecular sieves since 1981, and many of the examples given in the text come from our own work. This is not intended to reflect the size of our own contribution to the field, but is mostly dictated by purely practical considerations.

Keywords: Nuclear magnetic resonance spectrometry; Molecular sieves; Review; Solid state NMR

Molecular sieves are a class of porous open-framework solids, which includes aluminosilicates (zeolites), aluminophosphates and related materials of diverse structures. Zeolites, the original molecular sieves, are built from corner-sharing SiO_4^{4-} and AlO_4^{5-} tetrahedra and contain regular systems of intracrystalline cavities and channels of molecular dimensions. The net negative change of the framework, equal to the number of the constituent aluminium atoms, is balanced by exchangeable cations, M^{n+}, typically sodium, located in the channels which normally also contain water. The name "zeolite" (from the Greek $\zeta\epsilon\omega$ = to boil and $\lambda\iota\theta o\sigma$ = stone) was coined by Cronstedt [1] in 1756 to describe the behaviour of the newly discovered mineral stilbite which, when heated, rapidly loses water and thus seems to boil.

Correspondence to: J. Klinowski, Department of Chemistry, University of Cambridge, Lensfield Road, Cambridge CB2 1EW (UK).

The general oxide formula of a zeolite is

$$M_{x/n}(AlO_2)_x(SiO_2)_y \cdot mH_2O$$

where $y \geq x$. Aluminate tetrahedra cannot be neighbours in the frameworks of hydrothermally prepared zeolites, i.e. Al–O–Al linkages are forbidden. This requirement is known as the Loewenstein rule [2]. There are at present around 40 identified species of zeolite minerals (with $1 \leq y/x \leq 5$) and at least 135 synthetic species with a very wide range of aluminium contents.

Zeolites are conventionally prepared under mild (60–400°C) hydrothermal conditions in strongly basic media. The type and concentration of the base are important structure-directing factors and a variety of organic bases are now being used. In the last few years a novel, low pH, preparative method has been developed. Since silica is barely soluble in acidic media, the method relies on F^- anions to solubilize the reactants as complex fluorides. The "fluoride method" has been successful in synthesizing molecular sieves of various structures. The ZSM series (for *Z*eolite *S*ocony *M*obil) of highly siliceous zeolites is prepared from solutions containing alkylammonium bases. Other elements, such as Ga, Ge, B, Fe and P can substitute for Si and Al in the framework, and there are claims that many other elements can also do so.

Zeolites have a number of interesting physical and chemical properties. The three classes of phenomena which are of greatest practical importance are the ability to sorb organic and inorganic substances, to act as cation exchangers and to catalyse a wide variety of reactions.

The zeolitic channel systems, which may be one-, two- or three-dimensional and may occupy more than 50% of crystal volume, are normally filled with water. When water is removed, other species such as gaseous elements, ammonia, alkali metal vapours, hydrocarbons, alkanols and many other organic and inorganic species may be accommodated in the intracrystalline space. Depending on pore diameter and on molecular dimensions, this process, known as molecular sieving, is often highly selective. Zeolitic sorption is thus a powerful method for the resolution of mixtures. Commercial applications include thorough drying of organics, separation of hydrocarbons and of N_2 and O_2 in air and the removal of NH_3 and CS_2 from industrial gases.

Cations neutralising the electrical charge of the aluminosilicate framework can be exchanged for other cations from solution. Zeolites often possess high ion-exchange selectivities for certain cations, and this is used for their isolation and concentration. Molecular sieving properties of zeolites can be further modified by ion exchange. Thus Na-A sorbs both N_2 and O_2 while Ca-A sorbs nitrogen preferentially to oxygen.

However, it is the ability to catalyse a wide range of reactions, such as cracking, hydrocracking, oxidation and isomerisation of hydrocarbons, which by far overshadows all other applications of zeolites. Rare-earth exchanged and hydrogen forms (prepared indirectly by thermal decomposition of the ammonium form) of some zeolites, such as zeolite Y, mordenite, gmelinite and chabazite, have a cracking activity which is orders of magnitude greater than that of conventional silica/alumina catalysts. Zeolite-based catalysis was first discovered [3] in 1960 and two years later cracking catalysts based on zeolite Y were introduced. They have now almost completely displaced conventional catalysts. The synthetic zeolite ZSM-5, introduced in 1972 [4] is an even more powerful catalyst. Its high silica content (Si/Al ratio is typically 30) gives it high thermal stability, while the channel diameter is very convenient for many applications, particularly in the petroleum industry. The 10-membered channels of ZSM-5 are responsible for the quite striking shape selectivity. Catalytic properties of ZSM-5 include the ability to synthesise gasoline from methanol in a single step. Silicalite, a material which is isostructural with ZSM-5, but contains only small amounts of aluminium is, by contrast to most other zeolites, non-polar (i.e. hydrophobic) and organophilic. Silicalite is used in the removal of dissolved organics from water.

Since 1982 an entirely new family of porous solids has been synthesized. The $AlPO_4$ molecular sieves, with structures built from alternating AlO_4^{4-} and PO_4^{4-} tetrahedra, were the first to be discovered [5]. Some of them have the framework topologies of known zeolites, but many have novel structures. AlPO$_4$'s are synthesized from gels containing sources of aluminium, phosphorus and at least one organic structure-directing template. Incorporation of a silicon source into an aluminophosphate gel results in the formation of silicoaluminophosphates, SAPO, and the incorporation of a metal, Me (such as Mg, Mn, Fe, Co or Zn), into AlPO$_4$ and SAPO gives the MeAPO and MeAPSO sieves, respectively [6]. Some of these have high Brønsted acidities and thus a considerable potential as heterogeneous catalysts.

Synthetic zeolites are usually microcrystalline and furthermore typically contain *four* 10-electron atomic species (Si^{4+}, Al^{3+}, O^{2-} and Na^{+}) which makes them difficult to study by conventional techniques of structural elucidation. The development of high-resolution solid-state NMR techniques, such as MAS, gave zeolite chemistry a powerful structural tool to monitor all elemental components of such frameworks. Specialist monographs and numerous reviews on the structure and properties of molecular sieves are available [7–19].

^{29}Si, ^{27}Al, ^{31}P and ^{17}O have been observed in the frameworks of molecular sieves using MAS NMR. ^{29}Si NMR, which can resolve peaks originating from crystallographically inequivalent silicon atoms and relate them to structural parameters, has provided many new insights into the structure and chemistry of these materials. Pioneering studies in *high-resolution* solid-state ^{29}Si NMR spectroscopy have been performed by Lippmaa et al., who carried out the first comprehensive investigation [20] of a variety of silicates and aluminosilicates.

In principle, ^{27}Al ($I = 5/2$) is a very favourable nucleus for NMR: it has a 100% natural abundance with a large chemical shift range. However, the quadrupole interaction of ^{27}Al is usually large, which broadens and shifts the resonance lines. Because of these interactions, the detection and quantification of aluminium in solids by NMR is often difficult. The best spectra are obtained at very high magnetic fields and with fast magic-angle spinning. It is also essential to use strong radiofrequency pulses with small flip angles to obtain quantitatively reliable spectra [21–24]. The development of double-rotation (DOR) is a major advance in the study of quadrupolar nuclei, as it removes not only chemical shift anisotropy, but also second-order quadrupolar interactions [25–28].

High-resolution ^{1}H MAS NMR is a powerful tool for the measurement of catalytic acidity. In general, the difficulties involved in ^{1}H NMR in the solid state are the strong dipolar interactions, and the narrow range of proton chemical shifts. The consequence of this is that only a limited number of NMR peaks can be resolved. Fortunately, the protons in dehydrated zeolites are usually relatively far apart, which considerably reduces the dipolar interaction. As a result, important NMR information on the chemical status of hydroxyl groups in zeolites has been obtained. There has been much recent interest in the use of ^{129}Xe NMR spectroscopy as a probe for investigating microporous materials. ^{129}Xe is a nucleus with spin $I = 1/2$ and a natural abundance of 26.4%. This means that there are no quadrupolar effects to consider, and that the relative sensitivity of the nucleus is higher than, for example, those of ^{29}Si and ^{13}C.

COMPOSITION OF THE ALUMINOSILICATE FRAMEWORK AND THE NATURE OF EXTRA-FRAMEWORK ALUMINIUM IN ZEOLITES

Framework Si in zeolites is tetrahedrally coordinated, and thus there are five different possible environments of a silicon atom, denoted as Si(nAl) where n (≤ 4) signifies the number of aluminium atoms connected, via oxygens, to a silicon. Each type of Si(nAl) building block corresponds to a definite range of ^{29}Si chemical shift. When a ^{29}Si MAS NMR spectrum of a zeolite (a) contains more than one peak; and (b) is correctly assigned in terms of Si(nAl) units, the Si/Al ratio *in the zeolitic framework* may be calculated from the spectrum alone. This method is valid because in the absence of Al–O–Al linkages the environment of every Al atom is Al(4Si). Therefore, each Si–O–Al linkage in an Si(nAl) unit incorporates 0.25 Al atoms, and the whole unit 0.25 n Al atoms. The Si/Al ratio in the aluminosilicate framework may therefore be calculated directly from the ^{29}Si MAS NMR spectrum using the formula [29,30]

$$(\mathrm{Si/Al})_{\mathrm{NMR}} = \frac{I_4 + I_3 + I_2 + I_1 + I_0}{I_4 + 0.75\, I_3 + 0.5\, I_2 + 0.25\, I_1} \tag{1}$$

where I_n denotes the intensity (peak area) of the NMR peak corresponding to the Si(nAl) building unit. By comparing $(\mathrm{Si/Al})_{\mathrm{NMR}}$ values with the results of chemical analysis, which gives *bulk* composition, the amount of extra-framework aluminium can be calculated, which is important when dealing with chemically modified zeolites.

Equation 1 is independent of structure and applies to all zeolites with framework Si/Al ratios less than about 10 [29–34] provided the assumptions made in its derivation are justified. It can, by implication, serve as a test for the correctness of spectral assignment. Its validity has been tested in the case of zeolites X and Y, which can be synthesized in a range of compositions. The spectra can be deconvoluted using Gaussian peak shapes, and the areas of the individual deconvoluted peaks used in Eqn. 1. Very good agreement was found between the Si/Al ratios obtained by chemical analysis and those calculated from the spectra.

Formula 1 cannot be directly applied to spectra containing overlapping peaks from Si(nAl) units of crystallographically non-equivalent Si atoms. Furthermore, it cannot be easily used with zeolites containing framework defects (nests of hydroxyl groups), and to dealuminated zeolites in which vacant sites created by the expulsion of framework aluminium have not subsequently been re-substituted by silicon (see below). In the latter case, as aluminium is removed, the number of Si(0Al) [i.e. Si(4Si)] units is unchanged, and Si(3Al,1Si) units, for example, give rise not to Si(2Al,2Si) and Si(1Al,3Si) units, but rather to Si(2Al,1OH) and Si(1Al,2OH) groupings. These produce ^{29}Si NMR peaks which overlap with those from Si(nAl) groupings. Although the intensities of ^{29}Si peaks corresponding to silicons linked to one or more hydroxyl groups is enhanced upon cross-polarization, so that their presence can be easily established, their individual intensities cannot be easily determined because the efficiency of cross-polarization strongly depends on the distance between the silicon and the hydrogen atom. A further complication is that hydrogens belonging to template molecules which are often present may also be involved in cross-polarization.

^{29}Si MAS NMR is also of considerable assistance in determining the *ordering* of Si and Al atoms in the framework, beyond the restrictions of the Loewenstein rule. The areas under the peaks in the (deconvoluted) spectrum are directly proportional to the populations of the respective structural units in the sample. It is therefore possible to estimate these from the experimental data (see Fig. 1) and to compare them with the relative numbers of such units contained in models involving different Si,Al ordering schemes. For most Si/Al ratios more than one ordering scheme is compatible with the Si(nAl) intensities determined by ^{29}Si MAS NMR. The choice between the various schemes is made on the basis of (a) the degree of agreement between the *actual* spectral intensities and those required by the given model; (b) compliance with crystal symmetry requirements; and (c) minimum electrostatic repulsion within the aluminosilicate framework. As an example, Fig. 2 shows the preferred ordering schemes for Si/Al = 1.67.

^{29}Si MAS NMR has shown [35] that Si,Al ordering in synthetic ultramarine, which has the framework structure of the zeolite sodalite, is different from that of lazurite, its natural counterpart. Si–O–Si, Si–O–Al *and* Al–O–Al linkages are simultaneously present and Si and Al sites are fully disordered. In blue ultramarine the chromophore groups are the strongly paramagnetic S^{3-} and S^{2-} anions enclathrated in the sodalite cages. Figure 3 shows the ^{29}Si spectrum of a sample of ultramarine with Si/Al = 1.11. The five peaks correspond, as in the case of zeolites X and Y, to Si(nAl) units. Their relative intensities are most unexpected and have immediate implications for the Si,Al distribution in the framework. If this distribution were random, and Al–O–Al linkages were not allowed, the probability of an Si–O–Al linkage would be $p = 1/r$, where r is the Si/Al ratio. For $r = 1$ we have $p = 1$ and all linkages must be of the Si–O–Al type, that is, only Si(4Al) units are present and the ^{29}Si spectrum consists of a single line. As r increases, other units appear with relative populations given by the binomial formula. However, the number and the relative intensities of the measured peaks for $r = 1.11$ are quite incompatible with this model. If, on the other hand, the distribution of Si and Al were *truly* random (that is Al–O–Al linkages are allowed), $p = 1/(1+r)$ and the sample with $r = 1$ would contain *all five* Si(nAl) units in the population ratio of 6.25 : 25 : 37.5 : 25 : 6.25. Spectral intensities calculated for $r = 1.11$ using this model are clearly in a very good agreement with experimental results. We must bear in mind, however, that synthetic ultramarine is prepared pyrolitically. The Loewenstein rule applies to all hydrothermally synthesized zeolites examined so far.

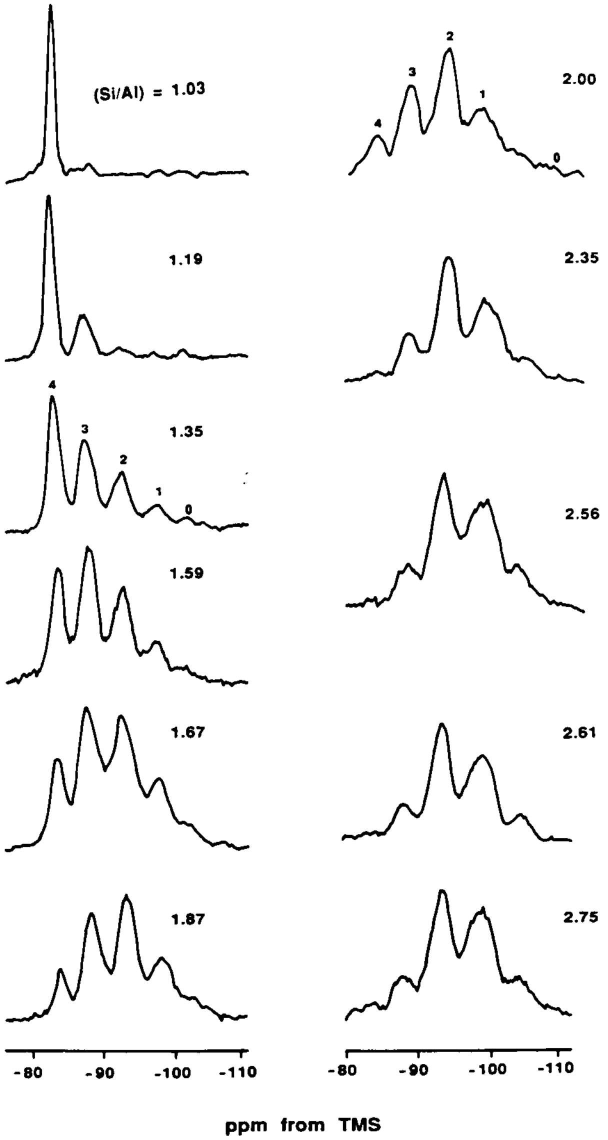

Fig. 1. High-resolution ^{29}Si MAS NMR spectra of synthetic zeolites NaX and NaY [31]. Si(nAl) peaks are identified by the n above the peaks.

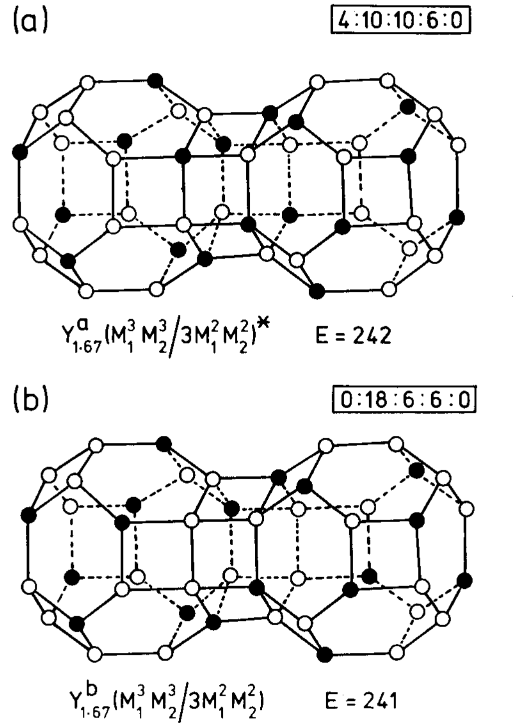

Fig. 2. Two of the possible Si, Al ordering schemes for zeolite Y with Si/Al = 1.67 [31]. Open circles denote Si atoms, closed circles Al atoms. The ratio of intensities Si(4Al) : Si(3Al) : Si(2Al) : Si(1Al) : Si(0Al) corresponding to each scheme is given in the upper right-hand corner. E is the calculated electrostatic energy for the double cage in units of $(qe)^2/a$, where a is the T–O–T distance. The asterisk denotes the preferred scheme.

RESOLVING CRYSTALLOGRAPHICALLY NON-EQUIVALENT TETRAHEDRAL SITES

In naturally occurring zeolites the Si/Al ratio is always less than about 5, but materials with much lower Al contents have been prepared in the laboratory. One of them, known as ZSM-5, has Si/Al ratio between 20 and many thousand and possesses remarkable catalytic properties. A crystalline microporous material called silicalite, isostructural with ZSM-5 but containing only traces of Al, has also been prepared.

In the light of the previous discussion, one might expect an uncomplicated spectrum for a highly siliceous zeolite, displaying the Si(0Al) peak, sometimes with a smaller Si(1Al) resonance, depending on the Si/Al ratio. The spectrum of a typical sample of as-prepared ZSM-5 is indeed almost featureless. The discovery [36] that the spectrum of silicalite with a particularly low Al content shows considerable fine structure was therefore a surprise. The chemical shifts of *all* the peaks in the spectrum are characteristic of Si(4Si) groupings in highly siliceous materials. The observed multiplicity arises from crystallographically inequivalent tetrahedral environments of the Si(4Si) sites. Spectra of silicalite of even higher resolution have subsequently been measured [37]. Figure 4 shows a spectrum in which as many as 19 individual lines can be separately resolved and the linewidth of the narrowest line is ca. 5 Hz, which brings it close to the realm of high-resolution NMR in liquids. The spectrum may be simulated by Gaussian peaks, and the total intensity of the spectrum is 24 times greater than the intensity of the smallest peak. This indicates that the space group of silicalite contains 24 nonequivalent sites in the unit cell.

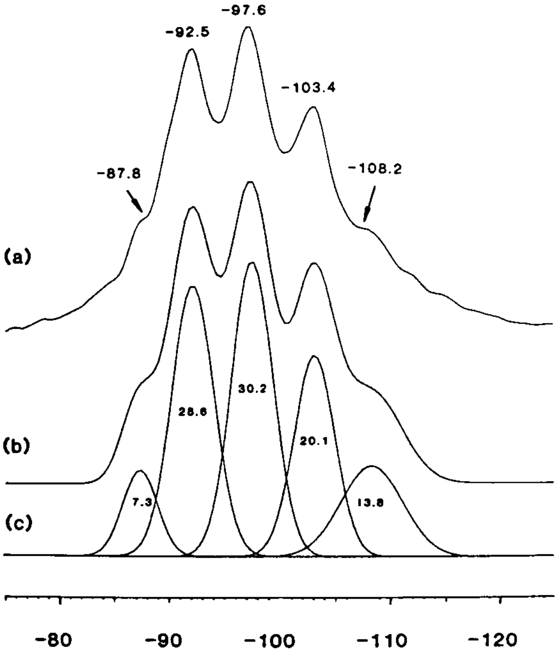

Fig. 3. (a) The ^{29}Si MAS NMR spectrum of pink ultramarine can be simulated, (b) using five Gaussian peaks, (c) with the ratio of intensity as indicated [35].

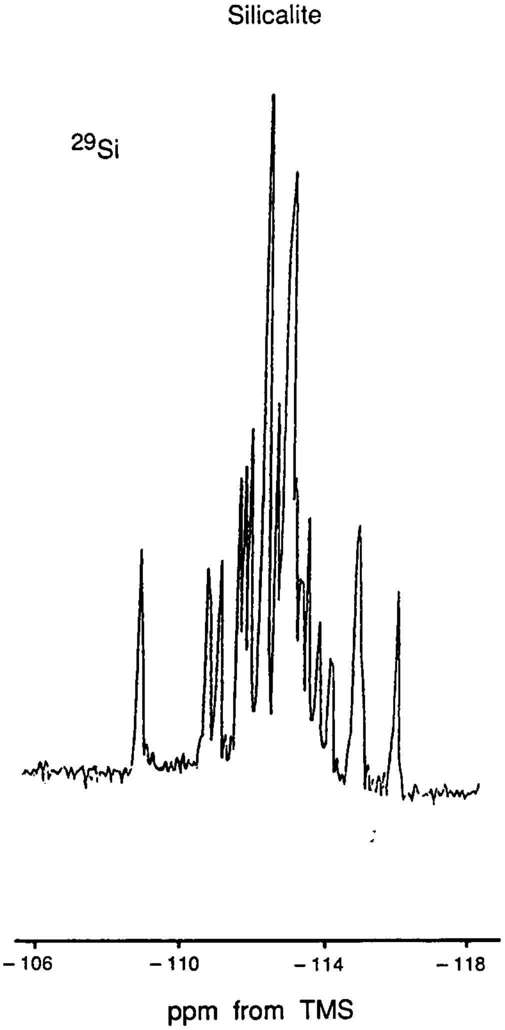

Fig. 4. ^{29}Si MAS NMR spectrum of silicalite at 293 K (courtesy Professor Yingcai Long).

X-ray diffraction (XRD) shows that silicalite can exist in the monoclinic and the orthorhombic forms and that the slight changes of symmetry involved are related to the residual aluminium content [38]. ^{29}Si MAS detects much more subtle changes in the structure of silicalite: minute temperature-induced variations in atomic positions [37,39,40] which do not necessarily involve symmetry changes detectable by XRD. NMR spectra measured in the range 153–403 K are sensitive even to small temperature changes and reveal that structural transformations continue over the entire temperature range. By contrast, the changes in the XRD pattern are slight. This demonstrates the remarkable sensitivity with which NMR can monitor atomic positions. The high-temperature spectrum shown in Fig. 5 can be simulated using Gaussian peaks of total intensity 12, indicating that above 363 K silicalite contains only 12 nonequivalent sites for silicon. It is interesting to note that the addition of very small amounts of adsorbed organics to dehydrated silicalite induces similar phase transitions and similar changes in the ^{29}Si NMR spectra [41–43].

The spectra of most synthetic zeolites do not reveal peaks which can be linked to specific silicon sites. However, when the ammonium form of a highly siliceous zeolite is heat-treated at temperatures of the order of 800°C in the presence of water vapour the resolution of the ^{29}Si spectrum improves dramatically [44–46]. Figure 6 shows the spectra of several zeolites before and after hydrothermal treatment. The framework Si/Al ratio of the products is of the order of several hundred. The intensities of the two peaks in the spectrum of the siliceous zeolite omega are in a 2:1 ratio corresponding to the two nonequivalent tetrahedral sites in the same population ratio. A similar situation exists in dealuminated offretite. The structure of mordenite, on the other hand, contains *four* nonequivalent sites in a 2:1:1:2 population ratio, and it is clear that the largest

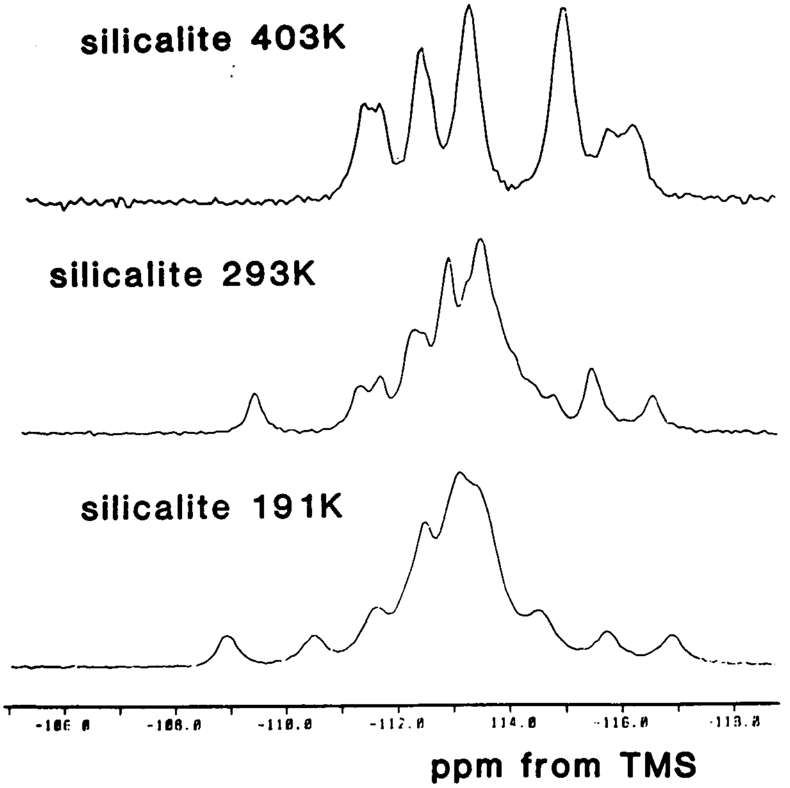

Fig. 5. ^{29}Si MAS NMR spectra of silicalite at 191 K, 293 K (compare Fig. 4) and 403 K [39].

peak at −115 ppm in Fig. 6 must be a composite (see below). The spectrum of dealuminated ZSM-5 is identical to that of silicalite.

One might expect crystallographic nonequivalence of the various Si sites to be observable by NMR not only when Al is isomorphously substituted by Si, but also when zeolites are purposely prepared with a very high Si/Al ratio. Unfortunately, relatively few zeolites can be synthesised with a sufficiently high Si/Al ratio for such detail to become perceptible in the spectra. High-resolution spectra of the highly siliceous zeolite ZSM-39 which contains only three kinds of silicon in a 1:4:12 population ratio demonstrate that the largest peak is split into three components of equal intensity [47,48]. This indicates loss of face centering of the Fd3m unit cell, which results in the disappearance of the three-fold symmetry axis.

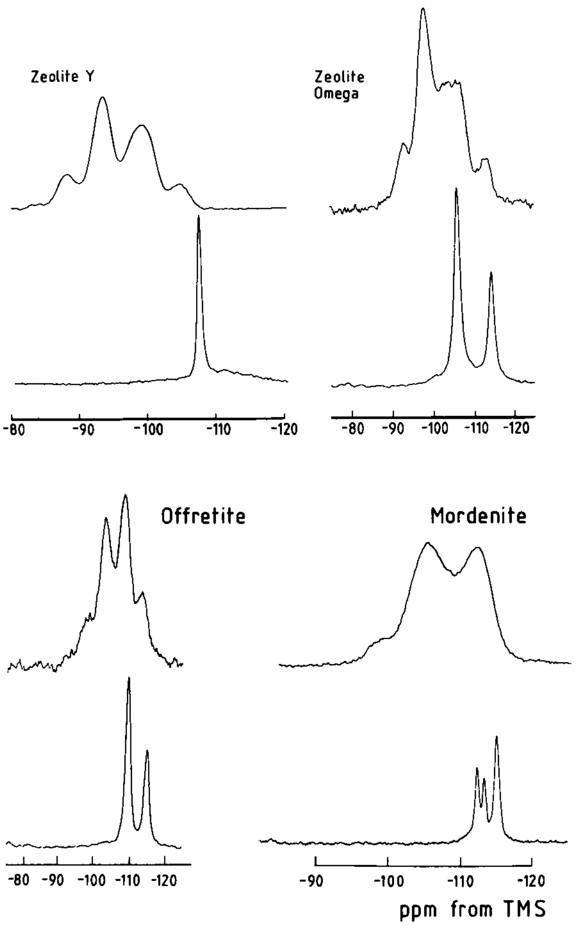

Fig. 6. ^{29}Si MAS NMR spectra of (above) zeolites Y, omega, offretite and mordenite; and (below) their dealuminated forms [44].

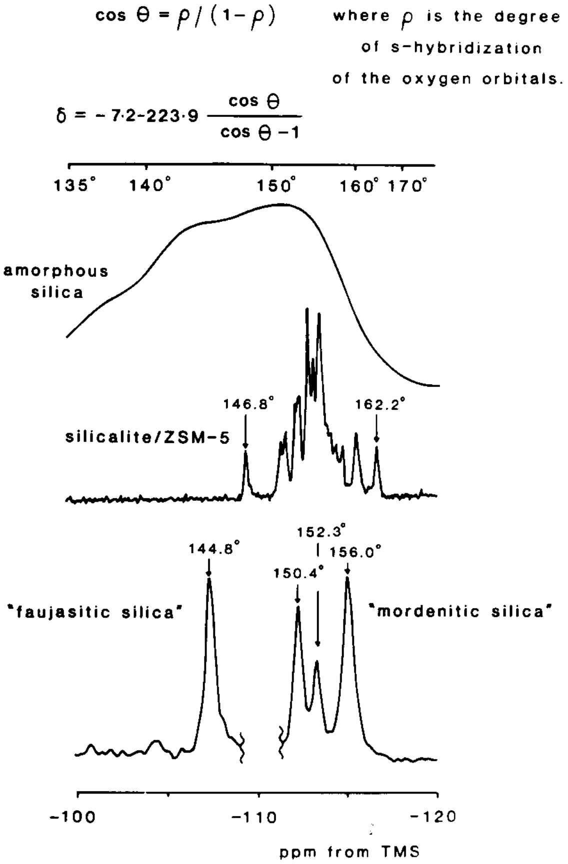

Fig. 7. The mean T–O–T angle versus the isotropic ^{29}Si chemical shift for amorphous silica and several purely siliceous equivalents of zeolites.

The fact that the ^{29}Si chemical shift is correlated with the T–O–T angles in zeolitic frameworks is very useful for structural determination [49–52,56]. Thus chemical shifts in the framework silicates cristobalite, quartz, albite and natrolite have been correlated with the mean Si–O bond *distances,* and relationships have been developed which are in good agreement with the results of semi-empirical calculations of chemical shift. A semi-empirical quantum-mechanical rationalization of the correlation between ^{29}Si chemical shift in framework silicates and the change of the *s* character of the oxygen orbitals in the Si–O–Si *s* bond has also been proposed [53,54] (see Fig. 7).

The observed correlation between chemical shifts of Si(nAl) units and mean bond angles has been explained [54] in terms of a simple quantum mechanical model and derived an equation confirmed by an extended set of experimental data consistent with various models involving θ, cos $\theta/(\cos\theta - 1)$, $\sin(\theta/2)$ and sec θ. The correlation works with these different functions of the angle because they are all approximately linear in the range of θ involved.

The original correlations were between the chemical shift of the Si(4Si) peak and the magnitude of the T–O–T angle. Ramdas and Klinowski [55a] extended these arguments to *all five* Si(nAl) peaks, and derived an approximately linear semi-empirical relationship between d of an Si(nAl) peak and the total (non-bonded) Si.....T distance (T = Si or Al) calculated from the T–O–T angle, assuming constant Si-O and Al–O bond lengths of 1.62 and 1.76 Å, respectively.

It is now easy to see why ^{29}Si MAS NMR peaks in the spectra of certain zeolites, such as mordenite and zeolite omega, lead to incorrect $(\mathrm{Si/Al})_{\mathrm{NMR}}$ values when assigned to individual Si(nAl) units in the simple fashion described above. When the chemical shift difference between peaks from non-equivalent Si(nAl) units with the same value of n (8.4 ppm in the case of $\mathrm{Si_A}$(0Al) and $\mathrm{Si_B}$(0Al) in zeolite omega) is similar to the shift difference between Si(nAl) and Si[($n \pm 1$)Al] units, the effects of Al substitution and crystallographic nonequivalence overlap. The peaks are composites, and their intensities $I_{\mathrm{Si}(n\mathrm{Al})}$ required in Eqn. 1 cannot be directly read off the spectrum. In the case of as-prepared zeolite omega the spectrum (see Fig. 6) is the sum of two mutually overlapping families of peaks. When this is taken into account, the entire spectrum can be correctly assigned and interpreted.

TWO-DIMENSIONAL SOLID-STATE NMR TECHNIQUES

Two-dimensional solid-state NMR techniques have been used to assign the individual NMR peaks to specific crystallographic sites [59–63]. In particular, two-dimensional homonuclear correlation spectroscopy (COSY), well established for the study of liquids, has been shown to be feasible with ^{29}Si in zeolites [57,58]. Isotopic enrichment in ^{29}Si was found to be useful.

The INADEQUATE experiment is very insensitive and requires an accurate estimation of the coupling constants. Despite this, there have been several successful ^{29}Si 2D INADEQUATE experiments in the solid state on highly siliceous zeolites. Excitation of a double quantum coherence can also be used in double-quantum filtered COSY. The only useful experiment of this type used a ^{29}Si-enriched sample of the highly siliceous zeolite ZSM-39 [58].

J-scaled COSY can provide useful information about zeolitic frameworks. The technique *scales up* the scalar splittings between the cross-peak components, thereby enhancing cross-peak intensities and consequently improving spectral resolution between adjacent diagonal and cross-peaks. The ^{29}Si J-scaled COSY experiment [63] with a scaling factor of 5, done at natural isotopic abundance, allows us to assign the spectrum of highly siliceous mordenite. The conventional ^{29}Si MAS NMR spectrum of the sample (Fig. 8) consists of three peaks in the intensity ratio of 2:1:3. This may be explained from the known structure of mordenite which contains four distinct tetrahedral crystallographic sites in the intensity ratio T1:T2:T3:T4 = 2:2:1:1 (Fig. 9), with two of the peaks overlapping. Assignment of the peaks on the basis of the correlation between ^{29}Si chemical shifts and the mean Si–O–Si bond angle (see above) is not possible in this case. The mean T–O–T bond angles in mordenite vary slightly with the degree of dealumination, cation type and water content, but the relative values remain approximately constant. The values for a highly siliceous mordenite given in Table 1 permit the immediate assignment of the downfield peak to the T1 site and show that the T2 site is a component of the strongest peak. However, the ⟨T3-O-T⟩ and ⟨T4-O-T⟩ bond angles are similar, so that it is not possible to assign the spectrum completely on the basis of bond angles alone. The two possible assignments of the three peaks in the spectrum are to T1:T4:T2 + T3 or to T1:T3:T2 + T4 crystallographic sites.

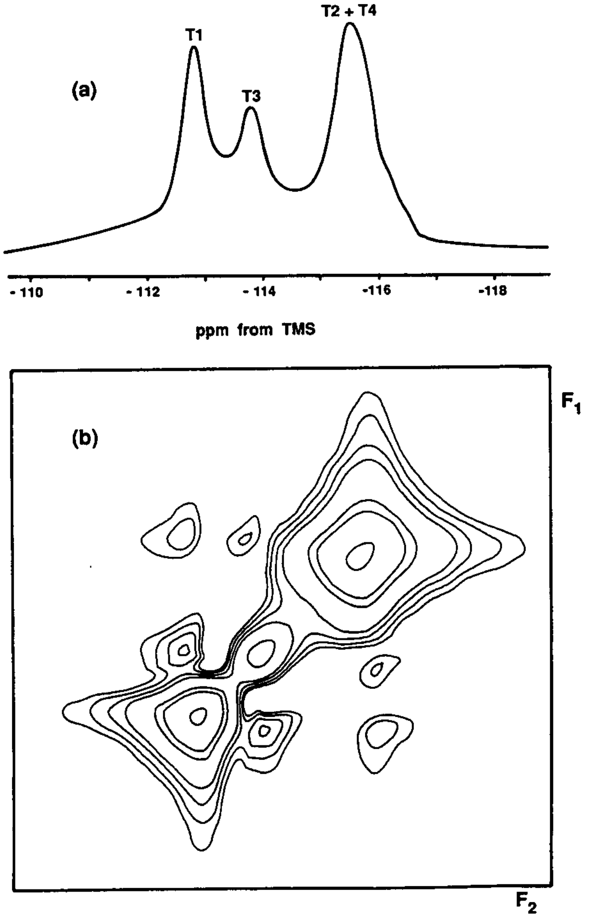

Fig. 8. NMR spectra of highly siliceous mordenite. (a) ^{29}Si MAS NMR spectrum; (b) J-scaled COSY spectrum [63].

The 2D J-scaled COSY spectrum of highly siliceous mordenite (Fig. 8) reveals three cross-peaks. On the basis of the known connectivities of the mordenite structure (Table 1), only two cross-peaks are predicted for the T1 : T4 : T2 + T3 assignment, while the T1 : T3 : T2 + T4 assignment implies that three cross-peaks should be observed. Thus the detection of three cross-peaks in the two-dimensional J-scaled COSY experiment shows that the correct interpretation is T1 : T3 : T2 + T4. Such unambiguous assignment of the spectrum is not possible by one-dimensional NMR or by conventional COSY.

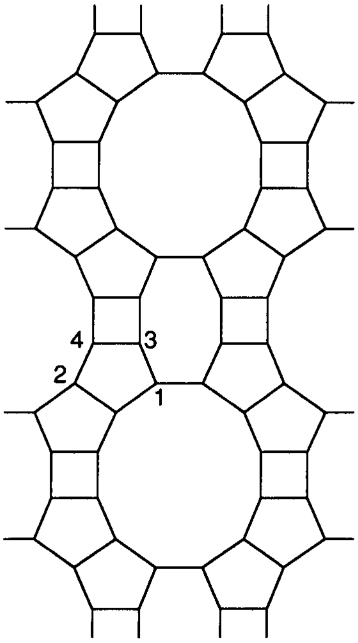

Fig. 9. The structure of mordenite viewed along [001] plane. The four kinds of crystallographic sites are indicated. Their relative populations (16 : 16 : 8 : 8 per unit cell) are not reflected in this projection.

DEALUMINATION AND REALUMINATION OF ZEOLITES

Solid-state ^{27}Al MAS NMR spectra of as-prepared zeolites generally contain a single peak corresponding to tetrahedrally coordinated Al. The apparent "chemical shift" of this peak as measured in a 9.4 T magnetic field ranges, for different materials, from ca. 51 to ca. 65 ppm from $Al(H_2O)_6^{3+}$. However, it must always be borne in mind that the second-order quadrupole interaction affects the position of the line, and

TABLE 1

Connectivities and typical mean T-O-T bond angles in the mordenite structure [63]

T-Site	No. per unit cell	Neighbouring sites	Mean T-O-T bond angle
T1	16	T1, T1, T2, T3	150.4°
T2	16	T1, T2, T2, T4	158.1°
T3	8	T1, T1, T3, T4	153.9°
T4	8	T2, T2, T3, T4	152.3°

the quadrupole correction to the chemical shift is strongly field-dependent. When this correction is made, the chemical shift is found to be related to structural parameters in a similar fashion to ^{29}Si chemical shifts. ^{27}Al MAS NMR spectra of chemically untreated zeolites are thus much simpler than their ^{29}Si counterparts. This is a direct consequence of the fact that while five types of Si(*n*Al) environments are possible for the silicon atom, only one possibility exists for the aluminium. However, while the coordination of Si in zeolites is always four-fold, Al can be 4- or 6-coordinated, and ^{27}Al MAS NMR is very sensitive to coordination. In aluminophosphate molecular sieves, 5-coordinated Al is often present.

Early work indicated that the amount of 6-coordinated (extra-framework) Al calculated from the difference between the result of chemical analysis and the quantity of *framework* Al measured from ^{29}Si spectra did not agree with the results of ^{27}Al MAS NMR: extra-framework Al was always underestimated by the latter. The

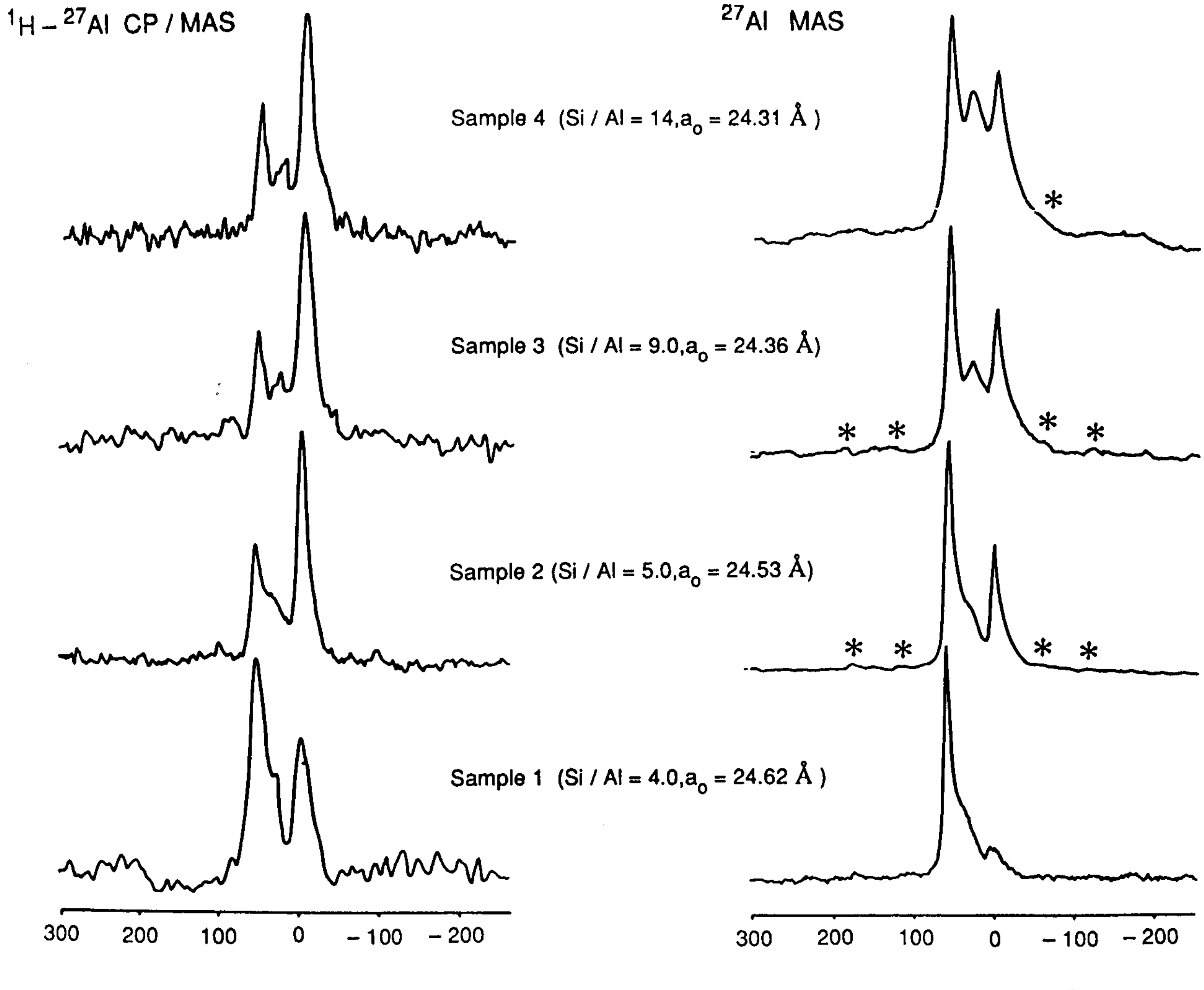

Fig. 10. ^{27}Al (MAS at 12–13 kHz) and ^{1}H–^{27}Al CP/MAS (MAS at 8–10 kHz) NMR spectra of increasingly dealuminated (from bottom to top) zeolite HY [72]. The Si/Al ratios calculated from ^{29}Si MAS NMR spectra and the unit cell parameters, a_0, are indicated. Asterisks denote spinning sidebands.

problem was resolved in the mid-80's when it was shown that quantitatively reliable ^{27}Al spectra must be obtained at very high magnetic fields, with fast magic-angle spinning, and using strong radiofrequency pulses with small flip angles [21–24].

Since Brønsted acid groups in zeolites are associated with 4-coordinated framework aluminium, their catalytic activity strongly depends on the concentration and location of Al in the structure. The aluminium content of the zeolitic framework can be decreased by a number of methods. Upon hydrothermal treatment of zeolite NH_4-Y, the process known as "ultrastabilization" [64], part of the aluminium is ejected from the framework into the intracrystalline space, and the vacancies are reoccupied by silicon from other parts of the crystal. As a result, thermal stability of the zeolite is greatly increased, so that the product retains crystallinity at temperatures in excess of 1000°C. Ultrastable zeolite Y has been extensively examined by ^{29}Si and ^{27}Al solid-state NMR [65–69]. Samples subjected to different types of treatment have been examined, while the Si/Al ratio were determined from spectral intensities using Eqn. 1. ^{29}Si NMR clearly shows that Al is removed from the framework, and that the resulting vacancies are subsequently re-occupied by silicon which, contrary to earlier speculations, does not come only from the surface or from amorphous parts of the sample, but also from its bulk, which may involve the elimination of the entire fragments of the framework. Chemical analysis shows no change in composition: the "missing" Al is now in 6-coordination, and there is a consequent loss of ion-exchange capacity. ^{27}Al MAS NMR shows how 6-coordinated non-framework Al species (Al^{NF}) build up at the expense of the 4-coordinated framework Al (Al^{F}) as the calcination temperature is increased.

In order to elucidate the nature of Al^{NF}, ^{1}H–^{27}Al CP/MAS NMR spectra of samples of the dealuminated samples were recorded [70–72]. Figure 10 clearly shows that the intensity of the peaks at 0 and 30 ppm increases relative to the peak at 60 ppm. This indicates that the 30 ppm peak is a separate ^{27}Al resonance, possibly due to 5-coordinated Al. Furthermore, the position of NMR peaks in ^{27}Al MAS NMR spectra reported in Ref. 70, recorded at the higher field of 11.7 T (as opposed to 9.4 T in Ref. 72), is the same at 0, 30 and 60 ppm. As the second-order quadrupole interaction is inversely proportional to the magnetic field, components of a quadrupolar lineshape must shift to high frequency when the magnetic field is increased. Since the distance between peaks is unchanged, they must correspond to independent resonances.

The ^{27}Al CP/MAS spectrum of zeolite Na–Y (not shown) contains two very faint peaks at 61 and 9 ppm, presumably due to a small amount of impurity. These peaks are an order of magnitude weaker than the peaks in the spectrum of dealuminated Y shown in Fig. 10. A peak at ca. 60 ppm is clearly seen in the ^{1}H–^{27}Al CP/MAS spectrum of dealuminated zeolite Y, probably associated with 4-coordinated non-framework Al. The possibility that two (or more) ^{27}Al resonances overlap at ca. 60 ppm must therefore be considered.

The process of ultrastabilization can be completely reversed by a simple hydrothermal treatment with aqueous solutions of strong bases [73,74]. The reaction can be profitably studied by NMR, which indicates that aluminium atoms hydrothermally eliminated from the framework of zeolite Y can be subsequently reinserted into the framework. Sample crystallinity is largely retained in the process, and is strongly dependent upon the residual sodium content of the parent material, the concentration of the base and the temperature.

^{29}Si MAS NMR spectra of dealuminated samples (middle traces in Fig. 11) indicate the removal of framework aluminium from the parent sample (top trace). However, the spectra of samples treated with KOH (lower traces) are dramatically different. The intensities of the Si(0Al) peaks are greatly reduced, and the intensities of the Si(1Al), Si(2Al), Si(3Al) and Si(4Al) peaks correspondingly increased, signifying that a considerable amount of aluminium has entered the framework. Using values of $(Si/Al)_{NMR}$ calculated from Eqn. 1 in conjunction with the values of the *overall* Si/Al ratio measured by X-ray fluorescence we can calculate the number of

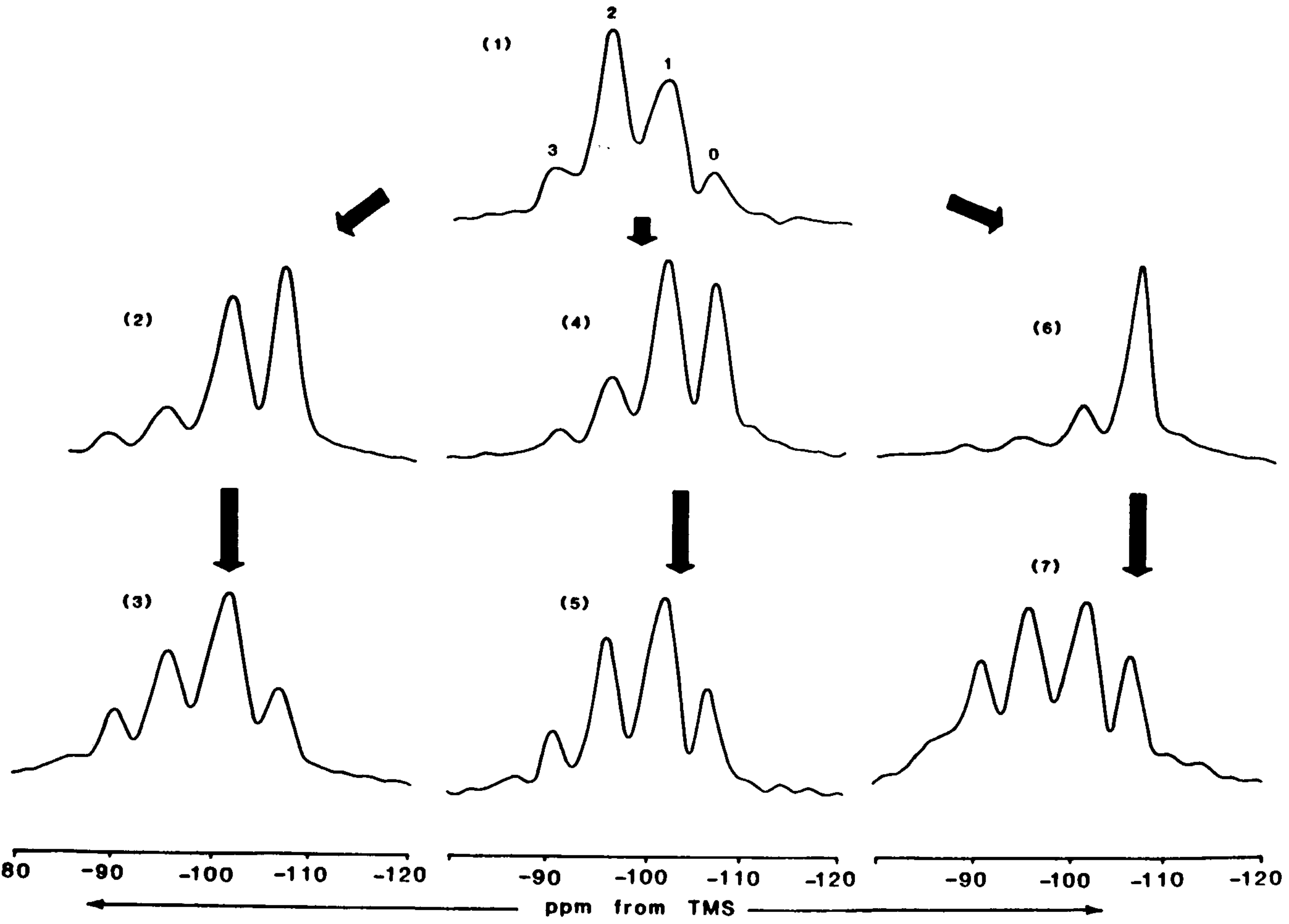

Fig. 11. ^{29}Si MAS NMR spectra of ultrastabilized and hydrothermally realuminated zeolites for the single ultrastabilization/realumination cycle [73]. Sample 1 (Si/Al = 2.56) is the parent for samples 2, 4 and 6 (Si/Al ratios 4.96, 4.26 and 7.98 respectively), which upon treatment with KOH solution give rise to samples 3, 5 and 7 (Si/Al ratios of 2.44, 2.70 and 2.09), respectively. Numbers above individual peaks give the *n* in Si(*n*Al).

framework and non-framework atoms per unit cell. The results show that all extra-framework Al atoms in samples 2, 4 and 6 have re-entered the framework to give realuminated samples 3, 5 and 7, respectively. Furthermore, the spectra of the realuminated samples are very different from that of the parent sample 1 despite the fact that the composition of all four samples is similar. This shows that although the overall structure of the crystal is known exactly, the Si, Al *distribution* among the tetrahedral sites is different in each case.

^{27}Al quadrupole nutation NMR offers insights into the dealumination-realumination process. In this technique [75–78], a series of free induction decays during the interval t_2 is acquired using powerful resonant radiofrequency pulses while monotonically increasing the length, t_1, of the pulse. Double Fourier transformation in t_2 and t_1 gives a two-dimensional nutation NMR spectrum (in the magnitude mode) with the axes F_2 (containing combined chemical shift and the second-order quadrupole shift) and F_1 (containing quadrupolar information only). The technique permits ^{27}Al sites with different quadrupole coupling constants to be resolved along F_1.

The nutation spectrum of the parent sample 1 (Fig. 12) consists of two peaks, at (60 ppm, 78 kHz) and (60, 195), both with the same linewidth and both corresponding to framework (F) aluminium. The presence of *two* peaks is due to the fact that the quadrupole interaction characteristic of framework ^{27}Al is of the same order of magnitude as the strength of the radiofrequency pulse. Sample D-1 has been mildly and sample D-2 strongly, dealuminated. Figure 12 clearly shows that the amount of framework aluminium decreases in the process. Similarly, the nutation spectra of realuminated samples R-3 and R-4 demonstrate that the aluminium does go back into the framework. As realumination progresses, the F peak increases at the expense of the other peaks.

NMR STUDIES OF THE STRUCTURE OF BRØNSTED ACID SITES

The study of acidic surface sites capable of donating protons to adsorbed molecules is crucial to heterogeneous catalysis. It is vital to know the concentration, strength and accessibility of the Brønsted and Lewis acid sites and the details of their interaction with the adsorbed organics. The Brønsted acidity of zeolites arises from the presence of accessible hydroxyl groups associated with framework aluminium ("structural hydroxyls"). However, the inherent difficulty with ^{1}H NMR in the solid state is the dipolar interaction with other protons and other magnetically-active nuclei which leads to substantially broadened NMR spectra. When groups of more than two interacting nuclei are present, the situation is complicated still further. It turns out that even then the method of moments, developed by Van Vleck [79] can provide important information about the sample. Extensive ^{1}H MAS NMR measurements of zeolites have led to the assignment of the various proton resonances as follows [80,81]:

Line "a", at 1.3–2.3 ppm from tetramethylsilane (TMS), due to non-acidic (silanol) hydroxyls on the surface of zeolite crystallites and crystals defects sites.

Line "b", at 3.8–4.4 ppm from bridging OH groups involving O_1 oxygen atoms and pointing towards the zeolitic supercages.

Line "c", at ca. 5 ppm from protons on O_3 atoms and pointing towards the other oxygens in the sodalite cages.

Line "d", at 6.5–7.0 ppm, due to residual NH_4^+ cations.

Line "e", at 2.6–3.6 ppm, due to Al–OH groups attached to non-framework Al.

^{1}H NMR of static samples can readily probe the geometry of the Brønsted acid site [82,83]. It is a convenient tool for the determination of the Al–H distance, because the second moment of the broad-line proton spectra, which is inversely proportional to the *sixth* power of the distance between the dipole-coupled nuclei, is dominated by the ^{1}H–^{27}Al interaction. Spectra are obtained by the Fourier transformation of the FID following the $\pi/2 - \tau - \pi$ pulse sequence. An argument based on the Van Vleck's formula has been used [84] to calculate the aluminium–proton distance, $r_{\text{Al-H}}$, from the second moment, M_2:

$$r_{\text{Al-H}} = \sqrt[6]{\frac{126.09}{M_2}} \qquad (2)$$

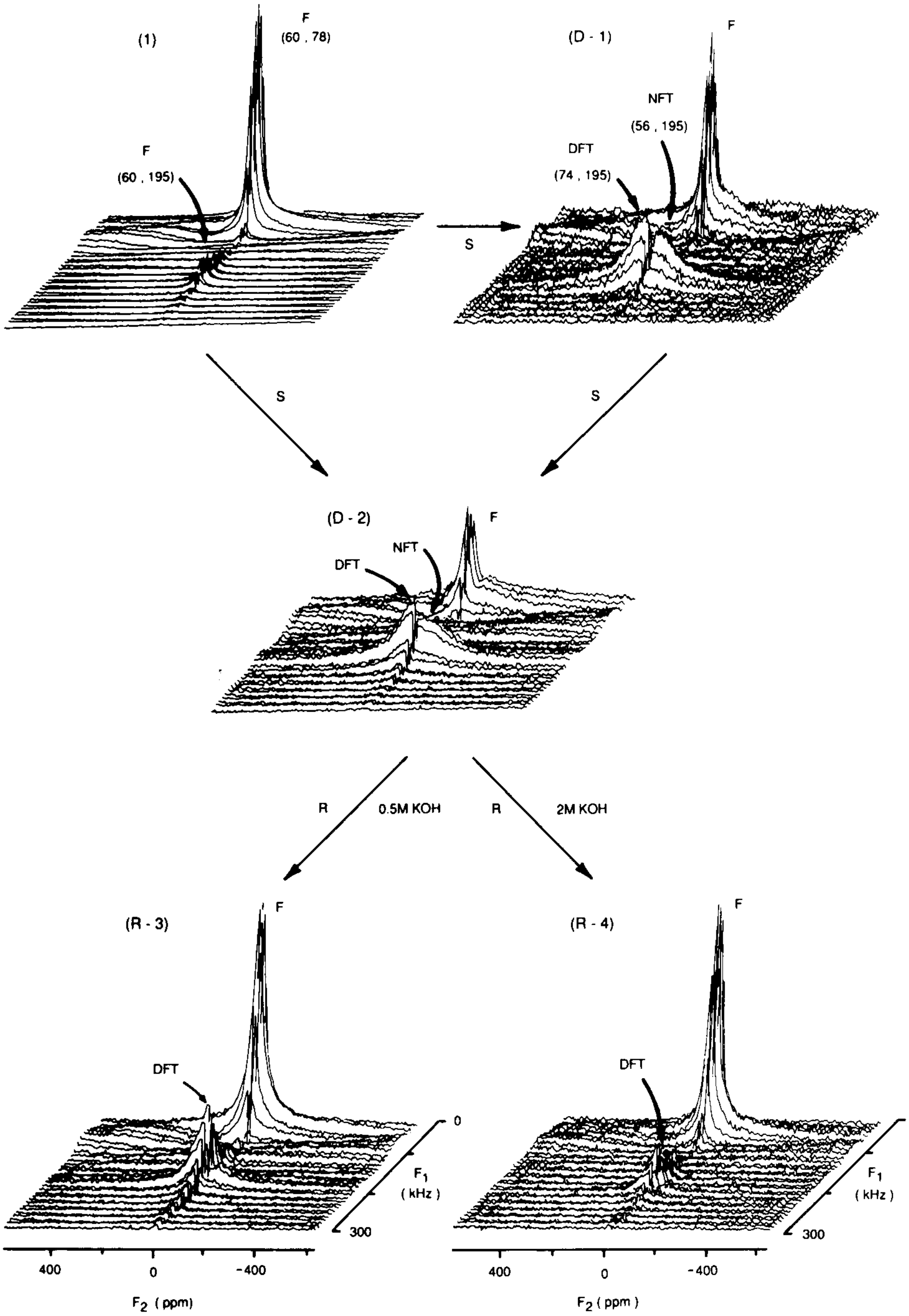

Fig. 12. ^{27}Al quadrupole nutation spectra of hydrothermal dealumination–realumination [76]. Parent sample 1 has been steamed (S) for various lengths of time to give dealuminated samples D-1 and D-2 (framework Si/Al ratios of 3.10 and 4.91). Sample D-2 has been realuminated (R) with KOH to give samples R-3 and R-4 (Si/Al ratios of 2.59 and 1.54).

where r_{Al-H} is in Å and M_2 in units of 10^{-8} T^2. The conditions which must be met for this method to be quantitatively correct are:

(1) dipole–dipole interactions additional to the interaction between a single proton and a *single* aluminium nucleus are either absent or taken into account;

(2) the non-resonant spins (e.g. ^{27}Al when observing ^1H) are oriented in the Zeeman field and not in the quadrupole field;

(3) line broadening due to chemical shift anisotropy is either negligible or taken into account;

(4) the protons are immobile and the apparent second moment is not motionally reduced.

^1H NMR studies of zeolite H–Y have concluded [81,82] that (i) the experimentally measured M_2 is 0.88×10^{-8} T^2; (ii) the interactions with other protons contribute 0.05×10^{-8} T^2; (iii) the mean total contribution of second-nearest Al atoms to M_2 of O_1 and O_3 hydroxyls is 0.06×10^{-8} T^2; (iv) the contribution of quadrupolar effects is negligible; (v) the anisotropy of the chemical shift contributes 0.08×10^{-8} T^2; and (vi) for the purpose of the second moment the zeolitic framework is rigid. Equation 2 shows that the final value $M_2 = 0.69 \times 10^{-8}$ T^2 for an isolated bridging hydroxyl group corresponds to $r_{H-Al} = 2.38 \pm 0.04$ Å.

In zeolite H-ZSM-5 the second moment arising from the interaction with other protons and second-nearest aluminium atoms is always negligible. The second moment attributable to SiOH groups on framework defects measured in the parent zeolite Na-ZSM-5 (which contains very few bridging hydroxyls) is $(0.40 \pm 0.2) \times 10^{-8}$ T^2. Considering that in H-ZSM-5 the SiOH groups amount to 20% of the total hydroxyl concentration, $M_2 = (0.54 \pm 0.04) \times 10^{-8}$ T^2 for bridging hydroxyl groups. The theoretical lineshape of a ^1H–^{27}Al pair is a superimposition of *three* Pake doublets: one due to the interaction of ^1H with ^{27}Al in the states with $S = \pm 1/2$ and two doublets due to $S = \pm 3/2$ and $S = \pm 5/2$. The second moment calculated from the distance between the $\pm 5/2$ singularities found in the spectrum gave $M_2 = (0.54 \pm 0.05) \times 10^{-8}$ T^2, which corresponds to $r_{H-Al} = 2.48 \pm 0.04$ Å for the bridging hydroxyl groups. The Al–H distance in zeolite H-ZSM-5 is larger than in zeolite H–Y because of the smaller T–O–T angles in a framework composed mostly of 5-membered rings.

There is at present only a handful of publications involving ^{15}N NMR of molecules sorbed on zeolites, but they establish the power of the technique for the study of zeolitic acidity and other surface phenomena. The nitrogen atom in molecules such as ammonia and pyridine has a lone pair of electrons and binds directly to the surface site. One is therefore observing large effects on a nucleus with a wide (ca. 900 ppm) range of chemical shifts, rather than more indirect influence as in the case of ^{13}C. Michel et al. [85,86] and Jünger et al. [87] measured the spectra of isotopically enriched ammonia, trimethylamine, pyridine and acetonitrile on various zeolites and found that resonance shifts depended strongly on the interactions of sorbate molecules with cations and Brønsted and Lewis acid sites. The ^{15}N chemical shift changes by 18.5 ppm as the pore-filling factor θ of $^{15}NH_3$ on zeolites Na–X, Na–Y, Na-mordenite and Na–Y varies between 0 and 1. In sodium forms, the resonance shift is mainly due to intermolecular interactions. For ultrastable zeolite Y, the ^{15}N resonance of ammonia does not change between $\theta = 0.2$ and 0.72, and is approximately equal to that measured for liquid ammonia. Michel et al. [85,86] concluded that at higher θ the ammonia molecules are packed so closely that their resonance shift becomes liquid-like. In ultrastabilized samples strong association of ammonia molecules occurs even at low coverages leading to constant chemical shift. At low coverages, the resonance shift of $^{15}NH_3$ on zeolite H–Y remains constant and is close to that for NH_4^+ solutions, which shows that all ammonia molecules are converted into ammonium cations as a consequence of interaction with structural hydroxyl groups. Consideration of the equilibrium between the surface sites and the sorbate allows the resonance shifts for the surface complexes to be obtained and to eliminate the influence of the exchange process. The formation of pyridinium ions in ultrastable zeolites has been followed, leading to direct determination of the number of interacting hydroxyl groups. ^{15}N is far superior to ^{13}C for this purpose. Acetonitrile can be conveniently used for characterization of interactions with the exchangeable cations and Lewis acid sites [85–87]. Electron acceptor strength of ultrastable zeolites increases with the increased temperature of activation, the rise being particularly drastic in the region 300–400°C. NMR shows unambiguously that the exchangeable cations in zeolite X act as adsorption centers.

Trimethylphosphine has also been used [88,89] as a probe in ^{31}P MAS NMR studies of zeolite H–Y. When a sample is activated at 400°C, the spectrum is dominated by the resonance due to $(CH_3)_3PH^+$ complexes formed by chemisorption of the probe molecule on Brønsted acid sites. At least two types of such complexes were detected: an immobilized complex coordinated to hydroxyl protons, and a highly mobile one which is desorbed at 300°C.

GALLOSILICATE AND BOROSILICATE ZEOLITES

Tetrahedral Al and Si in the zeolitic framework can be substituted by Ga, Ge, B, Ti, and possibly other elements, in the course of direct synthesis. (Si,Ga)-, (Ge,Al)- and (Ge,Ga)-zeolites are structurally similar to their Si,Al counterparts. Gallium analogues of a number of zeolites have been prepared. ^{29}Si MAS NMR spectra of (Si,Ga)-sodalites and (Si,Ga)-faujasites [90,91] allow $(Si/Ga)_{NMR}$ ratios to be calculated from a formula similar to Eqn. 1, which shows that the gallosilicate equivalent of the Loewenstein rule applies, i.e. that no Ga–O–Ga linkages are present. The composition of (Si,Ga)-sodalite is such that $Si/Ga > 1$, while for (Si,Al)-sodalite $Si/Al = 1.00$. Furthermore, the distribution of peak intensities corresponding to the various Si(nGa) units in gallosodalite is different from that measured in aluminosilicate zeolites ZK-4 and X of similar Si/T ratio (T = Al or Ga) which indicates that the distribution of Si and Ga in gallosodalites, while always Loewensteinian, is different from the distribution of Si and Al in aluminosilicate zeolites.

The ^{29}Si chemical shifts in gallium zeolites span a wider range (25.1 ppm in (Si,Ga)–X) than in the corresponding aluminosilicates (18.5 ppm in (Si,Al)–X). Also, the Si(nGa) silicon atoms are deshielded (i.e. their chemical shift is less negative) in comparison to Si(nAl) silicon atoms in ordinary zeolites with the same n. The difference is proportional to n, which indicates that it is the Ga in the *first* tetrahedral coordination sphere which is responsible for the effect.

Boron is another potential constituent of zeolitic frameworks. Early attempts at introducing B by direct synthesis from a gel containing silicates, aluminates and borates failed. This is because B has a low affinity for such frameworks in comparison with Al, and the latter is introduced preferentially when the concentrations of the two in the synthesis mixture are comparable. More recently, however, borosilicate zeolites containing as many as five B atoms per unit cell have been sucessfully prepared by adding boron compounds to synthesis mixtures used for the preparation of highly siliceous zeolites. ^{11}B spectra of some borosilicate zeolites show [92] that tetrahedral boron resonates at ca. −3.5 ppm from $BF_3 \cdot OEt_2$. On dehydrating (Si,B)–ZSM-5 (known as boralite) the intensity of the tetrahedral line reversibly decreases and a second broad line appears. The width of that line, assigned to trigonal B, is dependent on the magnetic field intensity, which indicates that the effect is quadrupolar in nature. The quadrupole coupling of ^{11}B in borates and borosilicates is as much as 2.4–2.8 MHz for trigonal boron and < 0.8 MHz for tetrahedral boron [93].

$AlPO_4$ MOLECULAR SIEVES

Aluminophosphate molecular sieves, designated as $AlPO_4$, are formally the porous crystalline equivalents of aluminium phosphate. Many such structures have been prepared, including a number which do not have analogues among conventional zeolites, including $AlPO_4$-5, first described by Bennett et al. [94], VPI-5, a remarkable material with 18-membered rings [95,96], the topology of which had been predicted [97] in advance of its being synthesized, and cloverite, a gallophosphate molecular sieve with 20-membered rings, the most porous molecular sive prepared so far [98]. The $AlPO_4$ are clearly a fascinating class of materials and a challenge to multinuclear solid-state NMR given the wide variety of new crystal structures, the fact that they contain two different kinds of 100% abundant nuclei (^{31}P and ^{27}Al) in close proximity and aluminium in 4-, 5- and 6-coordination with respect to oxygen. Blackwell and Patton [99] were the first to take up the challenge when they measured the spectra of $AlPO_4$-5, $AlPO_4$-11, $AlPO_4$-17 and $AlPO_4$-31 and compared them with some non-microporous materials, such as $AlPO_4$-quartz, metavariscite and $AlPO_4$-tridimite. The spectra were generally consistent with known framework structures, but the ^{27}Al chemical shift range was wide (from -18.7 to 44.9 ppm) and quadrupolar effects were very much in evidence even in the 9.4 T magnetic field. This indicates that electric field gradients in $AlPO_4$s are very considerable. The template molecules present in as-synthesised $AlPO_4$ affect the ^{31}P NMR chemical shifts.

The main challenge in NMR spectroscopy of $AlPO_4$s are the quadrupolar effects involving ^{27}Al as a result of which the quadrupole correction to chemical shifts is much larger than in conventional zeolites. The ^{29}Si chemical shifts in SAPOs are similar to those found in zeolites: -92 ppm in SAPO-5 and -90.2 ppm in SAPO-37, a material with the faujasite structure. ^{11}B in BAPO-5 resonates at -1.1 ppm and ^{31}P at -29 ppm. Both these values are typical of tetrahedral coordination.

Kolodziejski et al. [100] undertook a 2D ^{31}P NMR study of spin diffusion in $AlPO_4$ molecular sieves, and chose VPI-5 as a model sample. As mentioned above, VPI-5 is a crystalline aluminophosphate molecular sieve containing 18-membered rings of tetrahedral atoms. The large channel diameter (ca. 12 Å) gives VPI-5 considerable potential for the separation of large molecules, and for catalytic cracking of the heavy fractions of petroleum which at present are discarded as bottom-of-the-barrel residue. Rudolf and Crowder [101] were the first to refine the structure of the as-prepared material from the XRD pattern, but their refinement leaves a large difference between the observed and calculated patterns. Also, the ^{31}P and ^{27}Al MAS NMR spectra are difficult to reconcile with the proposed structure. First, the space group $P6_3cm$ calls for two crystallographically distinct phosphorous positions with relative occupancies 2:1, while the room-temperature ^{31}P MAS NMR spectrum contains three resonances (see Fig. 14). Second, the ^{27}Al MAS NMR spectrum contains peaks from 4- and 6-coordinated aluminium, but the latter cannot be accounted for in this model. Finally, the structure of VPI-5 was refined in the $P6_3$ space group [102] (see Fig. 13), which is fully consistent with the NMR results. This refinement locates all the water molecules inside the large pore of VPI-5: two molecules complete an octahedral coordination sphere around the framework aluminium atom between the fused 4-membered rings; four of the remaining water positions form a hydrogen-bonded chain linking the 6-coordinated aluminium atoms, thus forming a triple helix of water molecules. The last, less well defined, water position links the helices to one another. The ^{31}P MAS NMR spectrum of hydrated VPI-5 shows three peaks in an intensity ratio of 1:1:1. Variable-temperature studies [103] (Fig. 14) assigned the peaks at -23 ppm (1) and -27 ppm (2) to phosphorous atoms in 6–4 sites (P2 and P3) and the peak at -33 ppm (3) to phosphorous atoms in 4–4 sites (P1). However, it is was not known how peaks 1 and 2 are to be assigned to *particular* P2 and P3 sites. The structural inequivalence of the P2 and P3 sites results from framework distortion caused by the coordination of two water molecules to Al1. This distortion is so small that the correlation between the ^{31}P chemical shift and mean Al–O–P angle is not sufficiently sensitive to be useful for the assignment.

Spectral spin diffusion in the solid state involves simultaneous flip-flop transitions of dipolar-coupled spins with *different* resonance frequencies. The interaction of spins undergoing spin diffusion with the proton reservoir provides compensation for the energy imbalance. Spin diffusion results in an exchange of magnetization between the nuclei responsible for resolved NMR peaks, which can be conveniently detected by observing the relevant cross-peaks in the 2D spin-diffusion spectrum.

2D NMR reveals that spin diffusion is present in a wide range of mixing times. The spectra have a remarkably high signal-to-noise ratio (Fig. 15) and each pair of peaks gives rise to cross-peaks. However, Fig. 15 shows that spin diffusion can be slowed down by fast MAS. The proton reservoir is not relevant to the ^{31}P spin-diffusion process in VPI-5, and thus that this process is governed only by the ^{31}P–^{31}P dipolar interactions. Therefore, a reasonable assumption would be that only the strongest ^{31}P–^{31}P dipolar interactions survive under fast MAS, and this must be reflected in the dependence of the cross-peaks intensities on the rate of MAS. We compared the strongest ^{31}P–^{31}P dipolar interactions calculated from the XRD structure: P2–P3 (192 Hz) < P1–P2 (281 Hz) < P1–P3 (304 Hz) with the MAS rates (in brackets) corresponding to the inflection points of the curves: 1–2 (5.91 kHz) < 1–3 (6.03 kHz) < 2–3 (8.07 kHz). This showed that peaks 1, 2 and 3 should be assigned to sites P2, P3 and P1, respectively, and that spin diffusion could be useful for the assignment of spectral peaks in other phosphate molecular sieves.

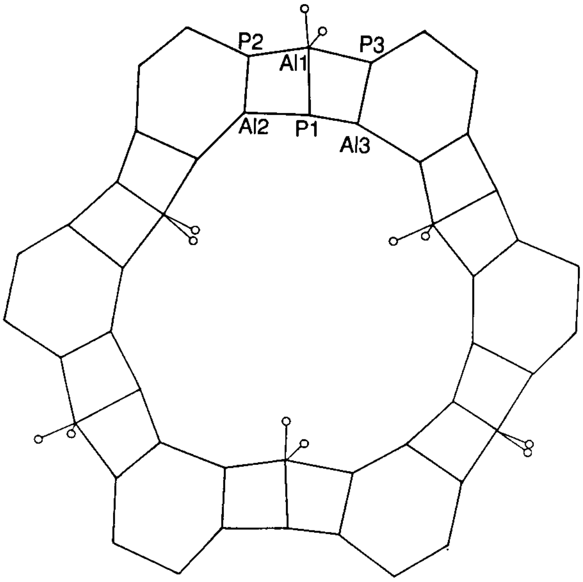

Fig. 13. One layer of the framework structure of hydrated VPI-5 taken from the stereoscopic view along the [001] direction according to McCusker et al. [102] showing the deviation from $P6_3cm$ symmetry. Aluminium and phosphorous atoms, linked via oxygen atoms (not shown for clarity) are located at the apices of the polygons. Sites located between two fused 4-membered rings are known as 4–4 sites; those located between 6-membered and 4-membered rings are known as 6–4 sites. P2 and P3, and Al2 and Al3 sites are inequivalent as a result of the distortion. The Al1 site is 6-coordinated as a result of bonding to four bridging oxygens and two "framework" water molecules. Other intracrystalline water is not shown.

^{2}H NMR STUDIES OF MOTION IN MOLECULAR SIEVES

The very small quadrupole interactions of ^{2}H makes it particularly useful in chemical studies. As a consequence of the presence of two ($1 \leftrightarrow 0$ and $0 \leftrightarrow -1$) different spin transitions, the spectrum of a deuterated organic in a solid is a doublet, the peak separation of which is related to the orientation of ^{2}H–^{13}C bond in the external magnetic field. Dipolar interactions of ^{2}H are up to 10 kHz, and manifest themselves as spectral broadening. Since the quadrupolar interactions of ^{2}H are sensitive to molecular motion, the nucleus is very useful for chemical studies of molecular motion at a wide range of frequencies. ^{2}H NMR is a convenient tool for the study of molecular ordering and molecular motion of adsorbed probe molecules, and may become an important complementary technique for the study of interface systems in general, and liquid crystals in particular. ^{2}H NMR is not a *direct* technique of spectral interpretation, but one which relies on the agreement between the spectra and a particular model. Experiments are performed with *static* samples, and dynamic information is extracted by comparing spectra measured at different temperatures with model computer simulations involving a number of adjustable parameters. An enormous amount of ^{2}H work in solids has been reported but, surprisingly, there are not many recent papers which are directly relevant to molecular sieves [104–111]. This area has a considerable potential, particularly in view of the ever increasing power of computer work-stations.

Eckman and Vega [106] investigated the dynamics of small organic molecules, such as methanol, benzene, toluene and *p*-xylene, adsorbed on a series of zeolites in a range of temperatures. They obtained information on the dynamics of the filling of the intracrystalline space, the motion of the adsorbed species and site-selective adsorption. Kustanovich et al. [107] interpreted the ^{2}H spectra of two deuteriated species of *p*-xylene, $CH_3C_6D_4CH_3$ and $CD_3C_6H_4CD_3$, on zeolite Na-ZSM-5 in terms of possible dynamic states and sorption sites of the guest molecules. Five dynamic states were identified, with relative populations varying with the level of loading and the temperature. Deuterium NMR results on *p*-xylene-d_6, toluene-d_3 and benzene-d_6 sorbed on H–ZSM-5 [108], as well as on mono-, di- and trimethylamine adsorbed on zeolites ZK-5 and Y [109] have been reported, in all cases yielding a wealth of dynamic information.

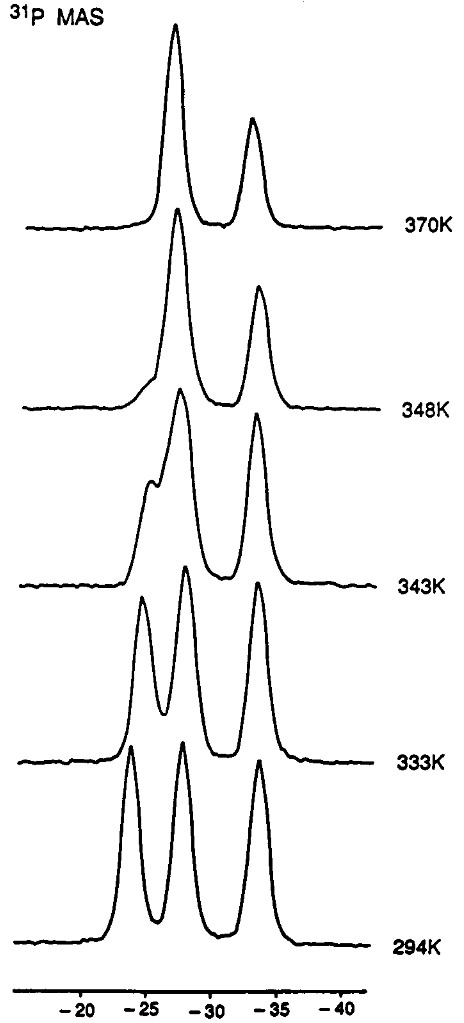

Fig. 14. ^{31}P MAS NMR spectra of VPI-5 at various temperatures.

Duer et al. [110] re-examined the dynamic behaviour of water in the channels of VPI-5 in order to arrive at a motional model which applies throughout the temperature range from 225 to 348 K. An earlier model [111] is unsuccessful in part of this range. There are at least two sites for the intracrystalline water: one is bound to framework aluminium, and undergoes rotational motion about the Al–OH_2 bond, the other is a free site within the VPI-5 channels. The motion in this site is approximately isotropic, with increasing tumbling rate with temperature. The results, discussed with reference to a six-site motional model, show an interesting dynamic behaviour in the temperature range 261–297 K.

CHEMICAL STATUS OF GUEST ORGANICS IN THE INTRACRYSTALLINE SPACE

The declining oil reserves have stimulated considerable efforts towards the exploration of alternative sources of energy and organic chemicals. One solution is to use the abundant supply of coal as a source of synthesis gas (CO + H_2) which is readily converted to methanol (MeOH). MeOH can then be transformed into higher molecular weight hydrocarbons (olefins, aliphatics and aromatics) over shape-selective zeolite catalysts, the most successful of which in this respect is H–ZSM-5, capable of converting MeOH to hydrocarbons up to C_{10}. The selective synthesis of ethylene and propylene, the key intermediates for the production of detergents, plasticizers, lubricants and a variety of chemicals, proceeds over smaller pore zeolites such as chabazite and erionite.

The transformation of methanol to hydrocarbons over zeolite H–ZSM-5 is the basis of several industrially important reactions, such as the MTG or the MTO processes [112,113]. The mechanism of the reaction, particularly as concerns the formation of the first C–C bond and the nature of the interactions between the CH_3OH molecules and the zeolitic framework has been the subject of controversy [114,115]. ^1H NMR has been used [116–118] to study the chemistry of methanol adsorbed on H–ZSM-5.

In MAS NMR experiments [117,118] samples

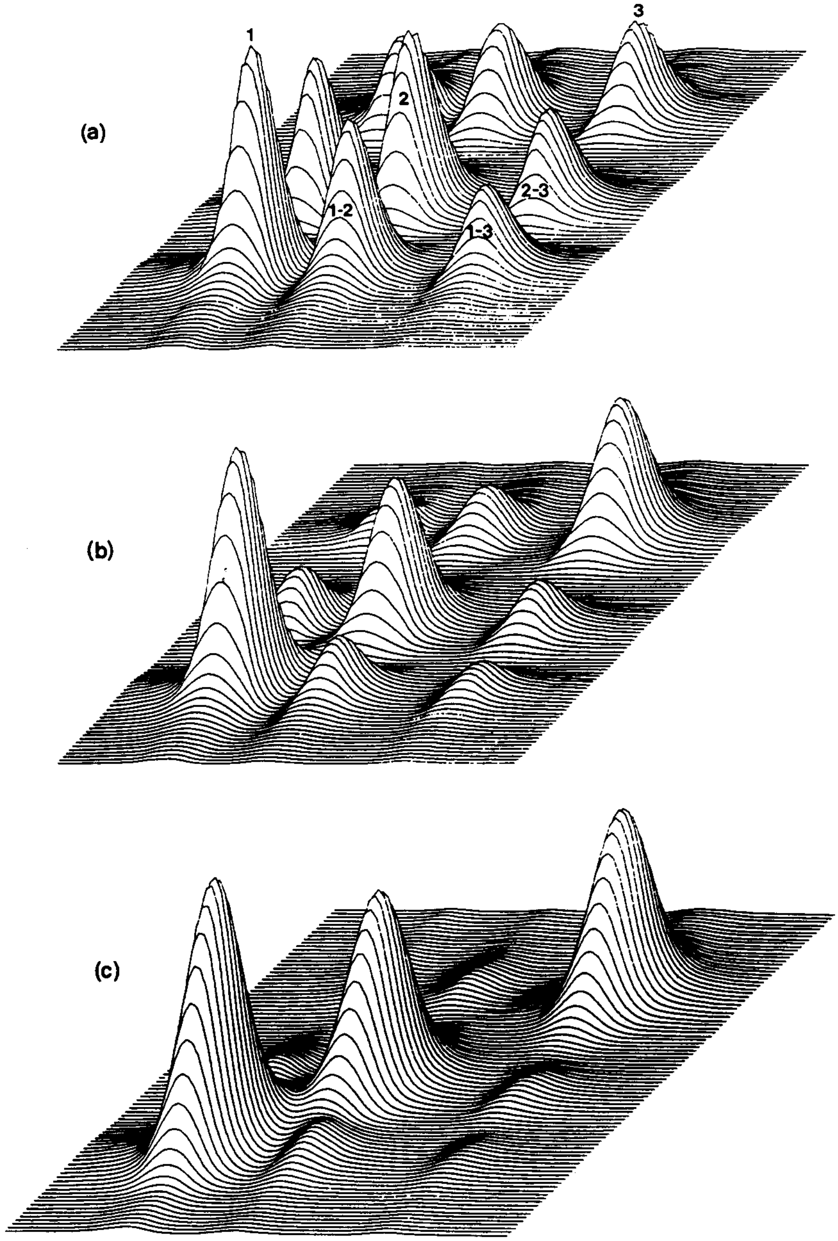

Fig. 15. Experimental 2D ^{31}P NMR spin-diffusion spectra of hydrated VPI-5 recorded with 3 s mixing time at various MAS speeds [100]. (a) 4.9 kHz; (b) 6.5 kHz and (c) 10.1 kHz. The three spectra are not on the same intensity scale, so that only the relative intensities within each can be compared.

were contained inside capsules [119] which could be spun inside the MAS NMR probehead at rates of up to 3 kHz. The design of the capsule allowed the samples to be dehydrated at 400°C under a pressure of 10^{-5} mbar before adsorption of the organic. Capsules were then sealed while keeping the sample at liquid nitrogen temperature in order to prevent the onset of chemical reactions. High-resolution ^{1}H MAS NMR spectra were recorded using 2 μs (20°) pulses with a repetition time of 5 s. Since the ^{1}H spin-lattice relaxation times of adsorbed alcohols on zeolites were found to be of the order of 0.2 s, such repetition times generate quantitatively reliable spectra.

Hydrogen bonding causes a downfield chemical shifts in alcohols because of the deshielding of the proton as a result of electrostatic polarization of the OH bond. In liquid CH_3OH hydrogen bonding causes a downfield shift of 3.1 ppm (Fig. 16b) relative to CH_3OH in CCl_3D where there is no hydrogen bonding (Fig. 16c). The proton MAS NMR spectrum of CH_3OH adsorbed on zeolite H-ZSM-5 (Fig. 16a) contains a peak at 4.1 ppm corresponding to the methyl protons and another at 9.1 ppm corresponding to the hydroxyl protons. When CD_3OH is adsorbed only the 9.1 ppm peak is observed, which demonstrates that all hydroxyls resonate at the same chemical shift. When 6 molecules of CD_3OH are adsorbed per Brønsted site on zeolite H-ZSM-5 (Fig. 17a) one peak corresponding to the hydroxyl groups is found at 9.1 ppm. By contrast, when CH_3OD is adsorbed (Fig. 17b), apart from the peak at 4.1 ppm corresponding to the methyl groups there is a small resonance at ca. 9.4 ppm. Adsorption of CD_3OD demonstrates that this latter peak originates initially from the framework Brønsted acid sites and not from the methyl group (Fig. 17c). The low-intensity peaks at 0–2 ppm are due to the probehead background. This was checked by repeating the experiments under identical conditions with the sample removed.

The large downfield shift of the hydroxyl resonance of the CH_3OH upon adsorption on H-ZMS-5 must be caused by very strong hydrogen bonding [120] and/or direct protonation of the alcohol. At the lower coverage of 2 molecules per Brønsted acid site, the hydroxyl peak moves from 9.1 ppm in Fig. 16a to 10.5 ppm. This experiment indicates the presence of fast exchange between the proton of the zeolitic acid site and the OD group of the adsorbed methanol.

The downfield shift of the hydroxyl resonance of MeOH is a measure of the proton donating ability of the solid acid catalyst. In zeolites H–Y and H–L the shifts are considerably smaller than in H–ZSM-5, which is consistent with their lower acidity. The advantage of our MeOH adsorption method for the measurement of catalytic acidity is that it monitors the species to which the proton is donated (the MeOH molecule) rather than the Brønsted acid site.

It is interesting to note that the chemical shift of the hydroxyl resonance is very sensitive to the type of zeolite on which methanol is adsorbed [118]. The change in the hydroxyl chemical shift in H–ZSM-5 is by far the largest (7.8 ppm downfield from $MeOH/CCl_3D$). The position of this resonance also depends on the method of synthesis of ZSM-5. When a zeolite with almost the same Si/Al ratio is prepared using the low-pH "fluoride" route, the corresponding increase of chemical shift is only 6.0 ppm. This result is intriguing. In terms of Si/Al ratio the zeolites are identical. The major difference is the lack of defect sites in the material synthesised via the fluoride method. This hints that defect sites such as SiOH nests might also be responsible for the extraordinary hydrogen-bonding properties of conventionally prepared H-ZSM-5.

IN SITU STUDIES OF CATALYTIC REACTIONS ON MOLECULAR SIEVES

The catalytic conversion of methanol to hydrocarbons in the gasoline boiling range using zeolite ZSM-5 at ca. 370°C has understandably attracted much attention. ^{13}C MAS NMR can probe directly the role of the active site in shape-selective catalytic reactions on zeolites in situ. The kind and quantity of chemical species present inside the particle can now be directly monitored [121–129]. This information, not forthcoming from other techniques, is usefully compared with the composition of the gaseous products to give new insights into reaction pathways on molecular sieves and to assist in the design of new shape-selective catalysts. These experiments have: (i) identified 29 different organic species *in the adsorbed phase* and monitored their fate during the course of the reaction; (ii) observed directly different kinds of shape selectivity in a zeolite; (iii) unequivocally distinguished between mobile and attached species. The results will assist in the design of shape-selective solids and provide a better understanding of catalytic processes in the intracrystalline space.

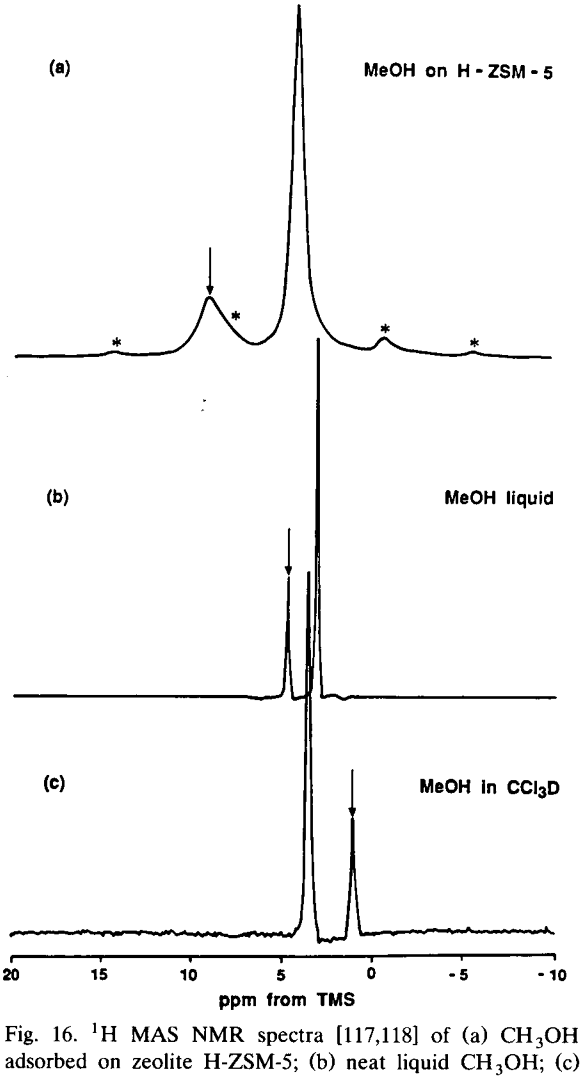

Fig. 16. ^{1}H MAS NMR spectra [117,118] of (a) CH_3OH adsorbed on zeolite H-ZSM-5; (b) neat liquid CH_3OH; (c) CH_3OH dissolved in $CDCl_3$. Asterisks denote spinning sidebands, arrows point to the position of the resonance from the methanol hydroxyl.

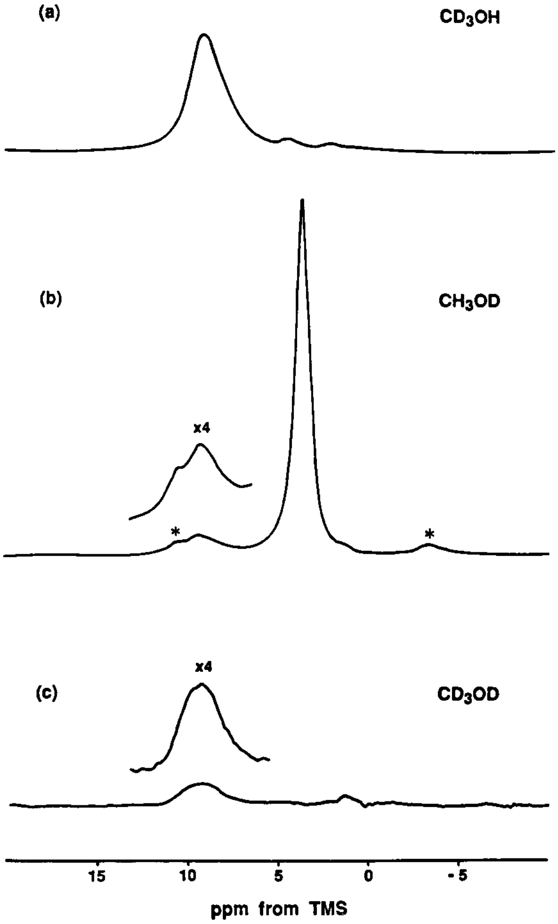

Fig. 17. ^{1}H MAS NMR spectra [117,118] of (a) CD_3OH adsorbed on H-ZSM-5; (b) CH_3OD adsorbed on H-ZSM-5; (c) CD_3OD adsorbed on H-ZSM-5. Asterisks denote spinning sidebands.

Shape selectivity of zeolites [3,130–133] arises from the fact that the probabilities of forming various products in the narrow intracrystalline cavities and channels are largely determined by molecular dimension and configuration. Three kinds of shape selectivity have been envisaged [3]. *Reactant selectivity* occurs when only certain molecules can access the intracrystalline space and react there, others being too large to enter the pores. In *product selectivity* only some of the various species formed within the channels and cavities can diffuse out of the crystallite and appear as reaction products. *Restricted transition state selectivity* takes place when certain reactions cannot proceed at all because they would involve transition states requiring more space than is available in the intracrystalline space. The evidence for the existence of the product and transition state selectivities available so far is indirect since it relies on the *absence* of certain species in the products rather than on the *presence* of others in the intracrystalline space, something which has not until now been directly monitored.

^{13}C MAS NMR of sealed H-ZSM-5 samples gives a considerable gain in resolution in comparison with earlier work [134–140]. The spectrum of a sample with adsorbed MeOH and maintained at 20°C (Fig. 18a), contains a single resonance at 50.8 ppm due to MeOH. After heating the sample to 150°C for 20 min the spectrum (Fig. 18b) is composed of two peaks, at 50.5 and 60.5 ppm, corresponding to MeOH and DME respectively.

Figure 19 shows the spectrum of a sample treated at 300°C for 35 min. MeOH and DME have been completely converted to a mixture of aliphatics and aromatics. The question arises as to how the various ^{13}C resonances are to be assigned to different hydrocarbon species, although some of them, especially those from methyl groups attached to aromatic rings, overlap. It turns out that all peaks can be reliably assigned [141–143]. First, note that most compounds give rise to several NMR peaks. In addition to chemical shift information, and the monitoring of the number and relative intensity of the various ^{13}C peaks, two-dimensional ^{13}C spectra have been used [142,143] to determine the connectivity of carbons and the number of protons attached to each carbon atom in the various organics and the details of ^{13}C–^{1}H couplings, enabling firm assignments for a number of resonances to be made.

A well-resolved two-dimensional J-coupled spectrum [142], measured using no decoupling during part of the evolution period while synchronising the time increment and the rotation period of the MAS spinner, is given in Fig. 20. The relative intensities of the $N+1$ lines in a spectrum of a spin 1/2 nucleus coupled to N equivalent spin 1/2 nuclei are given by Pascal's triangle as 1:1 for $N=1$; 1:2:1 for $N=2$; 1:3:3:1 for $N=3$ and 1:4:6:4:1 for $N=4$. Multiplicities of the lines confirm that our assignments, based on conventional one-dimensional spectra, are correct (see Table 2). For example, the resonance at −10.7 ppm in Fig. 20 is split into 5 components with a requisite intensity ratio in the 2D spectrum, which confirms that it must be due to adsorbed methane. Similarly, the 4-fold (methyl) and 3-fold (methylene) peaks clearly indicate the presence of propane adsorbed in the intracrystalline space.

The 2D spin diffusion ^{13}C NMR experiment allows us to examine further the spectral assigments obtained from the 1D and the 2D J-resolved experiments [143]. It also provides new details concerning distribution of hydrocarbons in zeolite ZSM-5. Spectral spin diffusion in the solid state involves simultaneous flip-flop transitions of dipolar-coupled spins with different resonance frequencies. The interaction of the X nuclei undergoing spin diffusion with the proton reservoir provides compensation for the energy imbalance. Spin diffusion results in an exchange of magnetization between nuclei responsible for resolved NMR peaks, which can be conveniently detected by observing the relevant cross-peaks in the 2D spin-diffusion spectrum. The technique is well established for solids. The rate of spin diffusion is very strongly dependent on the internuclear separation r, being proportional to $1/r^3$ for a rigid crystal lattice and to $1/r^6$ for species undergoing rapid isotropic motion. As a result, for all practical purposes spin diffusion occurs only between nuclei in adjacent functional groups within the same molecule (the intramolecular case) or between nuclei in neighbouring molecules mixed on a microscopic level (the intermolecular case). Both cases are observed in our system.

Figure 21 shows the 2D spin-diffusion spectrum of aliphatic hydrocarbons trapped in the zeolite. The 1D peaks, corresponding to the diagonal peaks in the 2D spectrum, have been assigned previously [121,122] but the assigment of peak b has subsequently been questioned [142]. It is clear that n-hexane and n-heptane are present, since peak e comes exclusively from their CH_3

groups. Therefore, considering the chemical shift of CH_2 groups of *n*-hexane and *n*-heptane, both hydrocarbons must contribute to peak b. In the *J*-resolved experiment this peak was not split into a triplet, because no homonuclear proton decoupling was applied during the first half of the evolution period, so that the splitting was obscured by substantial dipolar broadening. By contrast, CH_3 groups of isobutane undergo free rotation, which reduces the dipolar interaction and allows the quartet splitting of peak b to be observed. We note that peaks of *n*-butane in the spin-diffusion spectrum are missing, since cross-polarization has a tendency to underestimate peaks of mobile products, so that only those which are as abundant as propane appear (Table 3).

ZSM-5 contains no cages and its channel diameter only allows the hydrocarbon species in the channels to be lined up sequentially. For any two molecules to exchange their positions, access to an unocuppied channel crossing is required, which is difficult to satisfy at high adsorbate loadings. Hydrocarbon molecules are only capable of limited motion along the channels, which does not favour *intermolecular* spin diffusion. Free molecular rotation cannot occur, so that *intramolecular* dipolar interactions are present even for quite mobile functional groups, and make the intramolecular spin diffusion possible. Thus intramolecular spin diffusion in our system is preferred to intermolecular spin diffusion. The assignments of the various peaks are given in Table 2.

Munson et al. [127] questioned the suggestion in Refs. 121 and 122 that, since CO is observed prior to hydrocarbon formation, it is an intermediate in the reaction. Methanol-^{13}C and formic acid-^{13}C were first coadsorbed on the H–ZSM-5 catalyst, and an in situ NMR experiment was performed. It was found that the conversion rate of methanol was not affected by large quantities of CO. The authors then measured the spectra of a sample containing formic acid-^{13}C and unlabelled methanol. ^{13}CO was not incorporated in the reaction product. The conclusion is that CO is neither an intermediate nor a catalyst in MTG chemistry.

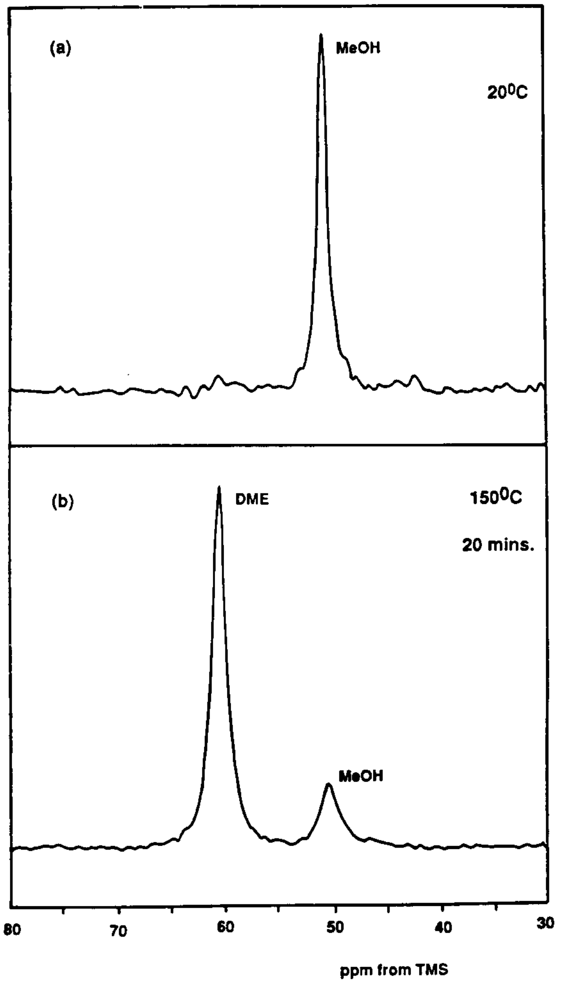

Fig. 18. ^{13}C MAS NMR spectra of H-ZSM-5 with 50 Torr of adsorbed MeOH and recorded at room temperature [121,122]. (a) no heating; (b) 150°C for 20 min. Experiments were performed at room temperature. High-power decoupling (but no cross-polarization) was used with 40° ^{13}C pulses and a 10 s repetition time. Asterisks denote spinning sidebands.

DIRECT OBSERVATION OF SHAPE SELECTIVITY

The *distribution* of adsorbed species in the sample of zeolite with adsorbed methanol treated at 300°C is very different from that observed in the reaction products [121,122]. The principal aromatics expected to be present are *m*- and *p*-xylene, 1,2,4-trimethylbenzene and toluene. However, the main species actually found in the adsorbed phase are *o*- and *p*-xylene and 1,2,4,5-

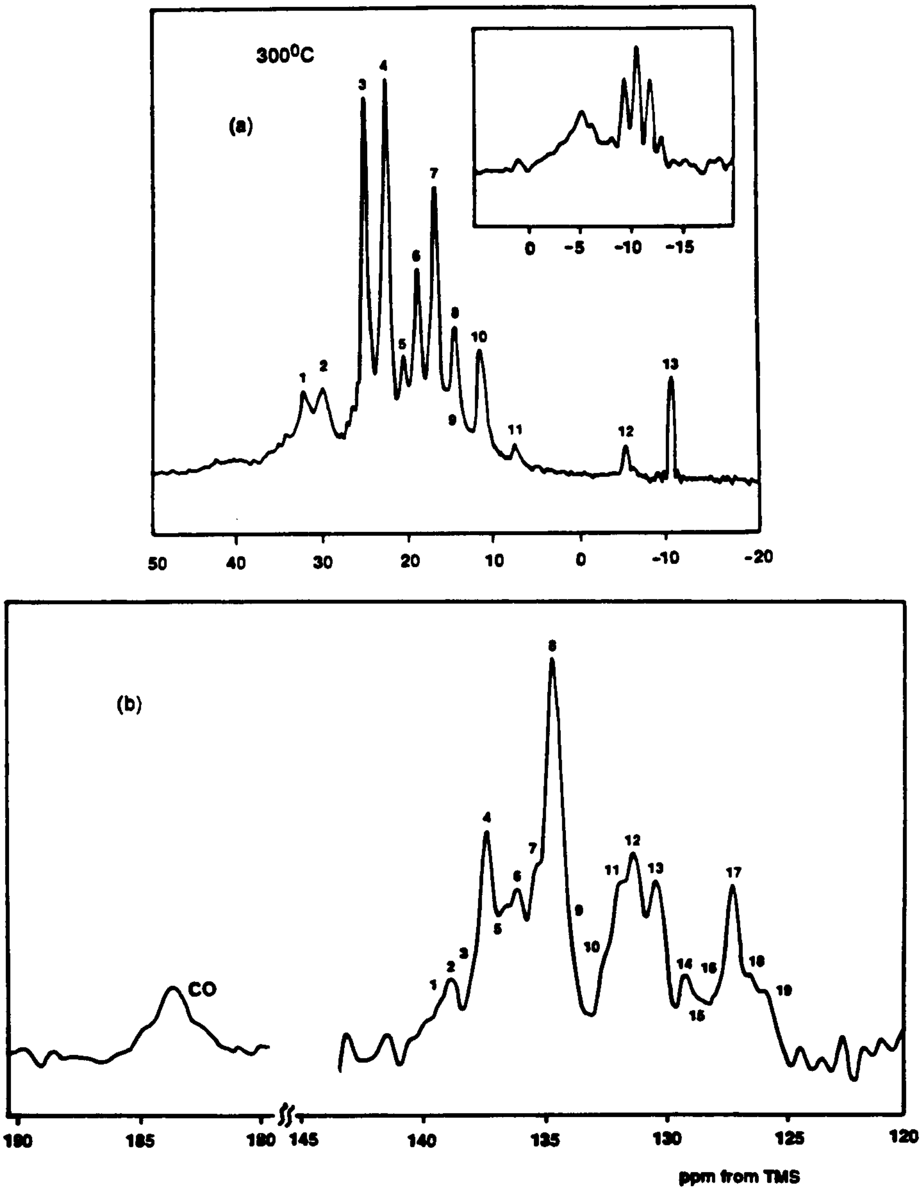

Fig. 19. ^{13}C MAS NMR spectra of a sample heated to 300°C for 35 min and recorded with proton decoupling only (a) aliphatic region; (b) aromatic and CO region [121,122]. Intensities in (a) and (b) are not on the same scale. The inset shows *J*-coupling of methane and cyclopropane carbons (recorded without decoupling). Spectral assignments are as follows [peak numbers and intensities (s = strong, m = medium, w = weak) are in brackets, { } for aliphatic and ( ) for aromatic]: isobutane {3,s}; propane {7,s}; *n*-butane {3,9,m}; *n*-hexane {1,4,8,m}; isopentane {1,2,4,10,m}; *n*-heptane {1,2,4,8,m}; methane {13,m}; ethane {11,w}; cyclopropane {12,w}; *o*-xylene (4,12,17,s){5}; *p*-xylene (7,13,s){6}; *m*-xylene (2,12,15,17,w){5}; toluene (2,13,14,18,w){5}; 1,2,4-trimethylbenzene (4,6,8,11,13,16,m){5,6}; 1,3,5-trimethylbenzene (3,16,w){5}; 1,2,3-trimethylbenzene (5,7,16,19,w){5,8}; 1,2,4,5-tetramethylbenzene (8,11,s){6}; 1,2,3,5-tetramethylbenzene (5,7,10,13,m){5,8}; 1,2,3,4-tetramethylbenzene (7,9,16,w){5,8}. Because of the different Overhauser enhancements of different carbons, peak intensities give only an approximate concentration of the various species.

tetramethylbenzene, with smaller amounts of 1,2,4-trimethylbenzene and 1,2,3,5-tetramethylbenzene. The other xylenes, tri- and tetramethylbenzenes are also found but in smaller amounts. The distribution of the three trimethylbenzenes in the adsorbed phases is very different from the thermodynamic equilibrium distribution (see Fig. 22). The fact that 1,2,3- or 1,3,5-trimethylbenzenes (with kinetic diameters of 6.4 and 6.7 Å, respectively) are not found among the products, but are present in the adsorbed phase, while the smaller 1,2,4-trimethylbenzene (6.1 Å) is found in both, clearly demonstrates the reality of the concept of product selectivity. The channel dimensions of ZSM-5 are 5.6 × 5.3 Å, but more space is available at the intersection of the straight and zig-zag channels. While the greater amplitude of thermal vibrations of the framework, which increases the maximum effective size of the channels, allows the smaller isomer to diffuse out of the crystal, the two larger isomers, although formed, are unable to diffuse out at 300°C and must isomerise to 1,2,4-trimethylbenzene.

The distribution of the tetramethylbenzenes in the intracrystalline space is most unexpected. None of them have ever been reported in the products of the reaction at 300°C and yet all three are clearly present in the adsorbed phase. Because of the restricted intracrystalline space they can only form at channel intersections, but (unlike the trimethylbenzenes) are not generated in the thermodynamic equilibrium distribution. 1,2,3,5-Tetramethylbenzene (6.7 Å) should be the dominant species on thermodynamic grounds; in fact it is 1,2,4,5-tetramethylbenzene (6.1 Å) which dominates. The thermodynamicallly least favoured isomer, 1,2,3,4-tetramethylbenzene (6.4 Å), is found in small quantities. The fact that tetramethylbenzenes are not found in the products again demonstrates product shape selectivity. Their *relative abundance* in the adsorbed phase, on the other hand, shows that an additional kind of shape selectivity occurs within the intracrystalline space. It does not rely on the ability of species to enter or to leave the crystal nor on the size of the transition state: isomerisation is sterically restricted within the crystallite at the active site itself.

It is instructive to compare the shape-selective catalytic conversion of methanol to low-molecular-weight olefins and aliphatics zeolite ZSM-5 with the results for the molecular sieve SAPO-34 [145]. The sieve, which has the framework topology of the natural zeolite chabazite [146,147] converts MeOH to hydrocarbons with a selectivity for C_2 of 33.8 mol%. In what follows, we shall refer to the gas species leaving the catalyst (and monitored by gas chromatography) as "products" and the compounds monitored by NMR in the intracrystalline space as the "adsorbed phase". Products were analyzed using a high resolution gas chromatograph. A sample of SAPO-34 was prepared with a chemical formula of $SiAl_6P_5O_{24}$.

At 300°C the most abundant species in the adsorbed phase are isopentane, propane, isobutane, methane and *n*-butane with less ethane, neopentane, C_6 and C_7 species. At 370°C the composition of the adsorbed phase is similar ex-

TABLE 2

Parameters of the two-dimensional spectrum shown in Fig. 20

Signal	Chemical shift (ppm)	Signal multiplicity	*J*-Coupling (Hz)	Tentative assignment [121]	2D *J*-resolved assignment
a	24.7	4	135	Isobutane	Isobutane
b	22.2	4	135	*n*-Hexane, isopentane, *n*-heptane	Isopentane
c	18.7	4	135	Methyl substituted benzenes	Methyl substituted benzenes
d	16.7	3	130	Propane	Propane
	16.0	4	130		
e	−11.0	5	135	Methane	Methane

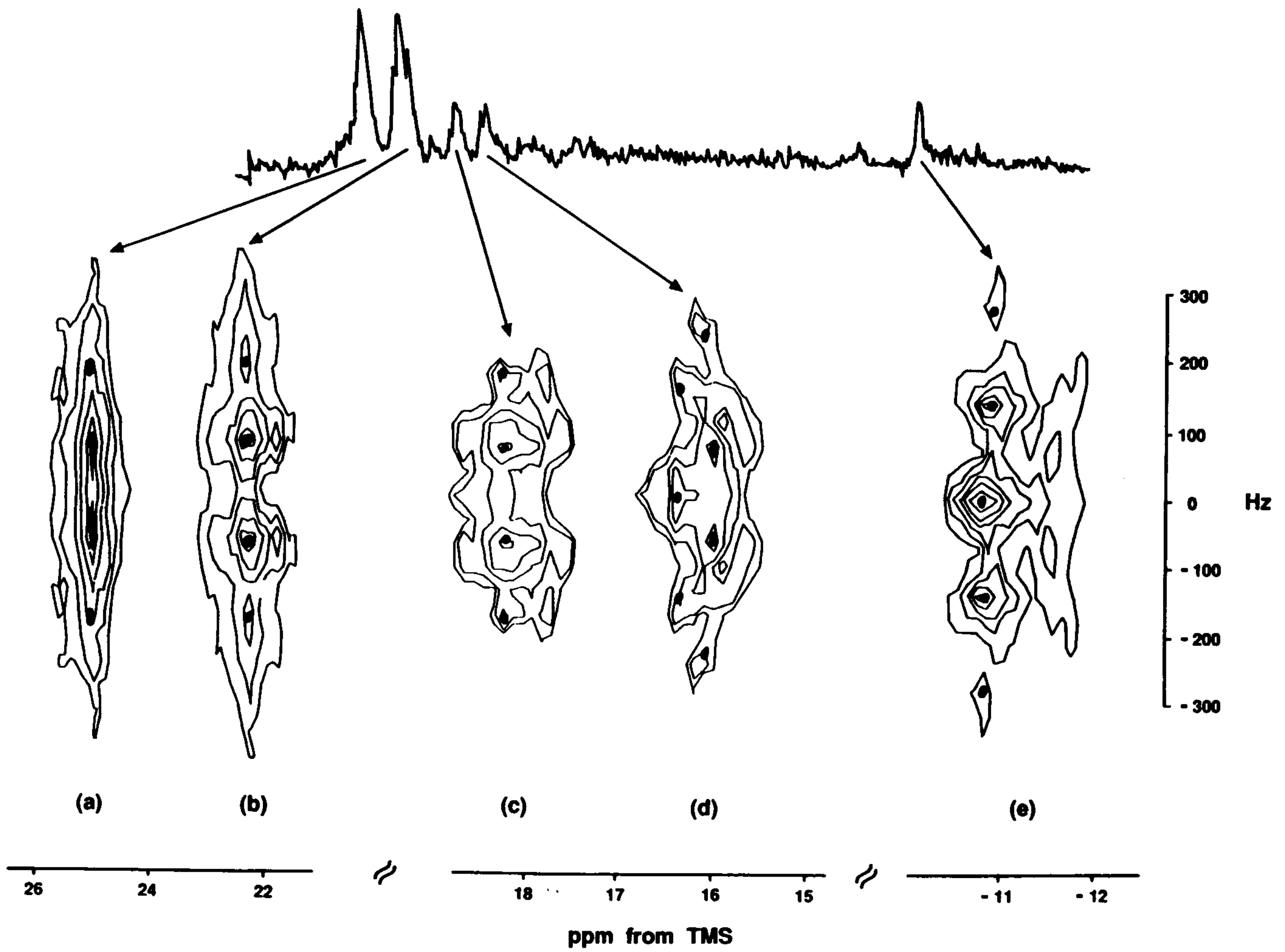

Fig. 20. Heteronuclear 2-dimensional *J*-resolved ^{13}C MAS NMR spectrum of zeolite H-ZSM-5 with adsorbed methanol treated at 300°C for 30 min [142].

cept that propane is now more abundant than isopentane. The relative concentrations of adsorbed species were calculated from spectra acquired with high-power proton decoupling but without cross-polarization. Unlike in the case of zeolite H–ZSM-5 (see above) no carbon monoxide intermediate and no aromatics are observed by NMR at any temperature.

The framework structure of SAPO-34 consists of hexagonal prisms (D6R units) linked by four-membered rings. This results in a three-dimensional channel system and a structure containing

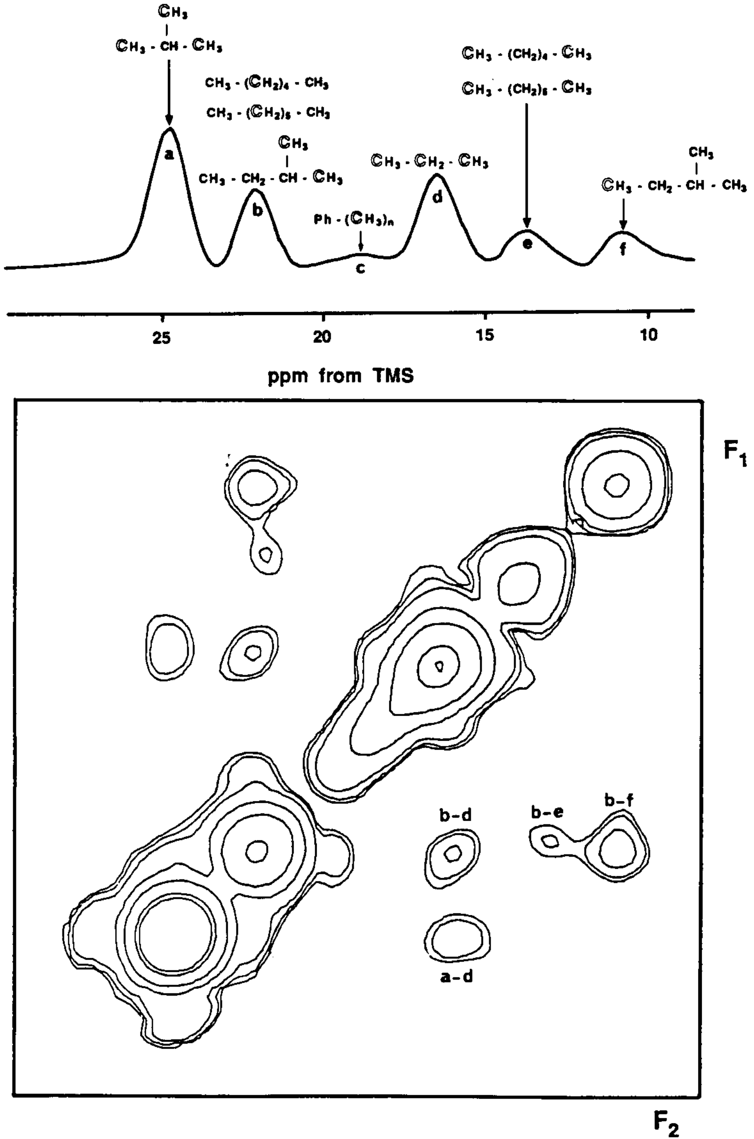

Fig. 21. ^{13}C NMR spin diffusion spectrum of products of methanol conversion into gasoline over zeolite ZSM-5 with the projection onto the F_2 axis (corresponding to a conventional spectrum) at the top [143]. Carbon atoms to which individual resonances are assigned are highlighted. For peak assignment see Table 2.

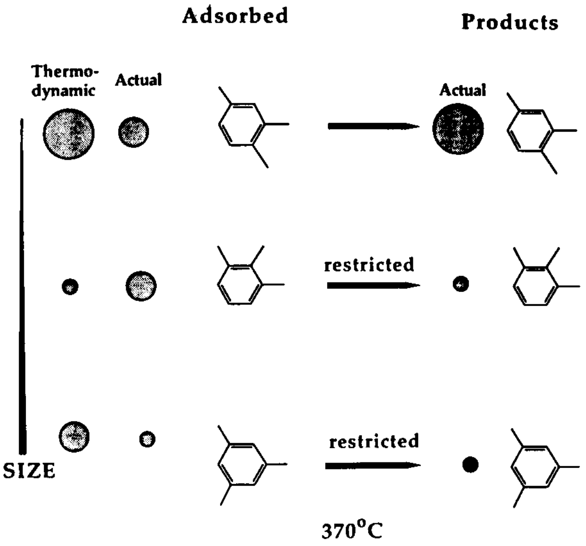

Fig. 22. Schematic representation of the expected and actual distribution of the three trimethylbenzenes in the intracrystalline space and in the gaseous products of the reaction. Diameters of the circles are proportional to the intracrystalline content of each compound; the effective molecular size increases from top to bottom.

large ellipsoidal cages 11 Å long and 6.5 Å wide. The cages are stacked in a hexagonal arrangement forming a three-dimensional network of cages linked by the narrower eight-membered windows. The cage and window dimensions for SAPO-34 are almost identical to those in chabazite and therefore similar molecular sieving properties can be expected. Entrance to the chabazite cages may only be gained through the eight-membered ring windows which are nearly circular with a diameter of approximately 3.8 Å. At room temperature chabazite very rapidly sorbs CH_4 and C_2H_6, slowly sorbs *n*-alkanes but completely excludes branched alkanes.

^{13}C MAS NMR indicates that after heating to 300°C MeOH and DME are completely converted to aliphatic hydrocarbons; no olefins are found. This is understood by reference to the gas chromatography results which show that at lower space velocities the products contain a smaller amount of olefins (Fig. 23). By extrapolating the data we predict that under static reactor conditions little or no olefins will be formed. A careful inspection of the chromatography results indicates that the relative amounts of C_1, C_2, C_3, C_4, etc. species (olefins + aliphatics) are roughly similar irrespective of space velocity. In other words, space velocity does not change oligomerization properties, but it does alter the extent of hydrogenation of products. NMR results, which give a

TABLE 3

Assignment of the 2D ^{13}C NMR spin-diffusion spectrum shown in Fig. 21 [143]

Diagonal peaks

Signal	Chemical shift (ppm)	Group	Assignment
a	24.7	CH_3	Isobutane
b	22.3	$CH_3CH_2CH(\mathit{C}H_3)_2$	Isopentane
		CH_2	*n*-Hexane + *n*-heptane
c	18.7	CH_3	Methyl-substituted benzenes
d	16.7	$CH_3 + CH_2$	Propane
e	14.3	CH_3	*n*-Hexane + *n*-heptane
f	11.2	$\mathit{C}H_3CH_2CH(CH_3)_2$	Isopentane

Cross peaks

Signals	Assignment	Type of spin diffusion
a–d	Isobutane–propane	Intermolecular
b–d	Isopentane–propane	Intermolecular
b–e	*n*-Hexane	Intramolecular
	n-Heptane	Intramolecular
b–f	Isopentane	Intramolecular

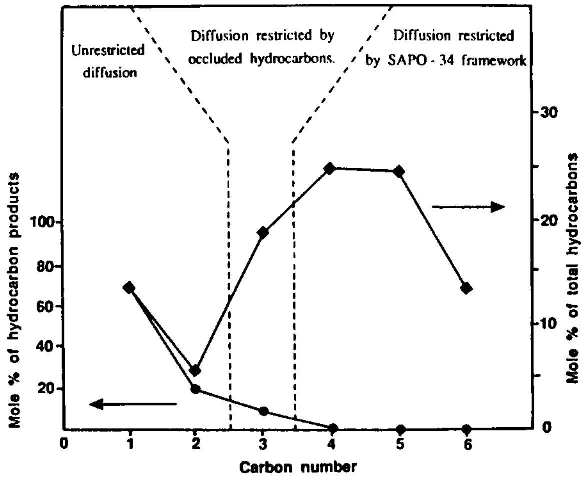

Fig. 23. Plot of concentrations of C_1 to C_6 hydrocarbons in SAPO-34 at 300°C in the gaseous products determined by gas chromatography (GC) and total hydrocarbons determined by NMR [145]. GC data are for LHSV = 0.3 h^{-1}. NMR and GC data are adjusted so that the concentrations of methane coincide.

fair representation of the total concentration of species formed in the adsorbed phase, can therefore be compared with their concentration in the gaseous products.

The most striking difference between the composition of the adsorbed phase and the products is the preponderance of branched aliphatics up to C_6 in the former. The effect is so clear as to amount to a textbook example of product shape selectivity. Early work has shown that these branched aliphatics are not sorbed by the chabazite crystals from the gas phase at room temperature. The same effect occurs here in reverse: branched-chain hydrocarbons formed *inside* SAPO-34 are not capable of leaving the intracrystalline space even at temperatures as high as 370°C.

Of the C_1, C_2 and C_3 species in the adsorbed phase the concentration of C_3 is always the highest. However, it is C_1 which is the most abundant in the gaseous products, followed by C_2 and C_3 species. The C_1/C_2 concentration ratio in the adsorbed phase is roughly equal to that in the gaseous products at 300°C. This suggests that C_1 and C_2 species have no difficulty in leaving the SAPO-34 crystallite. On the other hand, only 5–10% of the amount of C_3 found in the adsorbed phase is observed in the gas-phase products. Figure 23 illustrates the relative amounts of C_1–C_6 compounds in the products and in the adsorbed phase. The striking differences between the concentrations of C_1 and C_2 on the one hand and C_3 on the other are not easily explained on the basis of diffusion coefficients of aliphatic hydrocarbons in chabazite. At room temperature the diffusion coefficient of propane is ca. 20 times smaller than for ethane and methane. However, at elevated temperatures, such as 150°C, the difference disappears almost completely. It follows that at 370°C the expected diffusion coefficients for methane, ethane and propane should be of the same order of magnitude with a negligible activation barrier. The exclusion of much of the C_3 fraction from the product must therefore be a result of the additional constraints imposed by the presence of branched hydrocarbons which partially block the pore system and significantly alter the diffusional behaviour of other species. This further illustrates the need for knowing the contents of the intracrystalline space of a shape-selective catalyst during the course of the reaction. Since the available free space is modified by the occlusion of product molecules, it is not sufficient to take into account the crystallographic pore dimensions in order to predict shape-selective action.

The discovery that, despite the composition of the gaseous products, SAPO-34 in fact converts methanol more selectively to C_3 than to C_2 hydrocarbons suggests ways to modify the catalyst so as to enable the C_3 species to escape, thus making it more selective for propylene than ethylene. This might be done by preparing the catalyst with occluded material or partial exchange with cations large enough to prevent the formation of branched hydrocarbons. This would in turn allow the C_2 and C_3 species to diffuse more readily through the channel system without obstruction from the higher hydrocarbons. The fact that such a prediction can be made on the strength of MAS NMR in tandem with gas chromatography illustrates the remarkable potential of this two-pronged approach in the design of novel molecular sieve catalysts.

NEW NMR TECHNIQUES FOR THE STUDY OF MOLECULAR SIEVES

Multiple quantum NMR

Multiple quantum NMR [148–153] is an ingenious “spin counting” tool for characterizing homonuclear spin clusters in the solid state. The technique, which is paricularly well suited for studies of species adsorbed in the voids of molecular sieves [151,152], employs a 2D NMR pulse sequence [153] which forces nuclear spins to act collectively via their dipolar couplings, thus creating unobservable multiple-quantum (MQ) coherences. After conversion into observable single-quantum coherences, the MQ coherences are indirectly detected.

The collective behaviour of spins can be roughly understood as a simultaneous flip of two (double-quantum coherence), three or more spins (multiple-quantum coherence). In other words, the spin system coherently exchanges two, three or ΔM photons, respectively, with the resonant radiation. This can occur only if the preparation time τ is sufficient to establish communication, via pairwise dipolar interactions, within the group of spins intended to be excited. Dipolar interaction renders two spins correlated after a time period which is roughly proportional to the cube of their separation. It follows that multiple-quantum coherences develop at a rate determined by the spatial distribution of spins in the sample. For a uniform distribution the MQ transition order ΔM grows monotonically with increasing τ. If the system constitutes a collection of diluted, isolated clusters, the MQ count will reach a plateau corresponding to ΔM equal to the number of spins in the cluster (Fig. 24).

Spin-echo double resonance (SEDOR)

*S*pin-*E*cho *Do*uble *R*esonance (SEDOR) [154–156] is capable of measuring local heteronuclear dipolar interactions between selected (by the spectroscopist) nuclei of different species I and S. The magnitude of the effect is related to the magnitude of the heteronuclear I–S dipolar interactions, from which the relative spatial disposition of spins I and S can be deduced.

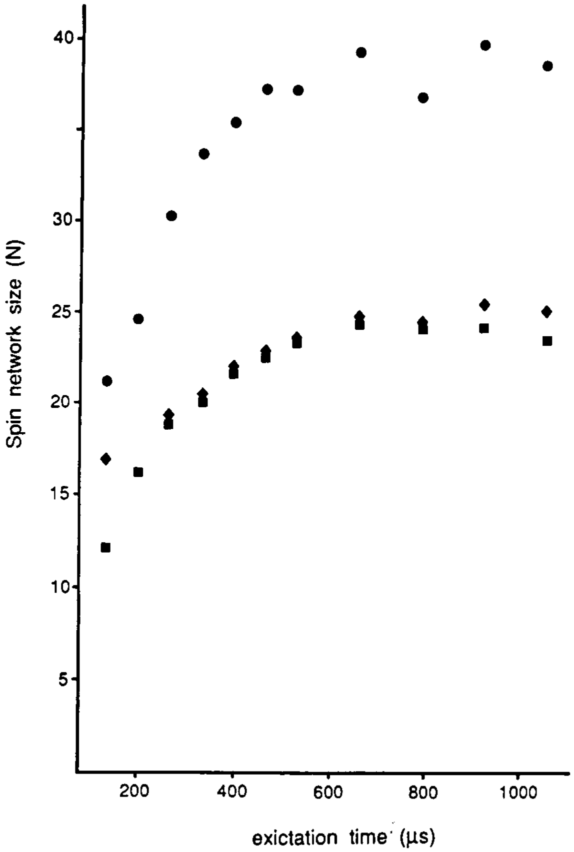

Fig. 24. Results of ^{1}H MQ NMR experiments for hexamethylbenzene (HMB) adsorbed at 573 K on dehydrated zeolite NaY [152]. The HMB molecule contains 18 hydrogens, so the spin cluster size is 18 per one molecule. At lower loadings (5.1 and 10.2 wt.%) the plateau corresponds to about one HMB molecule per supercage and at higher loading (20.4 wt.%) the plateau reflects an occupancy of two HMB guests per supercage.

A very useful feature of SEDOR is that by measuring the dipolar coupling between selected nuclei it probes only their immediate vicinity. This is because the dipolar interaction is inversely proportional to the cube of the internuclear distance, so that it falls off very quickly with internuclear separation. ^{27}Al–^{31}P SEDOR has been used to measure Al–P distances in aluminophosphate molecular sieves [157]. Such information can provide valuable insight into their local structure. For example, framework and extra-framework Al in zeolites can be distinguished.

Double resonance techniques may be tailored to study the defocusing process on rotational echoes generated by MAS rather than on static spin echoes. *R*otational Spin-*E*cho *Do*uble *R*esonance (REDOR) [158], *R*otary *R*esonance *R*ecoupling (RRR) [159] and *T*ransferred-*E*cho *Do*uble *R*esonance (TEDOR) [160] can selectively measure individual heteronuclear dipolar couplings in crystalline solids, which give rise to multiple-peak MAS NMR spectra. Fyfe et al. [161] used dipolar-dephasing MAS NMR for the study of mixed pairs of quadrupolar and spin 1/2 nuclei in VPI-5. Dipolar connectivities were examined in both directions between ^{31}P and ^{27}Al, REDOR and TEDOR experiments performed, as well as a two-dimensional extension of the TEDOR experiment. Such experiments restore the heteronuclear dipolar coupling under MAS via a train of radiofrequency pulses, thereby providing information about connectivities and distances between coupled nuclei. They clearly have a considerable potential for structural elucidation.

Double rotation (DOR) and dynamic angle spinning (DAS)

The development of double-rotation (DOR) and dynamic-angle spinning (DAS) is a major advance in the study of quadrupolar nuclei, as it removes not only chemical shift anisotropy, but also second-order quadrupolar interactions [25,26]. The second-order quadrupolar shift of the central transition is proportional to

$$A_0^0 + B_2^0(\alpha, \beta) P_2(\cos\theta) + B_4^0(\alpha, \beta) P_4(\cos\theta)$$

where the P_n (cos θ) are the angle-dependent Legendre polynomials

$$P_2(\cos\theta) = \tfrac{1}{2}(3\cos^2\theta - 1)$$

$$P_4(\cos\theta) = \tfrac{1}{8}(35\cos^4\theta - 30\cos^2\theta + 3).$$

and the remaining terms are constant for a given sample.

There is clearly no value of θ for which both the $P_2(\cos\theta)$ and the $P_4(\cos\theta)$ terms are zero. However, two ways have been devised of canceling these terms together. If the sample is spun *simultaneously* about two different axes θ_1 and θ_2, we have

$$P_2(\cos\theta_1) = 0$$

and

$$P_4(\cos\theta_2) = 0$$

with solutions $\theta_1 = 54.74°$ (the conventional "magic angle") and $\theta_2 = 30.56°$ or $70.12°$. The resulting complicated trajectory averages the anisotropic broadening to zero. This is the basis of the "double-rotation" (DOR) experiment.

Second-order quadrupole interaction may also be removed by dynamic-angle spinning (DAS), in which the sample is rotated *sequentially* about two different axes, θ_1' and θ_2', which are chosen so that

$$P_2(\cos\theta_1') = -P_2(\cos\theta_2')$$

and

$$P_4(\cos\theta_1') = -P_4(\cos\theta_2')$$

with the solutions $\theta_1 = 37.38°$ and $\theta_2 = 79.19°$. It is thus theoretically possible to remove the second-order interaction completely.

DOR and DAS open up whole new areas of research into the solid-state. Wu et al. [27] showed that ^{27}Al DOR is capable of resolving discrete framework aluminium sites in VPI-5, permitting quantitative investigation of site-specific adsorbate interactions (typically H_2O interactions) with the framework. Figure 25a and b shows the ^{27}Al MAS spectrum of dehydrated VPI-5 and the DOR spectrum of the same sample. Two peaks unresolved in the MAS spectrum, d at 33.3 ppm and e at 35.9 ppm, are observed in the DOR spectrum. From the 1:2 intensity ratio of these two peaks, peak d is assigned to Al1 sites and peak e to Al2 sites. During dehydration, 6-coordinated Al sites are converted to 4-coordinated sites, consistent with the disappearance of peak c at −18.4 ppm. Furthermore, in hydrated VPI-5, ^{27}Al tetrahedral sites (peaks a and b) are altered by dehydration to yield different ^{27}Al tetrahedral environments (peaks d and e). Two sharp lines which emerge upon slow rehydration, g at 37.3 ppm and h at 38.8 ppm, arise from Al2 species influenced by adsorbed water molecules.

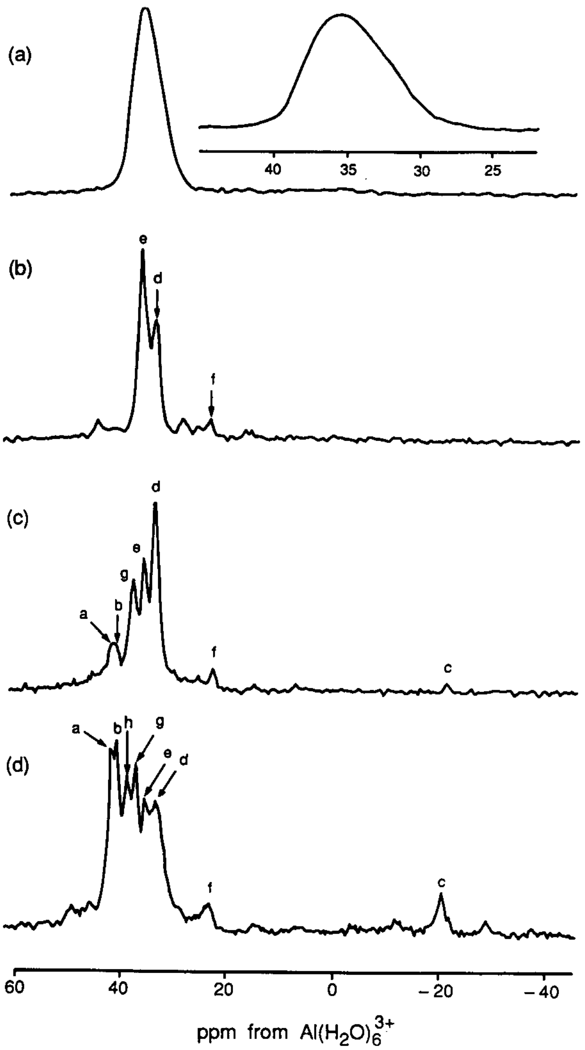

Fig. 25. ^{27}Al DOR spectrum of dehydrated and partially rehydrated VPI-5. (a) MAS spectrum of dehydrated VPI-5; (b) DOR spectrum of dehydrated VPI-5; (c) DOR spectrum after 2 days of rehydration; (d) DOR spectrum after 23 days of rehydration [27].

^{27}Al DOR distinguishes the extremely distorted 5-coordinated aluminium sites in the molecular sieve precursor $AlPO_4$-21 [28a]. Upon calcination, $AlPO_4$-21 transforms to $AlPO_4$-25, which has two 4-coordinated aluminium sites with similar isotropic chemical shifts which cannot be resolved in an 11.7 T field. However, the two tetrahedral environments have different quadrupole coupling constants and are distinguished by DOR at 4.2 T. DOR was used [28b] to monitor the nature of the phase transition of $AlPO_4$-11 observed when water is adsorbed. In the hydrated material, water is strongly attached to approximately 1/5 of the framework aluminium, producing 6-coordinated Al. All five suggested crystallographic sites are hydrated to an equal extent. Because of this, the ^{27}Al NMR peak due to the 6-coordinated species does not completely narrow upon DOR.

Conclusions

The future of NMR in the study of molecular sieves looks very bright. The structure of the solid catalyst itself can now be probed using various two-dimensional NMR techniques, and further developments are under way. Multi-dimensional NMR of solids clearly has considerable prospects. Quadrupole nutation NMR can probe the environment of nuclei in rigid solid catalysts, rotational resonance measures accurately the distance between specific sites, and surface-sensitive techniques, such as SEDOR with its modifications and ^2H NMR, overcome the traditional limitations of nuclear magnetic resonance. In situ techniques can identify the intermediates and products of catalytic reactions and elucidate their mechanism. Multiple-quantum NMR can count molecules present in porous solids. Finally, DOR and DAS effectively average second-order quadrupolar interactions. Applications of most of these techniques have hardly begun. At the same time, high magnetic fields and constant advances in NMR hardware made it possible to monitor virtually all chemical elements in solids. I have no doubt that the next few years will witness many exciting new experiments.

REFERENCES

1 A.R. Cronstedt, Kongl. Svenska Vetenskaps Acad. Handlingar, 17 (1756) 120.
2 W. Loewenstein, Am. Mineral., 39 (1954) 92.
3 P.B. Weisz and V.J. Frilette, J. Phys. Chem., 64 (1960) 382.
4 R.J. Argauer and G.R. Landolt, U.S. Patent, 3, 702, 886 (1972).

5 S.T. Wilson, B.M. Lok, C.A. Messina, T.R. Cannan and E.M. Flanigen, J. Am. Chem. Soc., 104 (1982) 1146.

6 E.M. Flanigen, B.M. Lok, R.L. Patton and S.T. Wilson, Pure Appl. Chem., 58 (1986) 1351.

7 W.M. Meier and D.H. Olson, Atlas of Zeolite Structure Types, Butterworths, Sevenoaks, 1992.

8 D.W. Breck, Zeolite Molecular Sieves: Structure, Chemistry and Use, Wiley, London, 1974.

9 R.M. Barrer, Zeolites and Clay Minerals as Sorbents and Molecular Sieves, Academic Press, London, 1978.

10 R.M. Barrer, Hydrothermal Chemistry of Zeolites, Academic Press, London, 1982.

11 R. Szostak, Molecular Sieves: Principles of Synthesis and Identification, Van Nostrand Reinhold, New York, 1989.

12 D. Naccache and Y. Ben Taarit, Pure Appl. Chem., 52 (1980) 2175.

13 B. Imelik, C. Naccache, Y. Ben Taarit, J.C. Védrine, G. Coudurier and H. Praliaud (Eds.), Catalysis by Zeolites, Elsevier, Amsterdam, 1980.

14 J. Klinowski, Progr. NMR Spectrosc., 16 (1984) 237.

15 J. Klinowski, Chem. Rev., 91 (1991) 1459.

16 G. Engelhardt and D. Michel, High-resolution Solid-State NMR of Silicates and Zeolites, Wiley, Chichester, 1987.

17 P.J. Barrie and J. Klinowski, Progr. NMR Spectrosc., 24 (1992) 91.

18 P.J. Barrie, in R.J.H. Clark and R.E. Hester (Eds.) Spectroscopy of Advanced Materials II, Vol. 22 of Advances in Spectroscopy, Wiley, New York, 1993.

19 J. Kärger and D.M. Ruthven, Diffusion in Zeolites and Other Microporous Solids, Wiley, New York, 1992.

20 E. Lippmaa, M. Mägi, A. Samoson, G. Engelhardt and A.-R. Grimmer, J. Am. Chem. Soc., 102 (1980) 4889.

21 A. Samoson and E. Lippmaa, Phys. Rev., B28 (1983) 6565; Chem. Phys. Lett., 100 (1983) 205.

22 P.P. Man, J. Magn. Reson., 67 (1986) 78 and 77 (1988) 148.

23 P.P. Man and J. Klinowski, Chem. Phys. Lett., 147 (1988) 581.

24 P.P. Man, J. Klinowski, A. Trokiner, H. Zanni and P. Papon, P. Chem. Phys. Lett., 151 (1988) 143.

25 A. Samoson, E. Lippmaa and A. Pines, Mol. Phys., 65 (1988) 1013.

26 A. Llor and J. Virlet, Chem. Phys. Lett., 152 (1988) 248.

27 Y. Wu, B.F. Chmelka, A. Pines, M.E. Davis, P.J. Grobet and P.A. Jacobs, Nature, 346 (1990) 550.

28 (a) R. Jelinek, B.F. Chmelka, Y. Wu, P.J. Grandinetti, A. Pines, P.J. Barrie and J. Klinowski, J. Am. Chem. Soc., 113 (1991) 4097; (b) P.J. Barrie, M.E. Smith and J. Klinowski, Chem. Phys. Lett., 180 (1991) 6.

29 G. Engelhardt, U. Lohse, E. Lippmaa, M. Tarmak and M. Mägi, Z. Anorg. Allg. Chem., 482 (1981) 49.

30 J.M. Thomas, C.A. Fyfe, S. Ramdas, J. Klinowski and G.C. Gobbi, J. Phys. Chem., 86 (1982) 3061.

31 J. Klinowski, S. Ramdas, J.M. Thomas, C.A. Fyfe and J.S. Hartman, J. Chem. Soc., Faraday Trans. II, 78 (1982) 1025.

32 M.T. Melchior, D.E.W. Vaughan and A.J. Jacobson, J. Am. Chem. Soc. 104 (1982) 4859.

33 J. Klinowski and M.W. Anderson, J. Chem. Soc., Faraday Trans. I, 82 (1986) 569.

34 R.H. Jarman, A.J. Jacobson and M.T. Melchior, J. Phys. Chem., 88 (1984) 5748.

35 J. Klinowski, S.W. Carr, S.E. Tarling and P. Barnes, Nature, 330 (1987) 56.

36 C.A. Fyfe, G.C. Gobbi, J. Klinowski, J.M. Thomas and S. Ramdas, Nature, 296 (1982) 530.

37 C.A. Fyfe, J.H. O'Brien and H. Strobl, Nature, 326 (1987) 281.

38 D.G. Hay, H. Jaeger and G.W. West, J. Phys. Chem., 89 (1985) 107.

39 J. Klinowski, T.A. Carpenter and L.F. Gladden, Zeolites, 7 (1987) 73.

40 H. Strobl, C.A. Fyfe, G.T. Kokotailo and C.T. Pasztor, J. Am. Chem. Soc., 109 (1987) 4733.

41 G.W. West, Aust. J. Chem., 37 (1984) 455.

42 C.A. Fyfe, G.J. Kennedy, C.T. DeSchutter and G.T. Kokotailo, J. Chem. Soc., Chem. Commun., (1984) 541.

43 C.A. Fyfe, G.C. Gobbi, G.J. Kennedy, J.D. Graham, R.S. Ozubko, W.J. Murphy, A. Bothner-By, J. Dadok and A.S. Chesnick, Zeolites, 5 (1985) 179.

44 J.M. Thomas, J. Klinowski, S. Ramdas, B.K. Hunter and D.T.B. Tennakooon, Chem. Phys. Lett., 102 (1983) 158.

45 C.A. Fyfe, G.C. Gobbi, W.J. Murphy, R.S. Ozubko and D.A. Slack, J. Am. Chem. Soc., 106 (1984) 4435.

46 C.A. Fyfe, G.J. Kennedy, G.T. Kokotailo and C.T. DeSchutter, J. Chem. Soc., Chem. Commun., (1984) 1093.

47 J.B. Higgins, D.E. Woessner, J.C. Trewella and J.L. Schlenker, Zeolites, 4 (1984) 112.

48 G.T. Kokotailo, C.A. Fyfe, G.C. Gobbi, G.J. Kennedy and C.T. DeSchutter, J. Chem. Soc., Chem. Commun., (1984) 1208.

49 J.M. Thomas, J. Klinowski, S. Ramdas, B.K. Hunter and D.T.B. Tennakoon, Chem. Phys. Lett., 102 (1983) 158.

50 J.V. Smith and C.S. Blackwell, Nature, 303 (1983) 223.

51 J.B. Higgins and D.E. Woessner, EOS Trans. Am. Geophys. Union, 63 (1982) 1139.

52 J.V. Smith, C.S. Blackwell and G.L. Hovis, Nature, 309 (1984) 140.

53 G. Engelhardt and R. Radeglia, Chem. Phys. Lett., 108 (1984) 271.

54 R. Radeglia and G. Engelhardt, Chem. Phys. Lett., 114 (1985) 28.

55 (a) S. Ramdas and J. Klinowski, Nature, 308 (1984) 521; (b) J.V. Smith and W.J. Dytrych, Nature, 309 (1984) 607.

56 C.S. Blackwell and R.L. Patton, J. Phys. Chem., 88 (1984) 6135.

57 C.A. Fyfe, H. Gies and Y. Feng, J. Chem. Soc., Chem. Commun., (1989) 1240.

58 C.A. Fyfe, H. Gies and Y. Feng, J. Am. Chem. Soc., 111 (1989) 7702.

59 C.A. Fyfe, Y. Feng and G.T. Kokotailo, Nature, 341 (1989) 223.

60 C.A. Fyfe, Y. Feng, H. Gies, H. Grondey and G.T. Kokotailo, J. Am. Chem. Soc., 112 (1990) 3264.
61 C.A. Fyfe, H. Grondey, Y. Feng and G.T. Kokotailo, J. Am. Chem. Soc., 112 (1990) 8812.
62 C.A. Fyfe, H. Gies, Y. Feng and H. Grondey, Zeolites, 10 (1990) 278.
63 W. Kolodziejski, P.J. Barrie, H. He and J. Klinowski, J. Chem. Soc., Chem. Commun., (1991) 961.
64 C.V. McDaniel and P.K. Maher, in Molecular Sieves, Society of Chemical Industry, London, 1968, p. 186; Zeolite Chemistry and Catalysis, ACS Monogr., 171 (1976) 285.
65 J. Klinowski, J.M. Thomas, C.A. Fyfe and G.C. Gobbi, Nature, 296 (1982) 533.
66 I.E. Maxwell, W.A. van Erp, G.R. Hays, T. Couperus, R. Huis and A. D.H. Clague, J. Chem. Soc., Chem. Commun., (1982) 523.
67 G. Engelhardt, U. Lohse, A. Samoson, M. Mägi, M. Tarmak and E. Lippmaa, Zeolites, 2 (1982) 59.
68 G. Engelhardt, U. Lohse, V. Patzelová, M. Mägi and E. Lippmaa, Zeolites, 3 (1983) 233.
69 G. Engelhardt, U. Lohse, V. Patzelová, M. Mägi and E. Lippmaa, Zeolites, 3 (1983) 239.
70 L. Kellberg, M. Linsten and H.J. Jakobsen, Chem. Phys. Lett., 182 (1991) 120.
71 J. Rocha and J. Klinowski, J. Chem. Soc., Chem. Commun., (1991) 1121.
72 J. Rocha, S.W. Carr and J. Klinowski, Chem. Phys. Lett., 187 (1991) 401.
73 H. Hamdan, B. Sulikowski and J. Klinowski, J. Phys. Chem., 93 (1989) 350.
74 P.J. Barrie, L.F. Gladden and J. Klinowski, J. Chem. Soc., Chem. Commun., (1991) 592.
75 A. Samoson, E. Lippmaa, G. Engelhardt, U. Lohse and H.-G. Jerschkewitz, Chem. Phys. Lett., 134 (1987) 589.
76 H. Hamdan and J. Klinowski, in M.L. Occelli and H.E. Robson (Eds.), Zeolite Synthesis, ACS Symposium Series, (1989) 398, 448 and 465.
77 G.A.H. Tijink, R. Janssen and W.S. Veeman, J. Am. Chem. Soc., 109 (1987) 7301.
78 H. Hamdan and J. Klinowski, J. Chem. Soc. Chem. Commun., (1989) 240.
79 J.H. Van Vleck, Phys. Rev., 74 (1948) 1168.
80 D. Freude, M. Hunger, H. Pfeifer and W. Schwieger, Chem. Phys. Lett., 128 (1986) 62.
81 D. Freude, M. Hunger and H. Pfeifer, Chem. Phys. Lett., 91 (1982) 307.
82 D. Freude, J. Klinowski and H. Hamdan, Chem. Phys. Lett., 149 (1988) 355.
83 D. Freude and J. Klinowski, J. Chem. Soc., Chem. Commun., (1988) 1411.
84 D. Freude, Adv. Colloid. Interface Sci., 23 (1985) 21.
85 D. Michel, A. Germanus, D. Scheler and B. Thomas, Z. Phys. Chem. (Leipzig), 262 (1981) 113.
86 D. Michel, A. Germanus and H. Pfeifer, J. Chem. Soc., Faraday Trans. I, 78 (1982) 237.
87 I. Jünger, W. Meiler and H. Pfeifer, Zeolites, 2 (1982) 310.
88 W.P. Rothwell, W. Shen and J.H. Lunsford, J. Am. Chem. Soc., 106 (1984) 2452.
89 J.H. Lunsford, W.P. Rothwell and W. Shen, J. Am. Chem. Soc., 107 (1985) 1540.
90 J.M. Thomas, J. Klinowski, C.A. Fyfe, G.C. Gobbi, S. Ramdas and M.W. Anderson, in G.D. Stucky and F.G. Dwyer (Eds.), Intrazeolite Chemistry, ACS Symposium Series, 218 (1983) 159.
91 H. Kessler, J.M. Chézeau, J.L. Guth, H. Strub and G. Coudurier, Zeolites, 7 (1987) 360.
92 K.F.M.G. J. Scholle and W.S. Veeman, Zeolites, 5 (1985) 118.
93 G.L. Turner, K.A. Smith, R.J. Kirkpatrick and E. Oldfield, J. Magn. Reson., 67 (1986) 544.
94 J.M. Bennett, J.P. Cohen, E.M. Flanigen J.J. Pluth and J.V. Smith, in G.D. Stucky and F.G. Dwyer (Eds.), Intrazeolite Chemistry, ACS Symposium Series, 218 (1983) 109.
95 M.E. Davis, C. Saldarriaga, C. Montes, J. Garces and C. Crowder, Nature, 331 (1988) 698.
96 M.E. Davis, C. Saldarriaga and C. Montes, J. Garces and C. Crowder, Zeolites, 8 (1988) 362.
97 J.V. Smith and W.J. Dytrych, Nature, 309 (1984) 607.
98 M. Estermann, L.B. McCusker, C. Bärlocher, A. Merrouche and H. Kessler, Nature, 352 (1991) 320.
99 C.S. Blackwell and R.L. Patton, J. Phys. Chem., 88 (1984) 6135.
100 W. Kolodziejski, H. He and J. Klinowski, Chem. Phys. Lett., 191 (1992) 117.
101 R.R. Rudolf and C.E. Crowder, Zeolites, 10 (1990) 163.
102 L.B. McCusker, Ch. Baerlocher, E. Jahn and M. Bülow, Zeolites, 11 (1991) 308.
103 J.P. van Braam Houckgeest, B. Kraushaar-Czarnetzki, R.J. Dogterom and A. de Groot, J. Chem. Soc., Chem. Commun., 666 (1991).
104 H.E. Gottlieb and Z. Luz, J. Magn. Reson., 54 (1983) 257.
105 E. Meirovitch and I. Belsky, J. Phys. Chem., 88 (1984) 4308.
106 R.R. Eckman and A.J. Vega, J. Phys. Chem., 90 (1986) 4679.
107 I. Kustanovich, D. Fraenkel, Z. Luz, S. Vega and H. Zimmermann, J. Phys. Chem., 92 (1988) 4134.
108 I. Kustanovich, H.M. Vieth, Z. Luz and S. Vega, J. Phys. Chem., 93 (1989) 7427.
109 I. Kustanovich, Z. Luz, S. Vega and A.L. Vega, J. Phys. Chem., 94 (1990) 3138.
110 M.J. Duer, H. He and J. Klinowski, J. Am. Chem. Soc., in press.
111 D. Goldfarb, H.-X. Li and M.E. Davis, J. Am. Chem. Soc., 114 (1992) 3690.
112 S.L. Meisel, J.P. McCullogh, C.H. Lechthaler and P.B. Weisz, Chemtech, 6 (1976) 86.

113 W.W. Kaeding and S. Butter, U.S. Patent, 3,911,041 (1975).
114 C.D. Chang, Catal. Rev. Sci. Eng., 25 (1983) 1.
115 G. Winde, A.V. Volkov, A.V. Kiselev and V.I. Lygin, Russian J. Phys. Chem., 49 (1975) 1716.
116 Z. Luz and A.J. Vega, J. Phys. Chem., 91 (1987) 374.
117 G. Mirth, J.A. Lercher, M.W. Anderson and J. Klinowski, J. Chem. Soc., Faraday Trans., 86 (1990) 3039.
118 M.W. Anderson, P.J. Barrie and J. Klinowski, J. Phys. Chem., 95 (1991) 235.
119 T.A. Carpenter, J. Klinowski, D.T.B. Tennakoon, C.J. Smith and D.C. Edwards, J. Magn. Reson., 68 (1986) 561.
120 M.W. Anderson and J. Klinowski, J. Chem. Soc., Chem. Commun., (1990) 918.
121 M.W. Anderson and J. Klinowski, Nature, 339 (1989) 200.
122 M.W. Anderson and J. Klinowski, J. Am. Chem. Soc., 112 (1990) 10.
123 B.R. Richardson, N.D. Lazo, P.D. Schettler, J.L. White and J.F. Haw, J. Am. Chem. Soc., 112 (1990) 2885.
124 N.D. Lazo, J.L. White, E.J. Munson, M. Lambregts and J.F. Haw, J. Am. Chem. Soc., 112 (1990) 4050.
125 J.L. White, N.D. Lazo, B.R. Richardson and J.F. Haw, J. Catal., 125 (1990) 260.
126 E.J. Munson and J.F. Haw, Anal. Chem., 62 (1990) 2532.
127 E.J. Munson, N.D. Lazo, M.E. Moellenhoff and J.F. Haw, J. Am. Chem. Soc., 113 (1991) 2783.
128 M.W. Anderson, M.L. Occelli and J. Klinowski, J. Phys. Chem., 96 (1992) 388.
129 J.F. Haw, B.R. Richardson, I.S. Oshiro, N.D. Lazo and J.A. Speed, J. Am. Chem. Soc., 111 (1989) 2052.
130 S.M. Csicsery, in J.A. Rabo (Ed.), Zeolite Chemistry and Catalysis, ACS Monograph, 171 (1976) 680.
131 N.Y. Chen, W.W. Kaeding and F.G. Dwyer, J. Am. Chem. Soc., 101 (1979) 6783.
132 W.W. Kaeding, U.S. Patent, 4,029,716 (1977).
133 W.O. Haag and D.H. Olson, U.S. Patent, 4,097,543 (1978).
134 E.G. Derouane, J.B. Nagy, P. Dejaifve, J.H.C. van Hooff, B.P. Spekman, J.C. Védrine and C. Naccache, J. Catal., 53 (1978) 40.
135 E.G. Derouane, P. Dejaifve, J.B. Nagy, J.H.C. van Hooff, B.P. Spekman, C. Naccache and J.C. Védrine, C.R. Acad. Sci. Paris, Ser. C, 284 (1977) 945.
136 J.B. Nagy, J.P. Gilson and E.G. Derouane, J. Mol. Catal., 5 (1979) 393.
137 E.G. Derouane, P. Dejaifve and J.B. Nagy, J. Mol. Catal., 3 (1977) 453.
138 E.G. Derouane and J.B. Nagy, ACS Symposium Series, 248 (1984) 101.
139 E.G. Derouane, J.P. Gilson and J.B. Nagy, Zeolites, 2 (1982) 42.
140 C.E. Bronnimann and G.E. Maciel, J. Am. Chem. Soc., 108 (1986) 7154.
141 J.B. Stothers, Carbon-13 NMR Spectroscopy, Academic Press, New York, 1972.
142 M.W. Anderson and J. Klinowski, Chem. Phys. Lett., 172 (1990) 275.
143 W. Kolodziejski and J. Klinowski, Appl. Catal., A81 (1992) 133.
144 M.T. Aronson, R.J. Gorte, W.E. Farneth and D. White, J. Am. Chem. Soc., 111 (1989) 840.
145 M.W. Anderson, B. Sulikowski, P.J. Barrie and J. Klinowski, J. Phys. Chem., 94 (1990) 2730.
146 B.M. Lok, C.A. Messina, R.L. Patton, R.T. Gajek, T.R. Cannan and E.M. Flanigen, J. Am. Chem. Soc., 106 (1984) 6092.
147 M. Ito, Y. Shimoyama, Y. Saito, Y. Tsurita and M. Otake, Acta Crystallogr., C41 (1985) 1698.
148 M. Munowitz and A. Pines, Science, 233 (1986) 525.
149 M. Munowitz and A. Pines, Adv. Chem. Phys., 66 (1987) 1.
150 A. Pines, in B. Maraviglia (Ed.), Proceedings of the 100th Fermi School of Physics, North Holland, Amsterdam, 1988.
151 R. Ryoo, S.-B. Liu, L.C. de Menorval, K. Takegoshi, B. Chmelka, M. Trecoske and A. Pines, J. Phys. Chem., 91 (1987) 6575.
152 B.F. Chmelka, J.G. Pearson, S.-B. Liu, R. Ryoo, L.C. de Menorval and A. Pines, J. Phys. Chem., 95 (1991) 303.
153 J. Baum, M. Munowitz, A.N. Garroway and A. Pines, J. Chem. Phys., 83 (1985) 2015.
154 D.E. Kaplan and E.L. Hahn, J. Phys. Radium, 19 (1958) 821.
155 M. Emshwiller, E.L. Hahn and D. Kaplan, Phys. Rev., 118 (1960) 414.
156 C.P. Slichter, Principles of Nuclear Magnetic Resonance, Springer-Verlag, New York 1978, p. 233.
157 E.R.H. van Eck and W.S. Veeman, Solid State NMR, 1 (1992) 1.
158 T. Gullion and J. Schaefer, J. Magn. Reson., 81 (1989) 196.
159 T.G. Oas, R.G. Griffin and M.H. Levitt, J. Chem. Phys., 89 (1988) 692.
160 A.W. Hing, S. Vega and J. Schaefer, J. Magn. Reson., 96 (1992) 205.
161 C.A. Fyfe, K.T. Mueller, H. Grondey and K.C. Wong-Moon, Chem. Phys. Lett., 199 (1992) 198.

Analytica Chimica Acta, 283 (1993) 967–985
Elsevier Science Publishers B.V., Amsterdam

Multinuclear solid state NMR of host–guest systems with TO_2 (T = Si, Al) host-frameworks. A case study on sodalites

G. Engelhardt

Institute of Chemical Technology I, University of Stuttgart, Pfaffenwaldring 55, D-7000 Stuttgart (Germany)

P. Sieger and J. Felsche

Faculty of Chemistry, University of Konstanz, D-7750 Konstanz (Germany)

(Received 15th January 1993)

Abstract

The application of high-resolution multinuclear solid state nuclear magnetic resonance (NMR) spectroscopy to the structural characterization of microporous host–guest systems is demonstrated by a series of sodalites with aluminosilicate, aluminate and silicate host-frameworks and a large variety of guest species (inorganic anions and cations, H_2O, OH^-, organic molecules) enclathrated in the sodalite cages. While ^{29}Si and ^{27}Al NMR provide information on the local structure and composition of the framework, ^{23}Na and ^1H NMR give insights into the structure and dynamics of the cage fillings. The number of crystallographically inequivalent Si, Al and Na sites in the sodalite structures is determined from the ^{29}Si, ^{27}Al and ^{23}Na NMR spectra and their local geometry is characterized by detailed interpretation of the isotropic chemical shifts and the ^{27}Al and ^{23}Na quadrupole parameters. Dynamic reorientation processes of the guest species and structural phase transitions of distinct sodalite compositions were studied by multinuclear magic angle spinning (MAS) NMR at variable temperature. Besides MAS NMR, double rotation (DOR) NMR experiments at different field strengths were performed for ^{27}Al and ^{23}Na to resolve strongly overlapping lines of the MAS NMR spectra.

Keywords: Nuclear magnetic resonance spectrometry; Host–guest complexes; Microporous compounds; Sodalites; Solid-state NMR

Host–guest systems of microporous materials with well defined cavities and channels of molecular dimensions are of high practical interest, e.g. as heterogeneous catalysts, molecular sieves, adsorbants, ion exchangers, and more recently in the development of nanocomposite materials with new electronic and optical properties. In addition, such materials are appropriate systems to study the fundamentals of host–guest interactions on the molecular level and to characterize the resulting structural changes of the host-framework and the guest species. Several experimental techniques are available for studies of this kind which include x-ray and neutron diffraction, elastic and inelastic neutron scattering, infrared and Raman spectroscopy, x-ray absorption spectroscopy (EXAFS, XANES), x-ray photoelectron spectroscopy, scanning tunnelling microscopy, and solid state nuclear magnetic resonance (NMR) spectroscopy. Since each of these techniques provides specific information which often complements each other, as many of them as possible should be applied. The aim of the present article

Correspondence to: G. Engelhardt, Institute of Chemical Technology I, University of Stuttgart, Pfaffenwaldring 55, D-7000 Stuttgart (Germany).

is, however, to demonstrate the unique features and the high potential of multinuclear solid state NMR spectroscopy in the description of the local structure and dynamics of host–guest systems exemplified by sodalite-type materials with different host-frameworks and guest species. To this end, after a short introduction into the structural characteristics of sodalites and the related features of solid state NMR, a concise review will be presented on the main information which can be derived from multinuclear NMR studies of sodalites with aluminosilicate, aluminate and silica frameworks containing a large variety of enclathrated guests. Prior to the NMR investigations the samples were carefully characterized by thermal analysis, x-ray powder diffraction, IR spectroscopy, and other techniques. While the information derived from the latter methods are a prerequisite for the reliable interpretation of the NMR spectra, their details have been or will be published elsewhere and will not be considered in this article.

The structure of sodalites

The framework of sodalites consists of a perfectly periodic array of all-space filling [$4^6 6^8$] polyhedra, also called β-cages or sodalite cages (but not "cubooctahedra" as often found in the literature!), formed by a network of corner-sharing TO_4 tetrahedra with T = Si and/or Al [1]. Figure 1a shows a single β-cage and Fig. 1b the connection of three cages by common six- and four-rings. Referred to a body-centered, pseudocubic unit cell comprising the equivalent of two β-cages, the general framework composition is $[T_{12}O_{24}]$. Sodalite frameworks containing aluminium atoms in their T sites possess a negative charge equal to the number of Al atoms which is balanced by exchangeable metal cations present in the β-cages. In addition, the sodalite cages may accomodate a large variety of guest species, e.g. monovalent or bivalent anions (A^-, and A^{2-}) and cations (M^+ or M^{2+}), H_2O, or organic molecules. Three types of sodalite frameworks are considered in the present study. (i) 1:1 Aluminosilicate sodalites (T = Si and Al) of general composition $[Na_4A^-]_2[Si_6Al_6O_{24}]$, $[Na_4A^{2-}][Si_6Al_6O_{24}]$, and $[Na_3(H_2O)_{4-x}]_2[Si_6Al_6O_{24}]$ with x = 0–4. Following an earlier suggestion [2], the guest species present in the distinct β-cages are enclosed in the first square brackets of these constitution formulas. In general, the Na^+ cations are located above the centers of the six-ring windows of the β-cages (see Fig. 1a) and the anions occupy preferably the center of the cage; (ii) aluminate sodalites (T = Al only) with divalent cations and anions as guest species of composition $[(M^{2+})_4A^{2-}]_2[Al_{12}O_{24}]$, and (iii) silica sodalites (T = Si only) with organic guest molecules

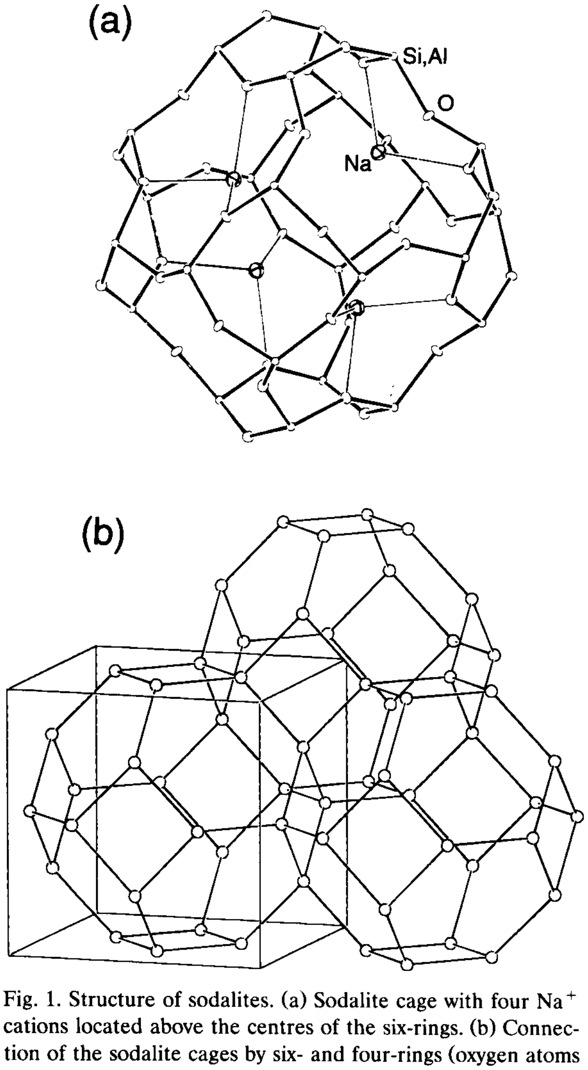

Fig. 1. Structure of sodalites. (a) Sodalite cage with four Na^+ cations located above the centres of the six-rings. (b) Connection of the sodalite cages by six- and four-rings (oxygen atoms omitted for clarity).

C of composition $[C]_2[Si_{12}O_{24}]$. The sodalite materials were prepared by standard procedures, the details are described in the related references.

Solid state NMR of sodalites – general features

The isotropic chemical shift, δ, of a certain line in a MAS NMR spectrum is determined by the local structure around the respective resonance atom, i.e. distinct lines are observed for atoms residing in different structural surroundings. Therefore, the number of crystallographically distinct sites of the NMR nucleus under study and (from line intensities) their relative populations can, in principle, be directly derived from the MAS NMR spectrum. In addition, detailed information on the local structural environment of the corresponding atomic site may be obtained from a careful interpretation of δ. However, even in highly crystalline materials the different lines in the spectra are not always sufficiently resolved to determine selectively their specific chemical shifts and intensities. This is especially true for atomic sites involved in dynamic exchange or reorientation processes which may cause severe line broadening or averaging of specific site interactions. In those cases NMR measurements at variable temperature are often helpful and may provide valuable information on specific features of the dynamic processes and possible structural phase transitions. Broad and complex line shapes are also observed in the MAS NMR spectra of quadrupolar nuclei (e.g. ^{23}Na, ^{27}Al) which arise from (second order) interactions of the nuclear quadrupole moment, eQ, with the local electric field gradient, eq, at the nuclear site. Since the electric field gradient depends on the charge distribution around the nucleus, the quadrupole interactions are an important source of structural information. The strength of the quadrupole interaction is characterized by the quadrupole coupling constant, $QCC = e^2qQ/h$, and the deviation from axial symmetry of the field gradient is described by the asymmetry parameter, η, with $0 \leq \eta \leq 1$ and $\eta = 0$ for an axially symmetric field gradient. However, QCC and η cannot be directly extracted from the MAS NMR spectra but have to be determined by spectral simulation or other techniques. Moreover, the peak positions are shifted by the second order quadrupole effects and must be carefully corrected to deduce the isotropic chemical shift [3,4]. In some cases the quadrupolar broadened lines overlap heavily in the MAS NMR spectra and are difficult to analyse. Line separation can, however, be achieved by application of the double rotation (DOR) NMR technique [5] which narrows the lines considerably due to averaging the anisotropic part of the second order quadrupole interaction (see below).

Specific investigations of the host-framework or of the guest species of sodalites can be performed by the selection of the appropriate atomic nuclei for the NMR experiments. While ^{29}Si and ^{27}Al NMR are particularly useful in the characterization of the framework structure, ^{23}Na and ^{1}H NMR provide information on the guest species located in the sodalite cages. In the next sections, characteristic examples of the application of the various NMR nuclei in structural studies of the above mentioned sodalite materials will be presented.

RESULTS AND DISCUSSION

^{29}Si NMR

General considerations

The ^{29}Si nucleus has a nuclear spin quantum number $I = 1/2$ and narrow lines are generally observed in the ^{29}Si MAS NMR spectra of well ordered aluminosilicate and silica sodalites. The chemical shifts, δ(Si), of the lines depend primarily on type and number of the T atoms (T = Si, Al) in the $Si(OT)_4$ environment of the silicon atom but are also affected by the SiOT bond angles, Θ. If only a single type of crystallographically equivalent $Si(OT)_4$ environment with identical SiOT bond angles is present in the sodalite framework (cubic structures), a single sharp line is expected in the ^{29}Si MAS NMR spectrum. Non-cubic structures with crystallographically inequivalent $Si(OT)_4$ units characterized by distinct SiOT bond angles give rise to splittings or broadenings of the lines. Linear correlations between

TABLE 1

^{29}Si chemical shifts δ(Si) of aluminosilicate sodalites with different cage contents

Cage content	δ(Si) (ppm)	Cage content	δ(Si) (ppm)
$[Na_4Cl]$	−84.5	$[Na_4\{B(OH)_4)\}]$	−88.0
$[Na_4Br]$	−85.8	$[Na_4(CO_3)], [Na_4]$	−87.8
$[Na_4I]$	−87.9	$[Na_4(SO_4)], [Na_4]$	−89.9
$[Na_4(NO_2)]$	−85.6	$[Na_4(CrO_4)], [Na_4]$	−90.4
$[Na_4(NO_3)]$	−87.5	$[Na_4(MoO_4)], [Na_4]$	−92.3
$[Na_4(ClO_4)]$	−90.3	$[Na_3(H_2O)_4]$	−82.5
$[Na_4(H_3O_2)]$	−84.3	$[Na_3(H_2O)_2]$	−86.5
$[Na_4(OH)]$	−81.2	$[Na_3]$	−90.5
$[Na_4(CN)]$	−85.2	$[K_3(H_2O)_4]$	−92.8
$[Na_4(SCN)]$	−89.1	$[K_3]$	−96.7
$[Na_4(HCOO)]$	−86.7	$[Li_4Cl]$	−76.6 [a]
$[Na_4(CH_3COO)]$	−89.5	$[Li_4Br]$	−77.6 [a]

[a] Ref. [8].

the arithmetic mean, $\overline{\Theta}$, of the four SiOT bond angles of the $Si(OT)_4$ structural groups and δ(Si) of framework aluminosilicates and silicates have been established empirically and by theoretical considerations which predict a high-field shift with increasing $\overline{\Theta}$ [6]. For cubic structures, Θ is directly correlated to the lattice parameter, a_0, and, therefore, a linear correlation also follows between δ(Si) and a_0. These correlations may be applied to estimate Θ and a_0 of cubic sodalite frameworks as well as $\overline{\Theta}$ of the distinct $Si(OT)_4$ sites in non-cubic structures from ^{29}Si chemical shifts [7].

Specific examples

Aluminosilicate sodalites with uniform cage fillings $[Na_4A]_2[Si_6Al_6O_{24}]$. The ^{29}Si MAS NMR spectra of cubic aluminosilicate sodalites containing preferably Na^+ but in a few cases also K^+ or Li^+ cations and a large variety of univalent or divalent anions in the β-cages (see Table 1) show throughout a single line for $Si(OAl)_4$ environments, confirming the alternating Si,Al ordering and cubic symmetry of the sodalite framework. The chemical shifts δ(Si) collected in Table 1 cover the range of −76.6 to −96.7 ppm indicating the large variation of the SiOAl bond angles Θ caused by the different steric and coordination requirements of the various guest species. δ(Si) correlates well with Θ taken from the literature or calculated from the lattice parameter a_0 [7]. Linear regression analysis of the 24 data points of Table 1 yields $\delta(Si) = -0.65\Theta + 5.50$ with a correlation coefficient of $r = 0.990$ and a standard deviation of 0.66 ppm. The corresponding correlation equation between δ(Si) and a_0 is $\delta(Si) = -22.59a_0 + 115.71$ with $r = 0.977$ and a standard deviation of 0.92 ppm. For the latter calculation the data of the probably non-cubic anhydrous sodium and potassium sodalite have been omitted. Similar correlations but with a less extended set of data have been published previously [7–9].

Aluminosilicate sodalites with mixed cage fillings $[Na_4A]_{2-x}[Na_4B]_x[Si_6Al_6O_{24}]$. It has been shown in the preceding section that δ(Si) of the sodalite framework depends heavily on the SiOAl bond angles which are determined by the type of guest species in the β-cages. If two or more types of cage fillings are present in the sodalite material, they may be distributed uniformely among the β-cages ("solid solution") or may form segregated phase domains of cages containing the same guest species. In the former case the SiOAl angles will adjust themselves to an average value satisfying the steric requirements of all guests, and the ^{29}Si MAS NMR spectrum will show a single line at the composition-weighted average of δ(Si) of the pure sodalite compositions. In the latter case the SiOAl angles will retain the discrete values of the distinct sodalite compositions forming the segregated phases, and more than one line will appear in the spectrum. Provided that the shift difference of the pure compositions is large enough to observe the line shift or to

Fig. 2. ^{29}Si MAS NMR spectra of sodium aluminosilicate sodalites with mixed cage contents. (a)–(d) $[Na_4Br]_{2-x}[Na_4(H_3O_2)]_x[Si_6Al_6O_{24}]$, (a) $x = 2$, (b) $x = 1.5$, (c) $x = 0.6$, (d) $x = 0.3$. (e)–(h) $[Na_4(ClO_4)]_{2-x}[Na_4(H_3O_2)]_x[Si_6Al_6O_{24}]$, (e) $x = 2$, (f) $x = 1.5$, (g) $x = 1.0$, (h) $x = 0$. The spectra were measured at 79.5 MHz (Bruker MSL-400) using 4 μs pulse width (70° flip angle), 5 s pulse repetition, high-power proton decoupling, 4 kHz spinning frequency and Q_8M_8 as external reference [$\delta(Me_3Si) = 12.4$ ppm relative to TMS].

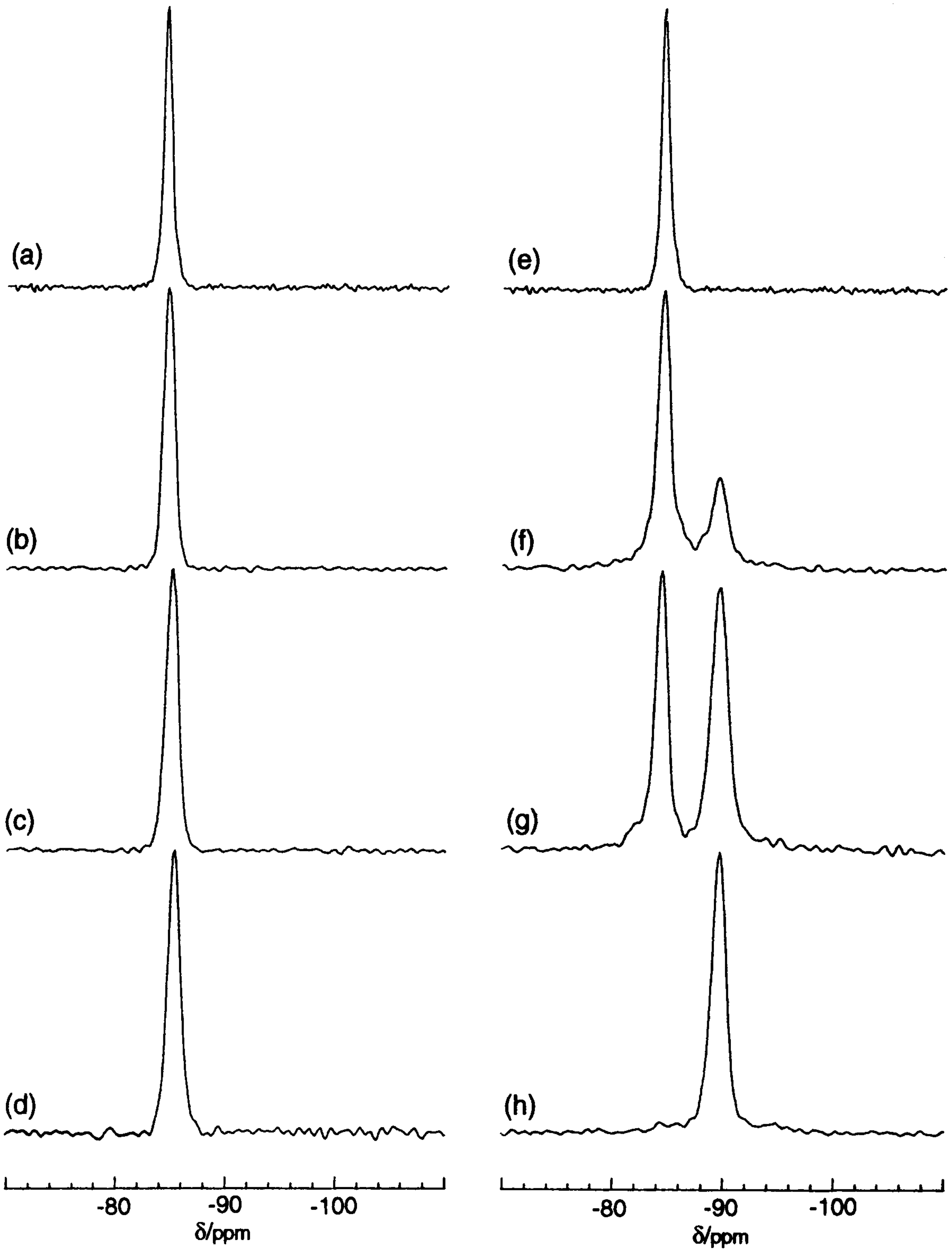
(a)
(b)
(c)
(d)
-80
-90
-100
δ/ppm
(e)
(f)
(g)
(h)
-80
-90
-100
δ/ppm

resolve distinct lines in the spectrum of the mixed products, ^{29}Si MAS NMR can be applied to prove the compositional phase purity of sodalites, to distinghuish between the two above-mentioned kinds of cage distributions, and to determine quantitatively the proportions of the different cage fillings in mixed sodalite materials. Experiments of this type have been performed to study the phase composition of as-synthesized hydrosodalites and their de- and rehydration products [2]. For example, three differently hydrated sodalite phases of composition $[Na_3(H_2O)_n]_2[Si_6Al_6O_{24}]$ with $n = 0$, 2 and 4 have been detected after stepwise rehydration of an anhydrous sodalite sample by their characteristic lines in the ^{29}Si MAS NMR spectrum at −90.5 ($n = 0$), −86.5 ($n = 2$) and −82.5 ppm ($n = 4$).

Figure 2 shows the ^{29}Si MAS NMR spectra of two types of mixed sodalites of general composition $[Na_4A]_{2-x}[Na_4B]_x[Si_6Al_6O_{24}]$ with $A = Br^-$ or ClO_4^- and $B = H_3O_2^-$ (the $H_3O_2^-$ anion is formed by a strong hydrogen bond between H_2O and OH^- [10]). For $0 < x < 2$ both sodalites contain a mixture of two types of cage fillings, $[Na_4A]$ and $[Na_4B]$, while for $x = 2$ only $[Na_4B]$ and for $x = 0$ only $[Na_4A]$ filled cages are present. The spectra show immediately that a homogeneous distribution of the differently filled cages exists in the sodalites with $A = Br^-$ (single line, Fig. 2a–d) while for the materials with $A = ClO_4^-$ a phase separation of the cages accomodating ClO_4^- and $H_3O_2^-$ anions is observed (two lines, Fig. 2e–h). Segregated phase domains have also been detected by ^{29}Si MAS NMR in mixed sodalites containing I^- and $H_3O_2^-$ anions as well as in hydrosodalites of composition $[Na_4A]_{2-x}[Na_3(H_2O)_4]_x[Si_6Al_6O_{24}]$ with $A = ClO_4^-$ or I^-, while the corresponding sodalites with $A = Br^-$ show again single-line spectra indicating solid solution-type distribution of the cage fillings. Further details of these studies including also other sodalite compositions and the results of thermoanalysis, IR spectroscopy and powder x-ray diffraction will be published elsewhere [11].

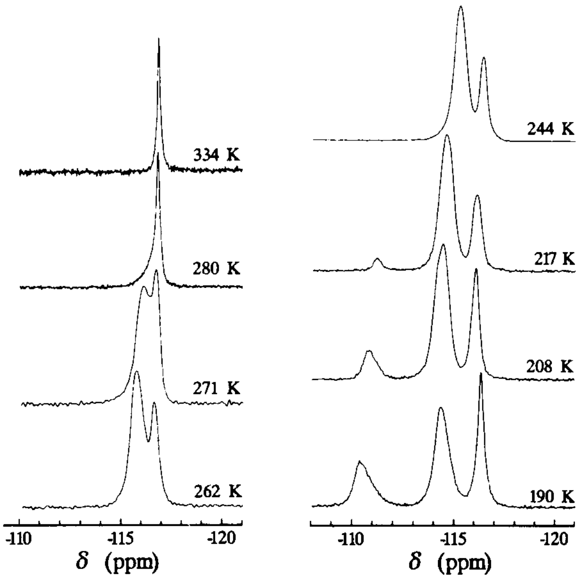

Fig. 3. ^{29}Si CP MAS NMR spectra of ethylene glycol silica sodalite $[(CH_2OH)_2]_2[Si_{12}O_{24}]$ at variable temperature. The spectra were measured at 79.5 MHz with 5 ms mixing time for cross-polarization, 10 s pulse repetition, 5 kHz spinning frequency and referenced as given in Fig. 2.

Silica sodalites $[C]_2[Si_{12}O_{24}]$. The ^{29}Si MAS NMR spectra of silica sodalites containing ethylene glycol [12], trioxane [13] or dioxolane [14] as guest molecules exhibit at room temperature a single and very narrow line at −116.8, −116.3 and −117.9 ppm, respectively, consistent with a single $Si(OSi)_4$ environment in a cubic structure. The small differences in δ(Si) indicate slightly different SiOSi bond angles in the framework of the three samples probably induced by the different steric requirements of the organic guest molecules. It should be noted that the splitting into three lines reported for ethylene glycol sodalite by Meinhold and Bibby [12] is not observed in our sample which exhibits a very narrow (half width 0.2 ppm) symmetrical line shape. Differential scanning calorimetry (DSC) and x-ray diffraction studies have shown that upon cooling ethylene glycol silica sodalite undergoes several structural phase transitions from cubic to lower symmetry [14,15]. These phase changes are clearly manifested in the ^{29}Si MAS NMR spectra measured in the temperature range of 334–190 K (Fig. 3). With decreasing temperature the single line of the cubic structure splits reversibly into two (271–244 K) respectively three lines (217–190 K), indicating the presence of crystallographically inequivalent Si sites to be expected for non-cubic crystal symmetry. From δ(Si) of the three lines observed at 190 K mean SiOSi bond angles of 158°, 153° and 147° can be deduced for the distinct $Si(OSi)_4$ sites of the non-cubic structure. This information derived from the ^{29}Si MAS NMR spectra may be helpful in the x-ray refinement of the crystal structure of the low-temperature phases which, however, has not yet been performed. Trioxane silica sodalite and dioxolane silica sodalite show no line splittings in their low-temperature spectra but small shifts to low field and some broadening of the single lines.

^{27}Al NMR

General considerations

In contrast to the ^{29}Si nucleus, ^{27}Al has $I = 5/2$, i.e. possesses a nuclear quadrupole moment, and is, therefore, involved in quadrupole interactions if the local charge distribution around the Al nucleus deviates from spherical symmetry. The Al atoms on T sites of the sodalite framework are tetrahedrally coordinated by four oxygen atoms, i.e. forming $Al(OSi)_4$ environments in aluminosilicate sodalites and $Al(OAl)_4$ environments in aluminate sodalites. For ideal tetrahedral symmetry of the AlO_4 coordination (no field gradient) the quadrupole interaction vanishes and narrow lines will appear in the ^{27}Al MAS NMR spectra at positions corresponding to the isotropic chemical shift, δ(Al). However, the tetrahedral symmetry of the AlO_4 sites in the sodalite frameworks is generally more or less distorted and quadrupolar broadened lines are observed in the ^{27}Al MAS NMR spectra. As mentioned above, the position (center of gravity) of those lines is not identical with the isotropic chemical shift, δ(Al), but must be corrected for quadrupolar shift contributions. Quadrupolar lines which strongly overlap in the ^{27}Al MAS NMR spectra may be resolved by DOR NMR experiments, and δ(Al) and QCC [precisely the value of $QCC(1 + \eta^2/3)$] of the distinct lines can be determined from DOR NMR spectra measured at different field strengths [16]. Information on the local structure of the $Al(OT)_4$ surroundings may be derived from the ^{27}Al spectral parameters. δ(Al) has been found to depend characteristically on the coordination number and next nearest neighbours of the aluminium atom [3]. For aluminium in $Al(OT)_4$ environments typical shift ranges of about 50–70 ppm has been observed for T = Si and of 70–80 ppm for T = Al. Similar to δ(Si), correlations between δ(Al) and the mean AlOT bond angles of $Al(OT)_4$ sites have been established [8,17]. QCC depends on the distortion of the AlO_4 tetrahedra and ranges from several kHz up to about 9 MHz for highly distorted structures (see below).

Specific examples

Aluminosilicate sodalites $[Na_4A]_2[Si_6Al_6O_{24}]$. The ^{27}Al MAS NMR spectra of aluminosilicate sodalites in general exhibit comparatively narrow and almost symmetrical lines indicating only moderate quadrupole interactions. QCC of 0.6–1.0 MHz and η of 0.3–0.6 have been reported by Nielsen et al. [18] for a series of sodium and lithium halide sodalites. The weak quadrupole interactions show that the AlO_4 coordinations in the framework of the aluminosilicate sodalites are not strongly distorted from tetrahedral symmetry which is in agreement with the known crystal structure of these materials [19]. The non-zero values of η indicate, however, significant deviations of the field gradient from axial symmetry, which have been ascribed to asymmetric charge distributions from the further distant coordination spheres, e.g. from the guest ions in the cages [18]. δ(Al) values between 60 and 73 ppm have been determined for the above aluminosilicate sodalites which correlate linearly with the corresponding AlOSi bond angles [8]. Although this structural dependency of δ(Al) resembles that of ^{29}Si, the larger line widths of the ^{27}Al MAS NMR spectra restrict their application to characterize subtle structural differences in the framework of aluminosilicate sodalites.

^{27}Al MAS and DOR NMR have been, however, successfully applied to study the structural phase transition of sodium tetrahydroxoborate sodalite, $[Na_4\{B(OH)_4\}]_2[Si_6Al_6O_{24}]$, which exhibits cubic symmetry (space group $P\bar{4}3n$) above room temperature [high-temperature (HT) phase] but undergoes a transformation to non-cubic symmetry at lower temperature [low-temperature

(LT) phase] [20]. A narrow line (half width 120 Hz) at 60.8 ppm is observed in the ^{27}Al MAS NMR spectrum at 350 K (not shown) which broadens considerably with decreasing temperature and shows a five times larger line width at 290 K (see Fig. 4a). Any attempt to simulate this MAS spectrum by distinct quadrupolar line shapes failed. However, application of ^{27}Al DOR NMR results in a remarkable line narrowing and besides two weak lines of an impurity, three lines can clearly be identified, designated by A–C in Fig. 4a. From the DOR spectra measured at 9.4 and 11.7 T δ(Al) and QCC have been estimated to, respectively, 60.4 ppm and 1.2 MHz (line A), 61.1 ppm and 1.8 MHz (line B), and 59.5 ppm and 1.7 MHz (line C). Thus the DOR spectrum reveals the presence of three crystallographically inequivalent Al sites in the framework of the LT form of the tetrahydroxoborate sodalite. While the x-ray structure of the LT form has not yet been solved, the presence of three Al sites agrees with the number of distinct T (T = Al, Si) sites derived from the tetragonal space group $P\bar{4}2_1c$ suggested for the LT structure from x-ray powder diffraction and crystallographic supergroup–subgroup relations [21]. It will be shown below that similar information has been derived from the ^{23}Na DOR NMR spectra. However, no line splittings but only some line broadening has been observed in the ^{29}Si MAS NMR spectrum of the LT form of tetrahydroxoborate sodalite, which shows that in this case the quadrupole interaction

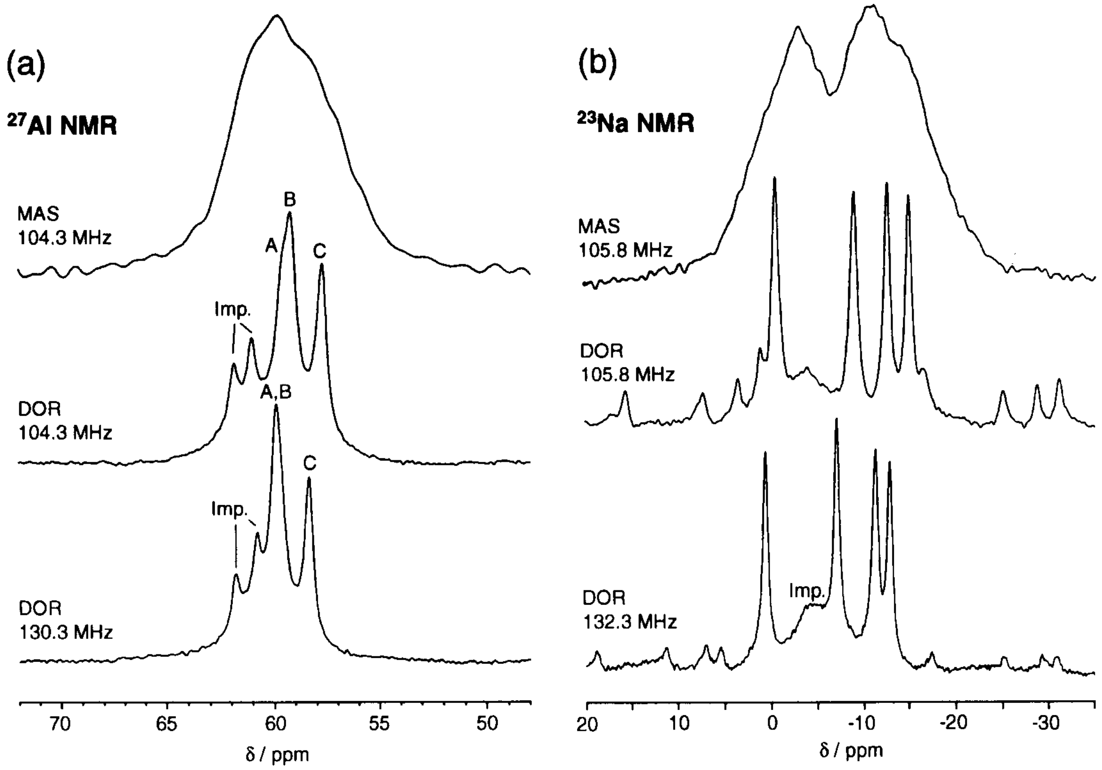

Fig. 4. ^{27}Al and ^{23}Na MAS and DOR NMR spectra of sodium tetrahydroxoborate sodalite $[Na_4\{B(OH)_4\}]_2[Si_6Al_6O_{24}]$ at 290 K. (a) ^{27}Al NMR spectra, (b) ^{23}Na NMR spectra. The MAS NMR spectra were measured at 104.3 MHz for ^{27}Al and 105.8 MHz for ^{23}Na with 0.6 μs pulse width, 1 s pulse repetition and 6 kHz spinning frequency. DOR NMR spectra were registered at 9.4 T (104.3 MHz for ^{27}Al and 105.8 MHz for ^{23}Na) and 11.7 T (130.3 MHz for ^{27}Al and 132.3 MHz for ^{23}Na) using Bruker DOR probes and spinning frequencies of 850 Hz (9.4 T) and 1 kHz (11.7 T) for the outer and about 5–7 kHz for the inner rotor. Rotor synchronized pulse excitation has been applied to eliminate the odd-numbered spinning side bands [16]. Solid NaCl was used as reference for ^{23}Na and an aqueous $Al(NO_3)_3$ solution for ^{27}Al.

of the ^{27}Al nucleus is more sensitive in detecting small structural differences than the ^{29}Si chemical shift.

Aluminate sodalites $[M_4^{2+}A^{2-}]_2[Al_{12}O_{24}]$. The framework of aluminate sodalites is built up entirely from AlO_4 tetrahedra, which, however, are strongly distorted from tetrahedral symmetry due to cooperative rotations of the tetrahedral units to adjust the framework to the size of the guest species [22]. This distortion induces strong field gradients at the ^{27}Al nucleus and, therefore, considerable quadrupole interactions which are much stronger than those in the aluminosilicate sodalites considered above. The strong quadrupole interaction is clearly reflected in the ^{27}Al MAS NMR spectra of calcium tungstate aluminate sodalite, $[Ca_4WO_4]_2[Al_{12}O_{24}]$ (CAW) [16], and strontium sulphate aluminate sodalite, $[Sr_4SO_4]_2$-$[Al_{12}O_{24}]$ (SAS) displayed in Fig. 5a and b. Due to superposition of strongly quadrupolar broadened lines of several crystallographically inequivalent AlO_4 sites, broad and poorly resolved spectral patterns are observed which are very difficult to analyse. However, Fig. 5c, d shows that application of the DOR technique again yields a dramatic increase in the spectral resolution, the total line width of several kHz in the MAS spectra being reduced to a number of narrow lines about 100–200 Hz wide accompanied by a manifold of spinning side bands. Detailed analysis of the DOR spectra measured at different spinning frequencies reveal the presence of seven central lines (designated by A–G in Fig. 5c) for CAW [16] and of four lines for SAS (A–D, Fig. 5d). The seven

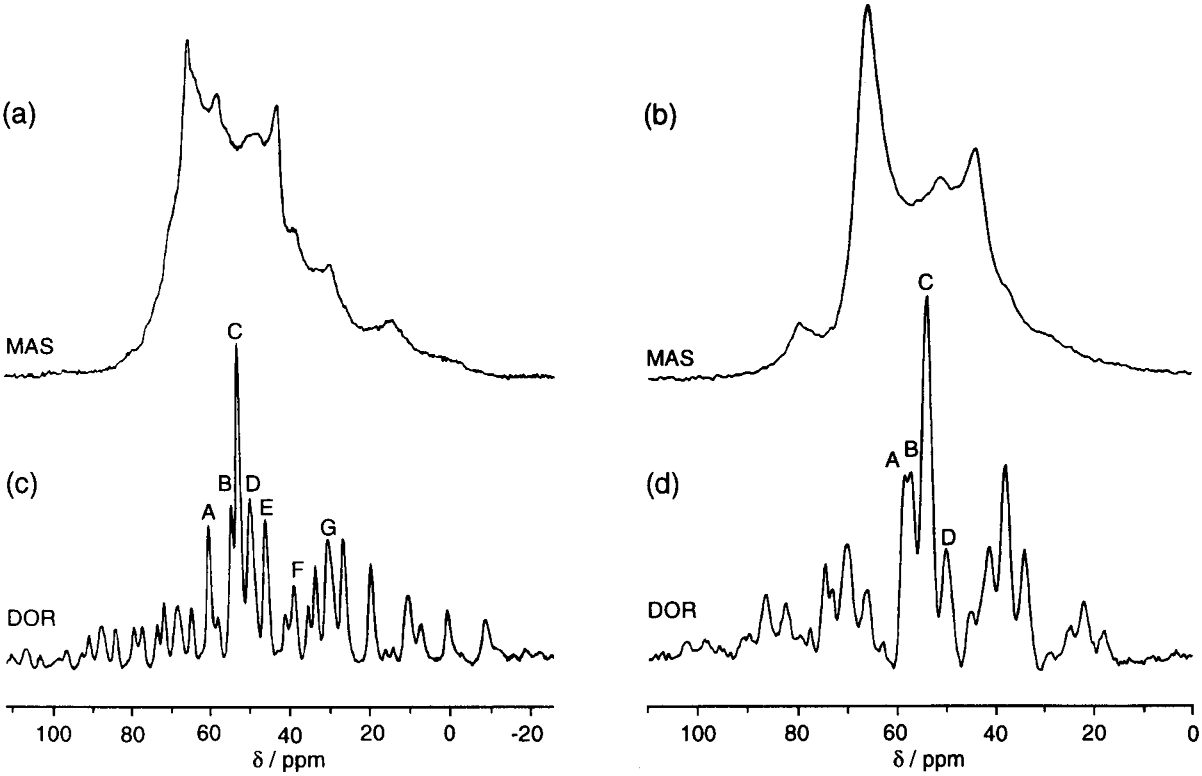

Fig. 5. (a, b) ^{27}Al MAS and (c, d) DOR NMR spectra of (a, c) calcium tungstate aluminate sodalite $[Ca_4(WO_4)]_2[Al_{12}O_{24}]$ and (b, d) strontium sulphate aluminate sodalite $[Sr_4(SO_4)]_2[Al_{12}O_{24}]$. The MAS NMR spectra were measured at 104.3 MHz with 0.6 μs pulse width, 2 s pulse repetition and 12 kHz spinning frequency. The DOR NMR spectra were recorded at the same resonance frequency following the conditions specified in Fig. 4, with spinning of the outer rotor at 1 kHz for (c) but 850 Hz for (d). All the lines in the DOR spectra not marked by a capital letter are spinning side bands.

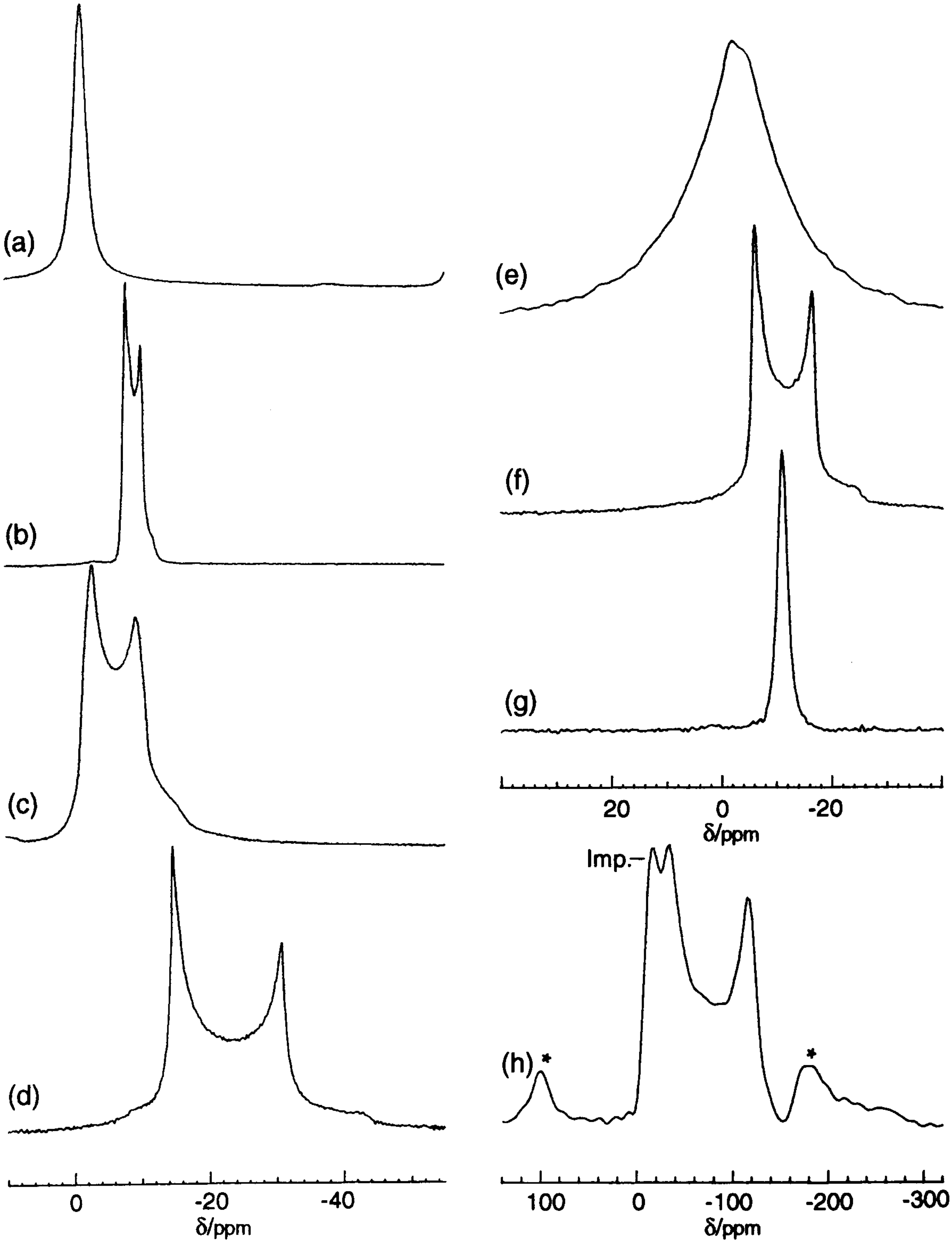
(a)
(b)
(c)
(d)
0
-20
-40
δ/ppm
(e)
(f)
(g)
20
0
-20
δ/ppm
Imp.
(h)
*
*
100
0
-100
-200
-300
δ/ppm

TABLE 2

^{23}Na NMR data of sodium aluminosilicate sodalites with different cage contents

Cage content	Line shape [a]	δ(Na) (ppm) [b]	QCC (MHz)	η
$[\mathrm{Na_4Cl}]^{3+}$	GL (170 Hz)	−1.1	0.3 [g]	–
$[\mathrm{Na_4Br}]^{3+}$	GL (300 Hz)	−0.9	0.72 [g]	0.12 [g]
$[\mathrm{Na_4I}]^{3+}$	QP	0.0	1.7	0.05
$[\mathrm{Na_4(NO_2)}]^{3+}$	QP	−6.6	1.0	0
$[\mathrm{Na_4(NO_3)}]^{3+}$	QP	−6.5	1.8	0.2
$[\mathrm{Na_4(ClO_4)}]^{3+}$	QP	−9.4	2.5	0.05
$[\mathrm{Na_4(OH)}]^{3+}$	QP	−4.0	2.0	0.1
$[\mathrm{Na_4(H_3O_2)}]^{3+}$	GL (1.9 kHz)	−2.5	–	–
$[\mathrm{Na_4(H_3O_2)}]^{3+}$, [c]	QP	−8.4	1.5	0.16
$[\mathrm{Na_4(CN)}]^{3+}$	GL (240 Hz)	−2.5	–	–
$[\mathrm{Na_4(SCN)}]^{3+}$	QP	−6.5	2.5	0.1
$[\mathrm{Na_4(HCOO)}]^{3+}$	GL (580 Hz)	−7.1	–	–
$[\mathrm{Na_4(CH_3COO)}]^{3+}$	GL (870 Hz)	−7.4	–	–
$[\mathrm{Na_4\{B(OH)_4\}}]^{3+}$, [d]	GL (240 Hz)	−4.7	–	–
$[\mathrm{Na_4\{B(OH)_4\}}]^{3+}$, [e]	[f]	2.5	1.1	–
		−3.9	1.5	–
		−9.0	1.3	–
		−9.0	1.6	–
$[\mathrm{Na_4(CO_3)}]^{2+}$	GL (350 Hz)	−13.1	–	–
$+[\mathrm{Na_4}]^{4+}$	QP	4.0	2.3	0
$[\mathrm{Na_4(SO_4)}]^{2+}$	QP	−12.8	1.0	0.15
$+[\mathrm{Na_4}]^{4+}$	QP	−3.0	2.1	0.2
$[\mathrm{Na_4(CrO_4)}]^{2+}$	QP	−13.7	1.6	0.05
$+[\mathrm{Na_4}]^{4+}$	QP	−4.8	2.6	0.05
$[\mathrm{Na_3(H_2O)_4}]^{3+}$	GL (350 Hz)	−10.9	–	–
$[\mathrm{Na_3}]^{3+}$	QP	3.0	5.9	0.1

[a] GL = Gaussian line with half width in parenthesis; QP = quadrupole pattern. [b] Reference solid NaCl. [c] At 160 K. [d] At 320 K. [e] At 290 K. [f] Four sharp lines in the DOR NMR spectrum. [g] Ref. [18].

lines observed for CAW correspond to the seven crystallographically distinct Al sites found in the single crystal x-ray structure of this material [23]. QCC of the seven lines, determined from ^{27}Al DOR NMR spectra measured at two different field strengths (9.4 and 11.7 T), range from 5 to 9 MHz indicating the large quadrupole interaction due to the strong distortion of the $\mathrm{AlO_4}$ tetrahedra. Moreover, QCC correlates well with a shear strain parameter (calculated from the OAlO bond angles of the x-ray structure) which describes quantitatively the degree of the distortion. Using this correlation, an assignment of the seven lines to the seven Al sites in the CAW structure has been suggested [16]. In contrast to QCC, δ(Al) is remarkably constant and varies only between 74 and 77 ppm. There is no correlation between δ(Al) and the mean AlOAl bond angles of the distinct $\mathrm{Al(OAl)_4}$ environments which shows that the relation between AlOSi angles and δ(Al)

Fig. 6. ^{23}Na MAS NMR spectra of sodium aluminosilicate sodalites with different cage contents. (a) $[\mathrm{Na_4Cl}]_2[\mathrm{Si_6Al_6O_{24}}]$, (b) $[\mathrm{Na_4(NO_2)}]_2[\mathrm{Si_6Al_6O_{24}}]$, (c) $[\mathrm{Na_4I}]_2[\mathrm{Si_6Al_6O_{24}}]$, (d) $[\mathrm{Na_4(ClO_4)}]_2[\mathrm{Si_6Al_6O_{24}}]$, (e) $[\mathrm{Na_4(H_3O_2)}]_2[\mathrm{Si_6Al_6O_{24}}]$, (f) $[\mathrm{Na_4(OH)}]_2[\mathrm{Si_6Al_6O_{24}}]$, (g) $[\mathrm{Na_3(H_2O)_4}]_2[\mathrm{Si_6Al_6O_{24}}]$, (h) $[\mathrm{Na_3}]_2[\mathrm{Si_6Al_6O_{24}}]$. Note the about six times larger spectral width in (h) relative to (e)–(g). * Designates spinning side bands. The spectra were measured at 105.8 MHz with 0.6 μs pulse width, 2 s pulse repetition and spinning frequencies of 12–14 kHz. Spectrum (h) was registered using the QUADECHO pulse sequence of the Bruker pulse program library.

observed for aluminosilicate sodalites cannot be simply extended to the AlOAl bond angles in aluminate sodalites. The four lines A–D observed in the ^{27}Al DOR NMR spectrum of SAS can be attributed to the six inequivalent Al sites suggested for this structure [24] if it is assumed that the strong line C corresponds to three sites in a similar structural environment. QCC and δ(Al) have been determined to, respectively, 4.9 MHz and 72.0 ppm for line A, 5.6 MHz and 74.5 ppm for line B, 5.9 MHz and 73.5 ppm for line C, and 6.5 MHz and 73.3 ppm for line D. The smaller range of QCC indicates that, on the average, the AlO_4 tetrahedra in SAS are less distorted than those in CAW.

^{23}Na NMR

General considerations

While ^{29}Si and ^{27}Al NMR have been applied in the preceding sections to study the structure of the sodalite framework, ^{23}Na NMR provides information on the guest species present in the β-cages of sodium aluminosilicate sodalites. Since ^{23}Na is a quadrupolar nucleus ($I = 3/2$), the general features of the quadrupole interactions considered above play also an important role in the ^{23}Na NMR spectra of the sodalites. The quadrupole interactions are determined by the charge distribution around the sodium ion, i.e. preferably by the effective charge and geometrical arrangement of the atoms in the first coordination shell of Na. In aluminosilicate sodalites the sodium cations are located above the center of the six-ring windows of the cages and are coordinated to three oxygen atoms of these rings (see Fig. 1a). Additional coordinative bonds are formed to distinct coordination sites of the anions or H_2O present in the sodalite cages. Thus deviations from centrosymmetrical charge distribution around the sodium ions and, therefore, specific quadrupole interactions may occur giving rise to more or less broadened lines with or without characteristic quadrupolar line shapes in the ^{23}Na MAS NMR spectra. Some typical examples of the spectra are shown in Fig. 6 and the spectral parameters δ(Na), QCC, and η of a number of aluminosilicate sodalites with different cage fillings are collected in Table 2. δ(Na) ranges from −13.7 to 4.0 ppm (referenced to solid NaCl) but no clear relations to the structure or composition of the various sodalites can be derived from these data. However, detailed considerations of the sodium–oxygen coordinations in a large variety of sodium compounds have shown that δ(Na) is related to the valence (sum of the cation–oxygen bond strengths) and the Na–O distances of the oxygen atoms located in a 3.4-Å sphere around the sodium atom [25]. QCC values between 0 and 5.9 MHz are obtained for the different sodium coordinations in the aluminosilicate sodalites demonstrating considerable differences in the charge distribution around the sodium cations which will be considered in more detail below. The η values between 0 and 0.2 indicate no or only slight deviations of the field gradient from axial symmetry as to be expected for most of the sodium coordinations in the sodalites.

Specific examples

Sodium halide aluminosilicate sodalites $[Na_4Hal]_2[Si_6Al_6O_{24}]$. The ^{23}Na MAS NMR spectra of the sodium chloride, bromide and iodide sodalites have been studied in detail by Nielsen et al. [18]. An increasing quadrupole interaction of the ^{23}Na nucleus in the order Cl < Br < I sodalite has been observed (see Table 2) which clearly reflects the increasing asymmetry in the charge distribution around sodium in the trigonal pyramidal O_3NaHal coordination. This asymmetry arises from the increasing Na–Hal distance (Na–Cl 2.74, Na–Br 2.89, Na–I 3.12 Å [18]) and the less effective charge polarization in the Na–Hal bond caused by the decreasing electronegativity in the order Cl > Br > I.

Sodium sodalites with monovalent polyatomic guest anions $[Na_4A]_2[Si_6Al_6O_{24}]$. In contrast to the halide anions considered above, polyatomic guest anions have more than one site available to coordinate with the sodium cations. Therefore, different structural surroundings may occur for the four sodium atoms in the cage. However, the ^{23}Na MAS NMR spectra of most of these sodalites exhibit a characteristic quadrupolar line shape ($A = NO_2^-$, NO_3^-, ClO_4^-, OH^-, SCN^-) or a narrow Gaussian line ($A = B(OH)_4^-$, CN^-) typical of a single type of sodium coordination (see Table 2). This observation may be explained by a fast dynamic reorientation of the anions averaging the distinct chemical shifts and field gradients at the sodium sites. If the reorientation is sufficiently slow, a distribution of chemical shifts and field gradients will appear leading to broad lines as observed in e.g. the spectra for the sodalites with A = $HCOO^-$, CH_3COO^- and $H_3O_2^-$ measured at ambient temperature.

To illustrate the relations between the ^{23}Na MAS NMR spectra and the crystal structure, selected sodalite compositions of which the x-ray structure is known will be considered in some detail. The ^{23}Na MAS NMR spectrum of sodium nitrite sodalite $[Na_4NO_2]_2[Si_6Al_6O_{24}]$ exhibits a single quadrupolar line shape (see Fig. 6b and Table 2) indicating the presence of a single type of sodium coordination with a non-centrosymmetric but axialsymmetric charge distribution. However, from powder [26] and single crystal [27] x-ray diffraction structure analysis of sodium nitrite sodalite at 295 K two structural models have been suggested characterized by the presence of orientational disordered NO_2^- anions and three (model I) respectively two (model II) types of sodium environments in the cage. While each of the sodium atoms is coordinated to three framework oxygens O1 [d(Na–O1) = 2.353 Å] further coordinations are formed to the oxygen O2 [d(Na–O2) = 2.47–2.54 Å) and the nitrogen atom [d(Na–N) = 2.48–2.67 Å] of the nitrite anion. In model I two Na are coordinated to a single O2, one Na to two O2 and the fourth Na to N, while in model II two Na are coordinated to a single O2 and two Na to both O2 and N. Clearly, for a static statistical model of orientational disorder of the nitrite anion the different sodium environments should give rise to several lines in the ^{23}Na MAS NMR spectrum. However, for a fast dynamic reorientation of the nitrite anion the distinct distances d(Na–O1) and d(Na–O2, N) of the different sodium environments are averaged to the mean values of 2.35 and 2.51 Å, respectively, i.e. on time average each sodium resides in the same trigonal pyramidal $Na(O1)_3(O2, N)$ environment. This conclusion agrees with the ^{23}Na MAS NMR spectrum of sodium nitrite sodalite (see Fig. 6b) which corresponds to a single sodium site characterized by an axial symmetric field gradient ($\eta = 0$) and a moderate quadrupole interaction (QCC = 1.0 MHz) [26].

As mentioned above, sodium tetrahydroxoborate aluminosilicate sodalite $[Na_4\{B(OH)_4\}]_2[Si_6Al_6O_{24}]$ has been found to undergo a structural phase transition near room temperature. Above about 300 K a cubic high-temperature form (HT) exists, which is transformed into a low-temperature structure (LT) of lower symmetry [20]. The ^{23}Na MAS NMR spectrum of the HT form measured well above room temperature exhibits a narrow Gaussian line which reveals that all sodium atoms in this structure reside in a single type of environment with an approximately centrosymmetrical charge distribution. However, the x-ray structure [21] of the HT form (at 323 K) shows orientational disorder of the $B(OH)_4$ anion and the presence of two different sodium coordinations. Three of the four sodium atoms in the cage are five-fold coordinated to three framework oxygens [d(Na–O1) = 2.45 Å] and two oxygen atoms of the $B(OH)_4$ anion [d(Na–O2) = 2.41 resp. 2.44 Å], while the fourth Na is four-fold coordinated to three framework oxygens [d(Na–O1) = 2.27 Å] and one oxygen of the anion [d(Na–O2) = 2.29 Å]. Assuming fast rotation of the $B(OH)_4$ anion, the different Na–O1 and Na–O2 distances are averaged to the same value of d(Na–O1) = d(Na–O2) = 2.40 Å, i.e. on time average all sodium atoms reside in an almost ideal tetrahedral $Na(O1)_3(O2)$ environment. For a purely tetrahedral charge distribution the field gradient and, therefore, the quadrupole interaction vanishes, and a narrow line is observed in the ^{23}Na MAS NMR spectrum. Similar to the nitrite sodalite a static statistical model of orientational disorder of the $B(OH)_4$ anions in the HT form of the sodalite structure can be excluded. Dramatic changes are observed in the ^{23}Na MAS NMR spectra of the $B(OH)_4$ sodalite measured at or below 290 K. A broad and complex line shape appears which consists of several overlapping quadrupolar broadened lines (see Fig. 4b). The interpretation of this spectrum with respect to the number of lines and their distinct quadrupole parameters and chemical shifts is difficult. However, application of the DOR technique yields a spectrum with four intense and narrow lines accompanied by weak spinning side bands and a broader line of residual parts of the HT form (see Fig. 4b and Table 2) [16]. Obviously, four distinct sodium environments are present in the LT form of tetrahydroxoborate sodalite formed by localized coordinations of the sodium atoms with $B(OH)_4$ oxygens due to the freezing of the dynamic reorientation of the $B(OH)_4$ anion. In agreement with the results of the ^{27}Al NMR studies considered above, the ^{23}Na NMR spectra confirm also the suggestion of the tetragonal space group $P\bar{4}2_1c$ with four crystallographically distinct sodium positions per sodalite cage [21]. Interestingly, two of the lines have the same isotropic chemical shift of −9.0 ppm but different quadrupole interactions (QCC = 1.3 and 1.6 MHz, resp.) demonstrating the high sensitivity of QCC against the structural environment of the sodium atoms.

Anhydrous and hydrated sodium aluminosilicate sodalites devoid of guest anions $[Na_3(H_2O)_x]_2[Si_6Al_6O_{24}]$ *($x = 4, 0$).* The anhydrous sodium aluminosilicate sodalite $[Na_3]_2[Si_6Al_6O_{24}]$ which does not contain an anion or water molecules but only three sodium cations per cage shows the largest quadrupole interaction (QCC = 5.9 MHz) observed so far for ^{23}Na. In this structure, the sodium cations are located close to the centres of the six-membered rings of the sodalite framework [28] thus forming a nearly planar coordination to six oxygen atoms of the same ring. This rather unusual geometry results in a large field gradient at the sodium sites and, therefore, in the large quadrupole interaction observed. A similar QCC of 5.8 MHz has been reported for dehydrated zeolite NaA [29] where the sodium cations are also located within the six-ring windows of sodalite cages which, however, are connected by four-membered rings forming double four-rings and larger α-cages. Different to the anhydrous sodalite the fully hydrated sodium aluminosilicate sodalite $[Na_3(H_2O)_4]_2[Si_6Al_6O_{24}]$ exhibits a comparatively narrow Gaussian line in the ^{23}Na MAS NMR spectrum indicating a rather small quadrupole interaction. This is in full agreement with the x-ray structure of this sodalite hydrate [28], which revealed a slightly distorted octahedral coordination of the sodium atoms to three framework oxygens O1 of the six-rings [d(Na–O1) = 2.51 Å] and three further oxygens O2 of the water molecules [d(Na–O2) = 2.45 Å). Residual field gradients at the sodium due to the slightly different Na–O1 and Na–O2 distances may further be averaged by dynamic reorientation of the water molecules and/or site exchange of the sodium cations.

Sodium aluminosilicate sodalites with divalent polyatomic guest anions $[Na_4A^{2-}][Na_4][Si_6Al_6O_{24}]$. Sodium aluminosilicate sodalites with divalent guest anions are characterized by two alternating types of differently filled cages, half of the cages containing the anion and four Na^+, while the other half containing four Na^+ only. Therefore, at least two different sodium environments are present in these sodalite compositions which should give rise to two lines in the ^{23}Na NMR spectra. Figure 7 shows the ^{23}Na MAS NMR spectra of the sodium sulphate and sodium chromate sodalites and their computer simulations by two superimposed lines, A and B, characterized by different quadrupole interactions and chemical shifts (see Table 2). The results of the simulations are confirmed by the ^{23}Na DOR NMR spectra (not shown), which exhibit two narrow lines at shift positions equal to the centres of gravity of the MAS lines [16]. The appearance of only two lines shows that there is only a single sodium environment in each of the two cages, i.e. any possible difference in the coordination of the sodium cations to the anions is averaged by fast dynamic reorientation of the anions. Since the sodium atoms in the cages not containing an anion are preferably coordinated to the six framework oxygens O1 of a single six-membered ring (similar to the anhydrous sodium aluminosilicate sodalite, see above) and only weakly bonded to the distant oxygen atoms O2 of the anions in the neighbouring cage, they should have a larger quadrupole interaction than the sodium atoms in the anion-containing cages which form a (probably dynamically averaged) more or less regular tetrahedral $Na(O1)_3(O2)$ coordination. Therefore, line B with the larger QCC is assigned to the sodium in the "empty" cage and line A with the smaller QCC to the sodium in the anion-containing cage. The quadrupole interaction observed for the latter sodium site (see Table 2) indicates a distortion of the tetrahedral symmetry of the $Na(O1)_3(O2)$ coordination, i.e. different Na–O1 and Na–O2 bond lengths in the SO_4 (QCC = 1.0 MHz) and CrO_4 sodalites (QCC = 1.6 MHz). In contrast, no quadrupole interaction is observed for line A of sodium carbonate sodalite (not shown), which reveals a dynamically averaged almost ideal tetrahedral symmetry of the charge distribution around sodium, i.e. similar Na–O1 and Na–O2 distances.

^1H NMR

General considerations

The application of ^1H NMR spectroscopy to solids is complicated considerably by heavy line

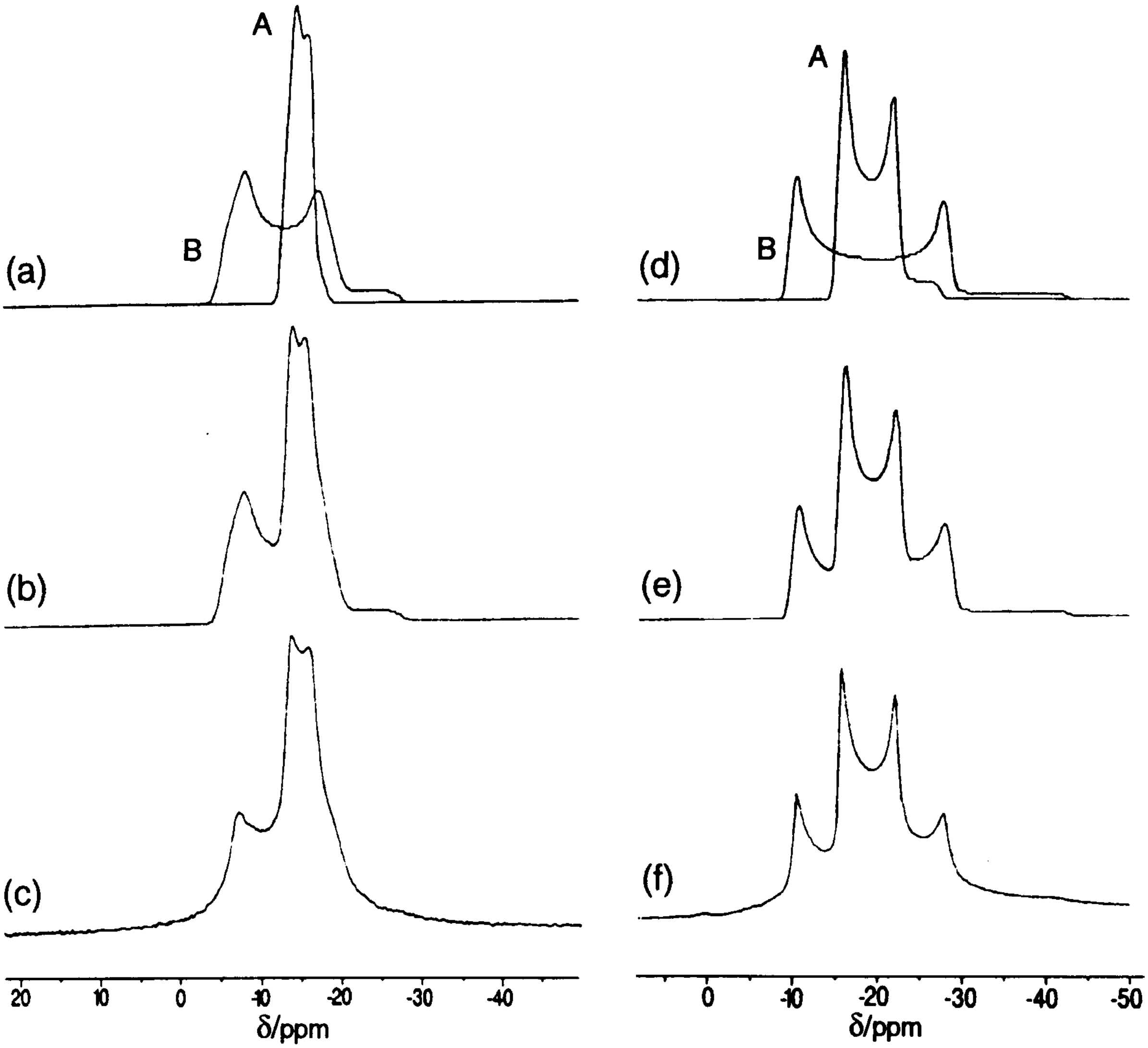

Fig. 7. Experimental and simulated ^{23}Na MAS NMR spectra of (a–c) sodium sulphate aluminosilicate sodalite $[Na_4(SO_4)][Na_4][Si_6Al_6O_{24}]$ and (d–f) sodium chromate aluminosilicate sodalite $[Na_4(CrO_4)][Na_4][Si_6Al_6O_{24}]$. (a, d) components A and B of the simulation, (b, e) simulated spectrum, (c, f) experimental spectrum. Experimental conditions as given in Fig. 6. The spectra simulations were performed using the program POWDER of the Bruker ASPECT 3000 software.

broadening due to the strong dipolar interactions of the protons and the small range of ^{1}H chemical shifts. Even under MAS conditions broad lines or a wide distribution of spinning side bands often appear in the spectra rendering the selective observation of distinct lines for protons in different structural surroundings difficult. However, the ^{1}H–^{1}H dipolar interactions may be reduced considerably or even eliminated if the protons are present in low concentrations, i.e. sufficiently separated to remove the mutual interaction of the dipolar fields, and/or are involved in fast dynamic site exchange which may average the dipolar interaction just like in liquids. Residual dipolar broadenings may then be removed by application of MAS at high spinning speeds. This

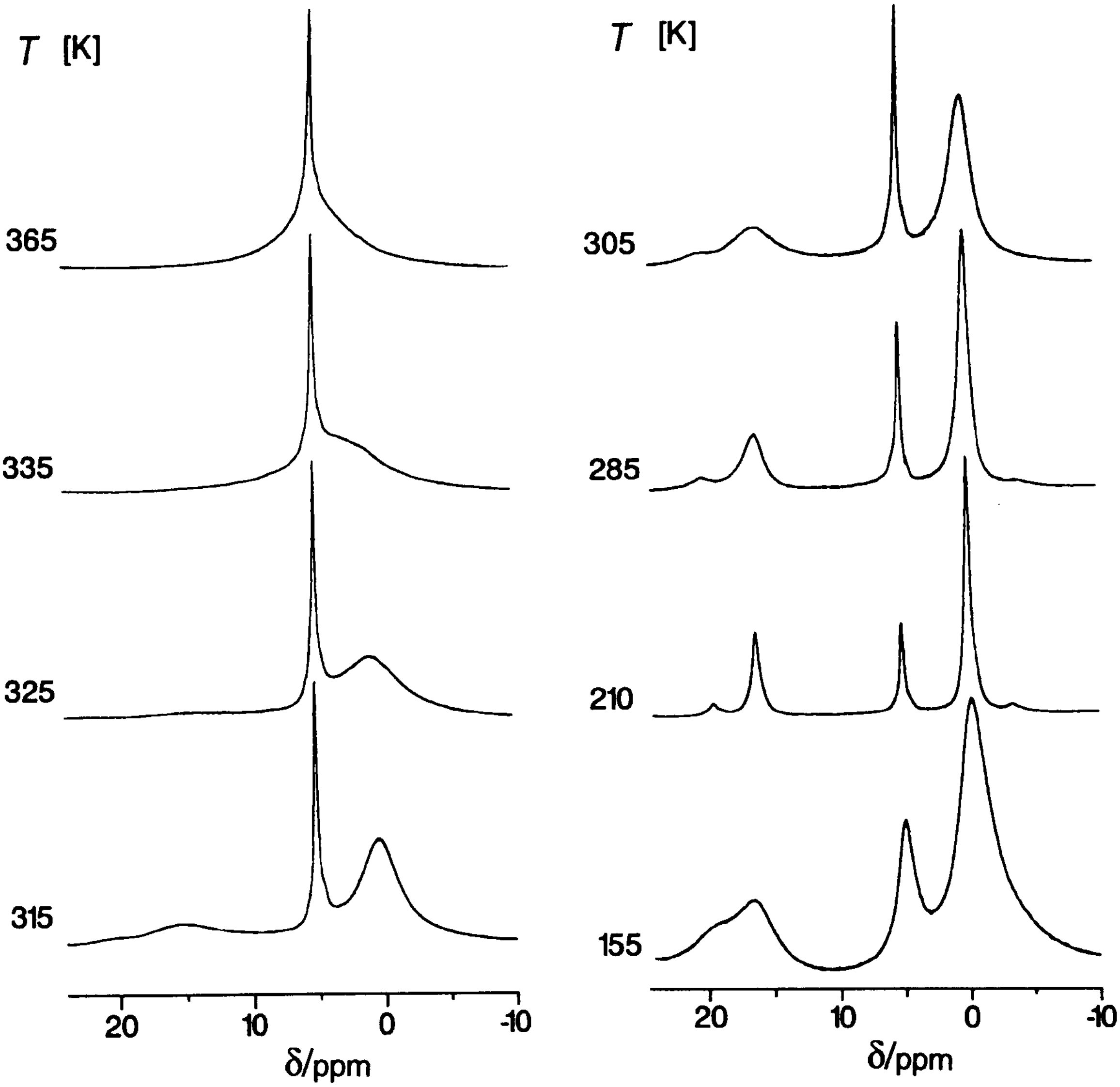

Fig. 8. ^{1}H MAS NMR spectra of sodium hydroxo sodalite hydrate $[Na_4(H_3O_2)]_2[Si_6Al_6O_{24}]$ at variable temperature. The weak signals at $\delta \approx 20$ ppm and and $\delta \approx -4$ ppm are spinning side bands. The spectra were recorded at 400.13 MHz with 3 μs pulse width (65° flip angle), 3 s pulse repetition and a spinning frequency of 8 kHz [30]. TMS was used as standard.

is in fact the case for sodalites containing only a few protons in the guest species enclathrated in the β-cages, which in addition may undergo fast dynamic reorientation. Therefore, narrow lines are generally observed in the high-speed ^{1}H MAS NMR spectra of sodalites with proton-containing guest species such as H_2O, OH^- or small organic molecules. Since single guest species or only small clusters of them (as for H_2O) are isolated in the sodalite matrix, ^{1}H MAS NMR of sodalites provides a unique possibility to study the structural features of such isolated species.

Specific examples

Sodium aluminosilicate hydroxosodalites $[Na_4(H_2O)_n(OH)]_2[Si_6Al_6O_{24}]$, *n = 1.0.* The x-ray structure of sodium hydroxosodalite hydrate $[Na_4(H_3O_2)]_2[Si_6Al_6O_{24}]$ revealed the presence of a hydrogen dihydroxide an ion $(H{-}O{-}H{-}O{-}H)^-$ in the β-cage formed from OH^- and H_2O by a strong central hydrogen bond [$d(O \cdots O) = 2.36$ Å] [10]. The ^{1}H MAS NMR spectra measured at various temperatures are shown in Fig. 8 [30]. At 210 K three sharp lines are observed at δ(H) of -0.1, 5.0 and 16.3 ppm. Due to their chemical shifts and integral intensity ratio of 2:1, the lines at -0.1 and 16.3 ppm have been assigned to the terminal and central protons of the $(H{-}O{-}H{-}O{-}H)^-$ anion, while the line at 5.0 ppm originates from H_2O in a small admixture of non-basic hydrosodalite $[Na_3(H_2O)_4]_2[Si_6Al_6O_{24}]$, which is difficult to avoid during the preparation of the hydroxosodalite hydrate [2]. The strong low-field shift of the central proton is typical of protons involved in strong hydrogen bonds and agrees with the recently established linear correlation between $OH \cdots O$ distances and ^{1}H chemical shifts [31] as well as with ab initio calculations of the isolated $H_3O_2^-$ ion [32]. The dramatic changes in the spectra, i.e. the broadenings, shifts and final collapse of the two lines observed at increasing temperature indicate clearly a dynamic exchange between the terminal and central protons of the $(H{-}O{-}H{-}O{-}H)^-$ anion. However, the line of the impurity at 5.0 ppm remains unchanged and is not involved in the exchange process. From the evaluation of the line widths an activation energy E_a for the exchange process of 39 ± 5 kJ mol^{-1} has been derived which led to the conclusion that the exchange cannot occur via a complete splitting of the hydrogen bond (which requires about 100 kJ mol^{-1}) but proceeds probably by the formation of a short-living intermediate with bifurcated hydrogen bonds between the two H_2O protons and the oxygen of the OH^- group [30]. Below 210 K all lines show considerable broadenings as a result of the increasing dipole-dipole interaction of the protons due to the freezing of the dynamic reorientation of the whole $H_3O_2^-$ ion as well as the H_2O molecules of the impurity.

The ^{1}H MAS NMR spectrum of the dehydrated hydroxosodalite $[Na_4(OH)]_2[Si_6Al_6O_{24}]$ exhibits only a single narrow line at $\delta(H) = -3.8$ ppm [2], the position and half width of which is almost constant in the temperature range between 300 and 140 K. To the best of our knowledge this is the most high-field shifted line ever observed for a OH^- proton. However, from ab initio calculations an even higher shielding of $\delta(H) = -7$ ppm has been derived for the proton of an isolated OH^- group [33]. Thus, the low-field shift of about 3 ppm of the OH proton in the hydroxosodalite from the shift calculated for the free OH group obviously reflects the influence of the environment, most probably of the Na^+ cations, on the proton shielding.

Silica sodalites $[C]_2[Si_{12}O_{24}]$. Preliminary ^{1}H MAS NMR studies [34] of silica sodalites containing organic templates showed that information on structure and conformational dynamics can be obtained on organic molecules isolated in the sodalite cage which may be compared with corresponding properties in the liquid phase. The ^{1}H MAS NMR spectrum of ethylene glycol silica sodalite $[(CH_2OH)_2]_2[Si_{12}O_{24}]$ exhibits two narrow signals at 1.86 and 3.66 ppm (at 307 K) with an intensity ratio of 1:2 which have to be assigned to the OH and CH_2 protons of the ethylene glycol molecule, respectively. The strong high-field shift of the OH line in comparison to the liquid phase (e.g. 4.2 ppm in aceton solution) shows clearly that the OH group is no longer involved in intermolecular hydrogen bonds as can be expected for the isolated ethylene glycol molecule in the sodalite cage. At 190 K both lines shift slightly to high field and show some broadening probably due to the decreasing mobility of the ethylene glycol molecule in the cage and the concomitant increase in the dipolar ^{1}H interaction.

A single line at 5.1 ppm is observed in the ^{1}H MAS NMR spectrum of trioxane silica sodalite, $[C_3H_6O_3]_2[Si_{12}O_{24}]$, measured at 300 K, indicating fast ring inversion of the trioxane molecule. With decreasing temperature the line becomes broader and finally splits below 250 K into two lines at 5.4 and 4.7 ppm for the axial and equatorial protons, a clear indication that the inversion process is frozen at low temperature. An activation energy for the inversion of 55 ± 5 kJ mol^{-1} has been estimated from the ^{1}H MAS NMR spectra which is about 10 kJ mol^{-1} larger than that observed for the trioxane molecule in solution [35]. Obviously, the inclusion of the trioxane molecule in the sodalite cage increases its conformational stability.

Conclusions

It has been shown in the preceding sections that multinuclear solid state NMR spectroscopy is a versatile tool for the structural and compositional characterization of sodalite materials. While detailed information on the framework structure of aluminosilicate, aluminate and silica sodalites can be derived from ^{29}Si and ^{27}Al NMR, structure and dynamics of the guest species enclathrated in the sodalite cages can succesfully be studied by ^{23}Na and ^{1}H NMR spectroscopy. In addition, NMR of further nuclei not considered in this article may be useful. For example, ^{13}C MAS NMR may be used to study organic molecules and anions trapped in the sodalite cages [12,36] and ^{11}B MAS NMR has been applied to prove if boron is present as framework or non-framework constituent in boron-containing sodalites [20,21]. Solid state NMR also has a great potential for investigating the formation and structural transformation of precursors and intermediates of sodalites in the course of their synthesis and subsequent modifications by e.g. ion-exchange or intracage reactions [2,21,37]. Beyond the characterization of the sodalite structure, solid state NMR of distinct guest species isolated in the sodalite cages provides a unique possibility to study the specific structural features of almost "free" molecules or ions which do not interact with another and are often only weakly affected by interactions with the sodalite-framework. Finally, it should be pointed out that the methods and strategies discussed above for the structural characterization of sodalites by multinuclear solid state NMR spectroscopy are also applicable to other microporous materials such as e.g. zeolites, aluminophosphate molecular sieves and clathrasils [3].

The authors thank M. Wiebcke and H. Koller for helpful comments, W. Depmeier for the aluminate sodalites, P. Behrens and G. van de Goor for the silica sodalites, and A. Samoson for measuring the 11.7 T DOR NMR spectra in the Application Laboratory of Bruker Analytische Messtechnik, Karlsruhe. Support by the Deutsche Forschungsgemeinschaft, the Max-Buchner-Forschungsstiftung and the Alfried Krupp von Bohlen und Halbach-Stiftung is gratefully acknowledged.

REFERENCES

1 L. Pauling, Z. Kristallogr., 74 (1930) 373.
2 G. Engelhardt, J. Felsche and P. Sieger, J. Am. Chem. Soc., 114 (1992) 1173.
3 G. Engelhardt and D. Michel, High-Resolution Solid-State NMR of Silicates and Zeolites, Wiley, Chichester, 1987.
4 G. Engelhardt and H. Koller, Magn. Reson. Chem., 29 (1991) 941.
5 Y. Wu, B.Q. Sun, A. Pines, A. Samoson and E. Lippmaa, J. Magn. Reson., 89 (1989) 3239.
6 G. Engelhardt, in J. Klinowski and P.J. Barrie (Eds.), Studies in Surface Science and Catalysis, Vol. 52, Recent Advances in Zeolite Science, Elsevier, Amsterdam, 1989, pp. 151–62.
7 G. Engelhardt, S. Luger, J.-Ch. Buhl and J. Felsche, Zeolites, 9 (1989) 182.
8 H.S. Jacobsen, P. Norby, H. Bildsoe and H.J. Jakobsen, Zeolites, 9 (1989) 491.
9 M.T. Weller and G. Wong, J. Chem. Soc. Chem. Commun., (1988) 1103.
10 M. Wiebcke, G. Engelhardt, J. Felsche, P.B. Kempa, P. Sieger, J. Schefer and P. Fischer, J. Phys. Chem., 96 (1992) 392.
11 P. Sieger, J. Felsche and G. Engelhardt, in preparation
12 R.H. Meinhold and D.M. Bibby, Zeolites, 6 (1986) 427.

13 J. Keijsper, C.J.J. den Ouden and M.F.M. Post, in P.A. Jacobs and R.A. van Santen (Eds.), Studies in Surface Science and Catalysis, Vol. 49, Part A, Zeolites: Facts, Figures, Future, Elsevier, Amsterdam, 1989, pp. 237–247.
14 G. van de Goor and P. Behrens, unpublished results.
15 J.W. Richardson, J.J. Pluth, J.V. Smith, W.J. Dytrych and D.M. Bibby, J. Phys. Chem., 92 (1988) 243.
16 G. Engelhardt, H. Koller, P. Sieger, W. Depmeier and A. Samoson, Solid State NMR, 1 (1992) 127.
17 E. Lippmaa, A. Samoson and M. Mägi, J. Am. Chem. Soc., 108 (1986) 1730.
18 N.C. Nielsen, H. Bildsoe, P. Norby and H.J. Jakobsen, Zeolites. 11 (1991) 622.
19 M.J. Dempsey and D. Taylor, Phys. Chem. Miner., 6 (1980) 197.
20 J.-Ch. Buhl, G. Engelhardt and J. Felsche, Zeolites, 9 (1989) 40.
21 J. Felsche, P. Sieger, M. Wiebcke, G. Engelhardt and P. Behrens, in preparation.
22 W. Depmeier, J. Incl. Phenom., 5 (1987) 279.
23 W. Depmeier, Acta Crystallogr. Sect. C, 40 (1984) 226.
24 W. Depmeier, personal communication.
25 H. Koller, G. Engelhardt, A.P.M. Kentgens and J. Sauer, submitted for publication.
26 P.B. Kempa, G. Engelhardt, J.-Ch. Buhl, J. Felsche, G. Harvey and Ch. Baerlocher, Zeolites, 11 (1991) 558.
27 P. Sieger, M. Wiebcke, J. Felsche and J.-Ch. Buhl, Acta Crystallogr. Sect. C, 47 (1991) 498.
28 J. Felsche, S. Luger and Ch. Baerlocher, Zeolites, 6 (1986) 367.
29 G.A.H. Tijink, R. Janssen and W.S. Veeman, J. Am. Chem. Soc., 109 (1987) 7301.
30 G. Engelhardt, P. Sieger and J. Felsche, Angew. Chem. Int. Ed. Engl., 31 (1992) 1210.
31 J.P. Yesinowski and H. Eckert, J. Am. Chem. Soc., 109 (1987) 6274.
32 C. McMichael Rohlfing, L.C. Allen and R. Ditchfield, Chem. Phys. Lett., 86 (1982) 380.
33 H. Fukui, K. Miura, H. Yamazaki and T. Nosaka, J. Chem. Phys., 82 (1985) 1410.
34 G. van de Goor, P. Behrens and G. Engelhardt, in preparation.
35 B. Pedersen and J. Schang, Acta Chim. Scand., 22 (1968) 1705.
36 C.J.J. den Ouden, K.P. Datema, F. Visier, M. Mackay and H.F.M. Post, Zeolites, 11 (1991) 419.
37 S. Hayashi, K. Suzuki, S. Shin, K. Hayamizu and O. Yamamoto, Chem. Phys. Lett., 110 (1984) 54.

Analytica Chimica Acta, 283 (1993) 987–995
Elsevier Science Publishers B.V., Amsterdam

Quantitative evaluation of gallium phosphide samples prepared from rapid solid state metathesis

Solid state ^{31}P and ^{69}Ga magic angle spinning NMR strategies

Deanna Franke and Hellmut Eckert
Department of Chemistry, University of California, Santa Barbara, CA 93106 (USA)

Richard B. Kaner and Randoph E. Treece
Department of Chemistry and Biochemistry and Solid State Science Center, University of California, Los Angeles, CA 90024-1569 (USA)

(Received 20th January 1993)

Abstract

Quantitative solid state nuclear magnetic resonance (NMR) techniques are capable of evaluating the crystalline quality of III–V semiconductor preparations. To this end, an analytical protocol consisting of magic angle spinning lineshape analysis, spin counting studies, and quadrupolar nutation NMR has been established, allowing sample comparisons on a numerical scale. This protocol is applied to a suite of gallium phosphide (GaP) samples prepared by a novel rapid solid state metathesis route from gallium halide and sodium phosphide. The results show that the quality and crystallinity of the GaP product phase depends sensitively on the gallium halide precursor used, with GaF_3 resulting in the highest-quality material.

Keywords: Nuclear magnetic resonance spectrometry; Gallium phosphide; Semiconductors; Solid-state NMR

Recently, a new rapid solid state reaction has been introduced [1], enabling the synthesis of a wide range of chalcogenides, III–V semiconductors and related materials [2]. For instance pure GaP can be produced in self-sustaining metathesis reactions between mixtures of gallium halide and sodium phosphide according to:

$$GaX_3 + Na_3P \xrightarrow[\text{(2) ignite}]{\text{(1) heat in sealed tube, or}} GaP + 3NaX \xrightarrow{\text{wash}} GaP \qquad (1)$$

where X = F, Cl, I [3]. This reaction has a considerable time advantage over the traditional, time-consuming, methods currently used for the synthesis of III–V semiconductors. On the other hand, the desired III–V compound produced by this route may be contaminated with products from side reactions and may contain considerable amounts of non-removable halide inclusions. Furthermore, due to the rapid synthesis mode, considerable lattice strain and high defect concentrations may be present. The optimization of such solid state reactions with respect to yield and product quality depends on the availability of suitable analytical techniques and structural

Correspondence to: H. Eckert, Department of Chemistry, University of California, Santa Barbara, CA 93106 (USA).

probes with which the products can be evaluated. Solid state NMR is an element-selective, inherently quantitative method that is ideally suited for such purposes. Previous NMR studies on gallium phosphide have widely employed the ^{31}P, ^{69}Ga and ^{71}Ga nuclear isotopes for characterizing the chemical bonding and electronic properties of this compound [4–7]. Furthermore, NMR studies of related III–V compounds have shown that the resonances of quadrupolar nuclei such as ^{27}Al, ^{69}Ga, ^{75}As, ^{115}In, and ^{123}Sb are extremely sensitive to the presence of defects and lattice strain generated in doped III–V semiconductors [8–15]. The present study is concerned with the use of NMR spectroscopy for quantitatively evaluating the purity and crystallinity of such materials generated by novel synthesis techniques. The analytical protocol includes: (a) ^{31}P and ^{69}Ga magic angle spinning (MAS) lineshape analysis, (b) ^{31}P and ^{69}Ga spin counting experiments, and (c) ^{69}Ga nutation NMR studies. Here, we report on the use of this protocol for assessing the influence of the gallium halide precursor (GaF_3, $GaCl_3$, GaI_3) on the quality and crystallinity of the gallium phosphide obtained via various synthesis routes.

TABLE 1

Summary of initiation conditions

GaX_3	m.p. (°C)	Pnictide	Decomp. (°C)	Initiation conditions
$GaCl_3$	78	Na_3P	> 550	Stirring together
GaI_3	212	Na_3P	> 550	Grinding w/ mortar and pestle
GaF_3	> 900	Na_3P	> 550	Heating w/hot wire

EXPERIMENTAL

Sample preparation and characterization

The precursor manipulations were carried out in a He-filled drybox where the metal halide and sodium pnictide were ground individually, mixed in equimolar quantities, and then ignited with a

TABLE 2

Solid state NMR ^{31}P and ^{69}Ga NMR parameters, δ (isotropic chemical shift, ±0.2 ppm), FWHM (full width at half maximum, ±5 Hz), percentage of phosphorus present in the form of GaP, and Ga/P NMR centerband intensity ratio relative to that measured in commercial GaP

Sample [a]	δ ^{31}P (ppm)	^{31}P FWHM (Hz)	^{31}P intensity per gram	%P fraction of GaP	δ ^{69}Ga (ppm)	^{69}Ga FWHM (Hz)	^{69}Ga intensity per gram	Ga/P ratio	^{69}Ga Nutation t_{90}^{eff} (μs)
GaP (Alfa 99.999%)	−142.9	343	100	98.7	0.00	278	100	1.000	5.50
F-GaP No. 1	−143.4	353	46	96.2	1.09	307	36	0.783	5.25
F-GaP No. 2	−143.6	315	54	97.4	1.06	302	45	0.833	5.75
F-GaP HT	−144.2	343	40	93.7	1.19	287	36	0.900	5.50
I-GaP No. 2	−144.1	340	58	90.7	1.37	346	45	0.776	4.75
I-GaP HT	−144.4	324	76	86.4	1.43	324	55	0.724	4.75
Cl-GaP No. 1	−144.2	359	16	66.3	1.41	340	10.5	0.656	4.25
Cl-GaP No. 2	−144.4	364	12	63.2	1.39	372	7.6	0.633	4.00
Cl-GaP HT	−144.4	400	73	80.1	1.29	371	45	0.616	4.00

[a] X–GaP (where X is F, Cl, or I) designations indicate the GaX_3 precursor used to prepare the GaP, and HT indicates the annealed samples.

hot filament in a bomb similar to those used in calorimetry experiments. The initiation conditions are summarized in Table 1. Details relevant to the synthesis techniques are presented elsewhere [16]. All of the products were analyzed by x-ray powder diffraction (XRD). In essence, regardless of the choice of the precursor or the synthesis method, GaP is the only crystalline material identifiable by XRD [lattice constants $a_0 = 4.454(1)$ Å for I–GaP and Cl–GaP, and $a_0 = 4.455(1)$ Å for F–GaP]. Comparisons of signal-to-noise ratios and peak shapes of the (hkl = 331) lines at $2\Theta = 76°$ suggest that the Cl–GaP samples possess lower crystalline quality than those prepared from the other two precursors. There is, however, no appreciable difference between XRD patterns of the GaP materials synthesized from the gallium fluoride and iodide precursors. The materials prepared from GaF_3, $GaCl_3$, and GaI_3 are henceforth denoted F–GaP, Cl–GaP, and I–GaP, respectively. Their NMR characterization was compared with that of a commercial single crystalline GaP sample (Alfa, 99.999%), which was coarsely powdered prior to the experiments.

Solid state NMR

Solid state ^{31}P NMR studies were carried out at 121.6365 MHz, using a General Electric GN-300 spectrometer, equipped with a 5-mm high-speed magic angle spinning NMR probe from Doty Scientific. ^{31}P MAS NMR spectra were recorded at spinning speeds around 8.5 kHz, with pulses of 4 μs length and 15 min relaxation delays. It was established that under these condi-

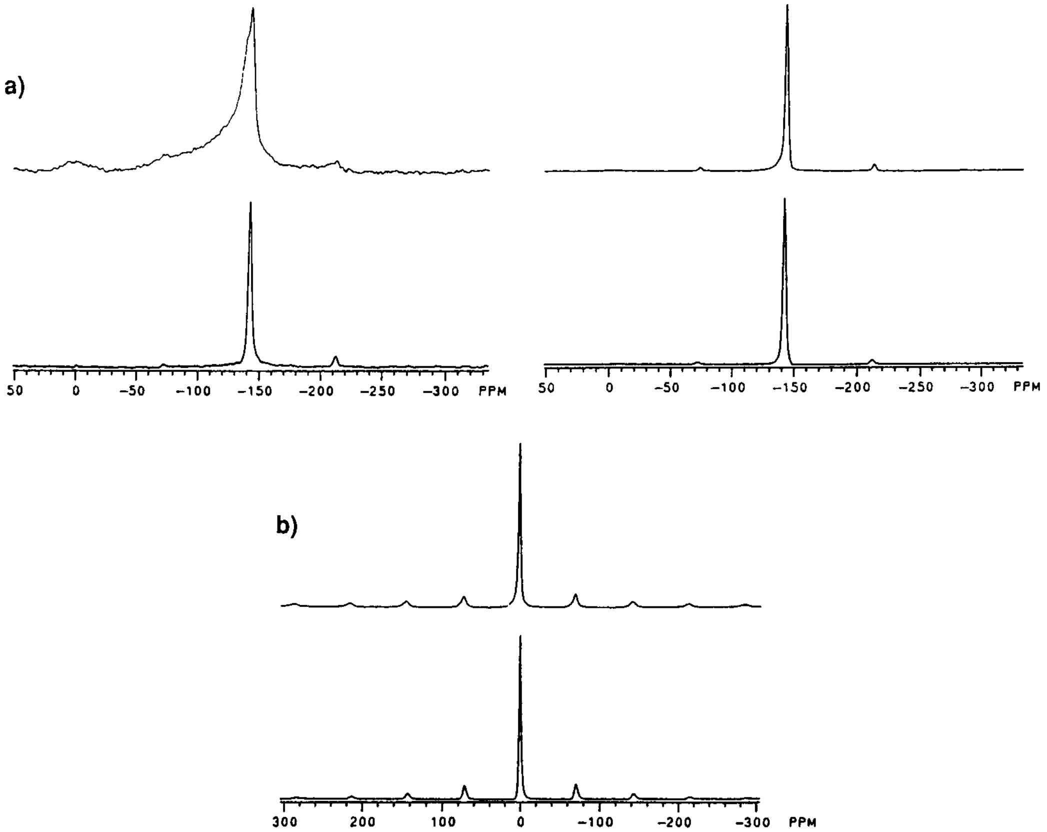

Fig. 1. Representative solid state NMR spectra comparing (top) polycrystalline GaP prepared from the ignition of GaI_3 and Na_3P and (bottom) commercial bulk GaP. In (a), 121.6365 MHz ^{31}P MAS NMR spectra are shown for two relaxation delays: 100 ms (left) and under quantitative conditions at 900 s (right). In (b), 120.073 MHz ^{69}Ga MAS NMR spectra are shown for the samples. A 10-s relaxation delay was used. Minor peaks symmetrically spaced around the sharp resonances are spinning sidebands.

tions the signal was not affected by saturation effects. Chemical shifts are referenced to 85% H_3PO_4. To assess the compositional purity of the samples, spin counting experiments were carried out with commercial GaP (Alfa, 99.999%) as the quantitation standard.

^{69}Ga NMR studies were carried out at 120.075 MHz using a General Electric GN-500 spectrometer at spinning speeds around 8.6 kHz, with a 2 μs pulse length and a 10 s relaxation delay. The commercial GaP sample served both as a chemical shift reference and as the reference standard for quantitative spin counting studies (see below). ^{69}Ga nutation NMR experiments were carried out on samples with successive pulse lengths of 0.5–16.0 μs with incrementation by 0.5 μs.

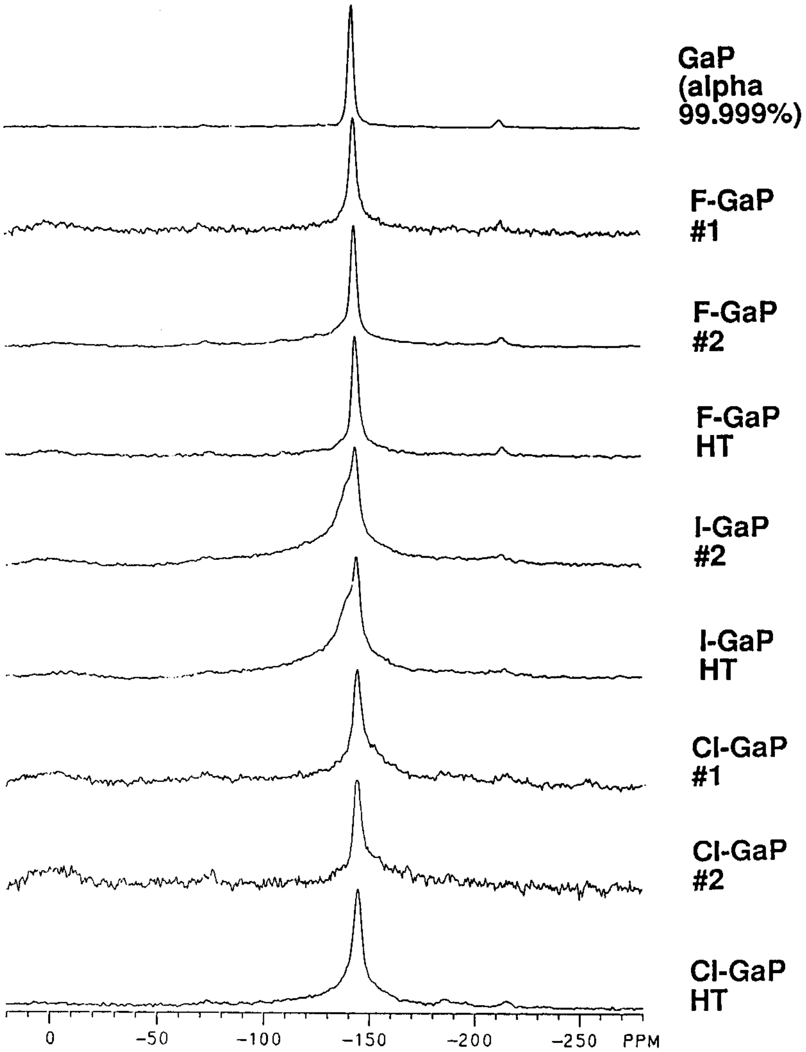

Fig. 2. 121.6365 MHz solid state ^{31}P MAS NMR spectra of polycrystalline GaP samples prepared from $GaCl_3$, GaF_3, and GaI_3 precursors. A 100-ms relaxation delay was used, resulting in the selective amplification of defect and impurity sites. The order of the compounds (top to bottom) follows the order shown in Table 2. Minor peaks around −80 and −220 ppm are spinning sidebands arising from first-order quadrupolar satellites.

RESULTS AND INTERPRETATION

Table 2 summarizes all of the measurements undertaken. The various gallium phosphide samples are evaluated on the basis of ^{31}P MAS NMR, ^{69}Ga MAS NMR, and ^{69}Ga nutation NMR experiments, with attention to the following spectroscopic observables: (1) the width and position of the central ^{31}p and ^{69}Ga MAS NMR signals, (2) the absolute intensity of these signals per gram of material studied ("spin count"), and (3) the average ^{69}Ga nutation frequency.

^{31}P MAS NMR

Figure 1a shows some representative ^{31}P MAS NMR spectra obtained for the samples under study. The presence of crystalline gallium phosphide manifests itself in sharp Gaussian ^{31}P central MAS resonances centered between −142.9 and −144.4 ppm, with half-height widths between 310 and 400 Hz for the various samples. These lineshape parameters are consistent with those previously published by us and other workers [4,5]. It is noticeable, however, that the Cl-GaP samples have consistently the broadest lines, and resonate the furthest upfield from bulk GaP. The broadening of the MAS NMR lines in excess of the width observed in bulk commercial GaP arises from a distribution of isotropic chemical shifts, and can serve as a relative measure of crystalline disorder. The upfield shift is likely to be an electronic doping effect arising from intrinsic or extrinsic defects. Thus, the 31P lineshape parameters relating to the GaP signal component confirm that the use of $GaCl_3$ as the precursor material results in less crystalline product, as compared to GaI_3 or GaF_3.

Several other phosphorus-containing impurities are identified in the spectra. Elemental phosphorus (evident in some of these samples by optical microscopy) gives rise to a very broad background resonance. The spin-lattice relaxation time associated with this background feature is very short, so that its relative contribution to the signal can be enhanced by rapid pulsing (see Fig. 2). The distinct T_1 difference between this species and GaP reveals the absence of spin diffusion and suggests that the P atoms giving rise to the sharp resonance (GaP) and to the broad background, respectively, are microscopically separated. However, this is not rigorous proof for the assumption that the broad feature is entirely due to elemental phosphorus impurities. We cannot rule out that part of this broad background belongs to strongly disordered phosphorus sites associated with defects, lattice strain, or grain boundaries in GaP. Finally, several samples (particularly those prepared from $GaCl_3$ precursor) show an extra resonance near 0 ppm. This chemical shift suggests assignment to a phosphate-like species, which may have arisen from some contamination with oxygen under synthesis conditions. Furthermore, weak and as of yet unassigned features at −170 and −200 ppm are observed in some of the samples prepared from GaI_3 and $GaCl_3$.

The ^{31}P spin count reveals that the signal intensity per gram in all of the samples studied is significantly lower than that for bulk commercial GaP. This observation indicates that these samples are heavily contaminated with non-P containing material, possibly sodium and gallium halides. It is likely that the yield of these reactions is not quantitative and that the washing procedure fails to remove some of the starting material. It is also possible that the sodium halide product forms non-removable microscopic amorphous inclusions in the desired GaP product phase. While previous electron microscopy and EDS studies revealed that the Ga to P ratio of the product is precisely 1:1 in samples prepared on a microscale, this may not necessarily be the case for the present samples, which were prepared on a 100-mg scale (to provide enough material for NMR studies). Furthermore, sorbed water due to the high surface area of the product phases formed may contribute to the lower ^{31}P spin count per unit mass. Since our discussion is focused on comparisons of sample quality rather than quantity the differences in yield and surface areas between the samples are of little interest in the present context and thus will not be discussed further.

The integration of the ^{31}P MAS NMR signals reveals that the percentage of phosphorus atoms attributable to the regular GaP sites (i.e. those contributing to the −144 ppm peak) depends distinctly on which precursor halide is used. Thus, in the samples prepared from GaF_3, 95–97% of all of the phosphorus are present as "regular" GaP, while this number drops to 87–91% and to 63–80% in the samples made from GaI_3 and $GaCl_3$, respectively.

^{69}*Ga MAS NMR*

Figure 1b shows typical ^{69}Ga MAS NMR spectra of the samples under study. All of the spectra show an intense MAS centerband in addition to a weak spinning sideband manifold arising from first-order nuclear electric quadrupolar perturbations (see below). Again, the spectral parameters of the F–GaP samples are closest to those measured in the bulk commercial GaP, while the Cl–GaP samples show the broadest resonances and the largest chemical shift differences from bulk GaP. These results are nicely consistent with the ^{31}P MAS lineshape analysis discussed above.

The ^{69}Ga isotope ($I = 3/2$) possesses a moderately large nuclear electric quadrupole moment that is known to be extremely sensitive to electric field gradients generated by its bonding and charge environment. This quadrupolar interaction broadens the NMR signals of gallium atoms in asymmetric environments such as present in GaF_3, $GaCl_3$, and GaI_3 beyond detectability. In contrast, well defined sharp ^{69}Ga resonances are observed in gallium phosphide, where the Ga atoms are located on sites with cubic point symmetry and the quadrupolar interaction vanishes. However, it has been previously shown that the ^{69}Ga resonance (and that of other constituent nuclei in III–V semiconductors) is extremely sensitive to defects or lattice strain introduced into the cubic zincblende lattice by dopant atoms [8–15]. The interaction between the nuclear electric quadrupole moment and such field gradients produces a first-order perturbation on the ^{69}Ga Zeeman energy levels and splits the ^{69}Ga resonance line into three components corresponding to the three allowed $\Delta m = \pm 1$ transitions [17]. Only the central $1/2 \rightarrow -1/2$ transition remains unperturbed to first order, whereas the locations of the other two resonances become orientationally dependent (see Fig. 3). Consequently, in a polycrystalline material these transitions give rise to broad powder patterns, which become a spinning sideband manifold under MAS conditions. This sideband pattern is expected to occur even in the purest, best-grown, and crystallographically most perfect GaP samples, because there is always a finite concentration of intrinsic defects, producing electric field gradients at gallium sites as far as 30 Å distant [11]. Due to this far-reaching effect of distance, a distribution of quadrupole splittings is expected, the details of which are difficult to model. Regardless of the electric field gradient magnitude, however, such splittings decrease the intensity of the dominant central line observed in the MAS NMR spectra. While nothing is known about the nature of the defects and disorder present in this suite of gallium phosphide samples, it is reasonable to expect that the absolute intensity of the central ^{69}Ga resonance is correlated with the number of gallium atoms on unperturbed, strictly-cubic sites. Thus, this

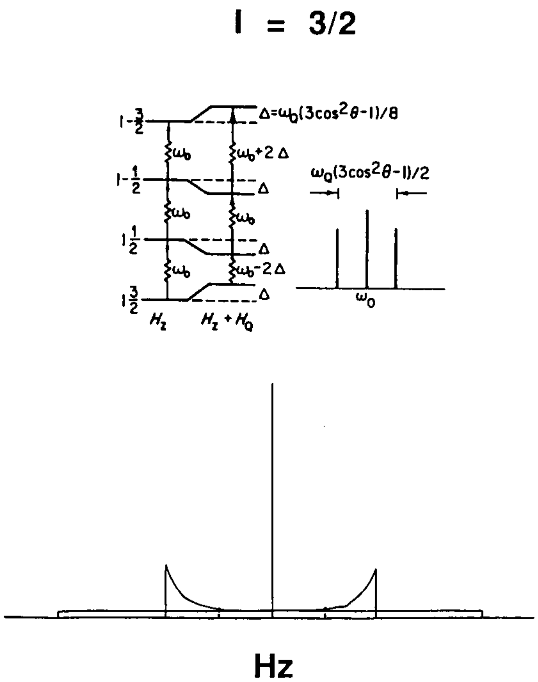

Fig. 3. Energy level diagram and resulting schematic NMR spectrum for a spin −3/2 nucleus subject to first-order quadrupolar perturbations. The upper part of this figure is reproduced from Ref. 18.

parameter can serve as a qualitative measure of sample crystallinity. Detailed spin counting results for the central ^{69}Ga MAS NMR peak are summarized in Table 2. These numbers attain particular significance if we calculate the ratio of the gallium to phosphorus spin counts normalized to that in commercial GaP (see Table 2). Note that for all of the samples prepared by solid state reaction this ratio is smaller than one, indicating that in the samples prepared from rapid solid state reaction, fewer ^{69}Ga nuclei are present on strictly-cubic sites than in the bulk commercial sample. Again, it is intriguing to observe that this ratio decreases consistently in the order F–GaP > I–GaP > Cl–GaP, indicating an increase in defect concentration and loss of crystallinity in this order. This conclusion is again nicely consistent with all the other independent NMR and XRD evidence.

^{69}Ga nutation NMR

The spinning sideband manifold observed in Fig. 1b extends well beyond the spectral window (142 kHz) employed in our studies. This is so because especially for nuclei in defect sites or close nearby, the ^{69}Ga quadrupolar interaction is very strong, and consequently the resulting powder patterns for the satellite transitions are extremely wide. If these powder patterns extend beyond the radio frequency excitation window, the corresponding Rabi frequencies of the ^{69}Ga nuclei are affected [16,19,20]. Two extreme situations can be distinguished with regard to the relative magnitude of the quadrupolar precession frequency ω_Q and the Rabi frequency ω_1 of unperturbed nuclei (such as present in non-viscous liquid solutions): in the limit of non-selective excitation, $\omega_Q \ll \omega_1$, all transitions lie completely within the rf excitation window and the Rabi frequency is identical with that measured for resonances in the absence of a static quadrupolar interaction. In the limit of completely selective excitation, $\omega_Q \gg \omega_1$, only the central $1/2 \rightarrow -1/2$ transition is excited, and the Rabi frequency is effectively increased to $\omega_1(I + 1/2)$, where I is the nuclear spin quantum num-

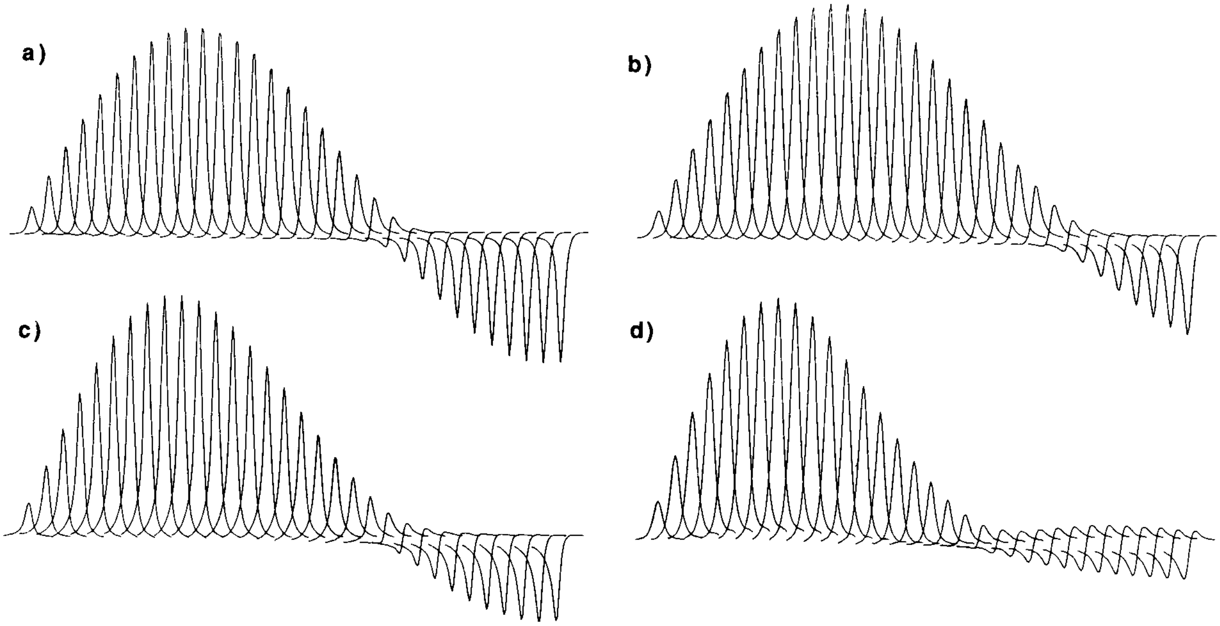

Fig. 4. ^{69}Ga nutation NMR plots of representative GaP samples investigated in the present study. Shown are stacked plots of 1-D Fourier transforms as a function of pulse length for the samples of (a) bulk GaP, and annealed polycrystalline GaP prepared from the ignition of Na_3P and (b) GaF_3, (c) GaI_3, and (d) $GaCl_3$. The increment is 0.5 μs. The pulse length for which maximum signal is obtained corresponds to the average ^{69}Ga 90° pulse length listed in Table 2.

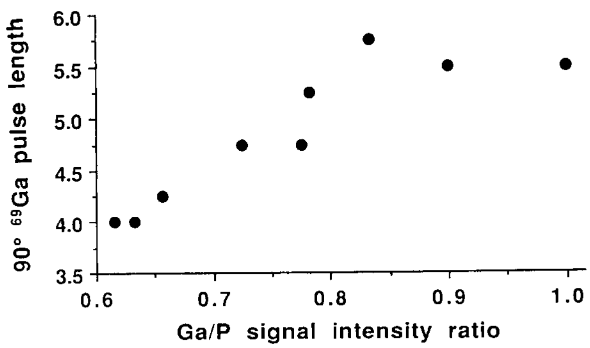

Fig. 5. Correlation of the Ga/P signal intensity ratio (relative to that observed in commercial bulk GaP) with the average 90° ^{69}Ga pulse length for the samples under study.

ber. Thus, for a spin $-3/2$ the effective 90° pulse length is a factor of 2 shorter than in solution. The intermediate case $\omega_Q \sim \omega_1$ is complicated and results in structured excitation spectra that can be simulated numerically [20].

Experimentally, the excitation spectrum is mapped out by recording the signal intensity with systematic incrementation of the pulse length ("nutation NMR"). In the present samples, the ^{69}Ga nuclei experience a wide distribution of quadrupolar interaction strengths, depending on their proximity to defects and on the nature of the latter. Consequently, a superposition of nutation behavior is measured (see Fig. 4), from which an average effective 90° pulse length t_{90}^{eff} can be determined (Table 2). Due to similar arguments used in the discussion of the absolute ^{69}Ga MAS NMR spin count, t_{90}^{eff} is expected to be correlated with the fraction of gallium atoms present on unperturbed, strictly-cubic lattice sites. The specifics of this correlation will depend on the nature of the defects and disorder in these samples, about which no further independent information is available for the present samples. Nevertheless, the parameter t_{90}^{eff} can be taken as a relative measure of sample quality and crystallinity. Additional confidence in this assumption can be gained upon inspection of Fig. 5, which shows that for all of the samples studied t_{90}^{eff} is well correlated with the ^{69}Ga/^{31}P spin count ratio. This correlation is expected if the underlying variable is a number of defects producing a wide distribution of quadrupole coupling constants: as with increasing defect concentration, fewer ^{69}Ga nuclei remain in strictly-cubic sites more and more ^{69}Ga nuclei experience such strong electric field gradients and quadrupole splittings, that their satellite transitions are no longer excitable. Consistent with all of the other NMR evidence, the nutation NMR spectra reveal that the crystalline quality of GaP samples produced by solid state metathesis reactions from gallium halide precursors, decreases in the order F–GaP > I–GaP > Cl–GaP. At the same time, the product quality is independent of the reaction mode (method 1 or 2 as outlined in the Experimental section).

Conclusions

Quantitative solid state NMR techniques are well-suited for evaluating the yield and product quality of III–V semiconductor preparations obtained by rapid solid state synthesis. Subtle differences between samples are easily resolved, and a numerical scale for their comparison can be established. According to the present study, the quality and crystallinity of gallium phosphide samples prepared from GaF_3 precursor approaches that of GaP prepared in the traditional fashion from elemental Ga and P, while the reaction from GaI_3 and $GaCl_3$ results in inferior products. The analytical NMR protocol established in the present study is generally applicable to all III–V semiconductors and will aid in the further optimization of their rapid solid state syntheses.

This work was supported by the National Science Foundation, grant DMR-8913738 (H.E.) and by Grant No. 8657822, through the Presidential Young Investigator Award Program, and by a David and Lucille Packard Foundation Fellowship in Science and Engineering (R.B.K.).

REFERENCES

1 P.R. Bonneau, R.F. Jarvis, Jr. and R.B. Kaner, Nature, 349 (1991) 510.
2 R.E. Treece, G.S. Macala and R.B. Kaner, Chem. Mater, 4 (1992) 9.

3 R.E. Treece, G.S. Macala, D. Franke, H. Eckert and R.B. Kaner, Inorg. Chem., in press.
4 R.A. Nissan and T.A. Vanderah, J. Phys. Chem. Solids, 50 (1989) 347.
5 J.E. McDougall, H. Eckert, G.D. Stucky, N. Herron and Y. Wang, J. Am. Chem. Soc., 111 (1989) 8006.
6 R. Tycko, G. Dabbagh, S.R. Kurtz and J.P. Goral, Phys. Rev. B, 45 (1992) 13452.
7 T.M. Duncan, R.F. Karlicek, W.A. Bonner and F.A. Thiel, J. Phys. Chem. Solids, 45 (1984) 389.
8 D.G. Andrianov, V.V. Karataev, M.G. Mil'vidskii and Y.B. Muravlev, Sov. Phys. Semicond., 17 (1983) 57.
9 R.K. Hester, A. Sher, J.F. Soest and G. Weisz, Phys. Rev. B, 10 (1974) 4262.
10 O.H. Han, H.K.C. Timken and E. Oldfield, J. Chem. Phys., 89 (1988) 6046.
11 E.H. Rhoderick, Philos. Mag., 3 (1958) 545.
12 E.H. Rhoderick, J. Phys. Chem. Solids, 8 (1958) 498.
13 W.E. Carlos, S.G. Bishop and D.J. Treacy, Appl. Phys. Lett., 49 (1986) 528.
14 W.E. Carlos, S.G. Bishop and D.J. Treacy, Phys. Rev. B, 43 (1991) 12512.
15 R.K. Sundfors, Phys. Rev., 185 (1969) 458.
16 A. Samoson and E. Lippmaa, Phys. Rev. B, 28 (1983) 6567.
17 M.H. Cohen and F. Reiff, in F. Seitz and D. Turnbull (Eds.) Solid State Physics, Vol. 5, Academic Press, New York, 1958, p. 321.
18 B.C. Gerstein and C.R. Dybowski, Transient Techniques in NMR of Solids, Academic Press, New York, 1985.
19 A. Samoson and E. Lippmaa, J. Magn. Reson., 79 (1988) 255.
20 A.P.M. Kentgens, J.J.M. Lemmens, F.M.M. Geurts and W.S. Veeman, J. Magn. Reson., 71 (1987) 62.

Analytica Chimica Acta, 283 (1993) 997–1005
Elsevier Science Publishers B.V., Amsterdam

Review

Applications of nuclear magnetic resonance spectrometry to solid polymers

Regan L. Silvestri and Jack L. Koenig

Department of Macromolecular Science, Case Western Reserve University, Cleveland, OH 44106 (USA)

(Received 1st November 1992)

Abstract

The applications of nuclear magnetic resonance (NMR) spectrometry to solid polymers are reviewed. Emphasis is given to the determination of chemical structure, and the characterization of molecular dynamics in the solid state. The types of information that can be obtained from NMR spectrometry are surveyed, focusing on the special experimental techniques necessary.

Keywords: Nuclear magnetic resonance spectrometry; Polymers; Review; Solid state NMR

With the advent of pulsed-Fourier transform techniques [1–5], nuclear magnetic resonance (NMR) spectrometry [6–10] has found many applications in polymer science [11–27]. Polymer composition, isomerization, morphology and motion can be studied by NMR. The most common NMR active nuclei used in the study of polymers are ^{13}C ($I = 1/2$), ^{1}H ($I = 1/2$) and ^{2}H ($I = 1$). Other NMR active nuclei include ^{19}F ($I = 1/2$), ^{29}Si ($I = -1/2$), ^{14}N ($I = 1$), ^{15}N ($I = -1/2$), ^{31}P ($I = 1/2$) and ^{17}O ($I = -5/2$).

The high resolution afforded by NMR spectrometry in solution facilitates the observation of fine structure in the spectrum. In solution, inequivalent chemical shifts can be resolved for (A) short-chain branching structures [28,29], (B) stereochemical or configurational isomers [13,14], and (C) directional isomers [30,31]. However, in the interest of using polymers as engineering materials, they must be studied as solids [32,33].

^{13}C NMR

High resolution in the solid state

To achieve high resolution in the solid state, the techniques of (A) cross polarization, (B) magic angle spinning and (C) dipolar decoupling must be combined.

Cross polarization (CP) enhances the ^{13}C signal by tapping the abundant ^{1}H spin reservoir. Spin-locking radio frequency (rf) pulses are applied simultaneously to the ^{13}C and ^{1}H. At the Hartmann–Hahn condition, both nuclei precess at the same frequency and magnetization is transferred from the abundant ^{1}H spin reservoir to the dilute ^{13}C spin reservoir [34,35].

Magic angle spinning (MAS) reduces line broadening caused by the high chemical shift anisotropy (CSA) in solids. Rapid sample spinning at an angle of 54.7° relative to the static magnetic field reduces the broad CSA pattern to a single peak at the isotropic chemical shift [36–38].

Dipolar decoupling (DD) reduces the line broadening caused by strong ^{13}C–^{1}H dipolar interactions. Heteronuclear decoupling is accom-

Correspondence to: J.L. Koenig, Department of Macromolecular Science, Case Western Reserve University, Cleveland, OH 44106 (USA).

0003-2670/93/$06.00

plished by high powered rf pulses at the ^{1}H frequency during the time which the ^{13}C signal is observed [39].

The combination of CP/MAS/DD results in a high resolution ^{13}C NMR spectrum in the solid state [40,41]. Figure 1 shows the effects of these techniques separately and simultaneously [42].

Conformational isomers

The precise measurement of ^{13}C chemical shifts is experimentally simple. Nonetheless, ^{13}C chemical shifts can be used to distinguish conformational isomers of solid polymers [43]. Conformational or geometric isomers are magnetically inequivalent due to their differing chemical bond angles and solid state packing environments.

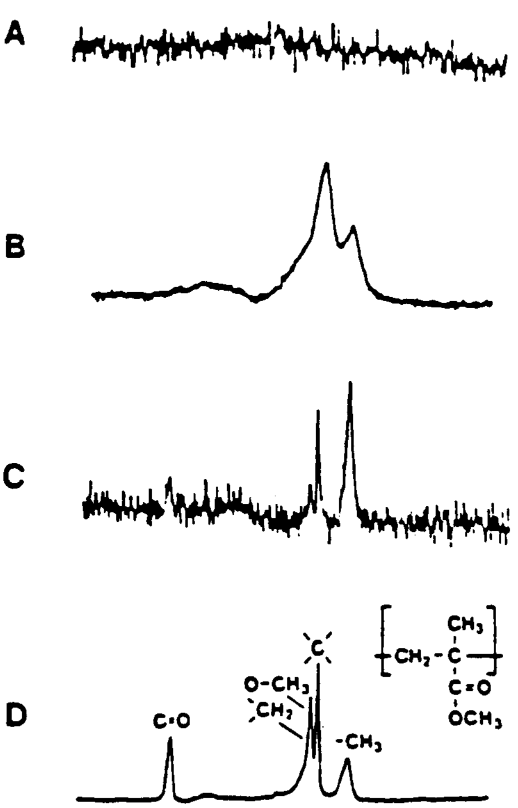

Fig. 1. The ^{13}C solid-state NMR spectra of poly(methyl methacrylate) with (A) solution conditions, (B) CP/DD, (C) MAS/DD, and (D) CP/MAS/DD (adapted from [42]).

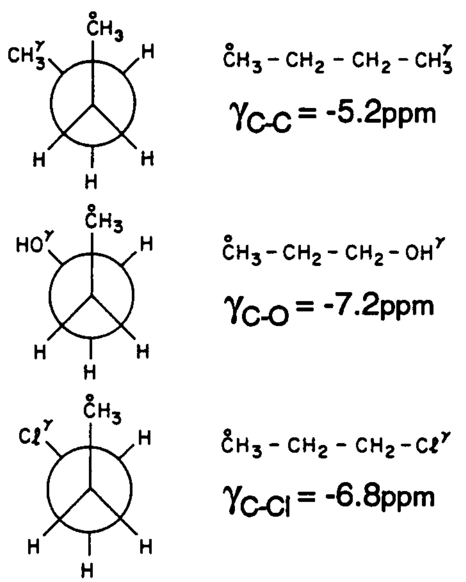

Fig. 2. The ^{13}C chemical shift γ-gauche shielding effects produced by the γ substituents C, OH, and Cl (adapted from [15]).

The through space distance between the observed carbon C_0 and the carbon three bonds away C_γ changes with rotation between the trans and gauche isomers. The distance from C_0 to C_γ is reduced in the gauche conformation. Therefore, in the gauche conformation C_0 is shielded by C_γ, resulting in an upfield shift of the chemical shift of C_0. A γ carbon in the gauche conformation causes a shielding of −5.2 ppm [15]. Two γ-gauche carbons, one on each side of C_0, will double the amount of shielding. As summarized in Fig. 2, a γ oxygen causes a shielding of −7.2 ppm, a γ chlorine causes a shielding of −6.8 ppm [15], and a γ fluorine causes a shielding of −2 to −5 ppm [30]. This phenomenon is called the γ-gauche effect.

Since rotation between trans and gauche isomers occurs faster than the NMR time scale, separate peaks are not observed for the two isomers. Instead, there is a single peak whose chemical shift is indicative of the ratio of isomers. The chemical shift of C_0 is representative of isomerization at the central bond between C_0 and C_γ.

Chemical shifts can also be used to distinguish various helical conformations. Again, different helical conformations have different solid state packing environments and therefore inequivalent chemical shifts.

Crosslinking

Chemically crosslinked polymers form network structures that have limited solubility. High-resolution NMR spectrometry in the solid-state can be used to (A) characterize the chemical structures of crosslinked systems, (B) imply the mechanisms of network formation, and (C) characterize the segmental and chain motions at the molecular level [29]. When there is a variety of crosslink structures, not only can the types of crosslink structures be determined, but also the quantities of various structures. NMR spectrometry has been used to characterize the network structures in elastomers [44], epoxies [45–48], polyethylene [49,50], and a variety of other crosslinked polymers [21,51].

Due to the intrinsically narrow solid-state ^{13}C resonance lines of elastomers, the study of these systems has been particularly profitable. New resonance lines in the spectra of crosslinked rubbers have been assigned to various structural units of the network [29]. Vulcanization forms short-chain crosslinks, long-chain crosslinks, cyclic structures, and pendant groups. A number of elastomers have been studied with various cure recipe mixtures [52–61].

Since the network structure is responsible for the physical and mechanical properties of a polymer, a complete characterization of the network structure enables tayloring of the properties [29].

Relaxation phenomenon

The relaxation of magnetization back to equilibrium is caused by molecular motion [62]. Relaxation rates can be measured and related to molecular correlation times [63,64].

The measurement of relaxation rates provides information about local molecular dynamics in many frequency regimes [26]. A number of relaxation parameters can be measured, probing different motions over a wide range of frequencies. As shown in Fig. 3, each of the relaxation parameters is characteristic of motions in a different range of frequencies. Internal motions with frequencies in the MHz regime are characterized by a spin-lattice relaxation time in the static field, ^{13}C T_1 [65,66]. Slower motions with frequencies in the kHz regime are characterized by a spin-lattice relaxation time in the rotating frame, ^{13}C $T_{1\rho}$ [67–70]. Spin–spin relaxation, ^{13}C T_2, is most sensitive to the motions of nonrigid solids and viscous liquids [71].

^{1}H NMR

The natural abundance of the ^{1}H isotope (99.9%) of hydrogen leads to a high NMR sensitivity in solutions. In solids, this high abundance leads to strong ^{1}H–^{1}H dipolar interactions that produce large line widths. Multipulse sequences are used to reduce the line widths [72]. Combined rotational and multiple pulse spectroscopy (CRAMPS) uses magic angle spinning to reduce chemical shift anisotropy, and multipulse trains

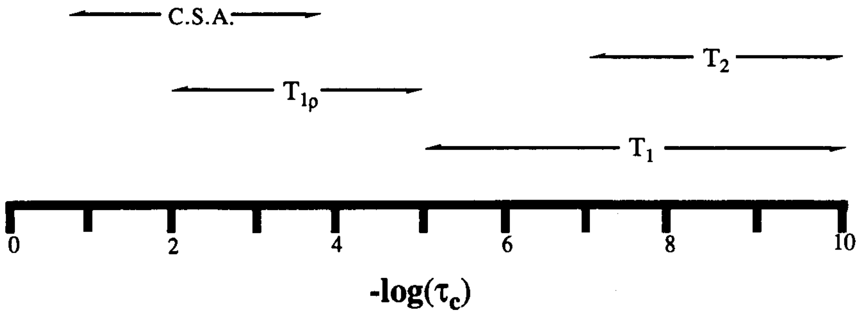

Fig. 3. Solid-state ^{13}C NMR experiments and the approximate molecular correlation times they are sensitive to.

to reduce homonuclear dipolar coupling. These multipulse techniques can be tedious because they require accurate adjustments of pulse lengths and phases. Fortunately, techniques have been developed that simplify spectrometer set-up and improve pulse length and phase accuracy [73].

The simplest multipulse sequence that suppresses homonuclear dipolar interactions is a four pulse cycle called WA-HU-HA [74]. Expanding on this technique, an eight pulse train, REV-8, suppresses homonuclear dipolar interactions and furthermore corrects for rf inhomogeneity effects [75]. A twenty four pulse train, BR-24, eliminates the effects of higher order dipolar interactions [76].

By decreasing rf power and increasing pulse widths, the delays or "windows" between pulses become smaller and eventually vanish. A windowless pulse train is a sequence of joined pulses; continuous, phased-switched rf irradiation. The simplest fully windowless experiment is the twelve pulse BLEW-12 [77]. However, the forty eight pulse BLEW-48 is superior [77].

These multipulse sequences are effective at largely reducing homonuclear dipolar interactions. However, the residual linewidths are still significant such that proton resolution is limited. Since the dispersion of ^{1}H chemical shifts has a range of 10 ppm, residual line widths of ca. 1–2 ppm limit the number of resolvable peaks.

^{2}H NMR

The ^{2}H isotope of hydrogen has a spin quantum number $I = 1$. Thus, deuterium has a nonspherical charge distribution and an associated electric quadrupole moment [78,79]. As a result, deuterium has a powder pattern line shape [80–82]. Since the electric field gradient is axially symmetric about the C–D bond, line shapes can be easily interped in terms of order and dynamics of the C–D bond [79].

By selective deuteration, molecular order and dynamics can be examined at specific sites [83]. Motion of the C–D bond partially averages the quadrupolar line shape causing the powder pattern to collapse. Also, various orientations result in characteristic line shapes that are easily recognized. For partially oriented polymers, the distribution of orientations can be determined [84].

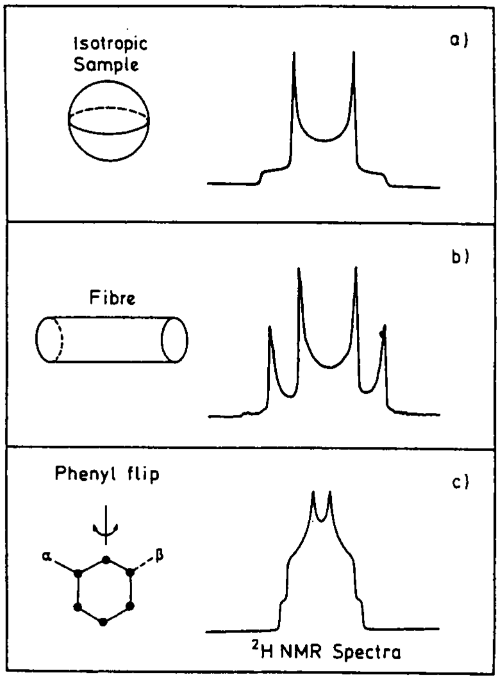

Fig. 4. Deuteron NMR line shapes of (A) a rigid isotropic powder, (B) a rigid uniaxially drawn fiber, and (C) an isotropic solid with flipping phenyl rings. (adapted from [78]).

Figure 4 shows the ^{2}H line shapes for (A) an isotropic powder (B) a uniaxially drawn fiber with a planar distribution of C–D bonds and (C) a motionally averaged pattern for the flipping of a phenyl ring [78]. The experimental strategy is to first calculate a theoretical pattern for an assumed motion and order. Then, the observed pattern is matched to the calculated, thereby specifying the motion and order. This is not a difficult procedure since various motions result in characteristic line shapes that can be easily recognized.

Deuterium line shapes are most commonly generated by the solid echo pulse sequence [85]. Deuterium line shape analysis is sensitive to slow molecular motions with correlation times of 10^{-3} to 10^{-8} s [86,87]. Faster motions can be characterized by deuterium T_1 which is sensitive to motions with molecular correlation times as short

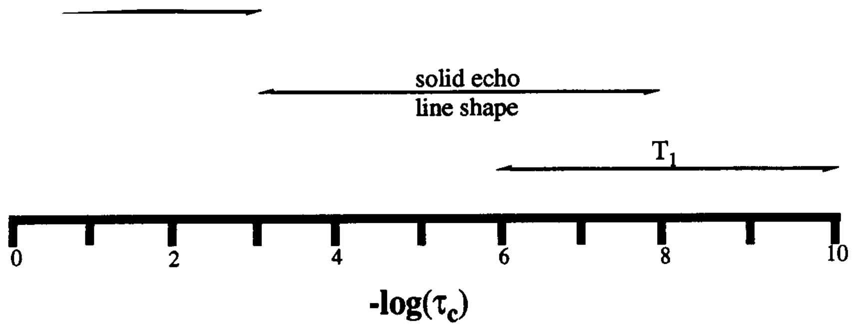

Fig. 5. Solid-state ^{2}H NMR experiments and the approximate molecular correlation times they are sensitive to.

as 10^{-6} to 10^{-10} s [81,87]. Ultra-slow motions can be studied by deuteron spin alignment [88] which is sensitive to motions with correlation times as long as 10^{-3} to 100 s [89]. These experiments, and the molecular motions they characterize, are summarized in Fig. 5.

CHEMICAL SHIFT ANISOTROPY (CSA)

Recall that magic angle sample spinning is used to reduce the effects of chemical shift anisotropy. If MAS is not used then a powder pattern line shape results from the distribution of orientations [90]. The CSA powder pattern can be used to study molecular order and dynamics in a manner analogous to deuterium line shape analysis.

If the polymer is oriented, the broad CSA pattern will partially collapse [91]. Figure 6 shows axially asymmetric and axially symmetric CSA powder patterns [11]. The broad asymmetric pattern shown in Fig. 6a is the sum of all possible random orientations. Uniaxial symmetry about σ_{11} averages the other two dimensions, σ_{22} and σ_{33}.

The CSA line shape can also be partially averaged by motion. For example, the ^{19}F CSA line shape of a static $-CF_3$ group shows the broad general pattern in Fig. 7a. However, rapid rotation of the $-CF_3$ group about its C_3 axis averages the two directions perpendicular to the spinning axis as shown in Fig. 7b [92].

Often, the order and motion are not ideal, and perfect models can not be specified. In this case, the CSA is described by its width and asymmetry [93]. When the polymer is not perfectly axially symmetric, the degree of orientation is given by the CSA width and asymmetry. Or when the exact motion can not be specified, the relative increase or decrease in mobility is given by the CSA width and asymmetry.

When multiple resonances overlap, it becomes difficult to characterize the CSA from the powder pattern of a non-spinning sample. Using slow-speed magic angle spinning, the CSA parameters can be calculated from the the spinning side band intensities [94].

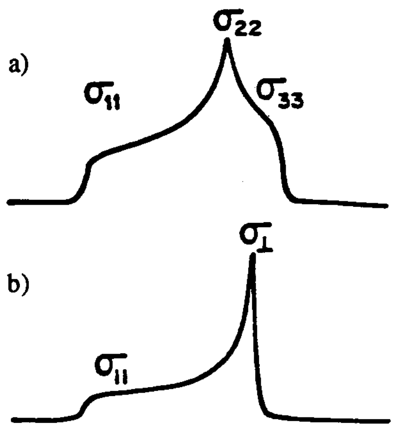

Fig. 6. Chemical shift anisotropy powder patterns for (A) a general asymmetric chemical shift tensor (B) an axially symmetric chemical shift tensor (adapted from [11]).

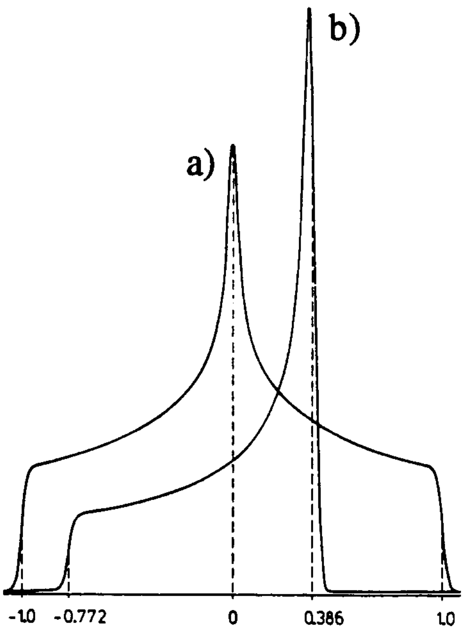

Fig. 7. The ^{19}F chemical shift anisotropy line shape for (A) a static $-CF_3$ group and (B) a $-CF_3$ group rotating about its C_3 axis (adapted from [33]).

TWO-DIMENSIONAL NMR

Two-dimensional NMR techniques [95–99] can be used to (A) enhance the resolution of the 1-D spectrum by spreading the peaks out in a second dimension, and (B) observe through space interactions to determine the three-dimensional conformation. Two-dimensional techniques in solution are becoming routine and indispensable, particularly with applications to determining globular protein conformation.

Two-dimensional correlation spectroscopy (COSY) [100,101] shows cross peaks between atoms that are spin-coupled. $^1H-^1H$ homonuclear spin-coupling is a through bond interaction. Therefore, cross peaks can be used to establish molecular connectivity. Likewise, heteronuclear correlation spectroscopy (HETCOR) [102–104] yields a two-dimensional correlation map of the chemical shifts of directly bonded $^1H-^{13}C$ atoms. Two-dimensional nuclear Overhauser spectroscopy (NOESY) [105,106] shows cross peaks between protons that are close enough to interact via the nuclear Overhauser effect. Since the nuclear Overhauser effect (NOE) occurs through space [107,108], cross peaks are seen for interactions due to chain folding. Two dimensional *J*-resolved spectroscopy [109] separates the chemical shift in one dimension from the *J*-coupling constant in the other dimension. Therefore, the projection on one axis is the simplified decoupled spectrum, and projections on the other axis can be used to measure *J*-coupling constants.

Due to the complexity of polymer systems, there may be substantial peak overlap even in a two-dimensional spectrum. In this case, three-dimensional NMR [110] spreads the peaks out in yet another dimension. Three-dimensional NMR is simply the combination of two 2-D experiments. For example, the combination of NOESY and *J*-resolved spectroscopy yields a three-dimensional spectrum in which the first two dimensions are spread out due to the NOE interaction and the third dimension is *J*-resolved. In this manner the *J*-coupling constant can be measured because overlap has been reduced by exploiting the NOE interaction [110]. These types of 2-D and 3-D experiments have been applied to polymeric engineering materials in solutions to determine chain conformation, molecular organization and chain packing [110].

In the solid state, modern techniques have been developed for two-dimensional NMR spectrometry. Heteronuclear $^{13}C-^1H$ correlation in solids incorporates multiple pulse trains to remove homonuclear dipolar interactions of the abundant ^1H spin. $^1H-^1H$ dipolar interactions can be suppressed during the evolution period by MREV-8 [111], by BLEW-12 [112] or by BLEW-24 [113]. Coherence transfer by isotropic mixing is commonly achieved by WIM-24 [112,113].

Heteronuclear correlation of structure and mobility in the solid state is possible without the use of sophisticated CRAMPS techniques. The wideline separation (WISE) pulse sequence [114] yields a ^1H wideline spectrum in one dimension for each ^{13}C resonance in the other dimension. Each ^{13}C resonance has a separate proton wideline spectra reflecting the $^1H-^{13}C$ dipolar coupling in the proximity of the respective ^{13}C moiety. Because the dipolar line width is reduced by motion, segmental mobility is reflected in the ^1H

line shape. Large-amplitude motions with rates exceeding the dipolar coupling, typically 50 kHz, average the proton line shape. Thus for each ^{13}C resonance, a narrow ^{1}H lineshape indicates high segmental mobility of the chemical structure assigned to the ^{13}C resonance [114].

To expand on the WISE technique, total suppression of sidebands (TOSS) [115,116] and ^{1}H spin diffusion may be incorporated into the pulse sequence. Rotor synchronized TOSS is used to suppress the unwanted ^{13}C spinning sidebands [115,116]. ^{1}H spin diffusion is incorporated to determine the relative spatial positions of components with different mobilities [114]. Exchange of ^{1}H magnetization by spin diffusion transfers the ^{1}H lineshapes among diffusing moieties. By increasing the length of time that spin diffusion is allowed to progress, spin diffusion can occur over larger distances. The WISE technique is particularly suited for the study of heterogeneous polymers systems [114].

Two-dimensional exchange spectroscopy [117–119] can be used to characterize ultraslow motions in the range of 10^{-3} to ca. 100 s [120]. This simple three-pulse sequence is commonly applied to ^{2}H, but can also be applied to ^{13}C with and without MAS [78,87]. Along the diagonal of the 2-D exchange spectrum is the familiar powder pattern. Off the diagonal are elliptical exchange ridges that describe the angle at which a selectively deuterated group rotates [117]. If rotation occurs around a precise angle, a well-defined ridge pattern is observed [118,121]. If rotation occurs about a distribution of angles, a broad exchange pattern is observed [117]. The angular distribution can therefore be determined from the 2-D spectrum. Two-dimensional exchange spectroscopy has been applied to the study of chain motions above the glass transition, and rotations about a helical axis in semi-crystalline polymers [87].

REFERENCES

1 F. Bloch, W.W. Hansen and M. Packard, Phys. Rev., 69 (1946) 127.
2 F. Bloch, Phys. Rev., 70 (1946) 460.
3 F. Bloch, W.W. Hansen and M. Packard, Phys. Rev., 70 (1946) 474.
4 E.M. Purcell, H.C. Torrey and R.V. Pound, Phys. Rev., 69 (1946) 37.
5 E.M. Purcell, Phys. Rev., 69 (1946) 681.
6 A. Abragam, The Principles of Nuclear Magnetism, Clarendon Press, Oxford, 1961.
7 C.P. Slicter, Principles of Magnetic Resonance, Springer-Verlag, New York, 3rd edn., 1990.
8 T.C. Farrar, An introduction to Pulse NMR Spectroscopy, Farragut Press, Chicago, IL, 1989.
9 E. Fukushima and S.B.W. Roeder, Experimental Pulse NMR: A Nuts and Bolts Approach, Addison-Wesley, Reading, MA, 1981.
10 E. Breitmaier and G. Bauer, ^{13}C NMR Spectroscopy: A Working Manual, Harwood, New York, 1984.
11 J.L. Koenig, Spectroscopy of Polymers, American Chemical Society, Washington, DC, 1992.
12 J.L. Koenig, Chemical Microstructure of Polymer Chains, Wiley, New York, 1980.
13 F.A. Bovey, High Resolution NMR of Macromolecules, Academic Press, New York, 1972.
14 F.A. Bovey, L. Jelinski and P.A. Mirau, Nuclear Magnetic Resonance Spectroscopy, Academic Press, New York, 2nd edn., 1988.
15 A.E. Tonelli, NMR Spectroscopy and Polymer Microstructure: The Conformational Connection, VCH Publishers, New York, 1989.
16 J. Schaefer, in G.C. Levy (Ed.), Topics in Carbon-13 NMR Spectroscopy, Vol. 1, Wiley, New York, 1974, pp. 149–208.
17 R.A. Komoroski (Ed.), High Resolution NMR Spectroscopy of Synthetic Polymers in Bulk, VCH Publishers, Deerfield Beach, FL, 1986.
18 W.M. Pasika (Ed.), Carbon-13 NMR in Polymer Science, ACS Symposium Series 103, American Chemical Society, Washington, DC, 1979.
19 P. Diehl, E. Fluck and R. Kosfeld (Eds.), NMR: Basic Principles and Progress, Vol. 4, Springer-Verlag, Berlin, 1971.
20 L.J. Mathias (Ed.), Solid State NMR of Polymers, Plenum Press, New York, 1991.
21 J.R. Havens and J.L. Koenig, Appl. Spectrosc., 37 (1983) 226.
22 F. Laupretre, Prog. Polym. Sci., 15 (1990) 425.
23 H. Saito and I. Ando, Annual Reports on NMR Spectroscopy, 21 (1989) 209.
24 I. Ando, T. Yamanobe and T. Asakura, Progress in NMR Spectroscopy, 22 (1990) 349.
25 B.C. Perry and J.L. Koenig, J. Appl. Polym. Sci.: Appl. Polym. Symp., 43 (1989) 165.
26 F.A. Bovey and L.W. Jelinski, J. Phys. Chem., 89 (1985) 571.
27 A.K. Roy and P.T. Inglefield, Progress in NMR Spectroscopy, 22 (1990) 569.
28 F.A. Bovey, F.C. Schilling, F.L. McCrackin and H.L. Wagner, Macromolecules, 9 (1976) 76.

29 M. Andreis and J.L. Koenig, Adv. Polym. Sci., 89 (1989) 69.
30 A.E. Tonelli, F.C. Schilling and R.E. Cais, Macromolecules, 15 (1982) 849.
31 R.E. Cais and N.J.A. Sloane, Polymer, 24 (1983) 179.
32 B.C. Gerstein and C.R. Dybowski, Transient Techniques in NMR of Solids, Academic Press, New York, 1985.
33 M. Mehring, Principles of High Resolution NMR in Solids, Springer-Verlag, New York, 2nd edn., 1983.
34 S.R. Hartmann and E.L. Hahn, Phys. Rev., 128 (1962) 2042.
35 A. Pines, M.G. Gibby and J.S. Waugh, J. Chem. Phys., 59 (1973) 569.
36 E.R. Andrew, A. Bradbury and R.G. Eades, Nature, 182 (1958) 1659.
37 I.J. Lowe, Phys. Rev. Lett., 2 (1959) 285.
38 J. Schaefer and E.O. Stejskal, J. Am. Chem. Soc., 98 (1976) 1031.
39 L.R. Sarles and R.M. Cotts, Phys. Rev., 111 (1958) 853.
40 C.S. Yannoni, Acc. Chem. Res., 15 (1982) 201.
41 D.L. VanderHart, W.L. Earl and A.N. Garroway, J. Magn. Reson., 44 (1981) 361.
42 C.A. Fyfe, Solid State NMR for Chemists, CFC Press, Guelph, Ontario, 1983.
43 D.M. Grant and B.V. Cheney, J. Am. Chem. Soc., 89 (1967) 5315.
44 R.A. Komoroski, J.P. Shockcor, E.C. Gregg and J.L. Savoca, Rubber Chem. Technol., 59 (1986) 328.
45 A.N. Garroway, W.B. Moniz and H.A. Resing, in W.M. Pasika (Ed.), Carbon-13 NMR in Polymer Science, ACS Symposium Series 103, American Chemical Society, Washington, DC, 1979, pp. 67–87.
46 A. Cholli, W.M. Ritchey and J.L. Koenig, in S.S. Labana and R.A. Dickie (Ed.), Characterization of Highly Cross-Linked Polymers, ACS Symposium Series 243, American Chemical Society, Washington, DC, 1984, pp. 233–239.
47 A.N. Garroway, W.M. Ritchey and W.M. Moniz, Macromolecules, 15 (1982) 1051.
48 E.A. Mertzel, D.R. Perchak, W.M. Ritchey and J.L. Koenig, Ind. Eng. Chem. Res., 27 (1988) 586.
49 A.L. Cholli, W.M. Ritchey and J.L. Koenig, Appl. Spectrosc., 41 (1987) 1418.
50 F. Horii, Q. Zhu, R. Kitamaru and H. Yamaoka, Macromolecules, 23 (1990) 977.
51 D.R. Bauer, Prog. Org. Coat., 14 (1986) 45.
52 J.L. Koenig and D.J. Patterson, Elastomers and Rubber Technol., 32 (1987) 31.
53 A.M. Zaper and J.L. Koenig, Rubber Chem. Technol., 60 (1987) 252.
54 A.M. Zaper and J.L. Koenig, Rubber Chem. Technol., 60 (1987) 278.
55 A.M. Zaper and J.L. Koenig, Makromol. Chem., 189 (1988) 1239.
56 M. Andreis, J. Liu and J.L. Koenig, J. Polym. Sci.: Part B: Polym. Phys., 27 (1989) 1389.
57 M. Andreis, J. Liu and J.L. Koenig, Rubber Chem. Technol., 62 (1989) 82.
58 R.S. Clough and J.L. Koenig, Rubber Chem. Technol., 62 (1989) 908.
59 M.R. Krejsa and J.L. Koenig, Rubber Chem. Technol., 64 (1991) 40.
60 S.R. Smith and J.L. Koenig, Rubber Chem. Technol., 65 (1992) 176.
61 M.R. Krejsa and J.L. Koenig, Rubber Chem. Technol., 65 (1992) 427.
62 N. Bloembergen, E.M. Purcell and R.V. Pound, Phys. Rev., 73 (1948) 679.
63 D. Doddrell, V. Glushko and A. Allerhand, J. Chem. Phys., 56 (1972) 3683.
64 R. Dejean de la Batie, F. Lauprêtre and L. Monnerie, Macromolecules, 21 (1988) 2045.
65 D.A. Torchia and A. Szabo, J. Magn. Reson., 49 (1982) 107.
66 R.L. Silvestri and J.L. Koenig, Macromolecules, 25 (1992) 2341.
67 J. Schaefer, E.O. Stejskal and R. Buchdahl, Macromolecules, 10 (1977) 384.
68 J. Schaefer, E.O. Stejskal, T.R. Steger. M.D. Sefcik and R.A. McKay, Macromolecules, 13 (1980) 1121.
69 T.R. Steger, J. Schaefer, E.O. Stejskal and R.A. McKay, Macromolecules, 13 (1980) 1127.
70 M.D. Sefcik, J. Schaefer, E.O. Stejskal and R.A. McKay, Macromolecules, 13 (1980) 1132.
71 H.Y. Carr and E.M. Purcell, Phys. Rev., 94 (1954) 630.
72 U. Haeberlen, High Resolution NMR in Solids: Selective Averaging, Academic Press, New York, 1976.
73 R.W. Vaughan, D.D. Elleman, L.M. Stacey, W.-K. Rhim and J.W. Lee, The Review of Scientific Instruments, 43 (1972) 1356.
74 J.S. Waugh, L.M. Huber and U. Haeberlen, Phys. Rev. Lett., 20 (1968) 180.
75 W-K. Rhim, D.D. Elleman and R.W. Vaughan, J. Chem. Phys., 58 (1973) 1772.
76 D.P. Burum and W.K. Rhim, J. Chem. Phys., 71 (1979) 944.
77 D.P. Burum, M. Linder and R.R. Ernst, J. Magn. Reson., 44 (1981) 173.
78 H.W. Spiess, Annu. Rev. Mater. Sci., 21 (1991) 131.
79 H.W. Spiess, Colloid Polym. Sci., 261 (1983) 193.
80 R. Hentschel and H.W. Spiess, J. Magn. Reson., 35 (1979) 157.
81 H.W. Spiess, Pure Appl. Chem., 57 (1985) 1617.
82 H.W. Spiess, J. Mol. Struct., 111 (1983) 119.
83 J.J. Wendoloski, K.H. Gardner, J. Hirschinger, H. Miura and A.D. English, Science, 247 (1990) 431.
84 R. Hentschel, H. Sillescu and H.W. Spiess, Polymer, 22 (1981) 1516.
85 J.G. Powles and J.H. Strange, Proc. Phys. Soc., 82 (1963) 6.
86 H.W. Spiess and H. Sillescu, J. Magn. Reson., 42 (1981) 381.
87 H.W. Spiess, Makromol. Chem., Macromol. Symp., 26 (1989) 197.
88 J. Jeener and P. Broekaert, Phys. Rev., 157 (1967) 232.

89 H.W. Spiess, J. Chem. Phys., 72 (1980) 6755.
90 W.S. Veeman, Progress in NMR Spectroscopy, 16 (1984) 193.
91 A.J. Vega and A.D. English, Macromolecules, 13 (1980) 1635.
92 M. Mehring, R.G. Griffin and J.S. Waugh, J. Chem. Phys., 55 (1971) 746.
93 T.M. Duncan, A Compilation of Chemical Shift Anisotropies, Farragut Press, Chicago, IL, 1990.
94 J. Herzfeld and A.E. Berger, J. Chem. Phys., 73 (1980) 6021.
95 R.R. Ernst, G. Bodenhausen and A. Wokaun, Principles of Nuclear Magnetic Resonance in One and Two Dimensions, Clarendon Press, Oxford, 1987.
96 R.R. Ernst, Chimia, 29 (1975) 179.
97 G.E. Martin and A.S. Zektzer, Two-Dimensional NMR Methods for Establishing Molecular Connectivity: A Chemist's Guide to Experiment Selection, Performance, and interpretation, VCH, New York, 1988.
98 W.S. Brey (Ed.), Pulse Methods in 1D and 2D Liquid-Phase NMR, Academic Press, San Diego, CA, 1988.
99 A. Bax and L. Lerner, Science, 232 (1986) 960.
100 W.P. Aue, E. Bartholdi and R.R. Ernst, J. Chem. Phys., 64 (1976) 2229.
101 K. Nagayama, A. Kumar, K. Wüthrich and R.R. Ernst, J. Magn. Reson., 40 (1980) 321.
102 A.A. Maudsley and R.R. Ernst, Chem. Phys. Lett., 50 (1977) 368.
103 R. Freeman and G. Morris, J. Chem. Soc. Chem. Commun., (1978) 684.
104 A. Bax and G.A. Morris, J. Magn. Reson. 42 (1981) 501.
105 J. Jeener, B.H. Meier, P. Bachmann and R.R. Ernst, J. Chem. Phys., 71 (1979) 4546.
106 S. Macura and R.R. Ernst, Molecular Physics, 41 (1980) 95.
107 J.H. Noggle and R.E. Schirmer, The Nuclear Overhauser Effect: Chemical Applications, Academic Press, New York, 1971.
108 E.G. Paul and D.M. Grant, J. Am. Chem. Soc., 86 (1964) 2977.
109 W.P. Aue, J. Karhan and R.R. Ernst, J. Chem. Phys., 64 (1976) 4226.
110 P.A. Mirau, S.A. Heffner, G. Koegler and F.A. Bovey, Polym. Int., 26 (1991) 29.
111 P. Caravatti, G. Bodenhausen and R.R. Ernst, Chem. Phys. Lett., 89 (1982) 363.
112 P. Caravatti, G. Bodenhausen and R.R. Ernst, Chem. Phys. Lett., 100 (1983) 305.
113 D.P. Burum and A. Bielecki, J. Magn. Reson., 94 (1991) 645.
114 K. Schmidt-Rohr, J. Clauss and H.W. Spiess, Macromolecules, 25 (1992) 3273.
115 W.T. Dixon, J. Magn. Reson., 44 (1981) 220.
116 W.T. Dixon, J. Schaefer, M.D. Sefcik, E.O. Stejskal and R.A. McKay, J. Magn. Reson., 49 (1982) 341.
117 S. Wefing and H.W. Spiess, J. Chem. Phys., 89 (1988) 1219.
118 S. Wefing, S. Kaufmann and H.W. Spiess, J. Chem. Phys., 89 (1988) 1234.
119 S. Kaufmann, S. Wefing, D. Schaefer and H.W. Spiess, J. Chem. Phys., 93 (1990) 197.
120 B. Blümich and H.W. Spiess, Angew. Chem. Int. Ed. Engl., 27 (1988) 1655.
121 C. Schmidt, S. Wefing, B. Blümich and H.W. Spiess, Chem. Phys. Lett., 130 (1986) 84.

Analytica Chimica Acta, 283 (1993) 1007–1024
Elsevier Science Publishers B.V., Amsterdam

Analysis of polymer stabilizers by means of solid state NMR: some case studies

W. Barendswaard, J. Moonen and M. Neilen
DSM Research, P.O. Box 18, 6160 MD Geleen (Netherlands)

(Received 24th December 1992; revised manuscript received 28th March 1993)

Abstract

In this article ^{13}C CPMAS NMR experiments have been applied to analyse some pure polymer stabilizers and to detect the molecular heterogeneity/homogeneity of a stabilizer in a polymer matrix. In the first part CPMAS ^{13}C NMR has been used to obtain information on the crystalline structure of a phenolic antioxidant and a phosphite. The phenolic antioxidant tetrakis[3-(3,5-di-*tert.*)-butyl-4-hydroxyphenyl)propionyloxymethyl]methane is found to be of particular interest because it can exist in different crystalline modifications. The relatively high symmetry of this molecule allows a detailed analysis of the NMR results in terms of the molecular symmetry in different crystalline surroundings. Results obtained by x-ray diffraction are shown to correlate well with those obtained by CPMAS NMR. In the second part an example is presented concerning the analysis of heterogeneity/homogeneity of a stabilizer in a polymer matrix in the nanometer range by means of $T_1\rho(^1H)$ relaxation times. The example, a Zn/Ca stearate in a PVC film cast from a THF solution, shows the Zn/Ca stearate to be heterogeneously distributed in the PVC matrix. The residual THF in the matrix, however, is found to be homogeneously distributed.

Keywords: Nuclear magnetic resonance spectrometry; Polymer stabilizers; Solid state NMR

Polymer stabilizers are added to polymer matrices to prevent degradation. The large number of stabilizers commercially available can be classified into different types, depending on the purpose of their employment. Extreme processing conditions, such as very high temperatures, may require a high-temperature stabilizer whereas a long-term stability during the life time of a product can be offered by e.g. a long term heat stabilizer. Within each type each specific stabilizer has its own polymer or range of polymers it can be effectively used for. Phenolic antioxidants are for instance commonly employed for long-term heat stability in polyolefines whereas Zn/Ca stearate is frequently used as a high-temperature stabilizer during the processing of PVC. Contrary to polymers, most of the stabilizers such as phenolic antioxydants and phosphites have very low molecular weights and a number of them can be obtained in a purely crystalline form. One of the phenolic antioxidants, tetrakis[3-(3,5-di-*tert.*)-butyl-4-hydroxyphenyl)propionyloxymethyl]methane, is particularly interesting in this respect because it can exhibit different crystalline modifications [1–4]. Unfortunately, from none of its modifications the space group has been determined, despite a number of publications concerning the different crystal structures. The differences among the modifications have been observed to affect the melting point and are also expected to be related to the long-term stability during storage [1].

Because stabilizers are added to polymer matrices, knowledge about their role and effectiveness in a polymer matrix are of vital importance.

Correspondence to: W. Barendswaard, DSM Research, P.O. Box 18, 6160 MD Geleen (Netherlands).

One of the important topics concerns the homogeneity of the distribution of a stabilizer in a polymer matrix. Although a homogeneous distribution on a molecular scale is thought to be the more efficient one, the extremely large differences in molecular weight and possibly also the amounts of added stabilizer may enforce a heterogeneous distribution to be the thermodynamically stable one if no strong molecular interactions exist between the polymer and the stabilizer [5]. In the first and main part of this article it is shown that solid state NMR can be used to gain information on the molecular symmetry of three stabilizers: Irganox1010, Irgafos168 and a blend of these two (IrganoxB225). To this aim the ^{13}C solution spectra of these stabilizers have been measured and assigned first. Secondly, the ^{13}C cross-polarization magic angle spinning (CPMAS) spectra of the three pure stabilizers are measured. Differences in the crystalline modifications of the Irganox1010 are observed to affect the CPMAS spectra dramatically. One of these modifications is studied in more detail because the large amount of peaks in the CPMAS spectrum complicates the interpretation to such an extent that additional experiments were necessary. X-Ray powder diffractometry is furthermore used to supply additional information on the crystalline structure. In the last part of this article an example is presented in which a stabilizer (Zn/Ca stearate) is studied in a polymer matrix (PVC). By studying the $T_{1\rho}(^1H)$ relaxation time of the stabilizer and of the polymer matrix, questions concerning the molecular heterogeneity/homogeneity of the stabilizer in the polymer could be addressed.

EXPERIMENTAL

The ^{13}C solution spectra have been obtained with a Varian UNITY 300 using 90° pulses of 8.7 μs and a waiting time of 5 s between the pulses. All samples were dissolved in $C_2D_2Cl_4$ and measured at room temperature. Solid state ^{13}C NMR spectra have been obtained with a Bruker CXP200 NMR spectrometer using ^{13}C 90° pulses of 4.25 μs. All spectra were acquired by using cross-polarization with protons and a magic angle spinning frequency varying between about 2500 to 3500 Hz. In one of the measurements the ^{13}C signal intensity as a function of the cross-polarization period (τ, see Fig. 1a) is measured in order to discriminate protonated carbons from non-protonated ones [6]. Since resonances arising from protonated carbons usually acquire signal intensity much faster than those originating from quaternary carbons, the signal growth rate (T_{CH}) can

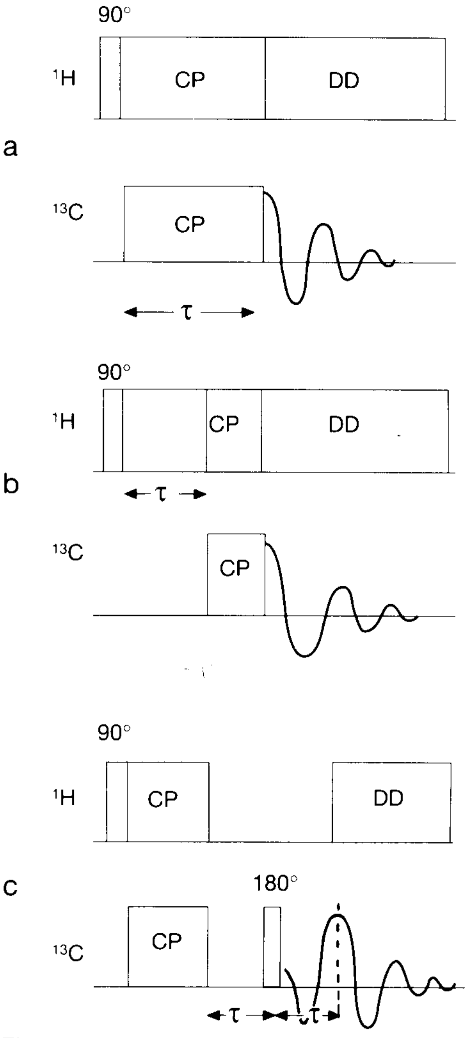

Fig. 1. Pulse sequences used in this study. Cross-polarization sequence. Pulse sequence to selectively detect quaternary carbons whereas the sequence in (c) is used to perform a $T_{1\rho}(^1H)$ experiment.

be used as an aid for the assignment of resonances. For $T_{1\rho}(^1H)$ measurements a proton spin-lock pulse of variable length with an ω_1 field of 60 KHz and a fixed cross polarization time of 1 ms is used, see Fig. 1b. In Fig. 1c a dipolar dephasing pulse sequence is shown, which is used to identify quaternary carbons [7] in spectra from crystalline solids. After a fixed cross-polarization period the signals from the protonated carbons dephase within some tens of μs in the absence of proton decoupling whereas the signals arising from quarternary carbons remain for a longer time. After a sufficiently long dephasing period a 180° refocussing puls is used before the spectrum of the quarternary carbons is acquired.

The x-ray diffractograms were recorded on a Philips PW1820 diffractometer using Cu-K_α (λ = 1.5418 Å). The diffractometer is equipped with Soller slits in the primary beam and a graphite monochromator in the reflected beam. The samples were applied as a very thin layer to a specially cut silicon single crystal. In this way, transparency errors are minimized without introducing any additional background scattering. The density of some of the samples was determined by a helium pycnometer (Micromeretics, AccuPyc 1330).

Samples

The stabilizers discussed in the article were obtained from Ciba-Geigy, Mitsui and Harcros Chemicals and are summarized in Table 1. The use of systematic names of the additives is avoided in the following for reasons of simplicity. Instead, the phenolic antioxidant and the phosphite are referred to by trade names such as Irganox and Irgafos. Unless otherwise stated, all samples measured are crystalline. As concerning the Irganox1010, two different crystalline powders are studied, referred to as powder A, which has been obtained from Mitsui Petrochemical Industries, and powder B, which has been supplied by Ciba-Geigy.

Since commercial stearates are often 'poluted' with a relatively high amount of palmitate the purity of the stearate was determined by means of mass spectroscopy (GC–MS with a Carlo Erba gas chromatograph connected to a Cratos MS80 mass spectrometer). The stearate used in this study was found to contain about 60% palmitate, 40% of stearate and a very small amount of myristate (about 1%).

TABLE 1

Chemical structure of the stabilizers studied

Irganox1010

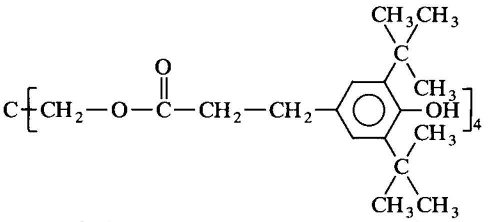

Tetrakis[3-(3,5-di-*tert.*-butyl-4-hydroxyphenyl)-propionyloxymethyl]methane

Irgafos168

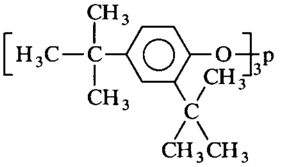

Tris(2,4-di-*tert.*-butylphenyl)phosphite

Zn stearate and Ca stearate

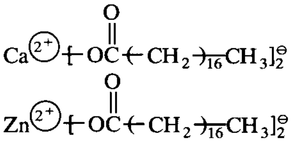

$$\mathrm{Ca^{2+}[-O\overset{\overset{O}{\|}}{C}-(CH_2)_{16}CH_3]_2^{\ominus}}$$

$$\mathrm{Zn^{2+}[-O\overset{\overset{O}{\|}}{C}-(CH_2)_{16}CH_3]_2^{\ominus}}$$

The PVC film containing Ca/Zn stearate was prepared by dissolving 100 g PVC in a THF solution which was stirred for 2 h at room temperature. Subsequently, 5 g of Ca-stearate and 3 g of Zn-stearate were added and after 15 min of stirring at room temperature the solution was cast on a glas plate. The film thus obtained was dried at 40°C for 60 h.

RESULTS

The ^{13}C solution NMR spectra of the Irganox1010 and Irgafos168 are shown in Fig. 2. All resonances in the solution spectra could be straightforwardly assigned on the basis of shift additivity rules [8] in combination with related

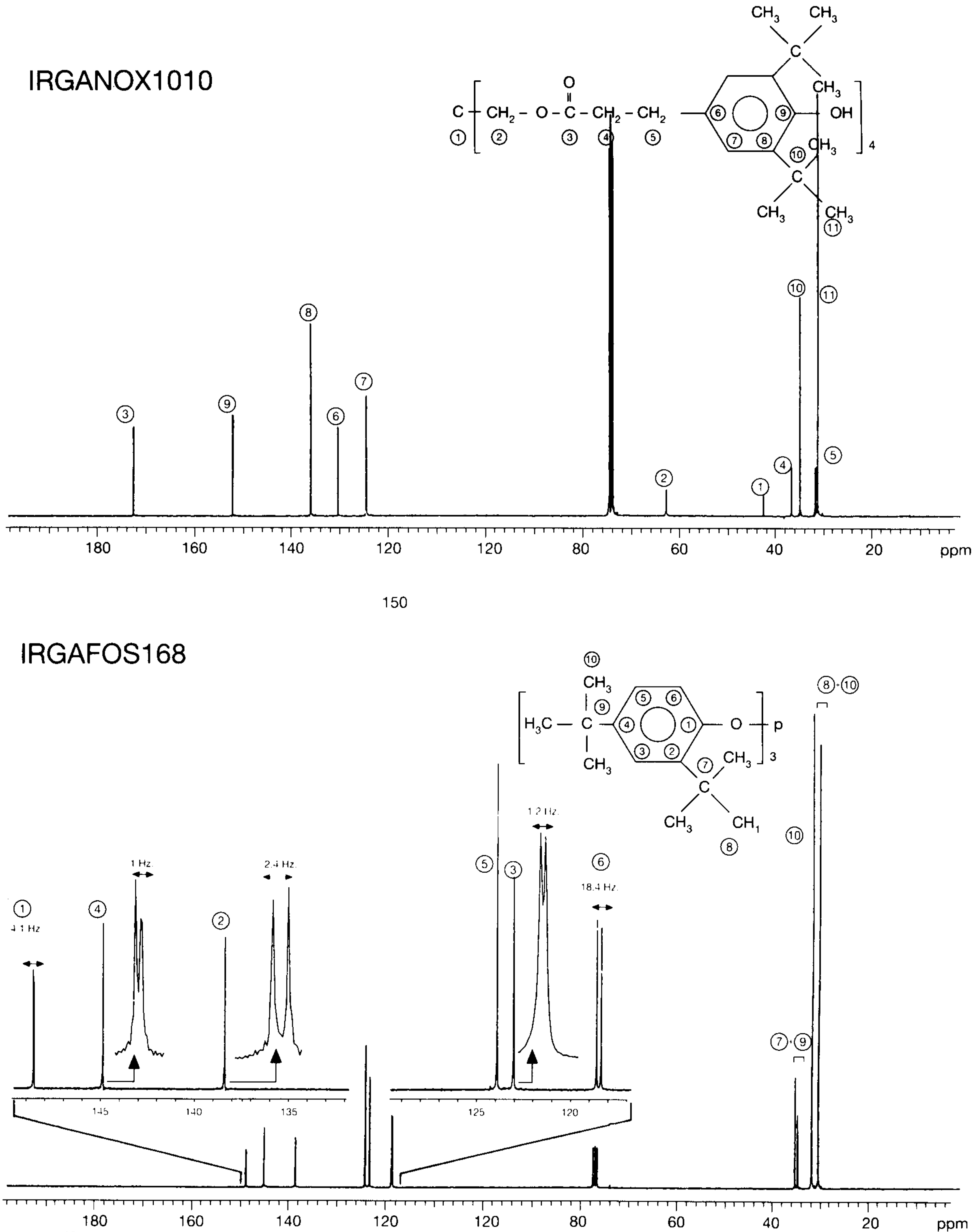

Fig. 2. ^{13}C solution spectra of Irganox1010 (top) and Irgafos168 (bottom). The molecular structure of the two stabilizers is graphically represented in the insets of the two spectra. The assignments of the different resonance peaks are indicated by numbers which correlate the different carbon atoms in the two molecules with the observed resonances.

spectra [9] and the relative intensity ratios of the resonances. The relative intensity ratios are thereby used in a qualitative way in view of possible differences in relaxation times and linewidths of the different resonances. The possible assignments of the differently numbered resonances are indicated in the insets of the spectra. In the spectrum of Irgafos168 a clear splitting of nearly all aromatic resonances into two peaks of about equal intensity is apparent. For the resonances originating from the two tertiary butyl groups on the other hand no such splitting can be detected. The observed splittings in the aromatic region, which vary between 1 and 18 Hz, can most probably be attributed to scalar coupling with the central ^{31}P nucleus. The solid state (CPMAS) spectrum of the Irgafos168 is reproduced in Fig. 3a. On first sight it appears more complex, especially in the tertiary butyl region, than its corresponding solution spectrum. On closer inspection it is seen that most chemically identical carbons in the aromatic as well as in the tertiary butyl region result in a pair of peaks with splittings far exceeding (15–50 Hz) those observed in the solution spectrum. The pairwise organization of the resonances in the tertiary butyl region of the CPMAS spectrum is clearly opposed to the absence of splitting due to scalar coupling in the solution spectrum of this region. The intensity ratio between the two resonances within each pair, apart from those near 125 and 150 ppm, furthermore seems about 1:2. These observations suggest that the relatively large splittings in the CPMAS spectrum in Fig. 3a do not originate from the scalar coupling with the ^{31}P but merely result from the fact that the molecules are situated in a crystalline surrounding. However, the apparently dominant splitting caused by the crystalline surrounding does not necessarily imply that the effect of scalar coupling will be obscured. In fact, in addition to the splitting caused by crystalline surrounding there seems some indication of scalar coupling between ^{31}P and two of the aromatic carbons. The carbons concerned are exactly those which in the corresponding solution spectrum show the largest spin-spin splittings (18 and 4 Hz at respectively 118.5 and 148.5 ppm). In the CPMAS spectrum these resonances are split up into four peaks (near 150 ppm) or appear as two relatively broad peaks (120 ppm). The observed intensity ratio of the four signals near 150 ppm is about 2:2:1:1. Since the signals heavily overlap each other a precise determination of this scalar 'fine-splitting' is difficult. A rough estimation of the splitting between the two intense as well as the two weaker shoulders is 10 Hz, which agrees in order of magnitude with that observed in the solution spectrum [a].

The relative broadness of the two resonances near 120 ppm could furthermore also originate from the overlap of signals by the combined effect of scalar coupling and the crystalline surrounding. For a more detailed discussion of the effect of the crystalline surrounding the reader is referred to the Discussion but here it is already concluded that the large splittings observed in the solid state spectrum are related to the crystalline structure. The additional splitting of the resonances from the *ipso* position and possibly also the broadening of the resonances from the unsubstituted *ortho* position are caused by the scalar coupling with the central ^{31}P nucleus.

The CPMAS NMR spectrum from Irganox-B225, which is a 50:50 mixture of Irganox1010 and Irgafos168, is shown in Fig. 3b. By comparing the spectrum of Irganox B225 with that of the pure Irgafos168 spectrum, the amount of peaks as well as the peak positions of the pure Irgafos168 can clearly be observed in the Irganox B225 spectrum. This not only indicates the spectra from the pure Irgafos and the Irgafos compound in the mixture to be identical but also points to a very limited overlap between the Irganox1010 spectrum with that of Irgafos168.

The third antioxidant to be studied in the solid state is the pure Irganox1010. From literature

---

[a] *Note.* From the spectrum of a very recent ^{13}C CPMAS experiment at a much higher radio frequency, 125.7 MHz, only two partially overlapping peaks could be observed without any 'fine splitting'. The distance between these two peaks (0.5 ppm) corresponds well with the distance between the average of the two higher intensity peaks and the average of the two weaker shoulders in the spectrum obtained at 50.3 MHz (0.4 ppm). This proves that the 'fine spliting' indeed originates from coupling with the central ^{31}P atom.

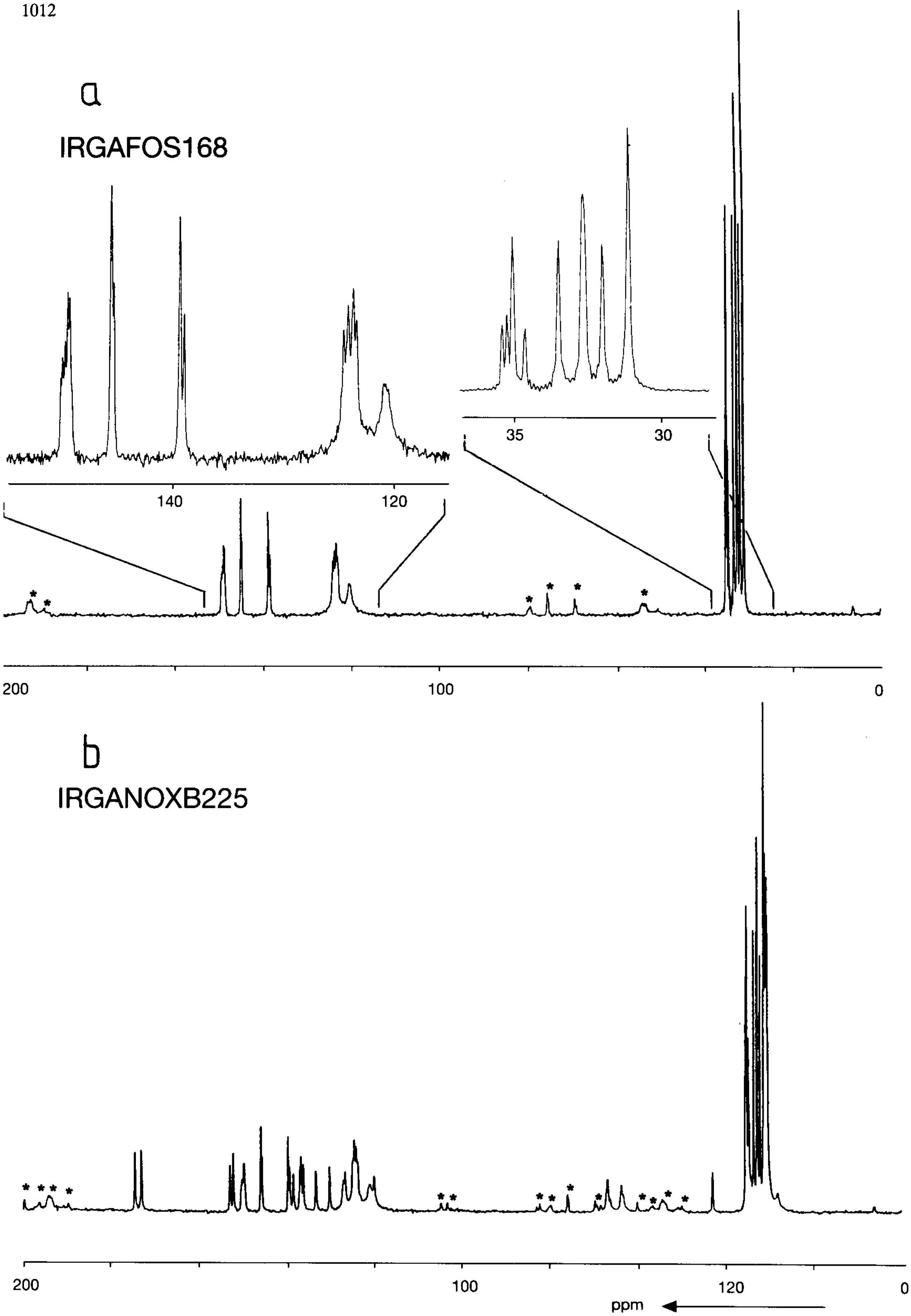

Fig. 3. ^{13}C CPMAS spectra of Irgafos168 (a) and IrganoxB225 (b). Both spectra are acquired with a waiting time of 10 s, a 1 ms contact time and a spinning frequency of 3500 Hz. The spinning sidebands are indicated by asterisks.

[1–4] it is known that Irganox1010 can not only be obtained as purely amorphous but can also exhibit several crystalline structures. The amorphous phase is reported to be relatively stable at ambient temperature because the glass transition temperature of this material is at about 45–50°C. The stability of the amorphous phase made it possible to measure an amorphous sample in addition. The amorphous Irganox1010 was prepared by fast cooling (immersing in liquid nitrogen) of an Irganox1010 melt at 150°C. Apart from the amorphous Irganox1010, two different crystalline samples (A and B) were measured. In Fig. 4b, c and e the spectra of resp. the amorphous and the two crystalline powders are reproduced. The spectrum in Fig. 4a is a solution spectrum of the Irganox1010 and is added for comparison. Upon dissolving the three Irganox1010 powders in $C_2D_2Cl_4$, spectra agreeing in detail with the one reproduced in Fig. 4a were obtained which verifies the identical chemical structure of the three samples.

The CPMAS spectrum of the amorphous Irganox1010 exhibits broad resonance peaks. The positions of the observed resonances roughly match those observed in the solution spectrum.

From the two crystalline powders (Fig. 4c and e) the spectrum of powder A (Fig. 4c) most closely resembles the solution spectrum regarding the amplitude and spectral position of observed resonances. A clear difference however can be detected in the aromatic region where six instead of four resonances are observed. The amount of peaks originating from the aliphatic carbons and from the quaternary carbon in the centre of the molecule is furthermore equal to that observed in the solution spectrum. The assignments of the different peaks are tabulated in Table 2.

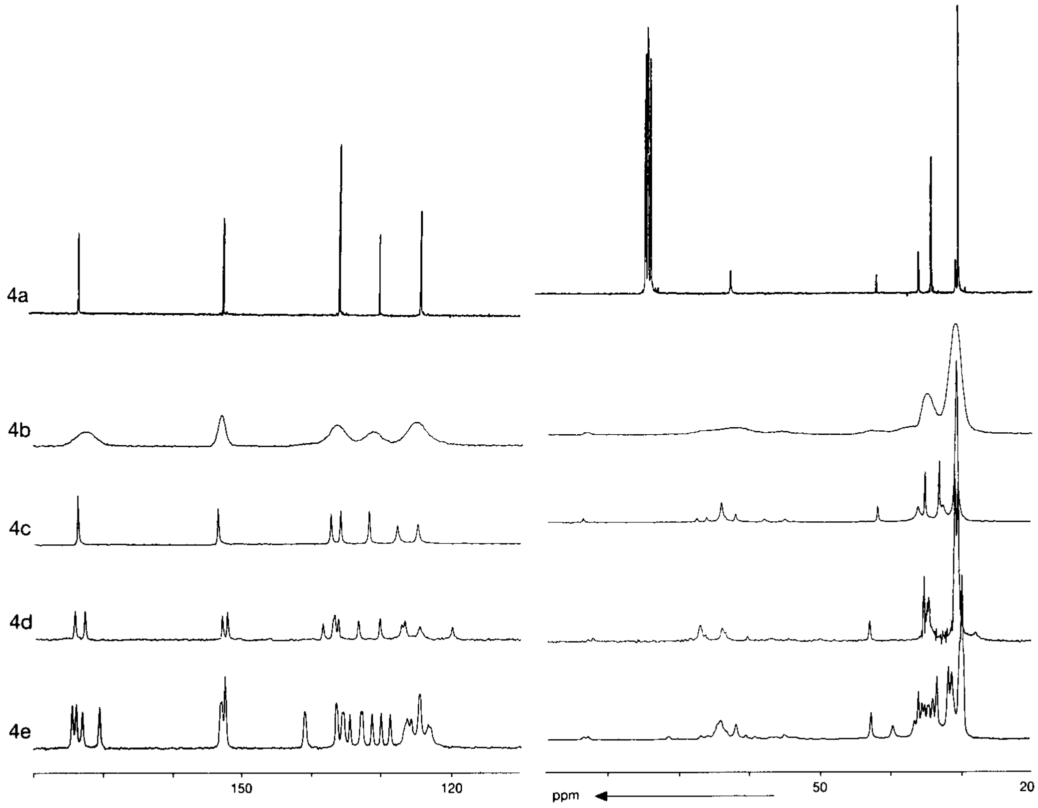

Fig. 4. ^{13}C CPMAS spectra of Irganox1010. (a) Solution spectrum shown for comparison. (b) CPMAS spectrum of amorphous Irganox1010. The ^{13}C CPMAS spectra of three crystalline structures are plotted in (c) structure A, (d) Irganox1010 component in the IrganoxB225 blend and (e) structure B.

The CPMAS spectrum of the crystalline B powder (Fig. 4e) is seriously more complex than that of powder A. The large number of (partially overlapping) peaks in spectrum B clearly complicates the assignment of a number of resonances in this spectrum. Still, important information can be obtained from this spectrum such as the assignment of the four peaks in the isolated 170–175 ppm region to carbonyls. Further "multiplicities" can be observed for the phenolic carbon atom (three peaks of which one has twice the intensity of the other two) and for the carbon neighboring the central quaternary carbon (three peaks, two of which seriously overlap with each other). The number of peaks originating from the quarternary carbon itself can be less easily determined. From the spectrum in Fig. 4e alone it is not clear whether the central quaternary carbon gives rise to two signals (at 42.7 and 39.5 ppm) or only one (at 42.7 ppm), because the peak at 39.5 ppm could also originate from the aliphatic carbon resonating at about 36 ppm in the liquid state NMR spectrum.

In order to further unravel the overcrowded CPMAS spectrum in Fig. 4e two selective measurements are carried out. In the first measurement, signals from quaternary carbons are selectively made visible by using the dipolar dephasing pulse sequence as shown in Fig. 1c [7]. In Fig. 5 a spectrum is reproduced with a delay time of 60 μs between the cross polarization time and the 180° puls. A first observation is that the 42.7 ppm peak is still present but the 39.5 ppm peak is not, which indicates that only the 42.7 ppm peak arises from the quaternary carbon in the centre of the Irganox molecule. The quaternary carbons of the tertiary butyl groups furthermore give rise to at least seven resonances in the 33–36 ppm region. The amount of signals arising from the other quaternary carbons, resonating at about

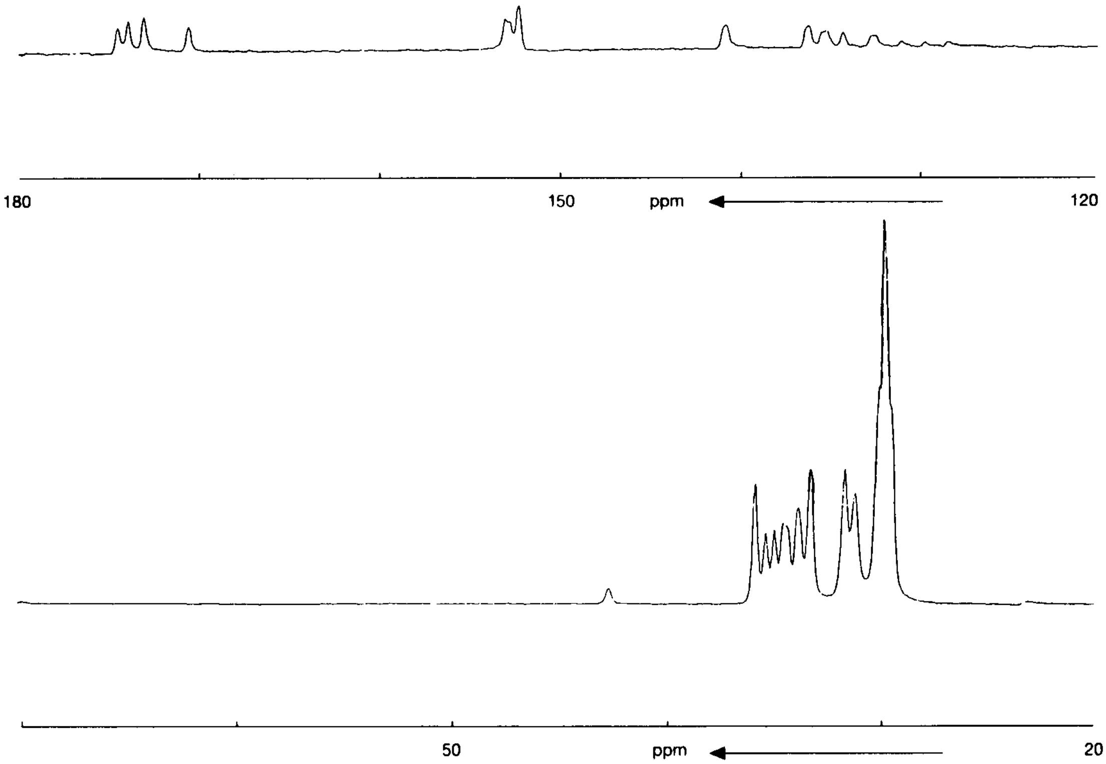

Fig. 5. Dipolar dephasing spectrum of the Irganox1010 B structure. The cross-polarization time used is 1 ms and the total delay time without proton decoupling amounts to 120 μs.

170 ppm, 150 ppm and 135 ppm, all agree with four resonances for each peak observed in the solution spectrum. The assignments of the resonance positions to the different quaternary carbons are tabulated in Table 2. In the second experiment, the cross-polarization time in a CP-MAS experiment is varied to discriminate resonances originating from protonated carbons from those arising from quaternary carbons. Fig. 6 shows spectra as a function of cross-polarization time. The intensities of all resonances remain practically constant from 1.5 to 5 ms contact time, suggesting $T_{1\rho}(^1H)$ decay rates which are relatively slow as compared to the T_{CH} values. Since protonated carbons acquire signal intensity much faster than quaternary carbons, the apparent signal growth rate (T_{CH}) of the different carbons was determined by fitting the observed signal intensities to the equation: $H(t_m) = A(1 - \exp(-(t_m)/T_{CH})$. In this equation $H(t_m)$ repre-

TABLE 2

Assignments of resonances in the ^{13}C CPMAS spectra of the three different crystalline modifications of the Irganox1010. Each tabulated T_{CH} value represents an average over the different resonances of each chemically identical carbon atom. The T_{CH} values of resonances exhibiting overlap with resonances originating from chemically different carbons are not taken into account for the table

Sample	Carbon No.	Resonance position(s) (ppm)	T_{CH}(μs)
A	1	41.9	
	2	63.9	
	3	173.6	
	4	36.2	
	5	32.7 (?)	
	6	131.6	
	7	127.7, 124.7	
	8	135.7, 137.2	
	9	153.3	
	10	33.1, 35.2	
	11	30.9	
Mixture	1	43.0	
	2	63.8, 67.0	
	3	172.7, 174.2	
	4	35.2, 35.4	
	5	(?)	
	6	129.9, 133.0	
	7	119.8, 124.2, 126.4, 126.9	
	8	135.9, 136.5, 136.7, 138.2	
	9	151.8, 152.6	
	10	34.6, 34.8, 35.0	
	11	30.5, 31.0	
B	1	42.7	175 ± 30
	2	61.6, 63.8, 64.2	43 ± 10
	3	170.5, 173.0, 173.9, 174.4	390 ± 70
	4	35.5, 36.5, 39.6	43 ± 10
	5	29.9, 31.0, 31.7, 32.7	290 ± 70
	6	128.5, 129.9, 131.0, 132.6	53 ± 10
	7	122.9, 123.3, 124.4, 125.6, 126.2, 126.5	53 ± 12
	8	132.9, 134.5, 135.4, 135.6, 136.5, 141.1	520 ± 70
	9	152.3, 152.8, 153.0	510 ± 70
	10	33.3, 33.9, 34.4, 34.6, 35.0, 35.3, 35.9	
	11	29.8, 29.9, 30.2, 31.1, 31.7	

sents the intensity of a peak and t_m the cross-polarization time. The constant A and the T_{CH} value are least-squares adjusted. The equation assumes the T_{CH} to be much smaller than $T_{1\rho}(^1H)$ and $T_{1\rho}(^{13}C)$, the proton and carbon rotating frame relaxation times [6]. The above equation is used in a least-squares fit procedure for all non-overlapping peaks.

The adjusted T_{CH} values showed only minor differences for the different resonances of each chemically identical carbon. For this reason, only the averaged values for each type of carbon is presented. The T_{CH} value of the 42.7 ppm peak is substantially larger (180 μs) than that of the 39.7 ppm peak (43 μs) which again points to the proton bearing nature of the 39.7 ppm peak. On the basis of the T_{CH} values and the spectra at the very short cross-polarization times, a number of peaks arising from protonated carbons could be assigned and their chemical shifts are added to Table 2. A final remark concerns the behavior of the three methyl groups. Although proton bearing in nature, they exhibit a long dipolar dephasing time and a very slow T_{CH} time. This clear deviation from the normal behavior is probably due to their fast motion which tend to average out the heteronuclear dipolar interaction. In concluding the experiments on powder B the following can be said. By comparing the results obtained from powder B with those of powder A (Table 2) it is concluded that for each single resonance detected in powder A, four resonances appear in the spectrum of powder B. The fact that not always four (or eight) resonances are actually observed is assumed to be due to 'accidental overlap'. The only exception is the quaternary carbon for which only one peak is observed.

The profound differences in the Irganox1010 CPMAS spectra of the two crystalline powders made us inquisitive about the spectrum of the Irganox1010 component in the IrganoxB225 mixture (Fig. 3b). Because the spectra of the pure

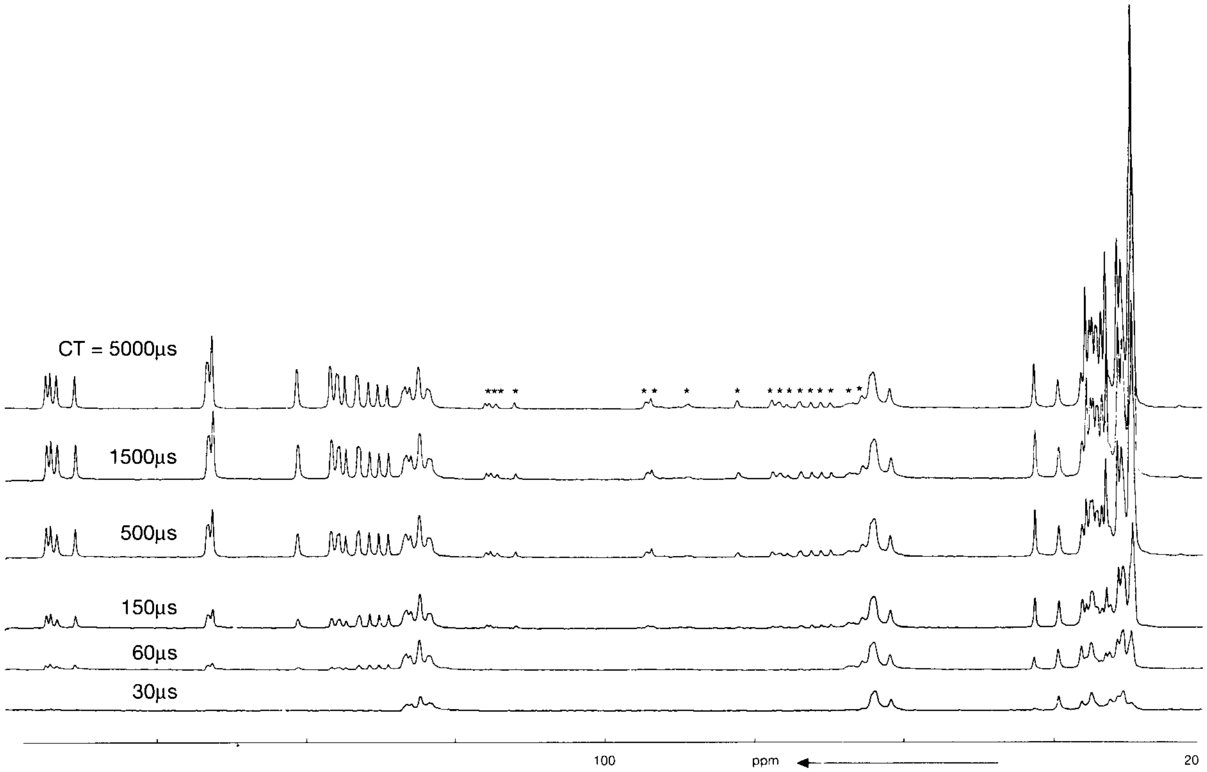

Fig. 6. ^{13}C CPMAS spectra as a function of cross-polarization time. In the reproduced spectra the contact time varies between 30 μs in the spectrum at the bottom to 5000 μs for the upper spectrum.

Irgafos168 and that of the Irgafos168 component in the mixture are very probably identical, it was tried to obtain the spectrum of the Irganox1010 component by means of spectral subtraction using the Irgafos spectrum in Fig. 3a. In the resulting difference spectrum in Fig. 4d no indication is

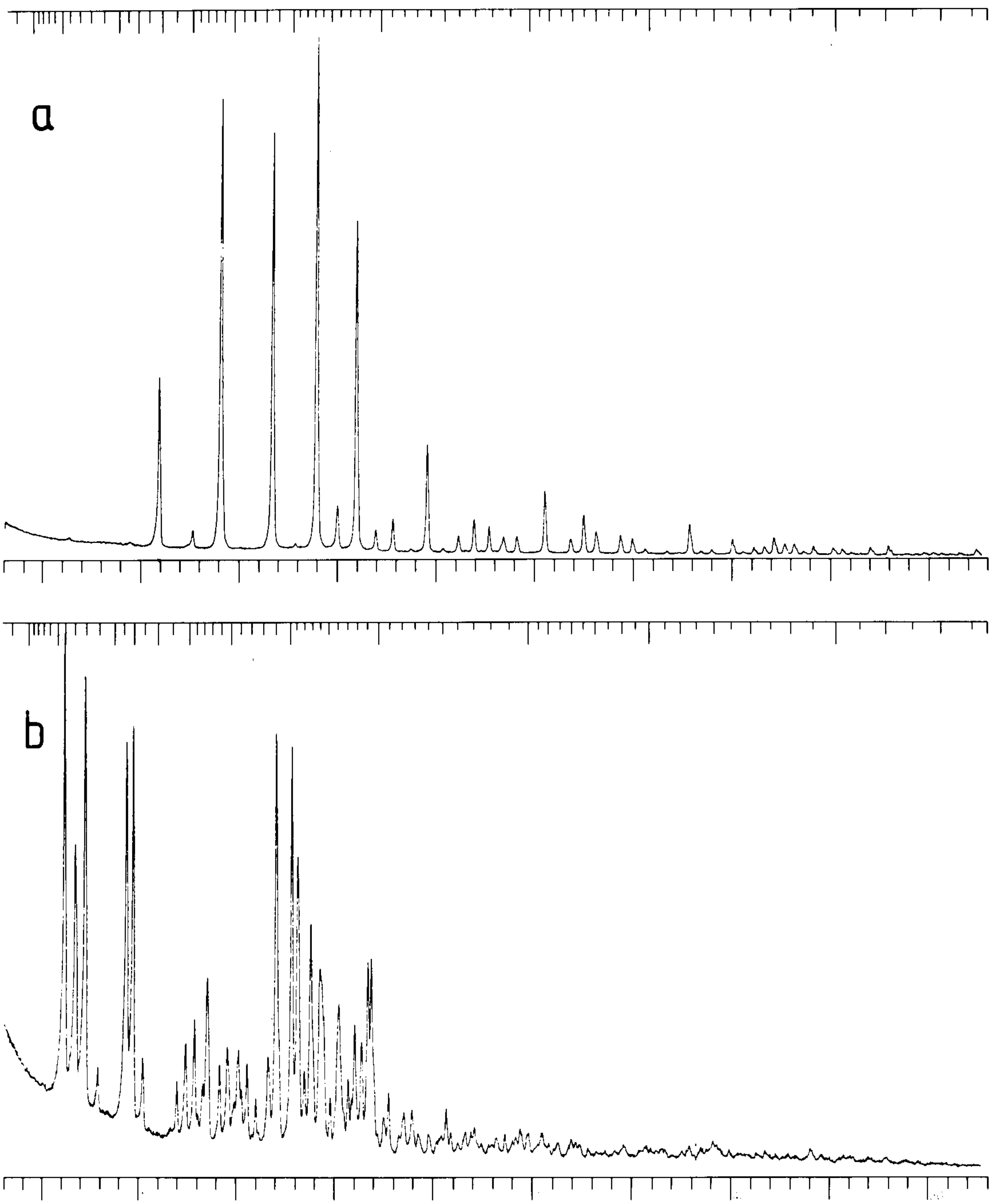

Fig. 7. X-Ray powder diffractograms. (a) Diffractogram of powder A. (b) Diffractogram of sample B.

found of a possible spectral mismatch between the Irgafos168 component in the mixture and the Irgafos168 spectrum which was used for the spectral subtraction (Fig. 3a). The difference spectrum does not match (part of) the Irganox1010 spectra of the A or B powders (Fig. 4c and e). If we compare the spectrum in Fig. 4d with the Irganox1010 spectrum of powder A it is seen that for nearly each single resonance in the spectrum of powder A, two resonances with equal intensity appear in the Irganox1010 spectrum obtained from the mixture. A clear exception is the quaternary carbon at the centre of the molecule, which appears again as a single resonance. All resonances could be assigned and are tabulated in Table 2.

In order to obtain additional information about the different crystalline structures of the Irganox1010, x-ray powder diffractograms were recorded. Diffractograms of samples A and B are given in Fig. 7a and b, respectively. The most striking difference between the diffractograms is the much larger number of reflections observed for sample B. This immediately suggests that the crystal structure of sample A is of much higher symmetry than that of sample B. Werner's TREOR program [10] was used to try and index both patterns using the first 20 observed reflections. For sample A two alternative unit cells explaining all but the very weak reflection at $2\theta = 9.45°$ are indexed. Both unit cells are of tetragonal symmetry with cell dimensions $a = 13.995$Å and $c = 9.886$Å (cell I) and $a = 19.778$Å and $c = 8.836$Å (cell II), respectively. For both unit cells a special relation exists between the a and c dimensions. For the first unit cell the a-axis is $\sqrt{2}$ as long as the

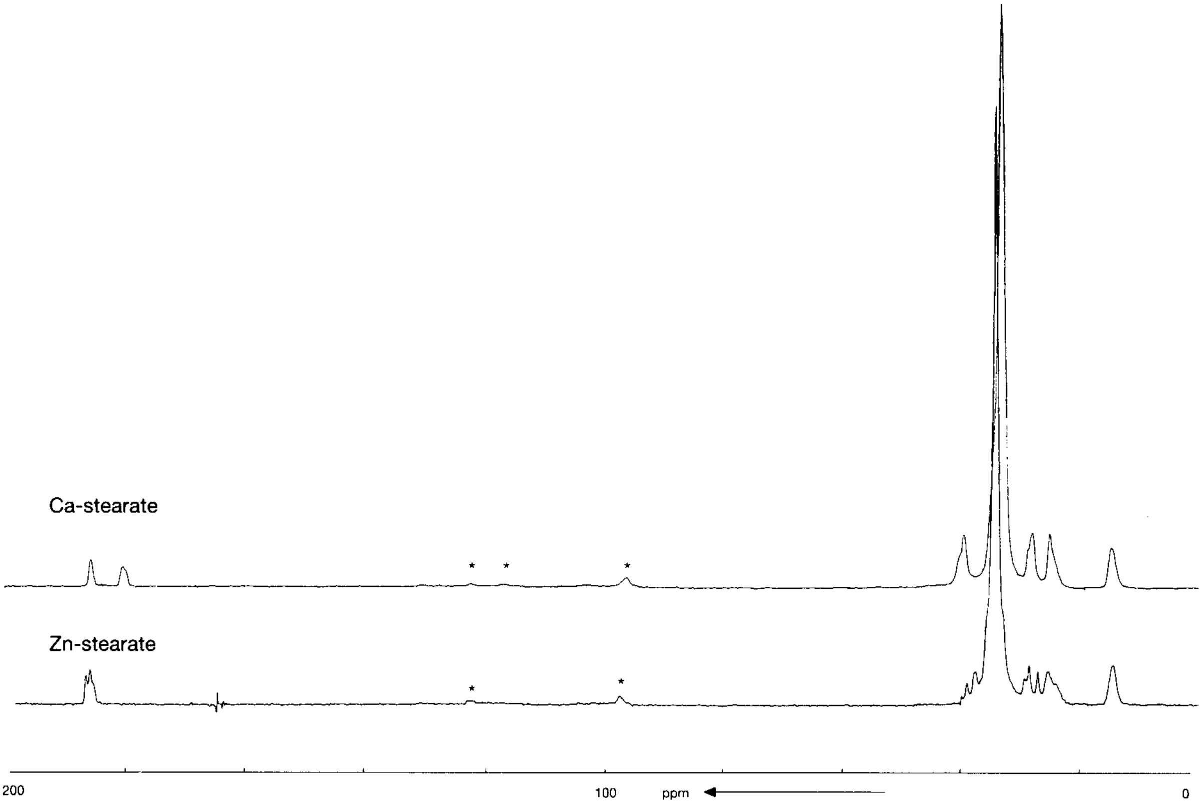

Fig. 8. ^{13}C CPMAS spectra of Zn stearate and Ca stearate.

c-axis. For the second unit cell the ratio is $\sqrt{5}$. These special relations will cause significant overlap of a large number of reflections. No satisfying solutions for the unit cell were found for sample B.

The last part of this section is devoted to the use of solid state NMR to probe the molecular homogeneity/heterogeneity of a Zn/Ca stearate in a PVC matrix by means of $T_{1\rho}(^1H)$ measurements with ^{13}C detection via cross-polarization. The ^{13}C CPMAS spectra of the pure Zn and Ca stearates are shown in Fig. 8. Both spectra show at least three resonances in the carbonyl region.

This suggests that there are at least three inequivalent ester groups in both crystalline powders, possibly related to the different crystalline structures possible in both stearates [11,12]. As a first step for detecting whether or not the Zn/Ca stearate is molecularly dissolved in the PVC matrix, $T_{1\rho}(^1H)$ relaxation times of the pure components were determined (pure PVC from THF and a physical mixture of Zn stearate and Ca stearate). All measured relaxations were least-squares adjusted assuming a single exponential decrease in peak intensities. All peaks from the stearate exhibit, within experimental error, an identical $T_{1\rho}(^1H)$ relaxation time. The resulting values of the two different pure components are tabulated in Table 3. Subsequently, the $T_{1\rho}(^1H)$ relaxation of a PVC film containing the Zn and Ca stearates obtained from a THF solution was measured. The ^{13}C spectra as a function of proton spin-lock time are reproduced in Fig. 9. In this figure the resonances from the Zn and Ca stearates, as

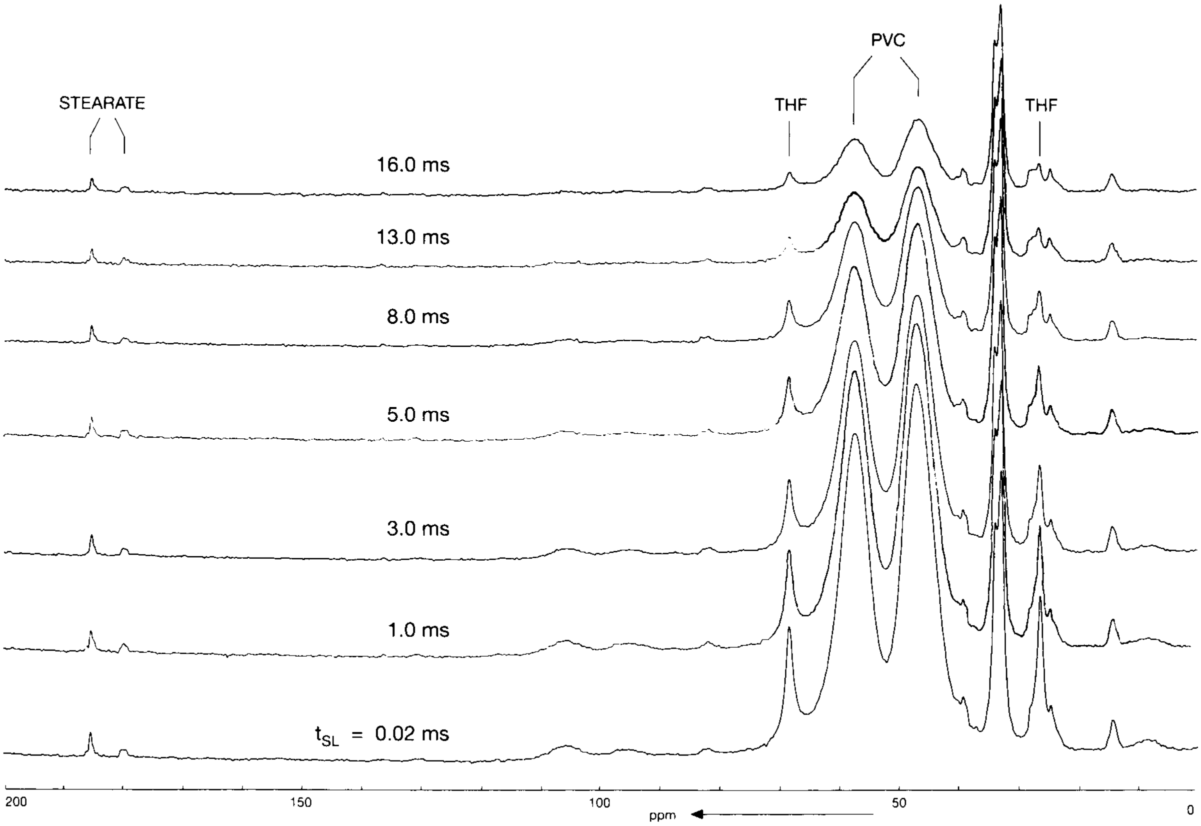

Fig. 9. ^{13}C CPMAS spectra as a function of proton spin-lock time. The proton spin-lock time is varied from 0.02 ms in the spectrum at the bottom to 16.0 ms in the upper spectrum.

observed in Fig. 8, are clearly seen. Beside the resonances originating from the PVC and the Zn/Ca stearate, there are two strong additional signals at 68 and 27 ppm. The chemical shift positions of these peaks agree with those of THF [9] indicating the presence of residual THF in the film. In Fig. 10 the heights of the different peaks are plotted as a function of the proton spin lock time. The least squares adjusted $T_{1\rho}(^1H)$ values of the different peaks are added in Table 3. The $T_{1\rho}(^1H)$ values of the different components are seen to be identical to their pure components.

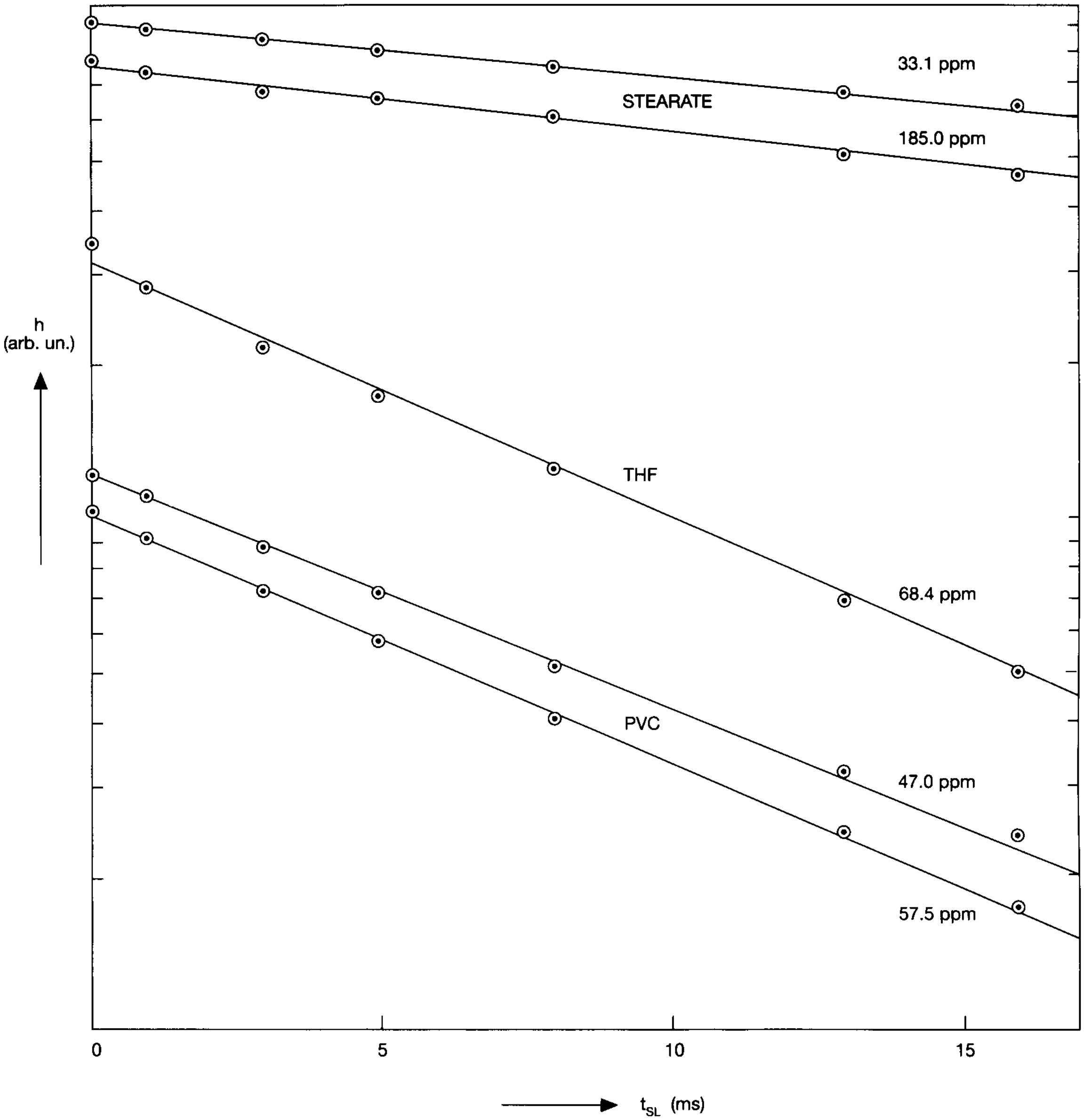

Fig. 10. Heigths of different resonances originating from PVC, Zn/Ca stearate and THF as a function of spin-lock time.

TABLE 3

Least-squares adjusted $T_{1\rho}(^1H)$ values for pure Ca stearate, Zn stearate, PVC film and the PVC film containing the two stearates

	$T_{1\rho}(^1H)$
Zn/Ca stearate	45 ±5
PVC film pure	8.7±0.5
PVC film containing stearates	
PVC	9.3±0.4
Stearate	42 ±5
THF	9.1±0.5

The peaks originating from the residual THF, however exhibit a relaxation time identical to that of the PVC matrix.

DISCUSSION

The NMR spectra of all crystalline stabilizers measured show a strong influence of the crystalline surrounding on resonance positions. The narrowness of the different resonances furthermore allows identification and/or interpretation of these spectra in great detail.

It is generally known [13] that molecular positions which are equivalent to one another in solution can lead to several signals in the solid state when molecules are situated at non-equivalent positions within a crystal or if the symmetry of the crystal is less than that of the molecule.

For the Irgafos168 all resonances are doubled as compared with the ^{13}C solution spectrum which indicates that the nuclei which are equivalent in solution, have lost their equivalence in the crystalline lattice. Although great care has to be taken to quantitatively interpret cross-polarization spectra in general, it is remarkable that most of the resulting two signals appear with an intensity ratio of 1:2. Regarding the molecular structure of the Irgafos168, in which three aromatic rings are connected to a central phosphorus nucleus, the highest attainable symmetry could be

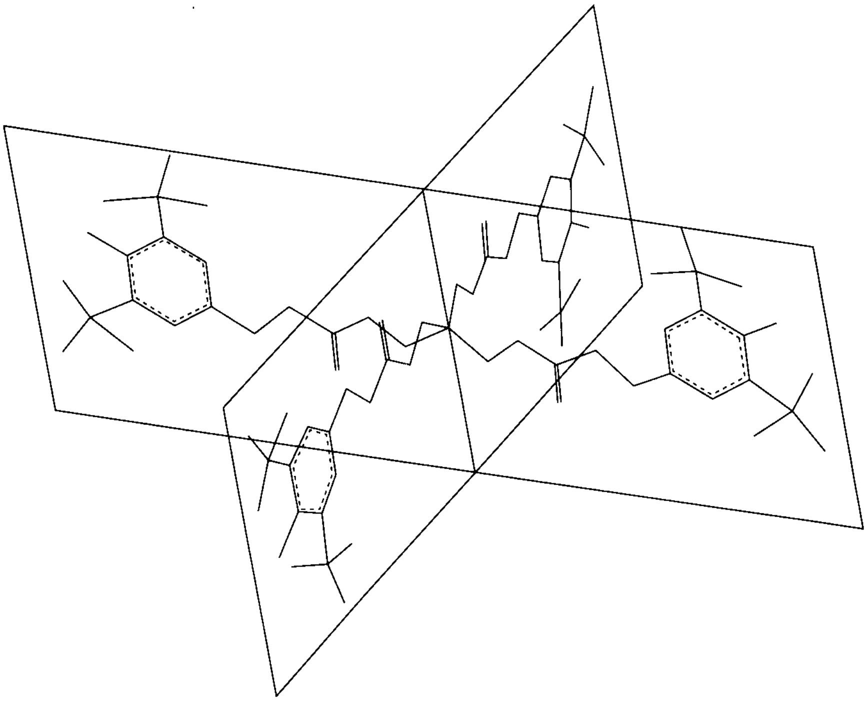

Fig. 11. Representation of the structure of the Irganox1010 molecule. In this figure the branches are situated in two perpendicular reflection planes and the symmetry of the molecule is assumed to be D_{2d}.

C_{3v} The observations either suggest two non-equivalent sites in the unit cell or they may point to a reduction of the molecular symmetry due to the crystal field. In the latter case the remaining symmetry is C_s with a σ reflection plane as the only remaining symmetry element. The measured intensity ratio within the different pairs of the signals are in support of this possibility. In order to draw a more definite conclusion about the number of non-equivalent molecules in the unit cell we are planning future ^{31}P MAS NMR experiments.

The large differences in the NMR spectra of the Irganox1010 powders are very interesting since they reflect the effective symmetry of the Irganox1010 molecule in a certain crystalline surrounding. The spectrum also reflects the existence of an amorphous surrounding by exhibiting broad resonances, possibly arising from a distribution of local surroundings of the Irganox1010 molecule on the timescale of the NMR experiment. The amorphous Irganox1010 shows a spectrum which exhibits an amount of resonances equal to that observed in the solution spectrum.

The Irganox1010 molecule has four chemically identical branches containing an ester group and a phenolic ring with two *tert*.-butyl groups attached, see Fig. 11. The measurements on the crystalline samples show that chemically identical carbons participating in the branches can give rise to one or more resonances but that the central quaternary carbon in all cases results in only one resonance. It could be argued that this central carbon experiences serious shielding from the crystal field by the four branches. However, the average splittings, which can be directly derived from the resonances positions tabulated in Table 2, do not show a decreasing order towards the interior of the molecule. Instead, they vary apparently random in the range 0.2–1.5 ppm. Moreover, the one central carbon, exhibiting an experimental linewidth which is even smaller than a number of other resonances (Fig. 4) does not show any indication of overlap. The occurrence of only one central carbon resonance indicates that the multiplicity of the other carbon signals does not originate from polycrystallinity. It secondly shows that in all measured crystalline powders only one type of crystal site is present in the unit cells. In other words, if there is more than one molecule in the unit cell they must all be symmetry related. It thirdly indicates that the (in)equivalence of the four branches is caused by the effect of the crystal field.

Before discussing the different crystalline structures in some more detail let us speculate about the highest possible molecular symmetry of the Irganox1010 molecule (see Fig. 11). The highest symmetry would be attained if the four branches would be situated in two perpendicular reflection planes whereas the branches in the refection planes would be symmetry related by a four-fold inproper rotational operation and by a two-fold axis bisecting the two reflection planes. The symmetry group can furthermore not contain a three-fold rotational axis because of the carbonyl and the aromatic ring. The highest attainable symmetry would thus be D_{2d}. In the presence of a crystalline surrounding a reduction of symmetry would follow the scheme:

$$\begin{tikzcd}
 & D_2 \arrow[dr] & & \\
D_{2d} \arrow[ur] \arrow[r] \arrow[dr] & S_4 \arrow[r] & C_2 \arrow[r] & C_1 \\
 & C_{2v} \arrow[r] \arrow[ur] & C_s \arrow[ur] &
\end{tikzcd}$$

In D_{2d}, D_2 and S_4 symmetry, all branches are observed to be equivalent in NMR. A $C_{2(v)}$ symmetry would be present if the branches are observed to be only pair wise equivalent whereas in a C_s symmetry only two out of four branches would be equivalent. A C_1 symmetry finally indicates all four branches to be inequivalent to each other.

In the spectrum of the Irganox1010 powder A (Fig. 2c) all chemically equivalent, non-aromatic resonances appear equivalent whereas the aromatic ring is observed to result in six resonance peaks instead of four as in the solution spectrum. The resonance positions of the six resonances clearly suggest a doubling of the signals arising from the *ortho* and *meta* positions. These positions have apparently lost their equivalence in the crystal field of this modification. It is therefore concluded that the four branches of the Irganox1010 molecule in this crystalline structure are equivalent whereas each carbon nucleus in the aromatic ring appears unique. The measured resonance positions are tabulated in Table 2. On the basis of these NMR data in combination with the possible molecular structures of the Irganox1010 molecule the symmetry can be D_{2d}, D_2 or S_4. If the symmetry is D_{2d}, the aromatic rings should lie parallel with or perpendicular to the σ_d reflection planes because in this situation there is no requirement concerning the equivalence of the two ortho and the two *meta* positions in the aromatic ring. In an S_4 or D_2 symmetry on the other hand no symmetry arguments impose the equivalence of these two positions.

From the x-ray powder pattern additional information can be extracted. From the unit cell dimensions found with TREOR and the molar mass which equals 1176 g/mole, the crystal density can be calculated. The densities thus found for cells I and II are 1.009 g/cm^3 and 1.129 g/cm^3 respectively assuming that the number of molecules equals 1 and 2 for cells I and II respectively. The density of powder A was experimentally determined using a helium pycnometer. A value of 1.130 g/cm^3 was found, which proves that unit cell II must be the correct unit cell. To derive the space group several data are available. The NMR data indicate a molecular symmetry in the crystalline field of D_{2d}, D_2 or S_4. They furthermore show that only one type of central quaternary carbon atom is present. Combining these findings with the existence of two molecules per unit cell, which follows from the cell dimensions, only space groups with $Z = 2$ for special positions and $Z = 8$ for general positions are possible options. Of all the spacegroups that fulfill these requirements only those that have special positions with site symmetry D_{2d}, D_2 of S_4 should be considered. All spacegroups with spacegroup symmetry D_{4h} and all centred spacegroups with spacegroup symmetry D_{2d}, D_4 and C_{4h} have 16(4) or 32(8) general (special) positions, which is too much. This leaves us with 8 D_{2d} spacegroups ($P\bar{4}2m$, $P\bar{4}2c$, $P\bar{4}2_1m$, $P\bar{4}2_1c$, $P\bar{4}m2$, $P\bar{4}c2$, $P\bar{4}b2$ and $P\bar{4}n2$), 4 D_4 spacegroups ($P4_122$, $P4_22_12$, $P422$ and $P42_12$), 3 C_{4h} spacegroups ($P4_{2/m}$, $P4/n$ and $P4_{2/n}$) and 1 S_4 spacegroup ($I\bar{4}$) as possible candidates for the spacegroup of sample A. For all these spacegroups all peak positions were calculated and compared with the experimentally observed reflections. All sixteen spacegroups explain all observed reflections, except for the small intensity at $2\theta = 9.45°$. However, $I\bar{4}$ not only explains all observed reflections, it also predicts only two reflections which are not observed in the experimental angular domains, whereas all other spacegroups predict a large number of not observed reflections.

This is due to the fact that $I\bar{4}$ is centred. For a centred spacegroup half of all reflections will be systematically extincted. For all other spacegroups only screw axes or glide planes can cause extinctions, but they will only be few. All other spacegroups predict about twice the amount of observed reflections. This is rather unlikely and therefore $I\bar{4}$ is most probably the actual space group for sample A. The molecular symmetry is therefore S_4.

The NMR spectrum of the Irganox1010 compound in the mixture reflects a lower symmetry than that of powder A. All resonances, except that from the central quarternary carbon at 43 ppm are doubled with respect to the spectrum of powder A. The data indicate the different molecules in the unit cell to be symmetry-related and each molecule to have two inequivalent types of branches in this crystalline structure. These results indicate a symmetry of C_{2v} or C_2. The symmetry cannot be C_s because this would lead to the appearence of three resonances for each chemically identical carbon because there is one reflection plane, making only two out of four branches equivalent. Because of the size and symmetry differences of the Irganox1010 and Irgafos molecule, one would not expect the IrganoxB225 mixture to be a molecularly mixed crystal. Moreover, it would seem very improbable, in view of the sensitivity of the resonance positions as a function of the crystalline field, that the spectrum from the pure Irgafos would be identical to that obtained from the Irgafos in the mixture. It is therefore proposed that two crystalline structures exist in the mixture, one from the Irganox1010 and one from the Irgafos168.

The NMR results from powder B indicate a crystalline structure in which there is only one type of crystal site having four inequivalent branches. We therefore conclude a reduction of molecular symmetry of the Irganox1010 molecule in this crystalline lattice to C1. From the x-ray diffractogram of this powder no quantitative information could be extracted because the attempt to determine the unit cell was not succesful. The large number of reflections, also at small angles, suggests a large unit cell of low symmetry. Such a unit cell requires very accurate data without systematic errors. Although it was attempted to measure the diffractograms as accurately as possible, they might still have been insufficient for a succesful indexation. Qualitatively one can conclude that the x-ray results support the conclusions drawn from the CPMAS NMR experiments which suggest a molecule devoid of any symmetry.

The experiments on the PVC film illustrate the potential of $T_{1\rho}(^1H)$ experiments to investigate whether or not stabilizers are molecularly dissolved in a polymer matrix. Until now, these measurements have been succesfully used to study molecular homogeneity in a number of polymer blends [e.g., 13] but publications on the detection of low molecular additives in polymers have been scarce [14], probably because of signal-to-noise problems. In the experiment the heterogeneity/homogeneity on a nm scale of a blend of two components A and B is detected by measuring the $T_{1\rho}(^1H)$ relaxation of both pure components separately: $T_{1\rho A}(^1H)$ and $T_{1\rho B}(^1H)$ If, after mixing of the two components, there is molecular homogeneity of A and B on a 1–2 nm scale in the blend, a common $T_{1\rho AB}(^1H)$ can be expected. If, on the other hand, there exists heterogeneity on a scale larger than about 50 nm, the two original $T_{1\rho A}(^1H)$ and $T_{1\rho B}(^1H)$ are measured. The tabulated $T_{1\rho}(^1H)$ values (Table 3) of the pure PVC, the pure Zn/Ca stearate and those of the PVC film containing the Zn/Ca stearate indicate that the scale of heterogeneity of the stabilizer in the PVC film is larger than about 50 nm. Although the relatively low signal-to-noise ratio of the stabilizer does not exclude the possibility that a small part (< 10%) is still dissolved (leading to a not analyzably small amount of stabilizer with a relaxation time of that observed for PVC), it is clear that the bulk of the stearate is not molecularly distributed in the PVC matrix. The appearance and $T_{1\rho}(^1H)$ behavior of the residual THF peaks on the other hand are at least interesting. The fact that a CPMAS spectrum of the THF can be generated at all firstly indicates a dramatic reduction of mobility as compared with a THF liquid. Secondly, the $T_{1\rho}(^1H)$ relaxation time from the resonances caused by the residual THF is, within experimental error, equal to those of PVC which indicates a homogeneous distribution of THF on a molecular scale within PVC.

The authors wish to thank G.W.H.M. Kolfschoten and J.W. Beulen for recording the solution spectra and our colleagues at the SON NMR facility in Nijmegen who generously offered the Irgafos168 sample to be measured on their Bruker MSL 500 MHz spectrometer. We further want to thank Prof. J.H. van der Waals for stimulating discussions and Dr. V. Litvinov for critically reading the manuscript. The investigations were financially supported by DSM Kunststoffen and the Limburgse Vinyl Maatschappij.

REFERENCES

1 I. Orban and W. Fussenegger (Ciba-Geigy AG), Eur. Pat., EP0210131A2, 1987.
2 H. Hasui, T. Furihata, K. Takanashi and M. Ohmori (Mitsui Petr. Ind. Ltd.), Eur. Pat., EP0032459A1, 1981.
3 C. Neri, N. Nodari and G. Sandre (Enichem Sintesi S.p.A.), Eur. Pat., EP0225743A1, 1988.
4 T. Mitsukuni (Ciba-Geigy AG), Eur. Pat. EP0244361A2, 1987.
5 O. Olabisi, L.M. Robeson and M.T. Shaw, Polymer–Polymer Miscibility, Academic Press, San Diego, CA. 1979.
6 R.A. Komoroski, High Resolution NMR spectroscopy of Synthetic Polymers in Bulk, VCH, Deerfield Beach, FL, 1986.
7 S.J. Opella and M.H. Frey, J. Am. Chem. Soc., 101 (1979) 5854.
8 H. Fukui, Magn. Reson. Rev., 11 (1987) 205.
9 The SADLER Standard Spectra, Sadler Res. Lab. Inc., Philadelphia, PA, 1976.
10 P.E. Werner, Z. Kristallogr., 120 (1964) 375.
11 V. Luzzati, A. Tardien and T. Gulik-Krzywicki, Nature, 217 (1968) 1028.
12 K. Volka, Z. Vymazal, J. Stavek and V. Seidl, Eur. Polym. J., 18 (1982) 219.
13 R. Voelkel, Angew. Chem., 27 (1988) 1468; and references cited therein.
14 C.M. Sultani, Polym. Bull., 20 (1988) 463.

Analytica Chimica Acta, 283 (1993) 1025–1031
Elsevier Science Publishers B.V., Amsterdam

Improving selectivity by using a multipurpose cross polarization magic angle spinning NMR pulse sequence

Characterization of π-conjugated compounds

Ivan Hoogmartens, Peter Adriaensens, Dirk Vanderzande and Jan Gelan

Limburg University, Institute for Materials Research (IMO), Research group organic chemistry, Universitaire Campus, B-3590 Diepenbeek (Belgium)

(Received 27th November 1992; revised manuscript received 17th February 1993)

Abstract

The use of a multipurpose cross polarization magic angle spinning nuclear magnetic resonance pulse sequence to simplify high resolution solid state ^{13}C NMR spectra is reported. Several kinds of experiments such as cross polarization, cross depolarization, proton dipolar dephasing and combinations of these are demonstrated for the well characterized *trans*-3,3′-bibenzo[*c*]thienylidene-1,1′-dione. The pulse sequence is further applied to the analysis of insoluble poly(isothianaphthene).

Keywords: Nuclar magnetic resonance spectrometry; *trans*-3,3′-bibenzo[*c*]thienylidene-1,1′-dione; Solid state NMR

Conducting polymers have been the subject of a great deal of research activity due to their interesting optical and electronic properties [1]. For polymers such as poly(*p*-phenylene), polypyrrole and polythiophene to be electrically conductive, doping with electron acceptors (*p*-type doping) or electron donors (*n*-type doping) is needed. This process results in the formation of radical ions (polarons) that can combine to form spinless di-ions (bipolarons) [2]. The resulting complex is very often less stable to atmospheric exposure than the neutral polymer. From that point of view, polymers having a high conductivity without the need for doping, would be very interesting. Such polymer systems, however, require a very small bandgap. The introduction of side groups to induce specific electronic interactions in the conjugated backbone, opened a way to design low bandgap systems. This synthetic approach was first considered by Wudl et al. [3] who successfully reduced the bandgap of polythiophene by fusing a benzene ring on each thiophene unit. The obtained poly(isothianaphthene) **1** (PITN, Fig. 1) possesses a 1-eV bandgap, as determined from optical absorption, compared to 2 eV for the parent thiophene polymer.

A conjugated polymer with a given bandgap may have either an aromatic (characterized by inter-ring bonds and β–β' bonds with a strong single bond character) or a quinoid geometric structure (characterized by inter-ring bonds and β–β' bonds with a strong double bond character). While the ground-state geometric structure of most conjugated polymers built from aromatic monomers clearly remains aromatic, that question had not been resolved unequivocally in the case of PITN partly due to the lack of solubility. Detailed experimental structural information of

Correspondence to: J. Gelan, Limburg, University, Institute for Materials Research (IMO), Research group organic chemistry, Universitaire Campus, B-3590 Diepenbeek (Belgium).

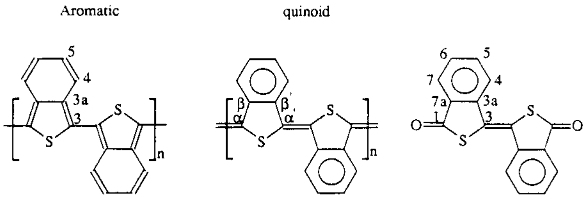

1a 1b 2

Fig. 1. Chemical structure of poly(isothianaphthene) and *trans*-3,3′-bibenzo[*c*]thienylidene-1,1′-dione.

PITN could however be very useful in terms of understanding the correlations between the π-electronic structure and the corresponding electrical and optical properties. We therefore focussed on the solid state ^{13}C NMR analysis of PITN [4]. High-resolution solid-state ^{13}C NMR spectra can be obtained with CP-MAS experiments [5], which combine high-power ^{1}H decoupling, cross polarization (CP), and magic angle spinning (MAS). Sensitivity is enhanced by cross polarization [6] in which ^{1}H nuclear magnetization is transferred to ^{13}C in a double-resonance experiment under the Hartmann–Hahn [7] condition. Magic angle spinning [8] removes the chemical shift anisotropy thereby enhancing the resolution. But even under ideal CP-MAS conditions, the resolution is limited by morphological disorder in amorphous materials (such as PITN). Another problem with regard to PITN concerns the small range in chemical shift of the inequivalent carbons. Therefore, a straightforward determination of the individual signals in a standard CP-MAS NMR spectrum is hindered by overlap of the four resonances (C_3, C_{3a}, C_4 and C_5). In this paper, we demonstrate the use of a multipurpose CP-MAS NMR pulse sequence to improve the spectroscopic resolving power. Selective carbon polarization is induced by optimizing the proper parameters.

EXPERIMENTAL

Synthesis

PITN was prepared by the chemical polymerization of 1,3-dihydrobenzo[*c*]thiophene with *N*-chlorosuccinimide [4]. The resulting powder was Soxhlet extracted with several solvents and the insoluble fraction was used for the structural analysis (after dedoping with aqueous ammonia).

trans-3,3′-Bibenzo[*c*]thienylidene-1,1′-dione **2** (Fig. 1) was prepared according to the procedure described by Markgraf et al. [9]. ^{1}H and ^{13}C NMR spectra of this compound in $C_2D_2Cl_4$ at 90°C were obtained with a Varian Unity 400 spectrometer. Assignment of these spectra is based on the coupling patterns, 2D homonuclear and heteronuclear correlation experiments, the latter optimized for $J = 140$ Hz and $J = 8$ Hz.

Solid state ^{13}C NMR

All solid state ^{13}C NMR spectra were recorded on a Varian XL-200 apparatus at 50.3 MHz. ^{13}C cross polarization measurements are performed using 25–5000 μs mixing times, high power (44 kHz) ^{1}H decoupling, and recycle times of 2 (for PITN) and 10 s (for *trans*-3,3′-bibenzo[*c*]thienylidene-1,1′-dione). Magic angle spinning was performed at 3.0 kHz (for PITN) and 6.0 kHz (for *trans*-3,3′-bibenzo[*c*]thienylidene-1,1′-dione) using Si_3N_4 rotors. Adamantane was used for shimming and the calibration of the proton π/2 pulse width (6.7 μs). The magic angle was set with KBr, while the Hartmann–Hahn condition was adjusted using the aromatic signal of hexamethylbenzene. The chemical shift of this signal was employed as a standard (the shift of the aromatic signal being 132.1 ppm from TMS).

The pulse sequence, we have used, is shown in Fig. 2. Four kinds of experiments can be distinguished by varying the cross polarization time

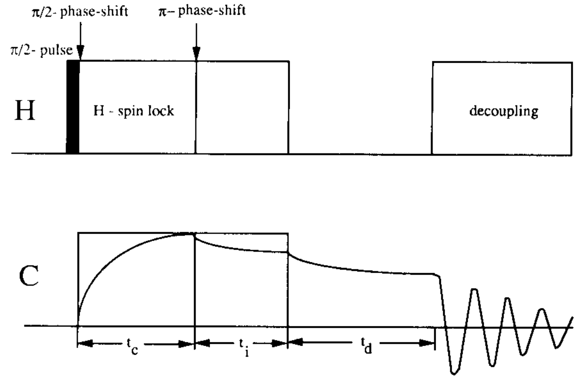

Fig. 2. Multipurpose CP-MAS NMR pulse sequence.

(t_c), the phase inversion or cross depolarization time (t_i) and the proton dephasing time (t_d).

(1) $t_i = t_d = 0$. Standard cross polarization conditions. Only the cross polarization (CP) time (t_c) can be varied in these experiments.

(2) $t_i = 0$ *and* $t_d = 50$ *μs*. In the absence of carbon spin-lock and proton decoupling during the time t_d (= 50 μs), the carbon magnetization is allowed to decay under the influence of the C–H dipolar coupling. Because of the dipole–dipole coupling, the transverse magnetization of tightly coupled (e.g., protonated) carbons is destroyed faster during t_d and a spectrum of only nonprotonated (and if present, weakly coupled very mobile methyl) carbons is obtained [10]. In this context, it is worthwhile to notice that the cross polarization time (t_c) may not be too short in these experiments.

(3) $t_d = 0$. After a certain CP time (t_c) and prior to carbon observation, the ^1H radiofrequency transmitter phase is inverted for a time (t_i). During this period carbon spins cross polarize in the reversed direction (cross depolarization). The protonated carbons depolarize faster than the nonprotonated carbons [11,12].

(4) $t_d = 50$ *μs*. Combining cross depolarization and proton dephasing in one experiment gives us the opportunity to selectively investigate the cross depolarization behaviour of nonprotonated carbons. In order to cross depolarize in an efficient manner, spin-lock conditions should be fulfilled for both the ^1H and ^{13}C magnetization. Therefore, the order of appearance of cross depolarization and proton dephasing may not be interchanged in the pulse sequence since this would destroy the required proton spin-locked magnetization.

RESULTS AND DISCUSSION

The four kinds of CP-MAS experiments will be demonstrated for the well characterized *trans*-3,3′-bibenzo[*c*]thienylidene-1,1′-dione (NMR in solution [13], IR [9], MS [14] and x-ray diffraction [15]). Having a fixed planar conformation, induced by its quinoid structure, no dramatic differences in chemical shift are expected when comparing the liquid to the solid state ^{13}C NMR spectra. The utility of the selectivity improvement of this multipurpose CP-MAS pulse sequence is further demonstrated in applying it to the structural analysis of insoluble PITN.

TABLE 1

Chemical shift and spin-lattice relaxation (T_1) data of *trans*-3,3′-bibenzo[*c*]thienylidene-1,1′-dione in $C_2D_2Cl_4$ at 90°C

	δ (ppm/$C_2D_2Cl_4$ [a]/TMS/90°C)
^1H	7.61 (t, H_6); 7.83 (t, H_5); 8.00 (d, H_7); 8.34 (d, H_4)
^{13}C	124.4 (C_7); 126.9 (C_4); 128.3 (C_3); 129.4 (C_6); 133.8 (C_5); 134.3 (C_{7a}); 142.3 (C_{3a}); 190.1 (C_1)
T_1 (s)	C_4 (2.0 ± 0.1); C_5 (2.3 ± 0.3); C_6 (1.8 ± 0.2); C_7 (1.5 ± 0.2); C_{3a} (25 ± 2); C_{7a} (22 ± 3); C_1 (46 ± 10); C_3 (32 ± 6)

[a] $C_2D_2Cl_4$: $\delta_H = 5.98$ and $\delta_C = 73.7$ ppm. t = Triplet d = doublet.

trans-3,3′-Bibenzo[*c*]thienylidene-1,1′-dione, hereafter referred to as a model compound (because of its appropriate structure for the demonstration of the pulse sequence), was first analyzed in $C_2D_2Cl_4$ at 90°C. The results are listed in Table 1.

$t_i = t_d = 0$; *standard CP-MAS experiment*

The cross polarization rate (T_{CH}^{-1}) can vary widely, especially in molecules containing both protonated and nonprotonated carbons. Under Hartmann–Hahn conditions, the CP rate depends on r_{CH}^{-6}, so that carbons which have no bonded protons will cross polarize more slowly. This disparity in CP rate can be turned to good use by running experiments as a function of the CP time (t_c) to distinguish between protonated and nonprotonated carbons. Accordingly, T_{CH} plays a role in CP experiments much comparable to T_{1C} in conventional non-CP NMR experiments. Figure 3 shows ^{13}C CP-MAS NMR spectra of the model compound with a CP time of 2 ms (b) and 50 μs (c). Based on the solution ^{13}C NMR spectrum (Fig. 3a), the lines at 125.0 and 135.0 ppm in the spectrum with the very short CP time are attributed to the protonated carbons C_7 and C_5, respectively. The other protonated carbons C_4 and C_6 are reflected in this spectrum as a broad resonance around 127–132 ppm. The three extra signals observed at 133.0, 141.0 and

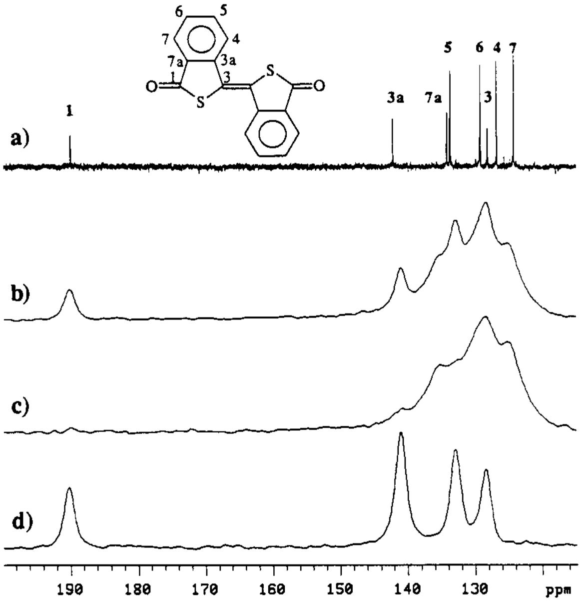

Fig. 3. ^{13}C NMR spectra of *trans*-3,3′-bibenzo[*c*]thienylidene-1,1′-dione: (a) in $C_2D_2Cl_4$ at 90°C; (b) CP-MAS, $t_c = 2$ ms; (c) CP-MAS, $t_c = 50$ μs; (d) PDP, $t_c = 5$ ms and $t_d = 50$ μs.

190.0 ppm in spectrum (b) compared to spectrum (c) arise from nonprotonated carbons since they cross polarize more slowly. From these data, it appears that standard CP-MAS experiments (b) and (c) permit only to observe three of the four nonprotonated carbons namely 133.0 (C_{7a}), 141.0 (C_{3a}) and 190.0 ppm (C_1).

Similar spectra for PITN are shown in Fig. 4a and b. One asymmetric signal can be observed with a maximum at ±126.5 ppm in Fig. 4b in which a very short CP time is used (50 μs), arising from the protonated carbons C_4 and C_5. The signal at 139.0 ppm in Fig. 4a cannot be observed in Fig. 4b and is therefore assigned to one of the nonprotonated carbons (C_3 or C_{3a}).

$t_i = 0$ and $t_d = 50$ μs; proton dipolar dephasing (PDP) CP-MAS experiment

In proton dephasing, a short delay t_d (= 50 μs) is inserted between cross polarization and data acquisition. During this time, t_d, the carbon spins are dipolar coupled with the protons. The resulting dephasing decay due to the ^{13}C–^{1}H dipolar interaction is more pronounced for the protonated carbons because the dipolar interaction has a r_{CH}^3 dependence.

For *trans*-3,3′-bibenzo[*c*]thienylidene-1,1′-dione, three signals of nonprotonated carbons of the model compound have already been identified by varying the CP time (Fig. 3b and c). Proton dephasing is however more suitable for this differentiation. Four lines can be observed in the PDP spectrum (Fig. 3d) of this compound. From the three solid state spectra in Fig. 3, it is now clear that the fourth nonprotonated carbon at 128.0 ppm (in Fig. 3d, C_3) could not be identified by varying t_c because of the overlap with the protonated carbons C_4 and C_6 (127–132 ppm).

The signal at 139.0 ppm in a CP-MAS spectrum ($t_c = 2$ ms) of PITN was assigned to one of the nonprotonated carbons since it could not be observed with a very short CP time. This is confirmed with the aid of proton dephasing (Fig. 4c) using a CP time of 5 ms. The latter technique was necessary in order to identify the second nonprotonated carbon (126.0 ppm).

The above-mentioned more classical experiments show that proton dephasing is more suitable for the distinction between protonated and nonprotonated carbons than only varying the CP time (t_c), especially in the case of overlap.

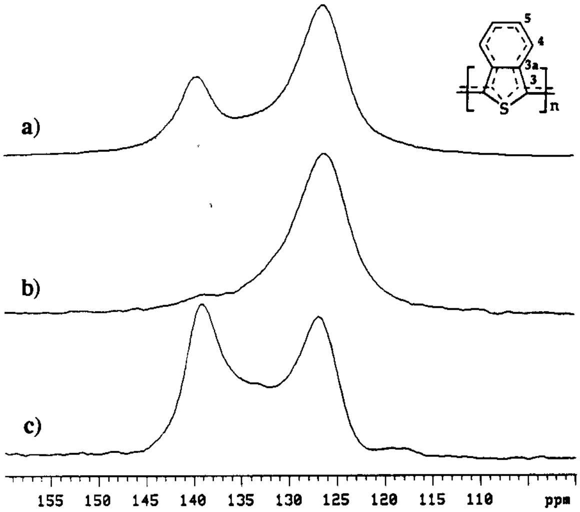

Fig. 4. ^{13}C CP-MAS NMR spectra of poly(isothianaphthene): (a) $t_c = 2$ ms; (b) $t_c = 50$ μs; (c) PDP, $t_c = 5$ ms and $t_d = 50$ μs.

$t_d = 0$; cross depolarization CDP-MAS experiment

The selectivity can be further improved by using a cross depolarization experiment. When the ^1H-radiofrequency transmitter phase is inverted after cross polarization, carbon spins polarize in the reversed direction during a time t_i. As a consequence, the carbon magnetization can vary in the following manner; it first decreases, vanishes at a certain moment and then increases along the opposite direction. As the cross depolarization time (t_i) is increased, the polarization of protonated lines is inverted first due to their higher polarization transfer rate (T_{CH}^{-1}) which depends on r_{CH}^{-6}. This cross depolarization technique (CDP) can thus also be used to differentiate between carbons with and without attached hydrogens. In addition, there is a higher selectivity due to the fact that signals evolve from positive over zero to negative intensities.

When cross depolarization spectra of the model compound are recorded with a CP time of 2 ms, the results are consistent with the PDP experiments. From CDP spectra with a very short CP time (50 μs), it appears that all protonated lines are suppressed after a time t_i of about 40 μs. The polarization transfer rate is mainly be determined by the attached hydrogen due to the r^{-6} dependence. This results in a very similar T_{CH}^{-1} for the protonated carbons (C_4, C_5, C_6 and C_7), a tendency which is reflected in the T_{1c} values (Table 1) in solution (this correlation is of course only valuable if dipole–dipole relaxation is the most important relaxation mechanism and if the overall tumbling of this rigid molecule is isotropic). Therefore, it is hard to further differentiate between the protonated carbons.

In the case of PITN, the protonated lines could anyhow be differentiated with CDP experiments. This differentiation is however artificial since it is induced by the accidental overlap of a protonated and a nonprotonated line. This becomes clear from the spectra in Fig. 5. For $t_c = 50$ μs and $t_i = 44$ μs (Fig. 5a), a signal can be observed at 125.0 ppm. With $t_c = 300$ μs and $t_i = 50$ μs (Fig. 5b), the behaviour of the line at ± 125 ppm interferes with the nonprotonated line at 126.0 ppm having a slower polarization transfer rate. This results in a signal at 128.5 ppm. We are aware of the fact that the signals in the spectra (Fig. 5a, b) may be slightly composed. Therefore, the chemical shifts of these lines (± 1 ppm) cannot be determined with the same accuracy as for the nonprotonated lines (± 0.5 ppm).

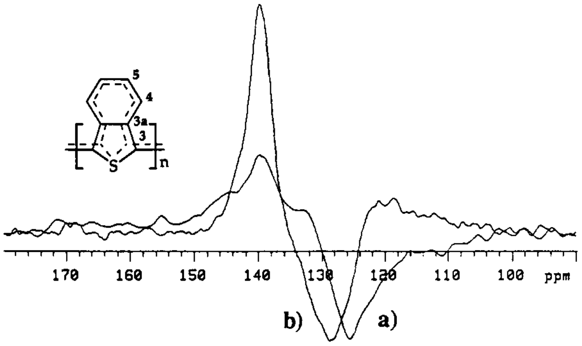

Fig. 5. ^{13}C CDP-MAS NMR spectra of poly(isothianaphthene): (a) $t_c = 50$ μs and $t_i = 44$ μs; (b) $t_c = 300$ μs and $t_i = 50$ μs.

$t_d = 50$ μs; combination of a CDP and a PDP experiment

After cross polarization for a time t_c and depolarization for a time t_i, the resulting magnetization of the carbons is dephased during a time $t_d = 50$ μs. This combination of cross depolarization and proton dephasing allows us to selectively investigate the cross depolarization behaviour of nonprotonated carbons. As already mentioned before, the polarization transfer rate of protonated carbons is mainly determined by the directly bonded hydrogen. For the nonprotonated carbons however, a distinction can be made in the case of our model compound. Carbons C_1 and C_3 are at a larger distance from the hydrogens H_7 and H_4 (2.879 Å [16]) than the carbons C_{3a} and C_{7a} (2.183 Å [16]). This results in a significant difference in T_{1C} value in solution for C_1 and C_3 (30–40 s, Table 1) compared to C_{3a} and C_{7a} (20 s). We investigated to which degree this difference is reflected in the cross depolarization behaviour of the nonprotonated carbons. The CDP/PDP spectrum in Fig. 6 is recorded with a CP time of 5 ms, a cross depolarization time of 1 ms and a dephasing time t_d of 50 μs. From this spectrum, it can be seen that the polar-

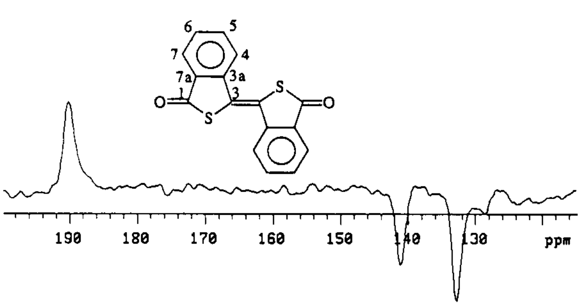

Fig. 6. ^{13}C CDP/PDP-MAS NMR spectrum of *trans*-3,3′-bibenzo[*c*]thienylidene-1,1′-dione: $t_c = 5$ ms, $t_i = 1$ ms and $t_d = 50$ μs.

ization of the lines at 133.0 and 141.0 ppm (C_{7a} and C_{3a} respectively) is inverted first. The difference in polarization transfer rate (T_{CH}^{-1}) between C_1 (190.0 ppm) and C_3 (128.0 ppm) may be explained by the dipolar interaction between C_3 and H_4 of the neighbouring unit ($r_{CH} = 2.948$ Å). The difference in T_{CH}^{-1} between C_{3a} and C_{7a} on one hand and C_1 and C_3 on the other hand is however not as striking as for the T_{1C} values in solution.

CDP/PDP spectra of PITN ($t_c = 5$ ms) with phase inversion times of 0, 800 and 2000 μs are shown in Fig. 7. After an inversion time $t_i = 800$ μs (Fig. 7b), the line at 139.0 ppm has disappeared while the resonance at 126.0 ppm is still positive. For the latter to become zero, a depolarization time of 2 ms is necessary (Fig. 7c). The significant lower polarization transfer rate of the signal at 126.0 ppm suggests a larger distance to the surrounding hydrogens which points to C3 at 126.0 ppm.

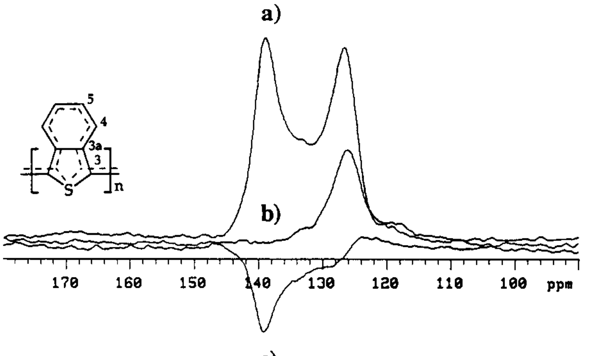

Fig. 7. ^{13}C CDP/PDP-MAS NMR spectra of poly(isothianaphthene) ($t_c = 5$ ms and $t_d = 50$ μs): (a) $t_i = 0$; (b) $t_i = 800$ μs; (c) $t_i = 2$ ms.

It appears thus that C–H distances may be correlated to some extend with the polarization transfer rate (T_{CH}^{-1}). A CDP/PDP combination can then be used to assign nonprotonated carbons. Attention should however be paid for packing effects in the crystalline solid state.

The ^{13}C CP-MAS NMR analysis of insoluble PITN with this multipurpose pulse sequence led to a more detailed characterization of its π-electronic structure. The comparison of these chemical shift data with those of soluble model compounds for an aromatic and a quinoid structure pointed to a π-electronic structure with a strong quinoid character. These results were important in terms of an understanding of the correlations between the structure and the corresponding properties of these low-bandgap conjugated polymers.

The authors are indebted to the Instituut tot Aanmoediging van Wetenschappelijk Onderzoek aan Nijverheid en Landbouw (IWONL) for a predoctoral fellowship to Ivan Hoogmartens. Sincere acknowledgement is also made to Professor Brédas for the AM1-optimized geometries of the π-conjugated compounds.

REFERENCES

1 T.A. Skotheim (Ed.), Handbook of Conducting polymers, Marcel Dekker, New York, 1986.
2 T.C. Chung, J.H. Kaufman, A.J. Heeger and F. Wudl, Phys. Rev. B, 30 (1984) 702.
3 F. Wudl, M. Kobayashi and A.J. Heeger, J. Org. Chem., 49 (1984) 3382.
4 I. Hoogmartens, P. Adriaensens, D. Vanderzande, J. Gelan, C. Quattrocchi, R. Lazzaroni and J.L. Brédas, Macromolecules, 25 (1992) 7347.
5 J. Schaefer, E.O. Stejskal and R. Buchdahl, Macromolecules, 8 (1978) 291.
6 A. Pines, M.G. Gibby and J.S. Waugh, J. Chem. Phys., 59 (1973) 569.
7 S.R. Hartmann and E.L. Hahn, Phys. Rev., 128 (1962) 2042.

8 I.J. Lowe, Phys. Rev. Lett., 2 (1959) 285.

9 J.H. Markgraf, C.I. Heller and N.L. Avery, J. Org. Chem., 35 (1970) 1588.

10 S.J. Opella and M.H. Frey, J. Am. Chem. Soc., 101 (1979) 5854.

11 M.T. Melchior, presented at the 22nd Experimental NMR Conference, Asilomar, CA, 1981, Poster B29.

12 N. Zumbulyadis, J. Chem. Phys., 86 (1987) 1162.

13 I. Hoogmartens, R. Kiebooms, P. Adriaensens, D. Vanderzande and J. Gelan, in preparation.

14 C.W. Koch and J.H. Markgraf, J. Heterocycl. Chem., 8 (1971) 225.

15 R.L. Amey and R.L. Harlow, Acta Crystallogr., Sect. C: Crystal structure, 139 (1983) 1549.

16 J.L. Brédas, private communication.

Analytica Chimica Acta, 283 (1993) 1033–1043
Elsevier Science Publishers B.V., Amsterdam

Quantification of ^{13}C in solids using CPMAS-DD-NMR spectroscopy

David G. Rethwisch

Department of Chemical and Biochemical Engineering, University of Iowa, Iowa City, IA 52242 (USA)

Mary A. Jacintha and Cecil R. Dybowski

Department of Chemistry and Biochemistry, University of Delaware, Newark, DE 19716 (USA)

(Received 8th December 1992; revised manuscript received 8th April 1993)

Abstract

Quantitative analysis of several standard materials is used to evaluate various techniques for analysis of ^{13}C cross polarization magic angle spinning dipolar decoupling (CPMAS-DD)-NMR spectra. These results suggest that uncertainty in the kinetics of the initial cross-polarization process may lead to systematic errors in the fitting of CPMAS-DD-NMR data. Methods are suggested to minimize the effects of this potential source of error. These results indicate that ^{13}C CPMAS-DD-NMR can give quantitatively reliable results.

Keywords: Nuclear magnetic resonance spectrometry; Solid state NMR

The development of solid-state ^{13}C NMR spectroscopy using cross polarization (CP) [1], dipolar decoupling (DD), and magic angle spinning [2] (MAS) has eliminated many limitations associated with NMR spectroscopic studies of solids. The resolution of CPMAS-DD-NMR spectra is better than spectra collected without dipolar decoupling and magic angle spinning, and the accumulation time required to achieve a specified signal-to-noise ratio is typically significantly (> 200 times) less than for a Bloch-decay spectrum. Thus, chemists have come to identify carbon-containing solids with ^{13}C CPMAS-DD-NMR spectroscopy in much the same way they use ^{13}C NMR of organic materials in solution. Indeed, to some outside the field of NMR spectroscopy, "solid-state" NMR spectroscopy is synonymous with ^{13}C CPMAS-DD experiments.

Like ^{13}C NMR spectroscopy of solutions, ^{13}C CPMAS-DD spectra are not necessarily quantitative. Cross polarization is a kinetic process [3]. The simultaneous irradiation of ^{13}C and ^{1}H resonances increases the carbon magnetization by polarization transfer from the protons, but ultimately depletion of the carbon and proton magnetizations occurs by spin-lattice relaxation processes, with the rates varying from species to species in a sample, with the result that intensities may not directly represent the relative numbers of kinds of carbon in the sample.

Several cross-polarization kinetic studies have been reported, e.g. for ^{29}Si polarized from ^{1}H and for ^{13}C polarized by ^{1}H in adamantane [4,5] but these studies did not directly address the use of CPMAS-DD for quantitative comparison of two components. Perhaps the most heavily stud-

Correspondence to: C.R. Dybowski, Department of Chemistry and Biochemistry, University of Delaware, Newark, DE 19716 (USA).

ied materials with quantitative ^{13}C CPMAS-DD methods are coal [6] and coal-derived materials [7]. The problems of quantification of coal CPMAS-DD spectra have been discussed in great detail in this early work and in recent studies [8–10].

We report ^{13}C CPMAS-DD-NMR experiments on three materials, two commonly used as solid-state spectroscopy standards [hexamethylbenzene (HMB) and adamantane (AD)], and a third [polystyrene (PS)] commonly used as an NMR polymer standard. We discuss and compare various methods for completely analyzing CPMAS-DD data to quantify single-component and multicomponent samples. The results lead to a proposed method of analysis.

EXPERIMENTAL

The variable-contact-time CPMAS-DD experiments were performed with a Chemagnetics m100S NMR spectrometer operating at 25.1 MHz for the ^{13}C resonance. The spinning speed was 2–3 kHz, using rotors made of Kel-F^{TM}. The 90° pulse width was 6.8 μs; an acquisition time of 50 ms was used. In most experiments, a relaxation delay of 2–5 s was used. Each spectrum was the result of the coaddition of 256–2000 transient responses (depending on the sample), collected with phase alternation. The range of contact times was chosen for each sample to map the amplitude change through the maximum and sufficiently far into the region of decay so that it decreased substantially (to roughly 1/6 the maximum amplitude, except in the case of adamantane). Contact times varied from 10 μs to 160 ms. It is advisable to be extremely careful in using spectrometers with such long irradiation times to avoid damage. Reproducible establishment of Hartmann-Hahn matching is critical for quantitative work. For these experiments, the tuning of the probe was adjusted at each contact time to ensure coupling between the probe and transmitter remained constant for all duty factors. Failure to retune the probe, particularly at longer contact times (on our spectrometer, for contact times > 15 ms) leads to unacceptable systematic errors in the measurement of parameters.

Hexamethylbenzene and adamantane were obtained from Aldrich. Polystyrene (MW = 125 000–250 000) was obtained from Scientific Polymer Products. The materials were used as received.

RESULTS AND DISCUSSION

Simulated data

A primary concern in quantification experiments is the effect of random noise on the parameters determined by the analytical method. In CPMAS-DD experiments, the evolution of ^{13}C magnetization with contact time is complex, and extracting the values of parameters is not straightforward. Generally one must employ some procedure to fit the data to an equation derived from a model. Various models have been proposed for the cross-polarization process [11,12]. As a practical matter, we use the equation given by Mehring for the contact-time (t_c) dependence of the ^{13}C magnetization, $M(t_c)$, of a single species:

$$M(t_c) = \frac{M_0}{(1-\lambda)}\left[\exp(-t_c/T_{1\rho H}) - \exp(-t_c/T_{CP})\right] \qquad (1)$$

where M_0 is the carbon magnetization that would be generated if spin-lattice processes were not active, $T_{1\rho H}$ is the spin-lattice relaxation time of protons in the rotating frame, T_{CP} is the cross-polarization time constant, and λ is $T_{CP}/T_{1\rho H}$. Equation 1 is derived under the assumption that relaxation and transfer processes are exponential, an assumption that may not be good in all cases [12]. In addition, T_{CP} depends critically on instrumental parameters, such as offset of the resonance from the irradiation frequency, the closeness of the Hartmann-Hahn match, and the spinning frequency [11].

We carried out unrestricted fits of simulated data containing random noise to Eqn. 1 with a Simplex procedure [13] to determine the robustness of the procedure. An example is shown in

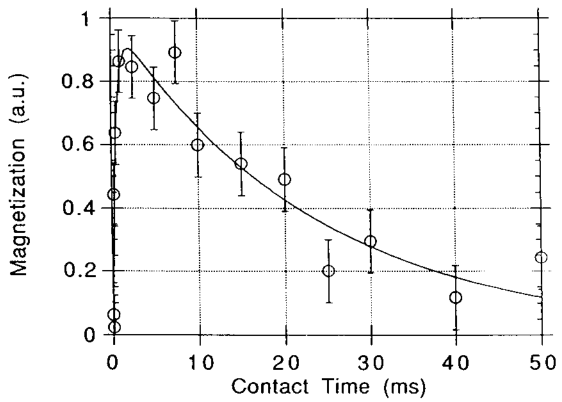

Fig. 1. Plot of simulated polarization-transfer data with random noise added. The actual values of $T_{1\rho H}$, T_{CP}, and M_0 are 23.0 ms, 0.105 ms, and 1.00, respectively. Fitting these data using a Simplex algorithm gives $T_{1\rho H} = 23.3(\pm 3.7)$ ms, $T_{CP} = 0.49(\pm 0.11)$ ms, and $M_0 = 0.986(\pm 0.075)$.

Fig. 1. By varying the amount of noise in these simulated data in two ways: (1) as a percentage of the amplitude at t_c and (2) as a percentage of the maximum amplitude (an appropriate case for actual data), we found that fits to Eqn. 1 give reasonable approximations to the actual parameters even when substantial noise is present. For example, with root mean square noise typically ca. 10% of M_0, $T_{1\rho H}$ can be determined with an accuracy of approximately 10%, the maximum deviation of T_{CP} from the true value is approximately 20%, and of M_0 6%. The fitted parameters are correlated, so caution must be exercised. We conclude that Simplex analysis of typical magnetization–evolution curves should give magnitudes, M_0, reliable to 10% or better for situations similar to those encountered in CPMAS-DD experiments, provided that the evolution obeys Eqn. 1.

Single-component analyses

Single-component analyses are important for relatively quantifying various carbon species in a molecule. What is the appropriate number of data points (i.e. spectra taken at different contact times) to obtain useful results? What is the best method to analyze the resulting magnetization–evolution curve to extract parameters such as M_0, $T_{1\rho H}$ and T_{CP}? In this section, we compare and contrast several methods for analyzing data: the standard method, extrapolation of long-time data, analysis by ratio, and use of an empirical method for modeling the cross-polarization process. These will be defined and described in detail below.

To compare these methods of analysis, we employ three data sets. The first is for pure polystyrene. The second set is for a mixture of

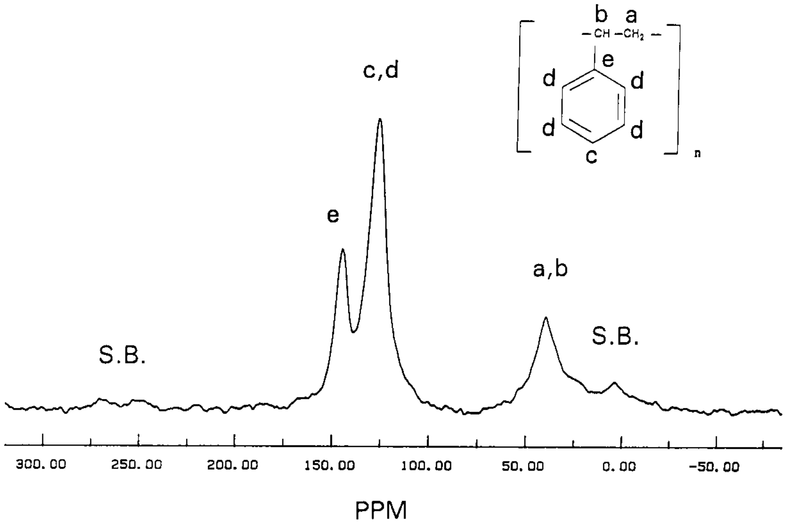

Fig. 2. The ^{13}C CPMAS-DD spectrum of polystyrene. $t_c = 1$ ms; relaxation delay = 5 s. Note the spinning sidebands of the aromatic resonances near 0 ppm and 250 ppm.

hexamethylbenzene (A) and adamantane. These two sets of data were obtained under conditions in which the spectrometer is carefully adjusted to optimize all parameters. The third set of data is for pure hexamethylbenzene (B), and is selected to represent a case in which data are collected under slightly less than optimal spectrometer conditions. This third set represents a typical situation one might find in practice.

A typical CPMAS-DD spectrum of PS is shown in Fig. 2. Two aromatic resonances are observed at ca. 128 and 145 ppm, while the aliphatic carbons give a peak at 40 ppm. The resonances for aromatic carbons c and d (at 128 ppm in Fig. 2), which are resolved in solution-state spectra, are unresolved in solid-state spectra. Similarly, the resonances of aliphatic carbons a and b are unresolved in these spectra. The small peaks around 0 to 250 ppm are sidebands of the aromatic resonances, which must be included in the measurement of the aromatic intensity. The primary aromatic signals were integrated as one group. Treating them as a single species is only strictly correct if all aromatic carbons have the same $T_{1\rho H}$ and T_{CP}. The magnetization–evolution curves for the aromatic and aliphatic resonances of PS are shown in Fig. 3. The maximum aliphatic amplitude occurs at a contact time between 0.5 and 0.75 ms, whereas the maximum for the aromatic component occurs slightly later.

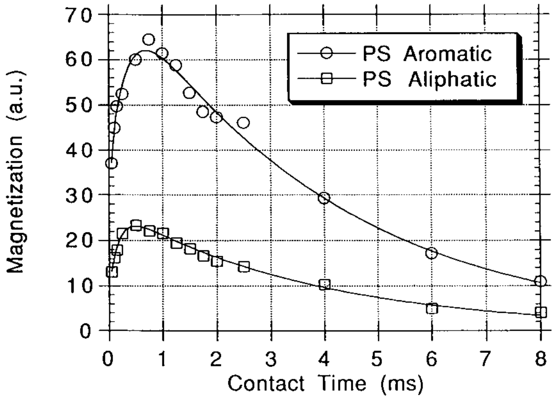

Fig. 3. Evolution of the magnetization components for polystyrene as a function of contact time, t_c. Solid lines show the best fits to Eqn. 1.

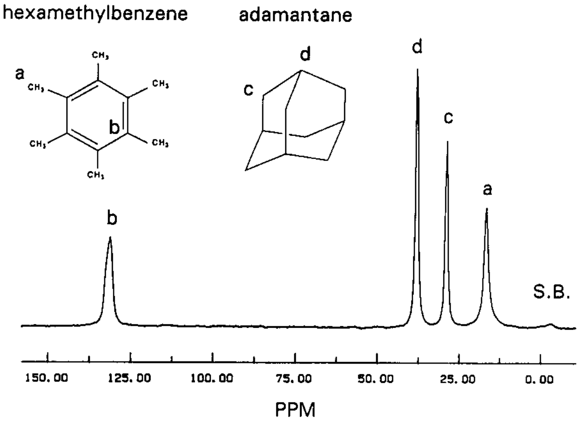

Fig. 4. The ^{13}C CPMAS-DD spectrum of a 50:50 (w/w) mixture of hexamethylbenzene and adamantane. $t_c = 20$ ms; relaxation delay = 2 s.

Figure 4 shows a CPMAS-DD spectrum of a ca. 50:50 (w/w) mixture of AD and HMB. The individual spectra of the two constituents are clearly resolved, allowing each resonance to be individually quantified. The bridging and nonbridging resonances of AD are observed at 29 and 38 ppm, and the aliphatic and aromatic resonances of HMB are observed at 17.6 and 132 ppm, respectively. Sidebands from the aromatic resonance of HMB appear at about 0 and 250 ppm. The magnetization–evolution curves for

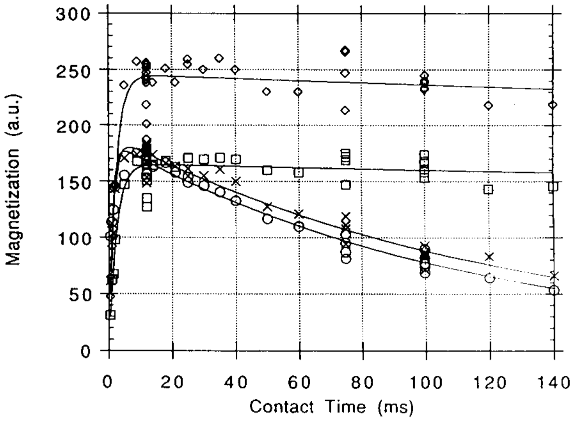

Fig. 5. Evolution of the magnetization components of adamantane and hexamethylbenzene in a 50:50 (w/w) mixture over the range to 120 ms. (×) aromatic carbons of HMB (A); (○) methyl carbons of HMB (A); (◇) bridgehead carbons of AD; (□) nonbridgehead carbons of AD.

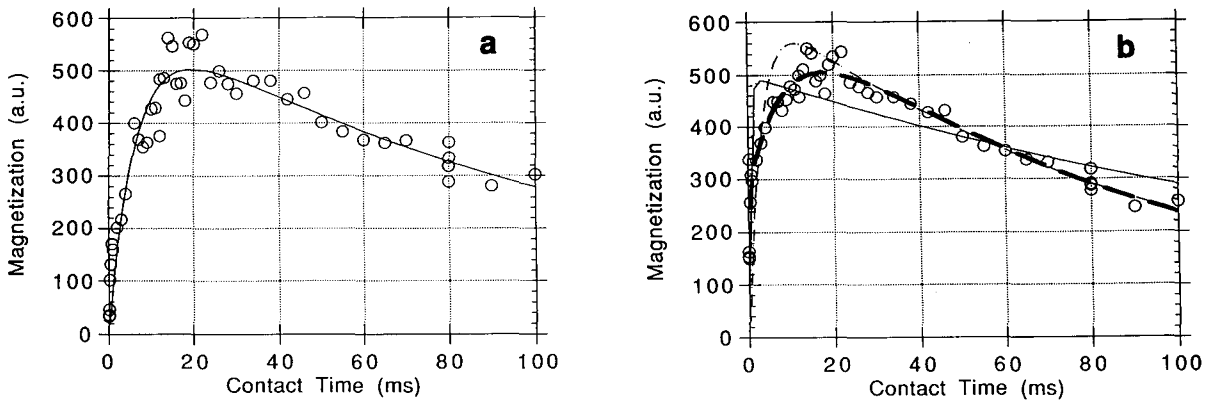

Fig. 6. Evolution of carbon magnetization of HMB (B) as a function of contact time, t_c. (a) aromatic carbons; (b) aliphatic carbons. The line in (a) shows the best fit to Eqn. 1 using the standard method. The light, continuous line in (b) is the best fit to Eqn. 1 by the standard method. The light dashed line shows the best fit to Eqn. 1 using the long-time method. The heavy dashed line in (b) shows the best fit to Eqn. 4.

TABLE 1

Analysis of polystyrene (PS), adamantane (AD), and hexamethylbenzene (HMB) magnetization–evolution curves by the standard method, the long-time method, and the three-pool method [a]

Sample	Peak	Method of analysis	M_0 (a.u.) [b]	$T_{1\rho H}$ (ms)	T_{CP} (ms)	k_{HH} (ms^{-1})	k_{HC} (ms^{-1})	ϵ'
PS	Aromatic	Standard	69.6 (3.2)	4.80 (0.60)	0.098 (0.014)	–	–	–
Fig. 3		Long-time	75.7 (2.1)	4.10 (0.23)	0.122 (0.010)	–	–	–
		3-Pool	76.5 (2.4)	3.96 (0.27)	–	6.0 (3.0)	23 (12)	0.92 (0.47)
	Aliphatic	Standard	25.5 (0.8)	4.11 (0.34)	0.095 (0.009)	–	–	–
		Long-time	26.4 (0.7)	3.85 (0.20)	0.103 (0.007)	–	–	–
		3-Pool	26.4 (0.5)	3.82 (0.18)	–	16 (230)	46 (670)	1.6 (23)
AD	Nonbridgehead	Standard	166 (3)	2900 (2400)	2.41 (0.26)	–	–	–
Fig. 5		Long-time	172 (4)	1200 (450)	2.81 (0.26)	–	–	–
		3-Pool	[c]	[c]	–	[c]	[c]	[c]
	Bridgehead	Standard	246 (4)	2500 (2000)	2.25 (0.25)	–	–	–
		Long-time	254 (6)	1300 (500)	2.50 (0.25)	–	–	–
		3-Pool	[c]	[c]	–	[c]	[c]	[c]
HMB (A)	Aromatic	Standard	188 (2)	129 (6)	1.42 (0.11)	–	–	–
Fig. 5		Long-time	193 (4)	123 (6)	1.50 (0.11)	–	–	–
		3-Pool	196 (7)	121 (9)	–	0.43 (0.43)	0.46 (0.46)	0.76 (0.76)
	Aliphatic	Standard	188 (3)	115 (6)	1.04 (0.09)	–	–	–
		Long-time	189 (5)	110 (5)	1.11 (0.08)	–	–	–
		3-Pool	188 (3)	110 (5)	–	0.59 (0.55)	3.3 (3.2)	0.71 (0.67)
HMB (B)	Aromatic	Standard	599 (26)	125 (16)	6.26 (0.72)	–	–	–
Fig. 6		Long-time	615 (28)	118 (10)	6.68 (0.35)	–	–	–
		3-Pool	634 (33)	106 (13)	–	0.12 (0.07)	4.0 (2.5)	0.15 (0.09)
	Aliphatic	Standard	500 (17)	182 (32)	0.51 (0.09)	–	–	–
		Long-time	624 (17)	101 (5)	3.01 (0.46)	–	–	–
		3-Pool	630 (22)	97 (8)	–	0.18 (0.04)	5.5 (1.1)	0.61 (0.13)

[a] Numbers in parentheses are standard deviations. [b] a.u. indicates arbitrary units. [c] In this case the algorithm was unable to converge on a solution to Eqn. 4.

these resonances are shown in Fig. 5. The HMB resonances reach their maxima more rapidly than do the resonances of AD. The latter show no pronounced decay, because of the very long $T_{1\rho\text{H}}$ of AD. The magnetization–evolution curves for HMB(B), which was taken under less-than-optimal conditions, are given in Fig. 6.

Analysis by the standard method

The solid lines in Figs. 3, 5 and 6 were obtained by an unrestricted fitting of the data of Eqn. 1 (i.e., all parameters were freely optimized by the Simplex method). We refer to this technique as the standard method. The resulting values of M_0, $T_{1\rho\text{H}}$, and T_{CP} are given in Table 1. For the majority of the data sets, there is good agreement between the experimental variation of the magnetization and the fitted line obtained from Eqn. 1 (solid lines in Figs. 3, 5 and 6a). However, there is a clear systematic deviation in the fit for the HMB (B) aliphatic resonance (Fig. 6b). We discuss this fact more fully below. $T_{1\rho\text{H}}$s for HMB (A) are slightly different when determined through the two kinds of carbon, and the T_{CP}s differ by about a factor of 1.5. For AD the T_{CP}s differ slightly for the two kinds of carbon, but the most noticeable feature of the results is the large uncertainty in the measured values of $T_{1\rho\text{H}}$ for AD. This arises from the limited range of the data.

The relative quantification of these materials by CPMAS-DD can be verified by comparing the ratios of the M_0 values determined for the two types of carbon within a single molecule. For PS and HMB one can calculate the ratio of the aliphatic and aromatic carbons as $r_\text{a} = M_{0\text{al}}/M_{0\text{ar}}$, while for AD the ratio of the bridging to non-bridging carbons, $r_\text{b} = M_{0\text{br}}/M_{0\text{nbr}}$. From the known structure (neglecting end effects), PS should have $r_\text{a} = 0.333$. Using the values of the Table 1, we estimate an NMR derived ratio of 0.37($\pm$0.02). While this is somewhat too large, it is within two standard deviations of the theoretical value. For AD, the theoretical value of r_b is 1.50. while the standard method gives an estimate of 1.48($\pm$0.04).

The quality of the agreement for HMB depends on the data set. For HMB (A) (Fig. 5), there is excellent agreement. Theoretically $r_\text{a} =$ 1.00, and the fitted value using this set is 1.00 ($\pm$0.02). For HMB (B), which was taken under less-than-ideal conditions, the standard method gives a value of r_a of 0.83 ($\pm$0.05). This value is clearly too low. An examination of Fig. 6b shows that the fitted line is systematically in error, with the initial part of the magnetization–evolution curve being ill-fit. This suggests that one needs to use a different fitting method to extract parameters from this curve.

Analysis by extrapolation of long-time data

Equation 1 assumes relaxation and transfer processes are of first order. However, deviations from exponential behavior for short contact times have been predicted and observed [14,15]. In extreme cases, polarization transfer dominated by a single ^{13}C–^{1}H dipolar coupling results in an oscillatory dependence of $M(t)$ on the contact time [16]. These observations suggest that data analysis emphasizing the initial (increasing) portion of the evolution curve may introduce errors into derived properties such as $T_{1\rho\text{H}}$ and M_0. A simple method to overcome the uncertainty about the early-time development and the problems of convergence in multivariable fitting schemes [13] such as the standard method is extrapolation of the long-time section of $M(t_\text{c})$ to $t_\text{c} = 0$. By "long time", we mean the analysis should include only data for $t_\text{c} > 5T_{\text{CP}}$, for data obeying Eqn. 1. This procedure is equivalent to considering the second term of Eqn. 1 to be 0 for an initial analysis. Our experience has shown that, in general, data collected beyond the maximum in the magnetization-evolution curve obey the limiting form well.

One cannot independently evaluate λ and M_0 by such a long-time analysis. One means of dealing with this lack of information is to assume $\lambda = 0$, which allows a determination of M_0 directly. This assumption is clearly not valid for all samples and will introduce error into any derived quantities, however the fact that λ is usually quite small means the errors introduced by this approximation are small.

To obtain more accuracy, a value of T_{CP} is required to calculate $\lambda = T_{\text{CP}}/T_{1\rho\text{H}}$. $T_{1\rho\text{H}}$ and $M_0/(1-\lambda)$ determined from long-time extrapolation may be conveniently used to make a restricted fit of the data to Eqn. 1, thereby obtaining T_{CP} and $1-\lambda$. As indicated in Table 1, M_0 calculated in this manner are typically larger than those calculated using the standard method. The standard method generally gives values of $T_{1\rho H}$ longer by up to 30% than this restricted-fitting method, which we refer to as the long-time method. In the present case, fitting the HMB (A), AD, and PS data by either the standard or the long-time method gives essentially the same ratio (Table 2). However, analysis of the HMB (B) data shows a substantial improvement in the aliphatic-to-aromatic ratio when this long-time method is used. By the standard method, the ratio was 0.83; using the restricted fitting of the long-time method, one obtains a value of 1.02($\pm$0.06), in agreement with the theoretical value. Indeed, the results in Table 1 suggest that the standard method underpredicted M_{0al} and overpredicted $T_{1\rho Hal}$, as compared to the long-time method. The improvement, as shown by the light, dashed line in Fig. 6b, suggests that for noisy data or data with other quirks, the long-time method is preferable to the standard method's unrestricted fitting.

Analysis by ratios

For quantitative work, the result of importance is almost always a ratio of two numbers. For example, in an analysis of molecular composition such as r_a(PS), the significant factor is the ratio of the number of carbons in one environment to the number in a second environment. In absolute quantification, the ratio of importance involves a number representing the unknown material and a number representing the standard material. This suggests that an analysis of ratios as a function of contact time may be more accurate than studies of the independent parameters. Such a procedure emphasizes differences in polarization transfer and spin-lattice relaxation, as can be seen for the HMB (B) aliphatic/aromatic ratio in Fig. 7. The scatter in this ratio is less than the scatter in the separate magnetization plots, suggesting that analysis of ratios also partially ameliorates instrumental instability in quantitative ^{13}C CPMAS-DD spectroscopy. Assuming the polarization transfer processes of both species obey Eqn. 1, and restricting the analysis to $t_c > 5T_{CP}$, one obtains

$$\frac{M_1(t)}{M_2(t)} = \frac{M_{01}}{M_{02}} \frac{1-\lambda_2}{1-\lambda_1} \exp\left[-(k_{1\rho H1} - k_{1\rho H2})t\right] \quad (2)$$

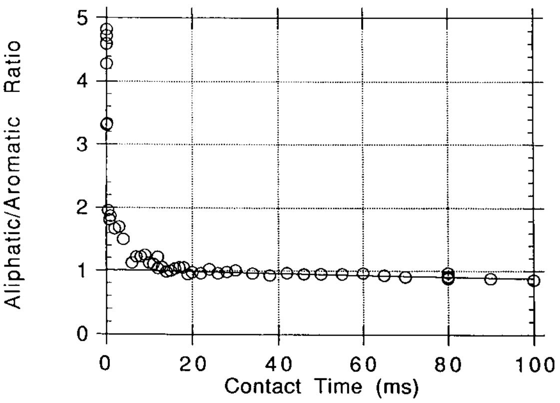

Fig. 7. HMB (B) aliphatic to aromatic intensity ratio as a function of contact time, t_c. The solid line was obtained by fitting the long-time data ($t_c > 15$ ms) using Eqn. 2.

TABLE 2

Analysis of the hexamethylbenzene to adamantane (HMB (A)/AD) ratio, HMB and PS aliphatic to aromatic ratio, and AD bridgehead/nonbridgehead ratio by use of the standard method, the long-time extrapolation method, the three-pool method, GC–MS, and analysis by ratio [a]

Method of analysis	PS aliphatic/aromatic	AD bridge/nonbridge	HMB (A) aliphatic/aromatic	HMB/AD ratio	HMB (B) aliphatic/aromatic
Standard	0.37 (0.02)	1.48 (0.04)	1.00 (0.02)	0.91 (0.03)	0.83 (0.05)
Long-time	0.35 (0.02)	1.48 (0.05)	0.98 (0.03)	0.90 (0.04)	1.02 (0.06)
3-Pool	0.35 (0.02)	–	0.96 (0.04)	0.90 (0.02)	0.99 (0.06)
Ratio	0.34 (0.01)	1.49 (0.01)	0.98 (0.02)	–	1.01 (0.03)
GC–MS [b]	–	–	–	0.87 (0.05)	–
Actual	0.333	1.50	1.00	–	1.00

[a] Numbers in parentheses are standard deviations. [b] Ratio quantified independently by gas chromatography–mass spectroscopy.

where $k_{1\rho H} = 1/T_{1\rho H}$. If the two kinds of carbon are polarized by the same proton reservoir (i.e., $T_{1\rho H1} = T_{1\rho H2}$), the ratio of magnetizations will be time-independent in this region ($t_c \gg 5T_{CP}$):

$$\frac{M_1(t)}{M_2(t)} = \frac{M_{01}}{M_{02}} \frac{1-\lambda_2}{1-\lambda_1} \tag{3}$$

The results of Fig. 7 suggest a slight dependence of the HMB aliphatic to aromatic ratio on t_c for $t_c > 20$ ms. The dramatic time dependence for $t_c < 10$ ms indicates the difference in cross-polarization processes for the two kinds of carbon. These data can be easily fit to Eqn. 2, to find that $M_{01}/M_{02} = 1.01$ (± 0.02).

As indicated in Table 2, analysis by the ratio method generally gives values similar to those obtained by the long-time or standard method. However, the standard deviation of parameters derived by the ratio method is typically less than half that obtained by the other methods. We propose that this reduction in the standard deviation is a result of the compensation of instrumental instability, as suggested above. The values of λ_1 and λ_2 in Eqn. 2 were determined by long-time fits to the individual magnetization–evolution curves.

For many organic systems, λ_i is small (ca. 0–0.05), and only a few percent error is introduced by assuming that the ratio $(1-\lambda_i)/(1-\lambda_j)$ is 1. It is our experience that this ratio is actually closer to 1 than either of the quantities $(1-\lambda_i)$. Therefore, for most cases we have examined, this assumption leads to at most a 2–3% error in the ratio of the magnetizations, for the case that the carbons are cross-polarized from protons with similar spin dynamics.

Two-proton-pool (three-pool) model

That the variable-contact-time data for the HMB (B) aliphatic carbons in Fig. 6b do not obey Eqn. 1 is surprising only because the HMB (B) aromatic carbons (Fig. 6a) obey it rather well under these conditions. This is a typical situation arising in practice. To improve the quantification, one must model the evolution curve of the aliphatic carbons more accurately than Eqn. 1 can. Both the aromatic and aliphatic carbons interact with the same types of protons, but the two kinds of carbon do have different proton–carbon dipolar couplings, and the neighboring protons of aromatic carbons will be subject to different transfer kinetics than those near aliphatic carbons. Thus, changes in the transfer in the first step caused by various instrumental missettings may affect the processes affecting these two kinds of carbon differently. A sequential two-step model in which two proton pools are connected to each other, with one being connected to the carbon pool, may be useful under these conditions. We assume the transfer kinetics of both steps are of first order and incoherent, making the model analogous to the method used to approximate thermal gradients at the boundary layer in traditional heat transfer problems. Müller et al. [16] modelled a similar situation but considered the first step coherent.

Assuming ^{13}C spin-lattice relaxation is negligible and all proton spin-lattice relaxation times are the same, one obtains the following result for the carbon magnetization as a function of contact time:

$$\begin{aligned} M(t_c) = {} & \frac{M_0}{1 - x_1\lambda_1 - (1-x_2)\lambda_2} \\ & \times \left[\exp(-k_{1\rho H}t_c) - x_1 \exp(-k_{x1}t_c) \right. \\ & \left. - (1-x_1)\exp(-k_{x2}t_c)\right] \end{aligned} \tag{4}$$

with

$$\lambda_i = \frac{k_{1\rho H}}{k_{xi}}; \qquad x_1 = \frac{b+c}{2b}$$

$$k_{x1} = a - b; \qquad k_{x2} = a + b$$

$$a = \frac{k_{1\rho H} + k_{HH} + (\epsilon' + 1)k_{HC}}{2}$$

$$b = \frac{\sqrt{\left(k_{1\rho H} + k_{HH} + (\epsilon' - 1)k_{HC}\right)^2 + 4\epsilon' k_{HC}^2}}{2}$$

$$c = \frac{k_{1\rho H} + k_{HH} + (\epsilon' - 1)k_{HC} + \dfrac{2\epsilon' k_{1\rho H} k_{HC}}{k_{HH}}}{2}$$

$$\epsilon' = \frac{N_C}{N_{H1}} \frac{\omega_C}{\omega_H}$$

where N_C and N_{H2} are the number of ^{13}C nuclei and protons in pool 2, respectively; ω_C and ω_H are, respectively, the carbon and proton rotating frame precession frequencies. $T_{1\rho H}(= 1/k_{1\rho H})$ is the proton spin-lattice relaxation time in the rotating frame, k_{HH} is the rate constant for transfer between the two proton pools, and k_{HC} is the transfer rate constant between proton pool 1 and the ^{13}C pool. In the limit that the proton pools are quickly equilibrated, Eqn. 4 goes over to Eqn. 1. This particular three-pool model is not unique. A model in which two proton pools transfer magnetization separately and directly to the carbon, but do not transfer magnetization between themselves, results in an equation identical in form. Thus, care must be exercised in overinterpreting the constants obtained using this equation; we use it only for empirical analysis.

Analysis of the HMB (B) aliphatic evolution curve with Eqn. 4 provides a significant improvement of fit, as indicated by the heavy dashed line in Fig. 6b, principally because of the additional fitting parameters. An improved fit of data to a particular equation does not necessarily validate the model. This is particularly true when the equation can be derived from at least two different models. One may attempt to rationalize the use of Eqn. 4 by asking if the derived parameters are realistic and consistent with other data and facts. The values of $T_{1\rho H}$ for the aromatic and aliphatic carbons of HMB derived from this procedure are essentially identical, showing that the proton pools relax with the same time constant, whereas by the standard method applied to Eqn. 1, the $T_{1\rho H}$s differed by almost a factor of 1.5. The M_0 values of HMB (B) determined by this three-pool method give agreement with the known structure of HMB.

Examination of the other values in Tables 1 and 2 indicates that using the three-pool method gives values of M_0 and $T_{1\rho H}$ indistinguishable, within experimental error, from the values derived using the long-time method. However, the long-time method requires fewer fitting parameters. In addition, the three-pool method requires very good initial guesses for convergence, which we generally obtained from initially fitting the data by the long-time method. Thus, the use of the long-time method is preferable to the three-pool method because of convenience and stability of fit.

Analysis of multiple-component samples

In a physical mixture, $T_{1\rho H}$, T_1 and T_{CP} may vary substantially from component to component. These differences may have significant effects on the quantification of such mixtures. To demonstrate the effects, we examined a physical mixture of adamantane and HMB (A), two materials having substantially different spin dynamics. The values of $T_{1\rho H}$ for HMB and AD differ by approximately an order of magnitude in these two materials, with adamantane having $T_{1\rho H} > 1000$ ms. As indicated above, within a single component, the carbon ratios give the correct stoichiometry, whichever method is used. Because $T_{CP}(AD) < 0.01\ T_{1\rho H}(AD)$, $\lambda < 0.01$. In our analysis, we assume it is identically zero, which introduces only a small error.

For quantitative analysis of a mixture one requires a measure of the ratio of the two components. In this example, the amount of HMB in the mixture may be determined by comparing total HMB (A) carbon intensities to total AD carbon intensities. This can be done by direct calculation from the M_0 values of Table 2, obtained through independent analyses of the two resonances. However, we demonstrate the ratio analysis for this situation. The ratio of the HMB to AD magnetization as a function of contact time is given by

$$\frac{M_{ar}(\mathrm{HMB}) + M_{al}(\mathrm{HMB})}{M_{br}(\mathrm{AD}) + M_{nbr}(\mathrm{AD})} = \frac{\dfrac{M_{0ar}}{1-\lambda_{ar}} \exp(-t/T_{1\rho Har}) + \dfrac{M_{0al}}{1-\lambda_{al}} \exp(-t/T_{1\rho Hal})}{\dfrac{M_{0br}}{1-\lambda_{br}} \exp(-t/T_{1\rho Hbr}) + \dfrac{M_{0nbr}}{1-\lambda_{nbr}} \exp(-t/T_{1\rho Hnbr})} \quad (5)$$

for $t_c > 5T_{CP}$. Further, assuming that $T_{1\rho H}$ is the same for all HMB protons $(= T_{1\rho HMB})$ and that $T_{1\rho H}$ is the same for all AD protons $(= T_{1\rho AD})$ and using an average value of $1 - \lambda_{HMB}$ for HMB and noting that $\lambda \approx 0$ for both AD carbons, one

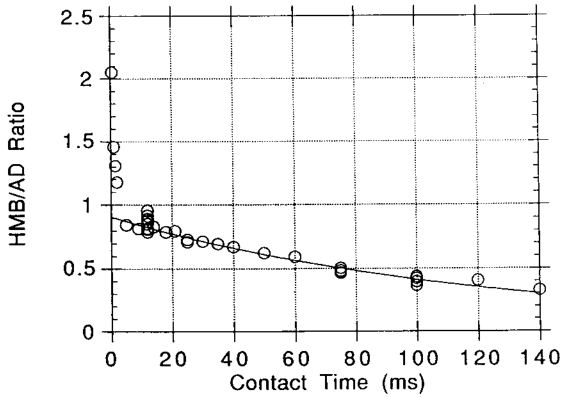

Fig. 8. HMB(A)/AD intensity ratio as a function of contact time. The solid line was obtained by fitting the long-time data ($t_c > 15$ ms) using Eqn. 6.

gets the following expression:

$$\frac{M_{\mathrm{ar}}(\mathrm{HMB}) + M_{\mathrm{al}}(\mathrm{HMB})}{M_{\mathrm{br}}(\mathrm{AD}) + M_{\mathrm{nbr}}(\mathrm{AD})} = \frac{M_0(\mathrm{HMB})}{M_0(\mathrm{AD})} \frac{\exp\left[-t\left(1/T_{1\rho \mathrm{HMB}} + 1/T_{1\rho \mathrm{AD}}\right)\right]}{1-\lambda_{\mathrm{HMB}}} \qquad (6)$$

Analysis of this long-time behavior of this ratio should give an intercept that is the desired ratio multiplied by $1/(1-\lambda_{\mathrm{HMB}})$. From such a plot (Fig. 8), the intercept gives $M_0(\mathrm{HMB})/M_0(\mathrm{AD}) = 0.91 \pm 0.02$, when corrected for the value of $1/(1-\lambda_{\mathrm{HMB}})$. The independent evaluations give essentially the same result, and they all agree with the value determined independently by GC–MS analysis (Table 2).

Conclusions

^{13}C CPMAS-DD-NMR spectroscopy can be used as a quantitative tool for investigating both pure solids and mixtures of solids, but care must be exercised. Single-contact-time measurements of the magnetizations cannot be guaranteed to be quantitative and should be avoided. In certain cases (e.g. PS at $t_c > 1$ ms) the aromatic to aliphatic ratio is constant at the correct value and a single-contact-time measurement appears to give the correct analysis. However, this constancy results from the fortuitous intrinsic NMR properties. When relaxation parameters vary from resonance to resonance, the complete magnetization–evolution curve must be analyzed.

The measurement of the t_c dependence of the carbon magnetization allows extraction of the values of M_0 and $T_{1\rho\mathrm{H}}$, as well as parameters like T_{CP}. In general, it is better to emphasize the long-time behavior to determine the values of $T_{1\rho\mathrm{H}}$ and $M_0/(1-\lambda)$, followed by a constrained fitting of the full evolution curve to determine T_{CP}, than to use an unrestricted fitting of the data. It is advisable to collect spectra for ca. 10–15 contact times, with about 75% of these data (7–10) at contact times greater than $5T_{\mathrm{CP}}$. In general, data collected beyond the maximum can usually be assumed to behave as long-time data. In principle, both the standard procedure and the long-time procedure should lead to the same result, but in practice sequential fitting avoids the pitfalls of false minima and minimizes the impact of uncertainty about the details of cross polarization on the results. Where the desired result is a ratio of two resonances, analysis by the ratio method is recommended.

The factor $(1-\lambda)$ is important in obtaining the ultimate accuracy. It is fortunately almost always nearly 1. More significantly the ratio $(1-\lambda_i)/(1-\lambda_j)$, which is important in comparing intensities of resonances, is often closer to 1. For highest accuracy, it should be determined, but for rough estimations, it may be assumed to be between 0.95 and 1.05.

In many cases, because of various problems, the short-contact-time rise of the magnetization does not seem to be exponential. In these cases we provide an empirical equation to aid in data analysis. It arises from a model in which magnetization transfer to the overall proton system is mediated by an intermediate proton reservoir incoherently coupled to the total proton pool and to the carbons. The resulting equation may be useful as a means to parameterize the evolution of decay in some situations in which Eqn. 1 does not accomodate the data well. The result is not unique to the particular model, and care must be used in interpreting the results.

The spectrometer was purchased through a grant from the US Department of Energy. CD acknowledges support for NMR studies of catalysts under grant CHE-9013926 of the National Science Foundation. We owe special thanks to Dr. Martha Bruch for her helpful discussions and to Dr. Gordon Nicol for the GC–MS analysis.

REFERENCES

1 (a) A. Pines, M.G. Gibby and J.S. Waugh, J. Chem. Phys., 56 (1972) 1776; (b) A. Pines, M.G. Gibby and J.S. Waugh, J. Chem. Phys., 58 (1973) 569.
2 J. Schaefer, E.O. Stejskal and R. Buchdahl, Macromolecules, 10 (1977) 384.
3 (a) R.S. Hartmann and E.L. Hahn, Phys. Rev., 128 (1962) 2042; (b) F.M. Lurie, and C.P. Slichter, Phys. Rev., 133 (1964) A1108.
4 G.E. Maciel and D.W. Sindorf, J. Am. Chem. Soc., 102 (1980) 7607.
5 A. Pines and T.W. Shattuck, J. Chem. Phys., 61 (1974) 1255.
6 (a) D.E. Axelson, Solid State Nuclear Magnetic Resonance of Fossil Fuels, Multiscience, Ottawa, 1985, Chap. 3; (b) D.L. vanderHart and H.L. Retcofsky, Fuel, 55 (1976) 202; (c) H.L. Retcofsky, F.K. Schweighardt and M. Haugh, Anal. Chem., 49 (1977) 585; (d) F.P. Miknis, M.J. Sullivan, V.J. Bartuska and G.E. Maciel, Org. Geochem., 3 (1981) 19; (d) R.L. Dudley and C.A. Fyfe, Fuel, 61 (1982) 651; (e) M.J. Sullivan and G.E. Maciel, Anal. Chem., 54 (1982) 1606; (f) B.C. Gerstein, P.D. Murphy and L.M. Ryan, in M.L. Gorbaty, J.W. Larsen and I. Wender (Eds.), Coal Structure, Academic Press, 1982, p. 87.
7 (a) J.M. Dereppe, J.M. Moreaux and H. Castex, Fuel, 57 (1978) 435; (b) T. Yokomo, K. Miyazawa and Y. Sanada, Fuel, 57 (1978) 555; (c) P.D. Murphy, B.C. Gerstein, V. Weinberg and T.F. Yen, Anal. Chem., 54 (1982) 522; (d) V. Weinberg, T.F. Yen, P.D. Murphy and B.C. Gerstein, Carbon, 21 (1983) 149.
8 (a) R.A. Wind, M.J. Duijvestijn, C. vanderLugt, J. Smidt and J. Vriend, Fuel, 66 (1987) 876; (b) R.A. Wind, G.E. Maciel and R.E. Botto, in R.E. Botto and Y. Sanada (Eds.), Magnetic Resonance of Carbonaceous Solids, American Chemical Society, Washington, DC, 1993, p. 3.
9 (a) M. Solum, R. Pugmire and D. Grant, Energy Fuels, 3 (1989) 187; (b) L. delaRosa, M. Pruski, D. Lang, B.C. Gerstein and P. Solomon, Energy Fuels, 6 (1992) 460.
10 (a) C. Choi, J.V. Muntena, A.R. Thompson and R.E. Botto, Energy Fuels, 3 (1989) 528; (b) J.V. Muntean and L.M. Stock, Energy Fuels, 5 (1991) 765; (c) J.A. Franz, R. Garcia, J.C. Linehan, G.D. Love and C.E. Snape, Energy Fuels, 6 (1992) 598.
11 M. Mehring, Principles of High Resolution NMR in Solids, Springer Verlag, Berlin, 1983.
12 M.H. Levitt, D. Suter and R.R. Ernst, J. Chem. Phys., 84 (1986) 4243.
13 J.H. Noggle, Practical Curve Fitting and Data Analysis, Prentice-Hall, Englewood Cliffs, NJ, 1993.
14 D.A. McArthur, E.L. Hahn and R.E. Walstedt, Phys. Rev., 188 (1969) 609.
15 D.V. Lang and J. Moran, Phys. Rev. B, 1 (1970) 53.
16 L. Müller, A. Kumar, T. Bauman and R. Ernst, Phys. Rev. Lett., 32 (1974) 1402.

Analytica Chimica Acta, 283 (1993) 1045–1058
Elsevier Science Publishers B.V., Amsterdam

Non-linear least squares procedure for the extraction of NMR parameters from multi-tensor solid state line shapes

J.M. Koons, E. Hughes and P.D. Ellis

Department of Chemistry and Biochemistry, University of South Carolina, Columbia, SC 29208 (USA)

(Received 1st November 1992; revised manuscript received 15th March 1993)

Abstract

A suite of nuclear magnetic resonance (NMR) line shape programs, that simulate five common interactions in solids, has been written. Non-linear least squares routines based on the SIMPLEX and Levenberg–Marquardt algorithms have been implemented to extract physical parameters from solid state NMR powder line shapes. Both optimization strategies produce error estimates for the parameters extracted. As an example to illustrate the difficulties of applying least squares in NMR, the system of mono- and dilabeled ^{13}C ethylene on silver, supported on γ-alumina was studied. The experimental line shapes produced were analyzed by non-linear least squares fitting to extract the principal components of the chemical shift (CS) tensor, the bond distance, and the orientation of the components of the chemical shift tensor in the molecular frame of ethylene. To evaluate the techniques performance, the reliability of the error estimates produced by the optimization has been investigated.

Keywords: Nuclear magnetic resonance spectrometry; Least squares procedure; Line shape program; Solid state NMR

In solid state NMR, information about the electronic environment and bonding of the nuclei can be obtained from the analysis of static powder line shapes. The observed spectrum depends upon the interactions present in the sample that add to the Zeeman splitting caused by the static field. Such interactions are dipolar, quadrupolar (for nuclei possessing a spin quantum number I greater than a half), chemical shift and scalar couplings. The magnitude of the interactions perturbing the Zeeman splitting is dependant upon the orientation of the crystallite in the static magnetic field, therefore as all orientations are present in a powder sample there will be a spread of frequencies contributing to the observed resonance.

How the analysis of a line shape proceeds depends upon the number and type of interactions that are present. If there is only one perturbation, such as the chemical shift, then the physical information present can be extracted by eye: measuring the positions of the discontinuities gives the three principal components of the chemical shift tensor in their principal axis frame (PAS) (e.g., Fig. 1). A similar, though more involved, treatment of powder pattern lineshapes of half integer spin quadrupolar nuclei has been reported by Granger [1].

In general, information concerning the orientation of a tensor interaction relative to the molecular frame is lost in a powder line shape. Single crystal experiments [2,3] have been traditionally used to determine the orientation of the principal axis system relative to the molecule's fixed frame. However, the experiment has not achieved widespread use due to experimental difficulties.

Correspondence to: P.D. Ellis, Department of Chemistry and Biochemistry, University of South Carolina, Columbia, SC 29208 (USA).

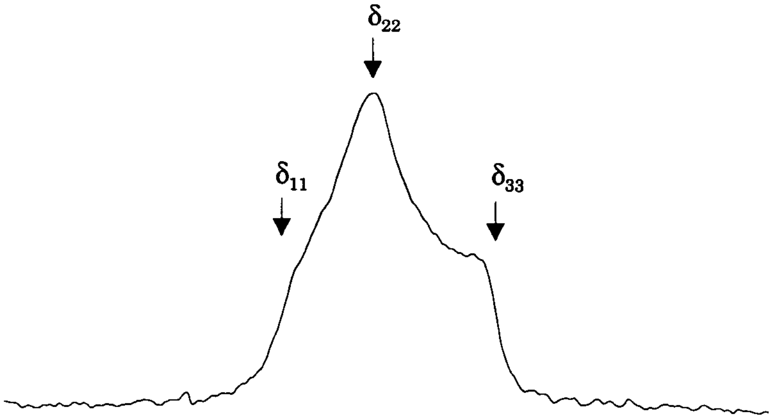

Fig. 1. Experimental spectrum of monolabeled ^{13}C ethylene on a silver supported γ-alumina, showing the positions of the principal components of the chemical shift tensor.

In the past decade, techniques based on 2D NMR [4] and 1D spectral simulation with non-linear least squares analysis (LS), have been developed and circumvent the need for the single crystal experiment [5–7]. The techniques take advantage of the fact that the dipole tensor is orientated along the internuclear vector of the atoms causing the interaction. This allows other tensor interactions to be related in space relative to the dipole interaction and therefore the fixed molecular frame.

LS analysis is not unique to NMR, rather it has become the most widely used technique to "fit" experimental data to a theoretical model [8]. Unfortunately, it has become so easy to do that it is possible to be seduced into a false sense of security concerning the result. Many factors can influence the validity of the solution, therefore a thorough understanding of the function and the limitations of the optimization techniques and experiments should be sought by the user.

The research carried out in our group relies heavily upon the use of simulated spectra and non-linear least squares fitting. The areas of interest range from biochemistry, in particular characterization of the bonding of the metals in metalloproteins, to the investigation of industrial catalyst processes. As such, the systems are far from ideal and therefore we have attempted to develop an in-house, integrated simulation package to more readily understand the limitations and validity of the fitting process in these systems.

Two programs have been written, one which performs optimization and is intended for use in a batch processing environment and the other an interactive graphical user interface centered around the Tektronix 42xx series terminals that allows a user to load, display and print spectra and free induction decays (FIDs), simple manipulations can also be performed on the FID prior to Fourier transformation such as zero filling, line broadening, etc. The majority of the two programs have been written in FORTRAN while C was used for input and output. They have been developed under a VAX VMS operating system and later, a streamlined version was ported to the AIX operating system.

As an example to illustrate the difficulties of applying LS in NMR, the system of ethylene on silver supported on γ-alumina [9–11] will be used. With this system we were interested in characterizing the chemical shift tensor of ethylene and its orientation in the molecule's fixed axis frame. To do this the dipolar interaction was used to relate the orientation of the components of the chemical shift tensor to the molecular frame. The strategies employed to fit the experimental data will be discussed, describing where necessary the fundamental concepts of LS as applied to this field of NMR, and the implications of the error estimates provided by the least squares fitting.

EXPERIMENTAL

The catalyst samples were prepared by using silver nitrate (99.99%), potassium oxalate monohydrate (99%), ethanolamine (99%) and ethylenediamine (99%) purchased from Aldrich. The γ-alumina pellets (No. SA 6173, 220 m^2/g) were provided by Norton Chemical Product Division. Mono- and dilabeled 99% (atom) ^{13}C ethylene were obtained from MSD Isotopes. A detailed description of the preparation of Ag/γ-alumina catalysts has been previously published [12]. All silver catalysts utilized in this work were 10% by weight.

^{13}C NMR spectra were obtained at 75.429 MHz with a Varian XL 300 spectrometer ($B_0 =$ 7.05 T). Catalyst samples (600 mg) were ground and packed into a 7 mm o.d. Zirconia rotor with KEL-F end caps. A double tuned, single coil 7 mm MAS probe (Doty Scientific, Columbia, SC) was employed for the experiments. Spectra were acquired at approximately 100 K using cross-polarization [13] with high power proton decoupling. The 90° pulse width was 7 μs, the contact time was optimized to be 200 μs, the recycle time was 120 s and 2048 transients were collected. NMR1 from NMRi [14] was used to preprocess the experimental data, in terms of zero filling the FID to 1 K and premultipling by a 400 Hz Lorentzian line broadening function before Fourier transformation. The spectra were subsequently phased and a polynomial baseline correction [15] was performed. Throughout this manuscript the chemical shift for ^{13}C has been reported with respect to external adamantane, where CH resonates at 29.50 ppm with respect to TMS. The ^{13}C shielding tensor can be calculated from the reported chemical shift data as follows: $\sigma_{ii} = 186.40 - \delta_{ii}$.

The theoretical spectra were generated by calculating a 128 point FID which was zero filled and exponentially multiplied in the same manner as that of the experimental spectrum. Baseline correction on both theoretical and experimental data was performed in the frequency domain, the average of the first 10% of the data was repeatedly subtracted from the entire spectrum until the difference between iterations was negligible to single precision. In addition, the first derivative of both the experimental and theoretical spectra was computed using the 5-point Savitzky–Golay first-derivative filter [16]. All calculations we performed either on a VAX Station 3540 or an IBM RISC 6000/550.

THEORETICAL

NMR theory

In the solid state an NMR spectrum is a function of the number of interactions effecting the nuclei. A Hamiltonian describing the energy of the spins of the nuclei will be the sum of the individual Hamiltonians describing the interactions present. The Hamiltonians have a spatial dependence and so must be related to a common reference frame before they can be summed. Typically, the Hamiltonians are expressed as the product of irreducible spherical tensors, where the spatial and spin and/or magnetic tensors have been separated [17],

$$H^{\lambda} = c^{\lambda} \sum_{l=0,2} \sum_{m=-l}^{+l} (-1)^{m} T^{\lambda}_{l,m} R^{l}_{l,-m} \tag{1}$$

λ represents the type of Hamiltonian, $T^{\lambda}_{l,m}$ represents the components of the irreducible spherical spin tensor and $r^{\lambda}_{l,m}$ the components of the spatial tensor. In the subscript, l is the rank of the tensor and m is the index of the component tensor.

The spatial tensor may be rotated using standard Wigner rotation matrices using Eqn. 2,

$$\begin{aligned} R^{\lambda}_{l,-m} &= \sum_{n} D^{\lambda}_{-m,n}(\alpha, \beta, \gamma)^{*} r_{l,n} \\ &= \sum_{n} D^{l}_{n,-m}(-\gamma, -\beta, -\alpha) r_{l,n} \end{aligned} \tag{2}$$

where l is the rank of the tensor, α, β, and γ are the Euler angles, $r_{l,n}$ are the components of the irreducible spherical tensor in the new reference frame, and the rotation matrix elements are defined by Eqn. 3.

$$D^{l}_{m,n}(\alpha, \beta, \gamma) = e^{-i(\alpha m + \gamma n)} d^{l}_{m,n}(\beta) \tag{3}$$

In the case of the system of interest here, there are two main interactions, the homonuclear dipole and chemical shift. The total Hamiltonian in the laboratory frame can be written in terms of Eqn. 4,

$$H_{\text{lab}}^{\text{tot}} = H_{\text{lab}}^{\text{CS}} + H_{\text{lab}}^{\text{D}} \tag{4}$$

where, the secular Hamiltonians are given by

$$H_{\text{lab}}^{\text{CS}} = \gamma_c T_{2,0}^{\text{CS}} R_{2,0}^{\text{CS}} \tag{5}$$

and

$$H_{\text{lab}}^{\text{D}} = -2\gamma_c^2 \hbar T_{2,0}^{\text{D}} R_{2,0}^{\text{D}} \tag{6}$$

Further,

$$T_{2,0}^{\text{CS}} = \sqrt{\tfrac{2}{3}}\, I_0 B_0 \tag{7}$$

$$I_0 = I_{\text{Z}} \tag{8}$$

$$\begin{aligned} T_{2,0}^{\text{D}} &= \frac{1}{\sqrt{6}}(3I_{01}I_{02} - I_1 I_2) \\ &= \frac{1}{\sqrt{6}}\left[2I_{\text{Z}1}I_{\text{Z}2} - \tfrac{1}{2}(I_1^+ I_2^- + I_1^- I_2^+)\right] \end{aligned} \tag{9}$$

A more detailed description of these terms can be found in [18].

The first step in the calculation is to transform the dipolar Hamiltonian, e.g., Eqn. 6, to the PAS frame of the chemical shift interaction and then to the PAS frame of the dipolar interaction, i.e.,

$$\begin{aligned} R_{2,0}^{\text{D}} = &\sum_{n=-2}^{+2} D_{n,0}^{2}(-\phi, -\theta, 0) \\ &\times \left[D_{0,n}^{2}(0, -\beta, -\alpha)\right] \rho_{2,0}^{\text{D}} \end{aligned} \tag{10}$$

In the dipolar PAS frame, $\rho_{2,0}^{\text{D}}$ is the only non-zero element, i.e., $\rho_{2,0}^{\text{D}} = (3/2)^{1/2}\ r_{cc}^{-3}$. This leads to the following expression for $R_{2,0}^{\text{D}}$,

$$\begin{aligned} R_{2,0}^{D} = \sqrt{\tfrac{3}{2}}\, r_{cc}^{-3}\big[&\tfrac{1}{4}(3\cos^2\theta - 1)(3\cos^2\beta - 1) \\ &- \tfrac{3}{4}\sin 2\theta \sin 2\beta \cos(\alpha + \phi) \\ &+ \tfrac{3}{4}\sin^2\theta \sin^2\beta \cos(2\alpha + 2\phi)\big] \end{aligned} \tag{11}$$

The chemical shift interaction can be treated by similar methods. However, the only transformation that is needed is from the lab frame to the PAS frame of the chemical shift interaction, i.e.,

$$R_{2,0}^{\text{CS}} = \sum_{n=-2}^{+2} D_{n,0}^{2}(-\phi, -\theta, 0) \rho_{2,n}^{\text{CS}} \tag{12}$$

where $\rho_{2,0}^{\text{CS}} = (3/2)^{1/2}\delta_{\text{cs}}$, $\rho_{2\pm1}^{\text{CS}} = 0$, and $\rho_{2\pm2}^{\text{CS}} = -1/2\delta_{\text{cs}}\eta_{\text{cs}}$. After substitution and trigonometric simplication. $R_{2,0}^{\text{CS}}$ becomes,

$$R_{2,0}^{\text{CS}} = \frac{\delta_{\text{cs}}}{2}\sqrt{\tfrac{3}{2}}\left(\cos^2\theta - 1 - \eta_{\text{cs}}\sin^2\theta \cos 2\phi\right) \tag{13}$$

δ_{cs} and η_{cs} are defined according to the conventions of Haeberlen [18]: $\delta_{\text{cs}} = \delta_{33} - \delta_0$, and $\eta_{\text{cs}} = (\delta_{22} - \delta_{11})/\delta_{\text{cs}}$, where δ_{11}, δ_{22}, and δ_{33} are the diagonal components of the symmetric chemical shift tensor in its PAS frame and $\delta_0 = (\delta_{11} + \delta_{22} + \delta_{33})/3$. In this convention, the principal components of the chemical shift tensor are ordered as follows, $|\delta_{33} - \delta_0| \geq |\delta_{11} - \delta_0| \geq |\delta_{22} - \delta_0|$, which imposes the constraint, $0 < \eta_{\text{cs}} < 1$.

Combining the respective spin and spatial components [18] of the dipolar and chemical shift Hamiltonians, expressions for the frequency for each interaction can be given as,

$$\omega_{\text{CS}} = -\nu_{\text{L}}\frac{\delta_{\text{cs}}}{2}\left(\cos^2\theta - 1 - \eta_{\text{cs}}\sin^2\theta \cos 2\phi\right) \tag{14}$$

and

$$\begin{aligned} \omega_{\text{D}} = \mp\tfrac{3}{4}\gamma_{\text{c}}^2 \hbar r_{\text{cc}}^{-3}\big[&\tfrac{1}{2}(3\cos^2\theta - 1)(3\cos^2\beta - 1) \\ &- \tfrac{3}{2}\sin 2\theta \sin 2\beta \cos(\alpha + \phi) \\ &+ \tfrac{3}{2}\sin^2\theta \sin^2\beta \cos(2\alpha + 2\phi)\big] \end{aligned} \tag{15}$$

The chemical shift line shape generated based on Eqn. 14 is dependant upon the spectral parameters δ_{cs} and η_{cs}. Whereas the dipolar line shape is given by the sum of Eqn. 14 and Eqn. 15 and is dependant upon the spectral parameters δ_{cs}, η_{cs}, r_{cc}, α, and β. From the definition of δ_{cs} and η_{cs}, it is clear that they are not independant, and therefore cannot be used explicitly in the non-linear least squares methods to be discussed. One must use the principal component of the chemical shift tensor in the optimization and calculate the values of δ_{cs} and η_{cs}. Furthermore, only two of the principal components of the chemical shift tensor are truly independent if the isotropic chemical shift is known. Therefore, care is required to implement this function into a general non-linear least squares method.

Calculation of the FID

The free induction decay observed at discrete time intervals from a powdered sample can be expressed by Eqn. 16,

$$G(t) = \int_{\phi=0}^{\pi/2}\int_{\theta=0}^{2\pi} \mathrm{e}^{i\omega(\theta,\,\phi)t} \sin\theta \,\mathrm{d}\theta \,\mathrm{d}\phi \qquad (16)$$

where $\omega(\theta, \phi)$ is the frequency contribution from each microcrystal in the powder and θ and ϕ are the polar and azimuthal angles describing the orientation of the magnetic field vector in the PAS of the molecule [19].

In terms of approximating Eqn. 16 numerically, the integrals are replaced with sums according to Eqn. 17,

$$\begin{aligned} g(t) &= \sum_{\phi=0}^{\pi/2}\sum_{\theta=0}^{2\pi} W\,\mathrm{e}^{i\omega(\theta,\,\phi)t} \\ &= \sum_{\phi\theta} W\,\mathrm{e}^{i\omega(\theta,\,\phi)t} \\ &= g(n) = \sum_{\phi\theta} W\,\mathrm{e}^{i\omega(\theta,\,\phi)n\Delta t} \qquad (17) \end{aligned}$$

where $\Sigma_{\phi\theta}$ indicates that the powder average is performed using the four-octant partition of the unit sphere described by Alderman et al. [20], W is the solid angle weighing factor, and for easy translation into a FORTRAN loop, the dwell time Δt and the number of points in the FID is used to express the time dependance. Further simplification of Eqn. 17 is performed using Euler's relationship and standard trigonometric identities to yield a form that requires no calls to special math functions inside the time propagation loop as given in Eqn. 18,

$$\begin{aligned} g(n) &= \sum_{\phi\theta} W\{\cos[\omega(\theta,\,\phi)n\Delta t] \\ &\qquad + i\sin[\omega(\theta,\,\phi)n\Delta t]\} \\ &= \sum_{\phi\theta} W\{\cos(nA) + i\sin(nA)\} \qquad (18) \end{aligned}$$

where $A = W(\theta, \phi)\Delta t$ and

$$\begin{aligned} \cos(nA) &= \cos(A)\cos([n-1]A) \\ &\qquad - \sin(A)\sin([n-1]A) \\ \sin(nA) &= \sin(A)\cos([n-1]A) \\ &\qquad + \cos(A)\sin([n-1]A) \qquad (19) \end{aligned}$$

Eqn. 19 is valid for all $n \geqslant 1$. Figure 2 shows the pseudo-FORTRAN code for calculating the real (C) and imaginary (S) parts of the FID expressed in Eqn. 18. This expression for the FID is perfectly general for all functions, leaving only $\omega(\theta, \phi)$ to be defined for each interaction.

```
Zero C and S
Do $\Sigma_{\phi\theta}$ tiling loop
    calculate wt
    calculate $\omega = \omega(\theta,\phi)$
    cosA = cos( $\omega$ $\Delta$t )
    sinA = sin( $\omega$ $\Delta$t )
    cosarg = 1
    sinarg = 0
    Do i=1,num_point_in_fid
      c(i) = c(i) + wt*cosarg
      s(i) = s(i) + wt*sinarg
      tcos = cosA*cosarg - sinA*sinarg
      tsin = sinA*cosarg + cosA*sinarg
      cosarg = tcos
      sinarg = tsin
    Continue
Continue
```

Fig. 2. Pseudo FORTRAN code for calculating the real (C) and imaginary (S) components of the FID observed for a powdered sample.

Constrained non-linear least squares analysis

Least squares analysis is commonly used to fit experimental data to a theoretical model. The fit proceeds by finding a solution of the theoretical function that satisfies some goodness of fit criterion, which in most cases, is taken as the minimum in the residual sum of squares (RSS) function [21–23]. Eqn. 20 expresses the solution of the fitting problem for the constrained case,

$$\tilde{\mathrm{RSS}} = \tilde{f} = \min_{x_k \in \Psi} \sum_i^N [Y_i - y(x_k)_i]^2, \quad k = 1, 2, \ldots, n \qquad (20)$$

where Y_i and y_i are the responses of the ith points from the experimental and theoretical data sets respectively, Ψ is the set on which the primary parameters x_k are defined, and $\tilde{\mathrm{RSS}}$ is the value of the residual sum of squares function at its minimum value, which is known as the grand minimum or truly lowest function value. All other points of minimum extrema in a finite region are referred to as local or false minima.

The analytical solution of Eqn. 20 can be obtained by solving Eqn. 21 simultaneously for all x_k,

$$\left(\frac{\partial \tilde{f}}{\partial x_k}\right)_{x_{k+1}} = 0$$

$$\left(\frac{\partial^2 \tilde{f}}{\partial x_k^2}\right)_{x_{k+1}} > 0, \qquad k = 1, 2, \ldots, n \qquad (21)$$

Unfortunately, setting the first partial derivative equal to zero on all but linear functions leads to a set of non-linear simultaneous equations in the parameters, which cannot be solved in general [24]. It is for this reason that a wide variety of algorithms has been developed that approximates the solution of Eqn. 20, however techniques other than Monte Carlo simulation cannot guarantee the solution provided corresponds to the grand minimum in the RSS function. Usually, the problem of getting trapped by false minima gets worse as the number of parameters increases and the signal to noise ratio decreases; both increase the uncertainty in the parameters obtained. Techniques for analyzing the validity of the solution of Eqn. 20 are left to the user.

Different approaches have been used to verify the reliability of the LS solutions described in this paper. First, the surface has been mapped by starting from a large number of initial guesses to verify that the solution found does have the lowest function value. In addition two different optimization strategies have been used in tandem to demonstrate the solution can be obtained reproducibly. In addition, the number of parameters in the fit have been kept to a minimum to help reduce the likelihood of being trapped by local minima.

The implementation chosen for the solution of Eqn. 20, namely the SIMPLEX [25] and Levenberg–Marquardt algorithms [22], have been selected because of the two techniques' widespread availability and because of their different mechanisms for locating the minimum.

Levenberg–Marquardt algorithm

Two primary analytical methods of estimating non-linear parameters have been the inverse Hessian [24] and the steepest descent (gradient) methods [26]. Gradient methods locate the minimum by moving in the direction where the function undergoes the greatest (downhill) rate of change. Whereas the inverse Hessian method approximates the surface with a Taylor series through quadratic terms and moves in the direction of the minimum of the resultant parabola. Both methods however, when used alone, often fail; the Taylor series method because of divergence of the successive iterates and the gradient methods because of agonizingly slow convergence after the first few iterations [27]. The Levenberg–Marquardt algorithm exploits the advantages of both LS techniques by utilizing an interpolation strategy that successively alternates between the Taylor series method and the gradient method as the minimum is approached. In this way, the convergence of the algorithm is the rule, rather than the exception.

Moré [28] has claimed that most implementation of the Levenberg–Marquardt algorithm are neither robust nor have theoretical justification and he has developed a solution to the problem namely the MINPACK library of routines [29]. The major feature of MINPACK is its proper use of implicitly scaled variables, which help to ensure global convergence from starting points that are far from the solution. The source code from the MINPACK project has been made available by Argonne National Laboratory and is the implementation of the Levenberg–Marquardt algorithm that we use.

One clear advantage of the MINPACK algorithm is that estimates for the errors associated with the parameters extracted can be obtained by a few straightforward calculations after the optimization finishes. A complete description of estimating uncertainties based on the Hessian matrix and the law of error propagation is presented by Bevington [26]. MINPACK is also conservative in the amount of internal storage required and for all practical purposes, the time spent in the routine which implements the modified Levenberg–Marquardt algorithm (LMDIF1), is negligible compared to the time spent calculating the FID.

However, the most noticed shortcoming of the technique is the difficulty in programming boundary conditions, for instance the constraints on η_{cs}. In our implementation of the "user-supplied" function, the chemical shift tensor is checked to ensure values generated by the optimization have not caused η_{cs} to become undefined. In such a case, a null vector is returned for the calculated function (FVEC) and MINPACK is forced to find a different solution. In addition, the MINPACK routine that calculates the Jacobian matrix, FDJAC2, has been modified so that it checks to see if a parameter becomes undefined as a result of a forward difference step. If the step cannot be made, the backwards difference algorithm is attempted. However, when both methods fail the optimization terminates.

SIMPLEX algorithm

The SIMPLEX method has been taken from *Numerical Recipes* [22]. The SIMPLEX locates the minimum of a function by only taking into account the response at a new position and the other responses held in the geometrical SIMPLEX shape. It moves across the response surface expanding and contracting depending upon the complexity of the local response surface. No attempt is made to calculate the gradient of the response surface, therefore there is no direct method of estimating the errors associated with te optimized parameters.

This limitation of the SIMPLEX method has been discussed by both Spendley et al. [30] and Nelder and Mead [31], who introduced the fixed sized SIMPLEX and the modified SIMPLEX methods, respectively. They both outlined a solution to the problem which involved constructing the Hessian matrix by fitting the response surface enclosed by the final SIMPLEX to a quadratic equation.

$$y = \mathbf{a}_0 = 2\mathbf{a}^{\mathrm{T}}x + x^{\mathrm{T}}\mathbf{B}x \qquad (22)$$

Eqn. 22 represents the quadratic approximation to the surface close to the minimum expressed in vector form where **a** represents the gradient and **B** the curvature matrix which can be used to derive error estimates. To estimate the coefficients of the equation $1/2(n+1)(n+2)$ points are required with their associated response values where n is the number of parameters in the fit. The SIMPLEX provides $n+1$ points and the further $1/2n(n+1)$ points can be found from the 'half-way points' of the edges of the SIMPLEX.

Phillips and Eyring [32,33] discuss the implementation of such a method and this has been coded in FORTRAN. In this method can occur when the difference between the response values at the coordinates of SIMPLEX are of the order of the round off error of the floating point calculations. To avoid such a problem the relative difference between the responses at the SIMPLEX coordinates are checked and if any are less than 10^{-3}, then the final SIMPLEX is expanded back out on all sides away from the minimum. This expansion can cause problems if the minimum is located close to boundary limits as the SIMPLEX may be prevented from being expanded. If this is the case, error estimates cannot be produced. Due to the complicated functions that are required to simulate the spectra and with an increasing number of parameters this failure to produce error estimates occurs frequently. In estimating the error in each parameter the response surface has to be approximated using a quadratic function. The validity of this approximation can be easily checked and is done so when error estimates are calculated by the method described by Phillips and Eyring [32,33]. If the approximation fails no error estimates are reported. The stringency level for the quadratic test

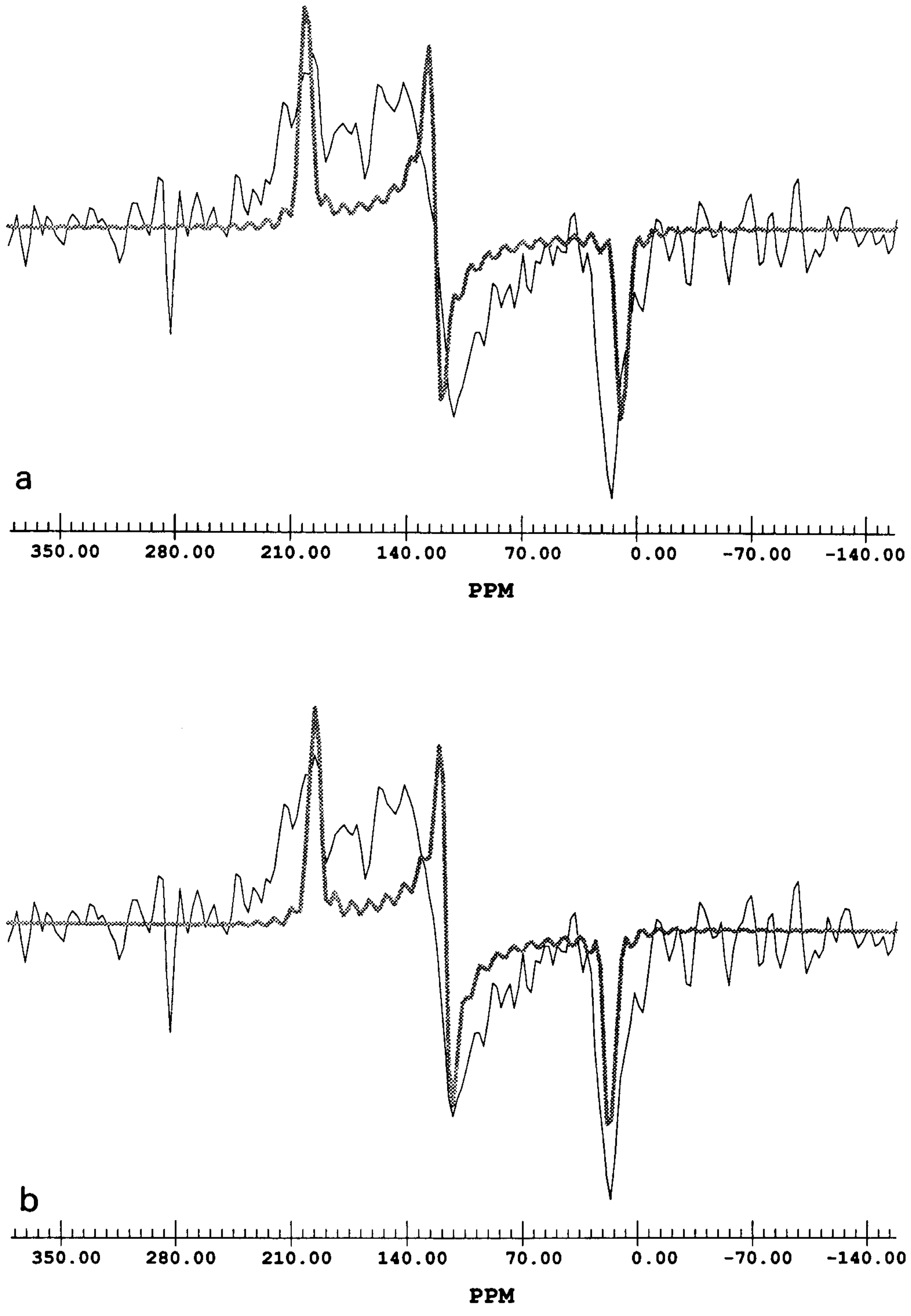

Fig. 3. First derivative overlap of the experimental and final simulated line shapes of monolabeled ^{13}C ethylene on a silver supported γ-alumina catalyst obtained by (a) optimizing the overlap of the spectra and (b) by optimizing the overlap of the first derivative line shapes.

has been set to that suggested by Brumby [34]. The implementation of such an error analysis scheme has greatly improved the usefulness of the SIMPLEX technique.

RESULTS AND DISCUSSION

Comments on the fitting method

Consider an experimental powder spectrum where all the spectral parameters are known. Using these parameters a theoretical spectrum can be calculated. The two spectra will almost certainly have different intensities therefore a scaling parameter will be needed to map one spectrum onto the other and this parameter will have a value that is not unity. This value along with the other parameters will give the best fit in terms of a minimum in the residual sum of squares. The scaling value is an exact value and is as unique as the set of parameters describing the system.

Now if the parameters were not known for the experimental spectrum, and arbitrary values were used as input to a least squares minimization method then the scaling value used initially would have no relation to the unique scale value associated with the true values of the parameters. It would therefore seem proper to include the scaling factor as a parameter in the fit and let it be optimized along with the physical parameters. This method has been tested and shown to work with theoretical data where Gaussian noise has been added. The measured signal-to-noise ratio was approximately equal to that observed in our experimental spectra (circa. 40).

Consider next a method where the scaling is not included among the optimized parameters, rather a scaling value is found indirectly by normalizing the highest peak in both the experimental and theoretical spectra to one and then calculating the RSS value. Using this approach the scaling factor is implicitly optimized reaching the 'true' value for the system as the other parameters are refined during the optimization process. This method has also been implemented and it has been shown to fit the same theoretical data. Although there is no difference between the final values that the two scaling approaches reach, it is fair to say that the routes the two methods follow to find the optimum will be different and that the relative importance of the scale on the RSS value in each strategy will be distinct. These differences will be shown to be of importance in fitting experimental spectra.

Due to the low signal-to-noise ratio and the large parameter set that defines the dipolar spectrum, the least squares analysis of the dipolar line shape was simplified. The chemical shift parameters were removed from the dipolar fit by previously extracting them by a least squares fitting of a monolabeled ^{13}C ethylene spectrum. Leaving only the bond distance and orientation angles to be extracted from the dipolar spectrum.

As previously discussed, the principal components of the chemical shift tensor in a powder lineshape may be found by estimating the positions of the three discontinuities. This was performed on the experimental spectrum to give the values of $\delta_{11} = 192$, $\delta_{22} = 117$ and $\delta_{33} = 12$ ppm. Using the isotropic chemical shift value of 107 ppm found from magic angle sample spinning [10] only two tensor elements are required to describe the lineshape. The choice of which elements to optimize is best made by considering which features in the lineshape are the most distinct. When least squares analysis was applied using overlapping spectra, no combination of tensor elements produced final values that were consistent with those found by inspection. It was only when the first derivatives of the two spectra were used that the least squares optimization produced consistent results. The success achieved by overlapping the first-derivative spectra is due to the fact that when δ_{11} and δ_{33} are chosen, the discontinuities appear as peaks in the first-derivative spectrum as they are defined by inflection points. Fitting the peak position will give the correct magnitudes of δ_{11} and δ_{33}. Fig. 3 shows the derivative overlap of the final simulated spectra optimized by (a) overlapping the spectrum and (b) by optimizing the first derivative. It is clear that the positions of the peaks in the experimental and simulated lineshape, indicative of the position of the inflection point, coincide for the case of the derivative fit. In the case of the fit using overlapping spectra there is a large difference in peak position between simulated and experimental spectra, indicating an incorrect least squares solution. The peak corresponding to the δ_{11} element is poorly defined in the experimental spectra, therefore the optimization was repeated using δ_{22} and δ_{33}, the final optimized values were still in good agreement with the previous results.

When considering the dipolar spectra, it was regarded that the overlap of the two horns was the crucial criteria for a 'good' fit, Figure 4, and lack of overlap at the base of the spectrum may be considered to be due to broadening introduced by the surface heterogeneity. As before, fitting the data by overlaying the two spectra directly did not work. Therefore, the first derivative overlay method was attempted. The first derivative will emphasize where the function is undergoing the greatest rate of change. In terms of the dilabeled spectrum this occurs in the region of the two horns, therefore in the first derivative lineshape this region is the most prominent. It was found that when the lineshape was fit, only the implicit scaling method produced a set of values for the parameters that produced a spectrum where the relative heights were in the correct proportions. This can be understood in how the two scaling methods effect the search for the optimum set of values. When the scale is included in the fit it undermines the importance of the other parameters by expanding or contracting the theoretical lineshape to maximize the agreement between it and the experimental spectrum over the most possible number of points (Fig. 5a). This will lead to final values of the physical parameters that correspond to the false minimum dictated by the scaling parameter. By implicitly scaling the overlap, the height of the peaks are emphasized as seen in Fig. 5b and the physical parameters are found naturally and correspond to the horns being in the correct proportions. The final values of the two fits are given in Table 1.

Comments on the error estimates

When using non-linear least squares analysis to fit a theoretical function to experimental data it is essential to give some estimate of the error in

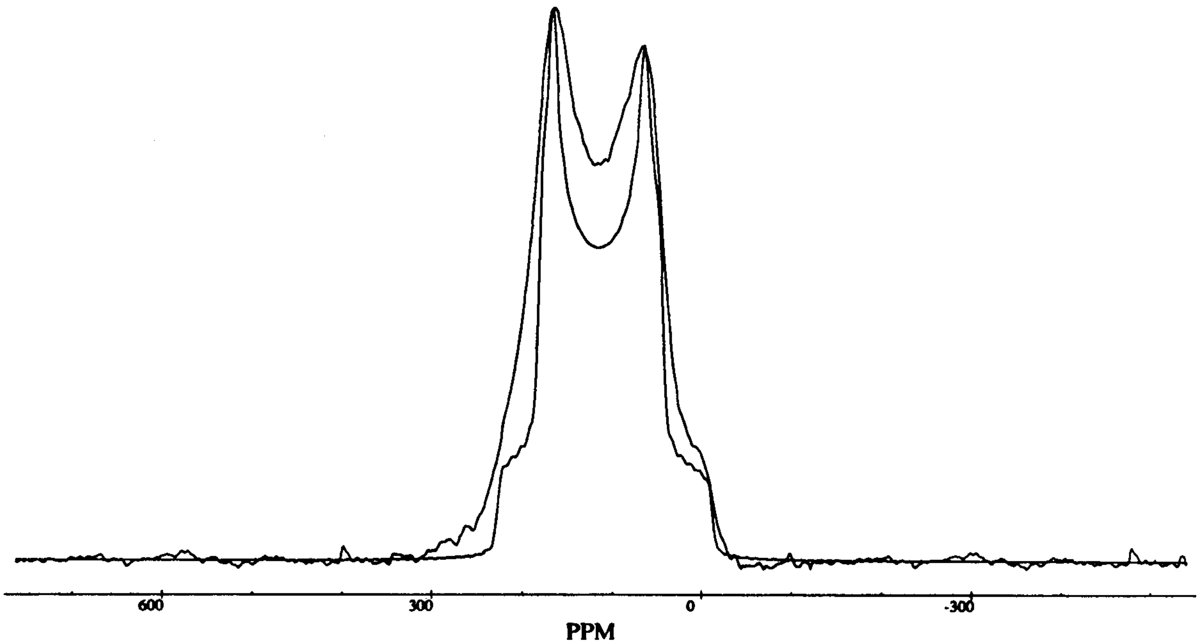

Fig. 4. Overlap of the experimental and final simulated line shapes of dilabeled ^{13}C ethylene on a silver supported γ-alumina catalyst obtained by optimizing the overlap of the first derivative using implicit scaling.

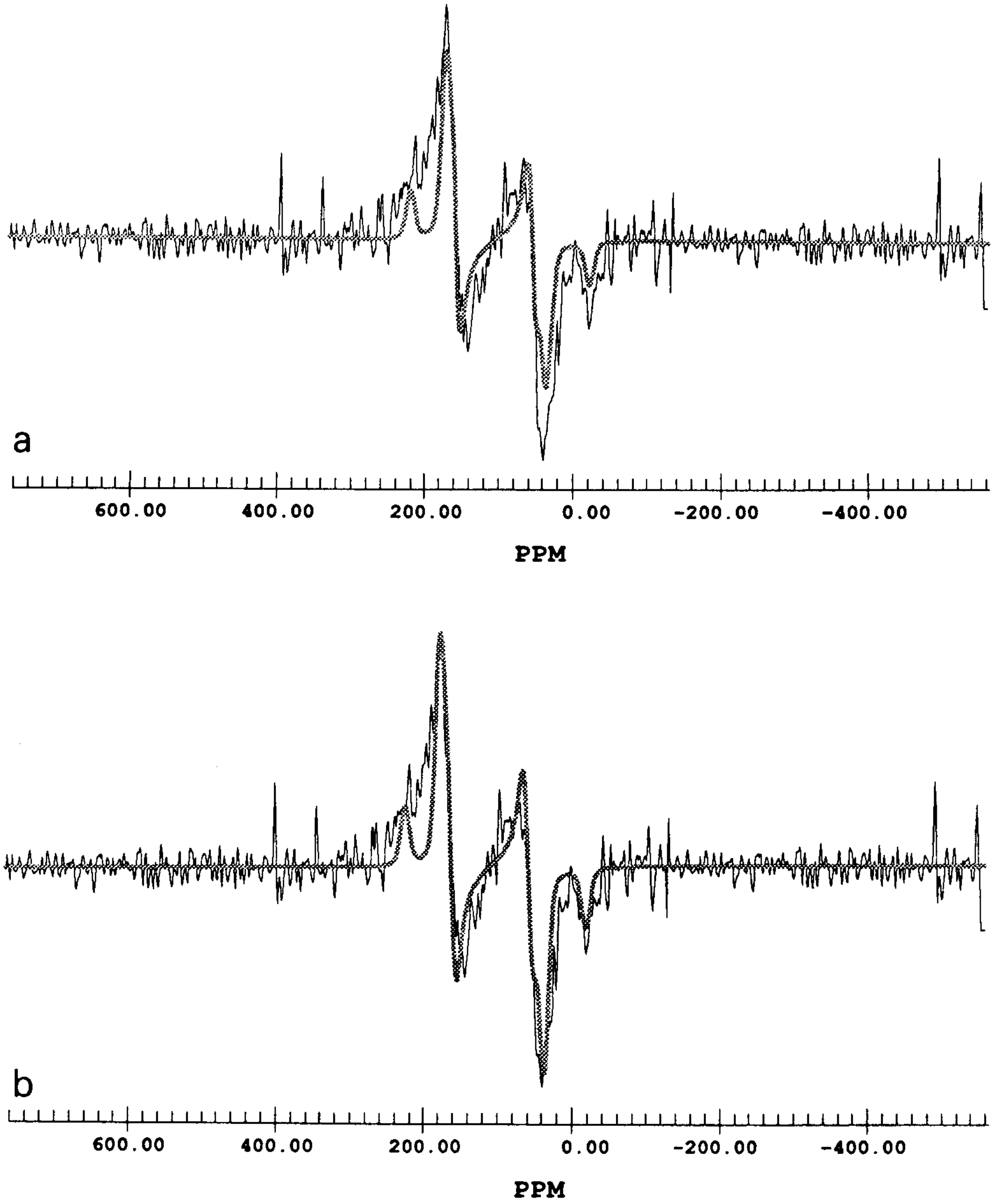

Fig. 5. First derivative overlap of the experimental and final simulated line shapes of dilabeled ^{13}C ethylene on a silver supported γ-alumina catalyst obtained by (a) including the scale in the fit and by (b) using implicit scaling.

the value produced by the fitting process. Both fitting techniques we have implemented are able to produce error estimates in the parameters that are optimized. The error estimation techniques used are based on the premise that the likelihood of finding the true value (μ) of a particular parameter follows a normal distribution [35–37].

Since the solution of the LS problem is the result of a search along the RSS hypersurface rather than an exact analytical solution, there is

TABLE 1

Optimum parameter values and error estimates obtained by the least squares analysis of both the mono- and dilabeled ^{13}C ethylene line shapes [a]

Parameter	Value extracted	Standard deviation
δ_{11} (ppm)	193.6	0.5
δ_{22} (ppm)	115.6	0.7
δ_{33} (ppm)	11.8	0.5
δ_0 (ppm)	107.0	taken to be exact
r_{cc} (Å)	1.339	0.007
α (°)	90.0	1.1
β (°)	95.8	0.3

[a] Chemical shifts for ^{13}C have been reported with respect to external adamantane, where the most shielded resonance (CH) has a shift of 29.50 ppm with respect to TMS.

no analytical form for the uncertainties in the final values of the parameters. Bevington [26] has shown that all of the information concerning the curvature about the minimum is contained in the inverse of the Hessian matrix and can be used to derive error estimates. However, only a perfectly symmetric behavior is predicated by this method [35]. In routine work where the system is well understood the quoting of such values will be totally satisfactory. It was thought appropriate in the study of this system to test the validity of the error estimates produced.

Table 1 shows the final values and their associated uncertainties. The validity of the standard deviations depends upon how close the actual response surface at the minimum reflects the parabola predicted by the curvature matrix. This can easily be shown by plotting out the response surface for each parameter around the minimum in steps of standard deviation units for each parameter. The results are shown in Fig. 6 where cross-sections of the error surface are plotted for the three parameters. It is clear that the β angle is better defined as the RSS values increases more steeply as the parameter is moved away from its optimum. Likewise the α angle shows more curvature than r_{cc} indicating that the bond distance has the largest uncertainty. Furthermore, the responses of both α and β could easily be described as being parabolic and symmetric in shape, indicating that error estimates derived from the curvature matrix are reliable. However, the error surface cross section for r_{cc} is at best unsymmetric and therefore the error estimates provided from the fitting do not accurately reflect the true uncertainty in the bond distance.

A more realistic estimate of the error in the parameters can be obtained by measuring a confidence interval which also takes into account the covariance [8]. This has been performed for the bond distance since this is the least defined pa-

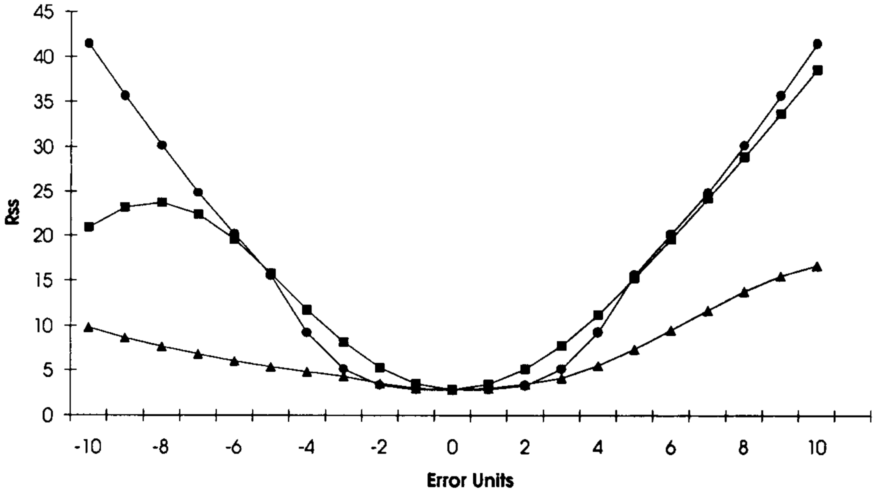

Fig. 6. Cross section of the response surface with respect to each parameter. (●) alpha E.U. = 1°; (■) beta E.U. = 0.3°; (▲) r_{cc} E.U. = 0.007 Å.

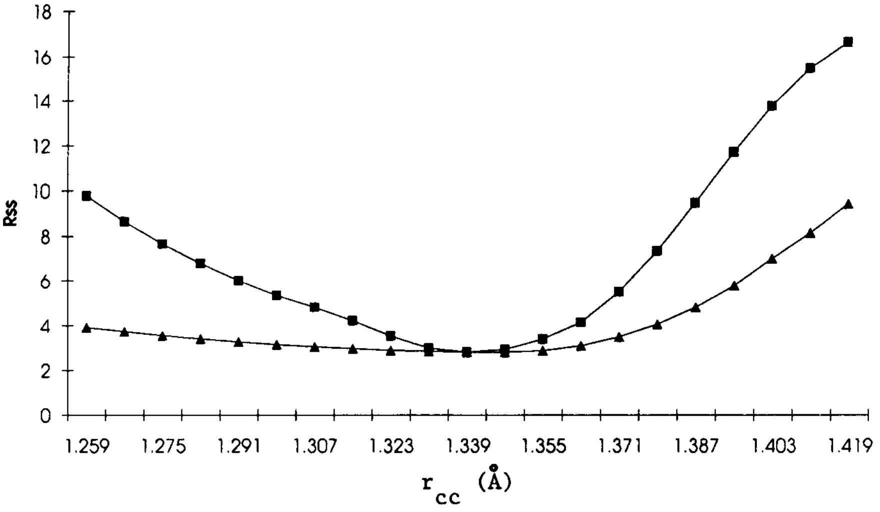

Fig. 7. Cross section of the error surface with respect to r_{cc} with and without the presence of correlated parameters. (■) Without optimization of correlated parameters; (▲) With optimization of correlated parameters.

rameter. The 95% confidence limits were found to be 1.339 (−0.036, +0.024) Å. The bottom curve in Fig. 7 shows the error surface that was used to calculate the confidence interval for the bond distance. It was calculated by stepping away from the minimum bond distance on both sides in steps of the error value and optimizing the two angles to give a RSS value. The top curve shows the RSS value as the bond distance is varied while keeping the angles at the values found for the overall optimum. The difference between the upper and lower curves has been attributed to the correlation between the angles and the bond distance. This conclusion is consistent with the covariance matrix obtained from the optimization procedures and the results of other workers [5,38] who have seen that the angles follow an increase in bond distance.

The implications of fixing the CS tensor in the dipolar fit have not been extensively pursued with our experimental data. We have, however, studied how errors in the chemical shift data affect the accuracy of the parameters extracted from the dilabeled spectrum by analyzing theoretical data. It was found that the standard deviation in the chemical shift data had to be on the order of 1 ppm to obtain results for r_{cc}, α, and β that were unaffected by the systematic error introduced by fixing the chemical shift tensor in the dipolar fit.

Conclusion

It has been shown that the powder line shapes from the systems of mono- and dilabeled ^{13}C ethylene on silver supported γ-alumina can be analyzed by non-linear least squares techniques. The steps taken to fit the experimental data have been necessary because of the unique nature of the system and the inability of the function to totally simulate the phenomena. The error analysis has shown how sensitive the experimental techniques are to the different physical parameters and have confirmed the validity of the error estimates provided by the two optimization methods.

We would like to acknowledge partial support for this research via a grant to P.D.E. from the National Science Foundation via Grant CHE 89-21632 and the NIH via grant GM 26295. We would also like to thank Dr. S.L. Morgan for his advice on the SIMPLEX optimization routine and Dr. Yen-Yuan James Wu for many helpful conversations about error propagation and the use of MINPACK. Copies of the source, data, and executable files are available via anonymous

FTP. An FTP session to our VAX can be started either by FTP ELLIS.NMR.SCAROLINA.EDU or FTP 129.252.33.3. The login id and password for the FTP account is **anonymous**. The source code, object files, and executable programs for VAX VMS and Unix versions are contained in the subdirectories vax_source, and unix_source, respectively. All data files and related materials are in the subdirectory called nmr_data. READ-LINESHAPE.ME files are available in the root directory to assist users with the use of the source and program files.

REFERENCES

1 P. Granger, Magn. Reson. Chem., 28 (1989) 156.
2 R.G. Griffin, J.D. Ellett, Jr., M. Mehring, J.G. Bullitt and J.S. Waugh, J. Chem. Phys., 57 (1972) 2147.
3 M.A. Kennedy and P.D. Ellis, Concepts in Magnetic Resonance, 1 (1989) 35.
4 M. Linder, A. Höhener and R.R. Ernst, J. Chem. Phys., 73 (1980) 4959.
5 R.D. Curtis, C.H. Penner, W.P. Power and R.E. Wasylishen, J. Phys. Chem., 94 (1990) 4000.
6 R.E. Wasylishen, G.H. Penner, W.P. Power and R.D. Curtis, J. Am. Chem. Soc., 111 (1989) 6082.
7 R.E. Wasylishen, W.P. Power, G.H. Penner and R.D. Curtis, Can. J. Chem., 67 (1989) 1219.
8 D.P. Schoemaker, C.W. Garland and J.W. Nibler, Experiments in Physical Chemistry, McGraw-Hill, New York, 1989.
9 J. Wang and P.D. Ellis, J. Am. Chem. Soc., 113 (1991) 9675.
10 Y. Chin, Ph.D. Thesis, University of South Carolina, Columbia, SC, 1990.
11 J. Wang, Ph.D. Thesis, University of South Carolina, Columbia, SC, 1992.
12 Y. Chin and P.D. Ellis, J. Am. Chem. Soc., 209 (1989) 243.
13 A. Pines, M.G. Gibby and J.S. Waugh, J. Chem. Phys., 59 (1973) 569.
14 NMR1, New Methods Research Inc., Syracuse, NY, 1990.
15 G.A. Pearson, J. Magn. Reson., 27 (1977) 265.
16 J.H. Noggle, Physical Chemistry on a Microcomputer, Little Brown, Boston, MA, 1985.
17 B.L. Silver, Irreducible Tensor Methods. An Introduction for Chemists, Academic Press, New York, 1976.
18 U. Haeberlen, High Resolution NMR in Solids Selective Averaging, Academic Press, New York, 1976.
19 B.C. Gerstein and C.R. Dybowski, Transient Techniques in NMR of Solids. An Introduction to Theory and Practice, Academic Press, New York, 1985.
20 D.W. Alderman, M.S. Solum and D.M. Grant, J. Chem. Phys., 84 (1985) 3717.
21 V.F. Dem'yanov and V.N. Malozemov, Introduction to MINIMAX., Dover, New York, 1974.
22 W.H. Flannery, B.P. Flannery, S.A. Teukolsky and W.T. Vetterling, Numerical Recipies, Cambridge University Press, New York, 1987.
23 Daniel and Wood, Fitting Equations to Data, Wiley, New York, 1980.
24 A.S. Deif, Advanced Matrix Theory for Scientists and Engineers, Abacus Press, London, 1982.
25 S.N. Demming and S.L. Morgan, Anal. Chem., 45 (1973) 278A.
26 P.R. Bevington, Data Reduction and Error Analysis for the Physical Sciences, McGraw-Hill, New York, 1969.
27 D.W. Marquardt, J. Soc. Indust. Math., 11 (1963) 431.
28 J.J. Moré, in G.A. Watson (Ed.), The Levenberg-Marquadt Algorithm, Implementation and Theory Numerical Analysis, Lecture Notes in Mathematics 630, Springer Verlag, Berlin, 1977.
29 P. Diehl, E. Fluck and R. Kosfeld, NMR Grundlagen und Fortschritte, Umfang 6, Springer Verlag, Berlin, 1972.
30 W. Spendley, G.R. Hext and F.R. Himsworth, Technometrics, 4 (1962) 441.
31 J.A. Nelder and R. Mead, Comput. J., 8 (1965) 308.
32 G.R. Phillips and E.M. Eyring, Anal. Chem., 60 (1988) 738.
33 E.M. Eyring, Anal. Chem., 60 (1988) 2656.
34 S. Brumby, Anal. Chem., 61 (1989) 1786.
35 F. James and M. Roos, Comput. Phys. Commun., 10 (1975) 343.
36 W.T. Eadie, D. Drijard, F.E. James, M. Roos and B. Sadoulet, Statistical Methods in Experimental Physics, North-Holland, Amsterdam, 1971.
37 A.J. Kilm and L.G. Butler, Concepts in Magnetic Resonance, 4 (1992) 205.
38 T.G. Oas, G.P. Drobny and F.W. Dahlquist, J. Magn. Reson., 78 (1988) 408.

Analytica Chimica Acta, 283 (1993) 1059–1079
Elsevier Science Publishers B.V., Amsterdam

Determination of proton densities on silica gel catalyst supports by *n*-quantum coherence in NMR

B.C. Gerstein [1,2], Marek Pruski [2] and Son-Jong Hwang [1,2]

Department of Chemistry [1], and Ames Laboratory [2], Iowa State University, Ames, IA 50011 (USA)

(Received 22nd April 1992; revised manuscript received 14th February 1993)

Abstract

The concepts involved in production and detection of *n*-quantum coherence in nuclear magnetic resonance (NMR) are considered. The use of coherent averaging to reduce internal Hamiltonians to zero, and to something other than their non-averaged values is reviewed. The experimental procedure necessary to produce and detect multiple quantum coherence in strongly dipolar coupled spin 1/2 solids is described. This procedure, using a single quantum propagator described in the initial sections, is then used to probe the *densities* (as distinguished from the chemical identities supplied by a 1-quantum fingerprint) of protons on silica gel surfaces of fumed, Cab-O-Sil HS5 silica gels which have: (a) not been relaxed by hydration, but have been reduced under flowing hydrogen; (b) been relaxed by hydration and subsequently reduced; (c) had deposited particles of metallic Ru, Pt, and Ag. As reflected in the highest order of multiple quantum coherence observed under a fixed time for development, the relaxed and reduced sample, and the sample with Ru deposited on it exhibit lower densities of protons than do the other samples. The implications to assuming that silica gel is an "inert" support for reactions involving reactions of hydrocarbons on supported metal catalysts are discussed.

Keywords: Nuclear magnetic resonance spectrometry; Catalysts; Silica gel; Solid state NMR

Since its discovery almost 50 years ago [1,2], and the subsequent realization [3] that the chemical shift of the nuclear resonance provides an incredibly delicate fingerprint of the chemical functionality of an element in a compound, NMR has provided chemists with one of the most powerful qualitative and quantitative analytical tools available to the chemist, materials scientist, and medical technician. The advent of high resolution techniques appropriate to nuclei in solids [4] supplied further dimensions to our ability to do qualitative analysis of chemical functionalities, in that added to the chemical shift were the dipolar interaction and the quadrupolar coupling, with attendant anisotropic information. In the present effort, we describe the application of yet another fingerprint supplied by dipolar coupled spin 1/2 nuclei in solids, that of the development of multiple quantum coherence, to probing differences among protons on surfaces of silica gel catalyst supports. This characteristic gives information about the *densities* of protons on these surfaces, as distinct from chemical shifts to identify chemical functionalities. These densities may be critically important in the chemistry taking place during reactions catalyzed over supported metal surfaces [5]. This development of multiple quantum coherence among dipolar coupled spin 1/2 nuclei in solids is one of a number of two-dimensional experiments in NMR which have been developed since the mid 1970s [6–8] and have since been extensively reviewed [9–13]. In the specific case of using MQ coherence to enumerate numbers of

Correspondence to: B.C. Gerstein, Department of Chemistry, Iowa State University, Ames, IA 50011 (USA).

strongly coupled spins in ensembles of coupled clusters of protons in solids [14,15] the initial work developed multiple quantum coherence in steps of two quanta, such that values of multiple quantum coherence, k, of 0, 2, 4, 6 ..., or 1, 3, 5, ... might be detected. Later work (vide infra) resulted in the use of pulse sequences which developed multiple quantum coherence in steps of one quantum, such that values of $k = 0$, 1, 2,... could be detected.

MULTIPLE QUANTUM COHERENCE IN DIPOLAR COUPLED SPIN 1/2 SYSTEMS

In liquids, the coupling mechanism used to produce multiple quantum coherence is the two-body scalar, or J-coupling. The secular portion of the spin-space part of this interaction is $I_z S_z$ for the heteronuclear case. In solids, the case to be discussed here, the interaction is the two-body homonuclear dipolar coupling between spin 1/2 systems, e.g., among protons in a solid. The secular portion of the spin-space part of this interaction is $I_1 \cdot I_2 - 3I_{z1}I_{z2}$. The pulse sequences used to develop multiple quantum coherence in the latter case will therefore differ from those used for the former, for the same reason that the dipolar echo sequence (τ, 90_x, τ, 90_y, τ) used to average the two-body homonuclear dipolar interaction to zero differs from the spin echo sequence (τ, 180_x, τ) used to average interactions scaling as I_z to zero. However, the extension of the present description to heteronuclear dipolar coupling, and to scalar coupling will hopefully be obvious, with the techniques used to generate, and detect multiple quantum coherence being more easily achieved than in the present case.

To introduce the subject matter of the present work, it is useful to ask "what is observed in an NMR experiment?" The answer is always a transverse component of spin angular momentum. With phase detection along y in the rotating frame, what is observed is a time decay of magnetization; the expectation value of the y component of nuclear angular momentum;

$$\langle I_y(t)\rangle = \mathrm{Tr}[\rho(t) I_y] \tag{1}$$

From this formalism it is immediately obvious that we are invoking the use of the quantum statistical method in that the density operator, ρ, *must* be used to describe the phenomena discussed here [16].

The decay of transverse nuclear angular momentum, the time dependence of which is given by $\rho(t)$, and phase of which is specified in this case by the operator I_y, is driven by the presence of time-independent Hamiltonians, $\hat{H}$, as follows:

$$\rho(t) = \exp-(i\hat{H}t)\cdot\rho(0)\cdot\exp(i\hat{H}t) \tag{2}$$

The spectrum is obtained by Fourier transformation of the time domain signal. We remind ourselves of the quantum mechanics involved in this statement with a short review.

We consider an ensemble of identical systems, each described by a set of stationary states. These identical systems for purposes of the present discussion might be "isolated" nuclear spins (e.g., ^{13}C nuclei at a natural abundance of 1.1% decoupled from other nuclei via strong rf decoupling), or isolated pairs of nuclear spins (e.g., pairs of protons in partially hydrated calcium sulfate, $CaSO_4 \cdot xH_2O$, with $x < 2$), or many ($\sim 10^{23}$) protons in strongly dipolar coupled solids. The nuclear spin basis functions appropriate to describe the systems of the ensemble will therefore in general be many-body stationary states which we lable $|M_s\rangle$. These are eigenstates of the total z component of nuclear spin angular momentum such that

$$I_z|M_a\rangle = a|M_a\rangle \tag{3a}$$

Two of these many body states, $|M_a\rangle$, $|M_b\rangle$, differ by $k = a - b$ in z component of total angular momentum. Further, the state of each system can in general be a time-dependent superposition of these stationary states:

$$|\psi(t)\rangle = \Sigma_j c_j(t)|M_j\rangle \tag{3b}$$

For example, in ensembles which consist of coupled pairs of spin 1/2 nuclei, where the coupling interaction is small compared to the Zeeman interaction, the stationary states of the coupled systems can be arranged to be eigenfunctions of the square of the total spin operator, I^2, and of the z component of spin I_z. Two coupled spins can have maximum total spin $I = 1$, and z component $-I \leq I_z \leq I$ in steps of unity. Three coupled spins 1/2 can have maximum total spin $I = 3/2$, etc. It is these many-spin states which are designated as $|M_a\rangle$ above.

We remember that the probability of finding any system in stationary state $|M_s\rangle$ is

$$P_s = \overline{c_s^*(t)c_s(t)} = \overline{c_s(t)c_s^*(t)} \tag{4}$$

where the bars above the c_s values mean an ensemble average. The operator ρ is defined by the ensemble average of the product

$$\rho = |\psi\rangle\langle\psi| \tag{5}$$

such that the i,jth matrix element is

$$\rho_{ij} = \overline{\langle i|\psi\rangle\langle\psi|j\rangle} = \overline{c_i c_j^*} \tag{6}$$

A non-vanishing value of ρ_{ss} therefore represents a population of the state $|M_s\rangle$. An observable signal in NMR means a non-vanishing value of $\rho_{s,s\pm1}$. This means that in the ensemble of systems being observed, there is a phase coherence in the ensemble associated with system states $|M_s\rangle$ and $|M_{s\pm1}\rangle$. We designated this a *single quantum coherence*. This is to say that we observe a decaying oscillation resulting from a coherence of the ensemble in which the time-dependent state responsible for the behaviour of the system is a superposition of two states differing from each other by a single quantum. The most familiar example is the case of an ensemble of single spin 1/2 systems, in which case the two basis states are $|M_r\rangle \equiv |\alpha\rangle \equiv |1/2\rangle$, and $|M_{r-1}\rangle = |M_s\rangle = |\beta\rangle \equiv |-1/2\rangle$. A non-vanishing component of transverse angular momentum is represented by a coherence in the ensemble of systems with a superposition of states consisting of two stationary states which differ from each other by 1 in expectation value of I_z;

$$\begin{aligned} |\psi\rangle &= c_{1/2}(t)|\alpha\rangle + c_{-1/2}(t)|\beta\rangle \\ &\equiv c_\alpha|\alpha\rangle + c_\beta|\beta\rangle \end{aligned} \tag{7}$$

such that the ensemble average of the product $c_\alpha(t)c_\beta^*(t)$ is non-zero. For example, such would be the case immediately after a 90_x^0 pulse, with rf field intensity ω_1/γ, and the values of the c_k values would be

$$c_\alpha(t = \pi/2\omega_1) = 1/\sqrt{2}$$

and

$$c_\beta(t = \pi/2\omega_1) = i/\sqrt{2} \tag{8}$$

In this case, one calculates that the expectation values of I_x and I_z are zero, and 1/2 for I_y.

Statistical thermodynamics enters when we consider that the ensemble in question is prepared in some equilibrium state before observation, i.e., we expose an ensemble of nuclear spins, I, in a field until equilibrium is achieved under the Zeeman interaction $\hat{H}_z$, and

$$\rho(0) \equiv \rho_{\text{eq}} = (1/Z)\exp-\left(\hat{H}_z/k_BT\right) \sim \Sigma_i I_{zi}, \quad i = 1,2\ldots \tag{9}$$

is the operator form of ρ. Z is the ensemble partition function.

It is next useful to be reminded of the results of coherent averaging [4] theory as applied to the spin portion of internal Hamiltonians. We first note that nuclear spin Hamiltonians may in general be expressed as a product of a constant characteristic of the interaction in question, of "real space" operators, and of "spin space" operators. For example, for the heteronuclear dipolar interaction between spins I and S, the constant is $(\gamma_I\gamma_S/r_{IS}^3)$, the "real space" portion is $(1 - 3\cos^2\theta)$, and the "spin space" portion is I_zS_z. It is assumed that the real-space portion of the internal Hamiltonians are constant in the experiments under consideration, i.e., there is no molecular motion or experimenter-supplied sample spinning.

When we manipulate $\hat{H}_{\text{int}}$ by rf pulse sequences which are cyclic (the ensemble is returned to its initial state after a cycle of rf pulses, meaning that the propagator $U_{\text{rf}}(t_c, 0)$ associated with the pulse train from time zero to time t_c, is unity at cycle times t_c, and integer multiples of these times) and periodic, the leading term in the result, observed at cycle times nt_c is

$$\rho(nt_c) = \exp\left(-i\bar{H}^{(0)}nt_c\right)\cdot\rho(0)\cdot\exp\left(i\bar{H}^{(0)}nt_c\right) \tag{10}$$

where $\bar{H}^{(0)}$ is the time average of a static internal Hamiltonian made time dependent by the rf pulses.

$$\bar{H}_{\text{int}}^{(0)} = (1/t_c)\int_0^{t_c} \mathrm{d}t\tilde{H}_{\text{int}}(t) \tag{11}$$

$\tilde{H}_{\text{int}}(t)$ is the instantaneous value of the internal Hamiltonian as determined by the rf pulses:

$$\tilde{H}_{\text{int}}(t) = U_{\text{rf}}^{-1}(t, 0)H_{\text{int}}U_{\text{rf}}(t, 0) \tag{12}$$

$U_{\text{rf}}(t, 0)$ is the propagation operator due to the rf pulses from time zero to time t. For n time intervals $\delta_1 = t_1 - 0$, followed by $\delta_2 = t_2 - t_1$, followed by … $\delta_n = t_n - t_{n-1}$, U_{rf} may be expressed as the product

$$U_{\text{rf}}(t, 0) = U_{\text{rf}}(\delta_n)\dots U_{\text{rf}}(\delta_1) \tag{13}$$

whereby

$$U_{\text{rf}}^{-1}(t, 0) = U_{\text{rf}}^{-1}(\delta_1)\dots U_{\text{rf}}^{-1}(\delta_n) \tag{14}$$

Equation 12 can always be expressed as a product of rotations in spin space acting on components of angular momentum operators. For example, if the rf pulse sequence (τ, 180_y, τ) with perfect δ function rf pulses produces U_{rf}, then at times $0 \le t < \tau$, when the rf Hamiltonian is zero, U_{rf} (t, 0) takes the form $\mathrm{e}^0 = 1$. In this time interval, $\tilde{I}_z = \mathrm{e}^0 I_z \mathrm{e}^0 = 1 \cdot I_z \cdot 1$ which we may formally identify as a rotation, R, of unity, performed on I_z, symbolized by $RI_z = 1 \cdot I_z$. At time $t = \tau$, the rf Hamiltonian corresponds to an infinitely sharp 180° rotation about the y axis. $U_{\text{rf}}(t = \tau) = \mathrm{e}^{i\pi Iy}$, and the physical result is a 180_y rotation, R_{180y}. For $\tau < t \le 2\tau$, the rf again is zero, and U_{rf} is unity. Under this sequence, therefore, with the spin portion of H_{int} being proportional to I_z, keeping in mind the time ordering dictated by Eqns. 12 and 14, we find

$$0 \le t < \tau,\ \tilde{I}_z = 1 \cdot I_z = I_z$$
$$t = \tau,\ \tilde{I}_z = 1 \cdot R_{180y} I_z \Rightarrow -I_z \tag{15}$$
$$\tau < t \le 2\tau,\ \tilde{I}_z = 1 \cdot R_{180y} \cdot 1 \cdot I_z = -I_z$$

The familiar result is that *at cycle times $2n\tau$*, under the spin-echo sequence $(\tau, 180, \tau)^n$, chemical shifts and field inhomogeneities, with spin operators I_{zk}, vanish (but other interactions, such as homonuclear dipolar coupling, do not). This is to say that at cycle times $2n\tau$, with the internal Hamiltonian being proportional to I_z, that $\bar{H}_{\text{int}}^{(0)}$ is zero; i.e.

$$H_{\text{cs}}^{(0)} \sim \int_0^{2\tau} \mathrm{d}tU_{\text{rf}}^{-1}(t)\tilde{H}_{\text{cs}}U_{\text{rf}}(t) = \omega_{\text{cs}}[I_z\tau + (-I_z)\tau]$$
$$= 0 \tag{16}$$

where ω_{cs} is a product of a constant and the real-space portion of the chemical shift Hamiltonian.

Another perhaps less familiar result is that under symmetry adapted dipolar decoupling sequences [τ, 90_x, τ, 90_y, τ], homonuclear dipolar terms vanish, but chemical shifts are scaled. Consider the WAHUHA symmetry adapted version of the above dipolar echo sequence, which is [τ, 90_x, τ, 90_y, 2τ, $90_{\bar{y}}$, τ, $90_{\bar{x}}$, τ]. Using Eqns. 12–14, we find for ideal δ function rf pulses, the following values of $\tilde{I}_z(t)$:

$$0 \le t < \tau;\ \tilde{I}_z = 1 \cdot I_z = I_z$$
$$t = \tau;\ \tilde{I}_z \Rightarrow 1 \cdot R_{90\bar{x}} I_z = -I_y$$
$$\tau < t < 2\tau;\ \tilde{I}_z = 1 \cdot R_{90\bar{x}} \cdot 1 I_z = -I_y$$
$$t = 2\tau;\ \tilde{I}_z \Rightarrow 1 \cdot R_{90\bar{x}} \cdot 1 \cdot R_{90\bar{y}} I_z = -I_x \tag{17a}$$

etc. We may then immediately infer that, the scalar product $\mathbf{I}_1 \cdot \mathbf{I}_2$ being invariant to rotation, the time dependence of the operator $H_{zz} = (\mathbf{I}_1 \cdot \mathbf{I}_2 - 3I_{z1}I_{z2})$ is as follows:

$$0 \le t < \tau;\ \tilde{H}_{zz} = H_{zz}$$
$$t = \tau;\ I_{z1}I_{z2} \Rightarrow I_{y1}I_{y2}$$

so

$$\tilde{H}_{zz} \Rightarrow H_{yy} \tag{17b}$$

Here, $H_{kk} = \mathbf{I}_1 \cdot \mathbf{I}_2 - 3I_{k1}I_{k2}$. Then the two-body homonuclear dipolar Hamiltonian averaged over the cycle time $t_c = 6\pi$ becomes

$$\begin{aligned}\bar{H}_{\text{DII}}^{(0)} = (\omega_{\text{D}}/6\pi)\big[&\tau(I_1 \cdot I_2 - 3I_{z1}I_{z2})\\ &+\tau(I_1 \cdot I_2 - 3I_{y1}I_{y2})\\ &+2\tau(I_1 \cdot I_2 - 3I_{x1}I_{x2})\\ &+\tau(I_1 \cdot I_2 - 3I_{y1}I_{y2}) + \tau(I_1 \cdot I_2 - 3I_{z1}I_{z2})\big]\\ \equiv \omega_{\text{D}}&(H_{zz} + H_{yy} + H_{xx})/3 = 0\end{aligned} \tag{18}$$

where ω_D is a product of a constant and the real-space portion of the space-spin product dipolar Hamiltonian.

An important result just seen is that the sum

$$(H_{xx} + H_{yy} + H_{zz})\tau = \Sigma H_{kk} = 0 \qquad (19)$$

for two spins I_1 and I_2. *In both of the above cases,* the average Hamiltonian for a specific interaction is made to vanish, leaving remaining interactions to be observed. However, it is possible to manipulate certain internal interactions such that the average Hamiltonian is not zero, but another desired quantity.

Using the above ideas, it is seen that for the development of multiple quantum coherence we seek an average Hamiltonian that allows the density operator at zero time, $\rho(0)$, to evolve in such a manner that $\rho_{i,i\pm k} \neq$ zero. k is the order of the multiple quantum coherence.

The process, then, is to manipulate some internal Hamiltonian with cyclic, periodic rf pulses such that at cycle times nt_c, we have an average Hamiltonian which allows zero-time equilibrium density operator,

$$\rho(0) \equiv \rho_{eq} \sim \Sigma_i I_{zi},\ i = 1, 2, \ldots$$

containing only diagonal terms representing populations in the Zeeman basis set, to develop multiple quantum coherence, i.e. to develop in such a manner that $\rho_{i,i\pm k} \neq$ zero, for $1 \leq k < \infty$. Since we can only detect single quantum coherence (1Q-COH) with NMR, we note in advance that once produced, the MQ-COH must be reduced to 1Q-COH *in a manner which reflects the MQ coherence therein contained* in order to be detected.

Examples of terms in the density operator which exhibit single quantum coherence might be single spin terms I_i^+ and I_i^-, or two-spin products of the form $I_1^+ I_{z2}$. Double quantum coherence is represented by two-spin product terms in the density operator such as $\Sigma_{i,j}(I_i^+ I_j^+ + I_i^- I_j^-)$. Triple quantum coherence would be represented by three-spin products such as $I_j^+ I_k^+ I_m^+$.

We can understand how this process works by example. An ensemble of spin 1/2 systems (e.g., protons in solid adamantane) is allowed to come to equilibrium in a static field for a time long compared to T_1. Then

$$\rho(0) \sim \Sigma_i I_{zi} \qquad (20)$$

The sum is over all spins in the sample. Under the influence of an average Hamiltonian, produced by coherent averaging in spin space as discussed for the cases of the spin echo and the dipolar echo, the nuclear magnetization of this ensemble is propagated in time. The formal time evolution formula may be expressed in terms of the product

$$\mathrm{f(A, B) = e^{A} \cdot B \cdot e^{-A}} \qquad (21)$$

where A and B are operators. This operator equation takes the form [17]

$$\mathrm{e^{A} \cdot B \cdot e^{-A} = B + [A, B] + [A, [A, B]]/2! + [A, [A, [A, B]]]/3! + \ldots} \qquad (22)$$

such that

$$\rho(nt_c) \sim \exp(-i\bar{H}nt_c) \cdot \Sigma_i I_{zi} \cdot \exp(i\bar{H}nt_c) = \Sigma I_{zi} + [\cdot \mathrm{int}_c \bar{H}, \Sigma I_{zi}] + [-\mathrm{int}_c \bar{H}, [-\mathrm{int}_c \bar{H}, \Sigma I_{zi}]]/2! + \ldots \qquad (23)$$

The leading term, $\Sigma_i I_{zi}$ represents populations. The following terms must then be arranged so as to evolve single and higher quantum coherences.

In order to understand how to choose an average Hamiltonian which will produce multiple quantum coherence in the time-developed density operator, $\rho(t)$, as given by Eqn. 23, it is necessary to look at the commutation rules for angular momentum operators. We know that

$$[I_{k1}, I_{k2}] = [I_{k1}, I_{k1}] = 0,\ k = x, y, z$$
$$[I_z, I^{\pm}] = \pm I^{\pm} \qquad (24)$$
$$[I^{\pm}, I^{\mp}] = \pm 2I_z$$

Given the form of $\rho_{eq} \equiv \rho(0) \sim \Sigma_i I_{zi}$, Eqns. 22 and 24 immediately tell us that we want $\bar{H}$ to contain terms such as $I_i^{\pm}$. Since we are using the internal homonuclear dipolar coupling Hamiltonian H_{zz} as that which is to be manipulated in order to develop the multiple quantum coherence according to Eqn. 23, we realize that we will always be dealing with products between two spins k and j containing terms such as $I_{mk}I_{mj}$, with $m = x, y, z$.

To begin to think about how rotations in spin space affect the two-body homonuclear dipolar Hamiltonian H_{zz}, it is useful to remember [18] that the effect of a rotation of the mth component of angular momentum, I_m, by the operation

$$R_j(\theta)I_m = e^{i\theta I_j} \cdot I_m \cdot e^{-i\theta I_j} = I_m \cos(\theta\epsilon_{jmp}) - I_p \sin(\theta\epsilon_{jmp}) \qquad (25)$$

where ϵ_{jmp} is zero if any two of j, m, p are the same, unity if j, m, and p represent some cyclic order of x, y, and z, and minus one if the order is anticyclic. Then a result which is found with some algebra is that a rotation of the two-body Hamiltonian for spins 1 and 2, H_{zz}, by ξ about the y axis, followed by a rotation by ϕ about the z axis yields

$$\begin{aligned} R_z(\phi)R_y(\xi)H_{zz} &= (\omega_D/2)(3\cos^2\xi - 1)H_{zz} - (3\omega_D/2) \\ &\quad \times\left[(I_{z1}I_2^+ + I_1^+I_{z2})\,e^{-i\phi}\right]\sin\xi\cos\xi \\ &\quad + (3\omega_D/2)\left[I_1^+I_2^+\,e^{2i\phi} + I_1^-I_2^-\,e^{-2i\phi}\right]\sin^2\xi \end{aligned} \qquad (26)$$

The interesting result shown by Eqn. 26 is that a general rotation of H_{zz} in spin space yields a propagator (the exponential of the rotated Hamiltonian) containing populations, (H_{zz}), single quantum terms ($I_1^{\pm}I_{z2}$) and double quantum terms ($I_1^{\pm}I_2^{\pm}$). As a special case of this result, we illustrate the formation of a two-quantum propagator under a particularly simple periodic and cyclic sequence [10]. This is the sequence (τ, 90_x, 4τ, $90_{\bar{x}}$, τ) which we shall denote x, $\bar{x}$. We assume ideal δ function pulses. Under this sequence, the operator $\tilde{I}_z(t)$ is as follows:

$$\begin{aligned} &0 \le t < \tau;\ \tilde{I}_z = 1 \cdot I_z = I_z \\ &t = \tau;\ \tilde{I}_z = 1 \cdot R_{90\bar{x}}I_z = -I_y \\ &\tau < t < 5\tau;\ \tilde{I}_z = -I_y \\ &t = 5\tau;\ \tilde{I}_z = 1 \cdot R_{90\bar{x}} \cdot 1 \cdot R_{90x}I_z = I_z \\ &5\tau < t \le 6\tau;\ \tilde{I}_z = I_z \end{aligned} \qquad (27)$$

Then, for example, in the time interval $0 \le t < \tau$, $\tilde{H}_{zz} = H_{zz}$ (see Eqn. 12). From an observation of the values of $\tilde{I}_z(t)$, and the recognition that H_{kk} contains the product $\tilde{I}_k\tilde{I}_k$ with $k = x, y, z$, it is possible to immediately infer the values of $\tilde{H}_{zz}(t)$, and thus to calculate the average Hamiltonian corresponding to H_{zz} to zeroth order in the Magnus expansion [19]:

$$\bar{H}_{zz}^{(0)} = (1/6\tau)\int_0^{6\tau} dt\tilde{H}_{zz} = (1/3)(H_{zz} + 2H_{yy}) \qquad (28)$$

With the identity $\Sigma_k H_{kk} = 0$, we find that under the above sequence

$$\bar{H}_{zz}^{(0)} \sim \{-H_{xx} - H_{yy} + 2H_{yy}\} = H_{yy} - H_{xx} \qquad (29)$$

Under the sequence y, $\bar{y} \equiv (\tau, 90_y, 4\tau, 90_{\bar{y}}, \tau)$ the average homonuclear dipolar Hamiltonian is the negative of that found in Eqn. 29, i.e., is proportional to $H_{xx} - H_{yy}$. Thus this sequence can be used to produce an average Hamiltonian which will act to reverse, in time, the effect of the average of the average Hamiltonian, $H_{yy} - H_{xx}$, which was used to produce the multiple quantum coherence. As will be seen, this reconversion is performed in such a manner that the information content associated with the multiple quantum coherence is not lost. The means of doing so (vide infra) is to phase shift the two-quantum excitation sequence x, $\bar{x}$ with respect to the two-quantum reconversion sequence y, $\bar{y}$ in steps of $2\pi/k_{\max}$, where $k_{\max}$ is the highest order of MQ-COH to be observed.

With $I^+ = I_x + iI_y$, etc., we find that the average two-body homonuclear dipolar Hamiltonian under the 2-Q excitation sequence x, $\bar{x}$ is proportional to

$$I_1^+ I_2^+ + I_1^- I_2^- \tag{30}$$

for the pair of spins I_1, I_2.

Now consider how this sequence can be used to develop multiple quantum coherence for an ensemble of *pairs* of dipolar coupled spins I_1 and I_2. We might anticipate in advance that for this simple case, using a two-quantum propagator, all that will be seen are populations, and two quantum coherence. Suppose the system has been prepared as previously described, i.e., allowed to come to equilibrium in a static field. Then with $\rho(0) \sim (I_{z1} + I_{z2})$, under this sequence, repeated for n cycle times, $t_c = 6\tau$, the time dependence of the density matrix becomes

$$\rho(nt_c) = U_{2Q}\rho(0)U_{2Q}^{-1}$$

where U_{2Q} is, to zeroth order,

$$U_{2Q} = \exp[-(\mathrm{int}_c\omega_D/2)(I_1^+ I_2^+ + I_1^- I_2^-)] \tag{31}$$

Then with $\theta = nt_c\omega_D/2$, Eqns. 22 and 23 yield

$$\begin{aligned}\rho(nt_c) = \{ & I_{z1} + I_{z2} \\ & + i\theta[(I_1^+ I_2^+ + I_1^- I_2^-), (I_{z1} + I_{z2})] \\ & + (i\theta)^2[(I_1^+ I_2^+) + (I_1^- I_2^-), \\ & [(I_1^+ I_2^+ + I_1^- I_2^-), \\ & (I_{z1} + I_{z2})]]/2! + \ldots\} \\ = {} & I_{z1} + I_{z2} - 2i\theta(I_1^+ I_2^+ + I_1^- I_2^-)\end{aligned} \tag{32}$$

Only the first two terms in the series represented by Eqns. 22 and 23 are non-zero. The remaining terms vanish. Only populations and double quantum coherence remain. At θ near zero, i.e., at times nt_c small compared to the inverse of the dipolar linewidth ω_D^{-1}, there exist only populations. As nt_c becomes of the order of the dipolar linewidth, two-quantum coherence makes its appearance. No more than two-quantum coherence is ever seen regardless of how long the system is allowed to evolve, as one would physically expect from an ensemble consisting of pairs of coupled pairs of spins 1/2. The reader will want to verify by performing the calculations $\langle m | \rho(nt_c) | m - k\rangle$ that for this representation of $\rho(nt_c)$ only the terms ρ_{11}, ρ_{22}, ρ_{33}, ρ_{13}, and ρ_{31} are non-zero within the triplet basis set $|I,I_z\rangle$, labelled $|1\rangle$, $|2\rangle$, and $|3\rangle$ in Eqn. 33.

$$\begin{aligned}|m\rangle &= |3\rangle = |1,1\rangle = |\alpha\alpha\rangle \\ |m-1\rangle &= |2\rangle = |1, 0\rangle = |(\alpha\beta + \beta\alpha) > /\sqrt{2} \\ |m-2\rangle &= |1\rangle = |1, -1\rangle = |\beta\beta\rangle\end{aligned} \tag{33}$$

For sufficiently long times, the ensemble will oscillate between zero and two quantum coherence with time.

The results just calculated for an ensemble of dipolar coupled spin 1/2 pairs indicate that under the propagator U_{2Q} developed by the sequence (τ, 90_x, 4τ, $90_{\bar{x}}$, τ) the selection rules are such that populations and double quantum coherence is observed for an ensemble of pairs of dipolar coupled spins 1/2.

We now must consider more closely what was meant by the past statement that the multiple quantum coherence, once produced, must be transferred to 1Q-COH in a manner which reflects the MQ-COH previously produced. As a thought experiment to begin the process, recall the inversion-recovery experiment to measure T_1. In this case, the system is prepared in a state of non-equilibrium populations by an inverting 180° pulse. After a time τ during which the system is allowed to evolve under "T_1 processes", these populations are converted into 1Q-COH using a 90° pulse. The initial intensity of the decay after the "read out" 90° pulse is used, as a function of τ, to calculate T_1. A similar reasoning applies to detecting multiple quantum coherence. The MQ-COH is developed as a function of multiples of the production sequence cycle time t_c. This development is only observable if it is converted into 1Q-COH. During the development, therefore, the MQ-COH is manipulated in such a manner that when converted back into 1Q-COH, the information content of the MQ-COH is contained in the initial intensity of the 1Q-COH which is detected.

To form a picture of how this works, it is useful to think about how the different orders of nQ-COH evolve with time. As indicated in the example in Eqn. 32, the higher orders of multiple quantum coherence develop as $\theta \sim nt_c\omega_{\mathrm{Dij}}$ increases for the i,jth pair of spins. Therefore, it seems reasonable that the evolution of, e.g., populations, 1Q-COH, and 2Q-COH might look as is shown in Fig. 1. I_0 represents populations, I_1 the intensity of single quantum coherence, I_2 the intensity of double quantum coherence, etc. Initially one starts with populations. As spin pairs begin to couple to form higher orders of nQ-COH, there is a net loss in populations, and a build up (in the particular example for which the calculation using Eqn. 32 was made), first of 2Q-COH, the second term in the expansion of the evolution of ρ, and then of higher orders of MQ-COH as time increases. In the example shown in Fig. 1, we assume that we are allowed to build MQ-COH in steps of single quanta, and we will later provide a single quantum propagator U_{1Q} which allows this development to be performed.

Given the development of MQ-COH shown in Fig. 2, caused by the single quantum propagator U_{1Q}, it is simple to conceive how one reverses the process to convert back to an observable 1Q-COH. One simply causes the system to evolve under the propagator U_{1Q}^{-1}. Since U_{1Q} will be of the form exp $\{-i\bar{H}nt_c\}$, with $\bar{H}$ being an average Hamiltonian created by manipulating the homonuclear dipolar interaction, time-reversal is achieved by manipulating the homonuclear dipolar Hamiltonian such that from time nt_c to $2nt_c$ the average Hamiltonian is $-\bar{H}$. In the case of the two quantum propagator, we have seen that

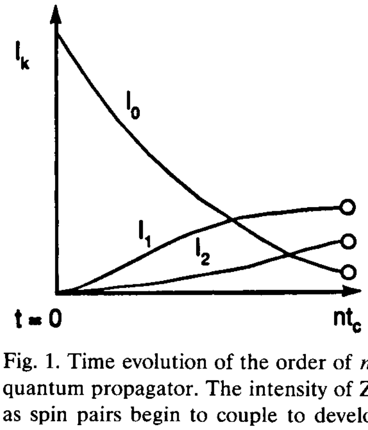

Fig. 1. Time evolution of the order of nQ-COH using a single quantum propagator. The intensity of ZQ-COH(I_0) decreases as spin pairs begin to couple to develop the higher order of MQ-COH and build up their intensity(I_1 and I_2).

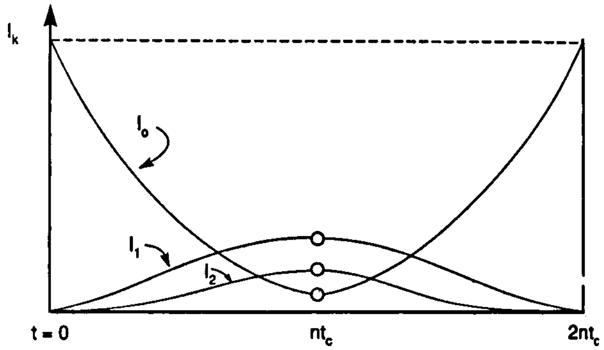

Fig. 2. The MQ-COH for higher orders are first created over a time period of nt_c, and then collected this MQ-COH back into ZQ-COH at the time $2nt_c$ by using the negative of the average Hamiltonian. Aside from relaxation, the preparation ($0 \le t < nt_c$) and mixing period($nt_c \le t < 2nt_c$) exactly mirror each other. This diagram illustrates the statement of the cyclic properties of U_{rf}. At the end of $2nt_c$, $I_0(t=0) = I_0(t=2nt_c)$.

the sequence ($\tau/4$, 90_x, τ, $90_{\bar{x}}$, $\tau/4$) produces the average Hamiltonian proportional to $H_{yy} - H_{xx}$. We have pointed out that the sequence ($\tau/4$, 90_y, τ, $90_{\bar{y}}$, $\tau/4$) results in the average homonuclear dipolar Hamiltonian $H_{xx} - H_{yy} \equiv -(H_{yy} - H_{xx})$. Thus the application of the sequence

$$(\tau/4,\ 90_x,\ \tau,\ 90_{\bar{x}},\ \tau/4)n,$$

$$(\tau/4,\ 90_y,\ \tau,\ 90_{\bar{y}},\ \tau/4)n$$

would first create the MQ-COH over a time of n cycle times t_c, and then by time-reversal accomplished by using the negative of the average Hamiltonian during the preparation period, "collect" this MQ-COH back into zero quantum coherence (ZQ-COH) at time $2nt_c$. The process might be visualized as is indicated in Fig. 2.

At this point, however, there is no information content in the ZQ-COH shown in Fig. 2 at time $2nt_c$ which would be indicative of the MQ-COH created during the times nt_c.

Therefore, as a second thought experiment, dictated by the knowledge that different orders of MQ-COH (vide infra) oscillate at multiples of the 1Q-COH under a frequency offset, let us assume that after the production period, nt_c, a frequency offset, δ/Hz, is imposed upon the experiment. Then the behaviour of ZQ-COH, 1Q-COH, and 2Q-COH might appear as indicated in Fig. 3. The

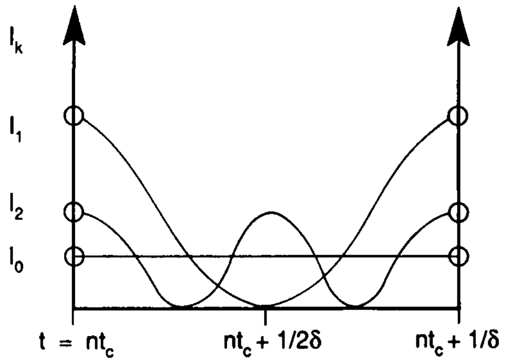

Fig. 3. The behavior of ZQ-COH, 1Q-COH and 2Q-COH with a frequency offset, δ/Hz, after the preparation period, nt_c. Then nQ-COH has the property of the cosine function, $I_n \propto \cos(n\delta/\text{Hz})$. See Eqn. 39.

ZQ-COH does not oscillate under an offset. The 1Q-COH will oscillate with period δ^{-1}. The 2Q-COH will oscillate with period $(2\delta)^{-1}$, etc.

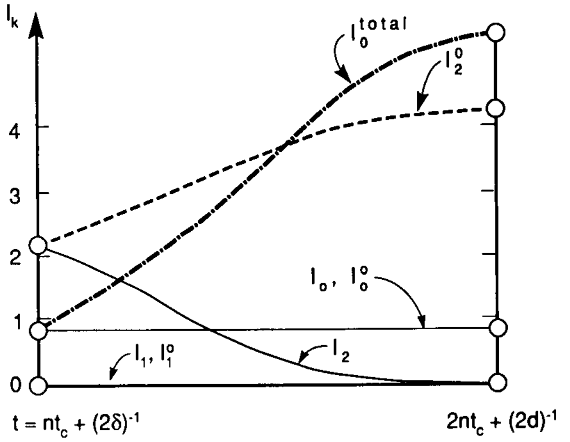

Fig. 4. The behavior of the MQ-COH at the evolution time $(2\delta)^{-1}$. I_k^0: the development of ZQ-COH with kQ-COH as its parent.

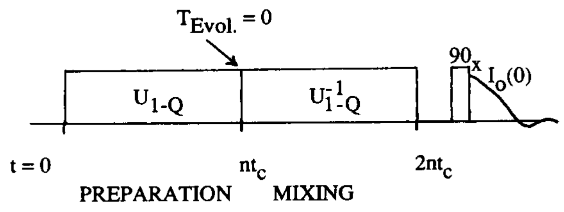

Fig. 5. The scheme of 2D NMR pulse sequence, composed of preparation, evolution, mixing and detection periods, is adapted to develop multiple quantum coherence. The evolution period is set to be zero.

Now suppose that the evolution time for MQ-COH under the offset, δ, were set to be $(2\delta)^{-1}$. Then at that time, I_1 would be zero, I_0 would retain its value at time $t = nt_c$, and I_2 would have oscillated to its value at time $(2\delta)^{-1}$, the period of its oscillation. Therefore, if the reconversion from non-vanishing off-diagonal elements of the density operator back to populations represented by diagonal elements were initiated at time $nt_c + (2\delta)^{-1}$, in the absence of an offset, the value of I_0 at time $2nt_c + (2\delta)^{-1}$ would contain *no contribution* from the 1Q-COH! The 1Q-COH monitored as the value of the initial intensity of the FID after a 90° pulse at time $nt_c + (2\delta)^{-1}$ would therefore be lower than that in the absence of an offset. One way of visualizing this result is shown in Fig. 4, where different symbols are used to trace the imagined evolution of MQ-COH back into populations after time $nt_c + (2\delta)^{-1}$. The symbol I_n, $n \geq 1$, means the nQ-COH. The symbol I_n^0 means the contribution of the nQ-COH developed at time $nt_c + (2\delta)^{-1}$ back into populations. The net magnetization associated with population differences, observed as the initial intensity of the FID after a "read-out" pulse converting population differences into 1Q-COH, is labelled I_0^{tot}. Clearly, I_0^{tot} will oscillate with time under a frequency offset during the evolution period, and this oscillation provides the means of detecting MQ-COH therein contained, as indicated more analytically below.

The scheme of production, and re-conversion of MQ-COH corresponding to the time development shown in Fig. 2, i.e., in the absence of an

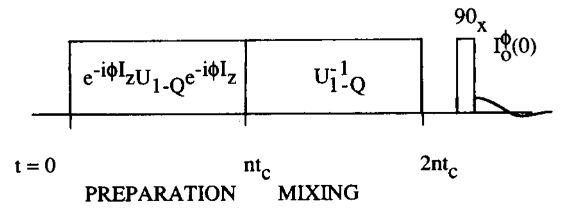

Fig. 6. The arrangement of pulse sequence and the way of phase shifting during the MQ experiment is shown. The phases of pulses only in the preparation period are shifted at the same time with the aid of a digital phase shifter, while the phases of the pulses in the mixing period remain unchanged.

offset, meaning in the absence of an evolution period, is indicated in Figs. 5 and 6; a single quantum propagator acts on the ensemble of coupled spins from time zero to time nt_c, and the inverse of that propagator acts for an equal period of time afterwards. The ZQ-COH at time $2nt_c$ is converted into observable 1Q-COH by a 90° "read-out" pulse, and is represented by the initial value of the FID. In the absence of irreversibility, the initial amplitude of the FID detected at time $2nt_c$ will be the same as that detected at time zero after a read out 90° pulse. The equality of these two amplitudes, incidentally, is one means of detecting one's ability to effectively perform time reversal, which is a measure of the perfection of the pulse sequences used.

The imposition of a frequency offset, δ, during the evolution period, to detect MQ-COH at the end of the mixing period, is not without its problems. One is that there is irreversible time evolution of the ensemble during the evolution period due to T_2 processes. A means of avoiding this problem is to realize that imposition of a phase shift [20], ϕ, *during the preparation period,* $0 \le t < nt_c$ is formally equivalent to imposition to a frequency offset, and causes the same oscillations of the various orders of MQ-COH as would be observed under a frequency offset.

The effect of a phase increment during the preparation period on the detected signal intensity at the end of the mixing period is now considered. In the absence of an evolution period, the initial intensity of the FID detected at the end of the mixing period, $t = 2nt_c$ is

$$\langle I_z(t=2nt_c)\rangle = \mathrm{Tr}\left[\rho(t=2nt_c)I_z\right] \tag{34}$$

But

$$\rho(2nt_c) = U_{1Q}^{-1}U_{1Q}\cdot I_z\cdot U_{1Q}^{-1}U_{1Q} = \langle I_z(t=0)\rangle \tag{35}$$

in the absence of irreversibility due to pulse imperfections, and interactions other than time independent homonuclear dipolar coupling. Looking more carefully at the combination of Eqns. 34 and 35, and leaving the subscript off the propagators, U, for simplicity, we find that

$$\begin{aligned}\langle I_z(t=2nt_c)\rangle &= \mathrm{Tr}\left(U^{-1}UI_zU^{-1}UI_z\right)\\ &= \mathrm{Tr}\left(UI_zU^{-1}UI_zU^{-1}\right)\\ &= \Sigma_r\langle r\,|\,UI_zU^{-1}UI_zU^{-1}\,|\,r\rangle\\ &= \Sigma_{r,s}\langle r\,|\,UI_zU^{-1}\,|\,s\rangle\langle s\,|\,UI_zU^{-1}\,|\,r\rangle\\ &= \Sigma_{r,s}\left|\langle r\,|\,UI_zU^{-1}\,|\,s\rangle\right|^2\end{aligned} \tag{36}$$

Eqn. 36 has an interesting interpretation. The quantity $U(nt_c,\ 0)I_zU^{-1}(nt_c,\ 0)$ measures how much multiple quantum coherence has been developed under the propagator, U. The quantity $\langle r|\,UI_zU^{-1}\,|s\rangle$ measures the k quantum coherence (kQ-COH), where $k = r - s$, as described earlier, and as will be again illustrated shortly. The term $|\langle r\,|\,UI_zU^{-1}\,|\,s\rangle|^2$ is the intensity of the kQ-COH. Thus the quantity detected as 1Q-COH by a proper "read-out" pulse at time $t = 2nt_c$ is the result of producing multiple quantum coherence under a propagator, U, acting for a time $t = nt_c$, and converting this coherence back into populations via the inverse propagator U^{-1} during an equal time nt_c.

Now we need to ask "what is the effect of a phase change, ϕ, imposed on *all* of the pulses during the preparation period, but not on the pulses during the mixing period, at the total evolution time $t = 2nt_c$?" In this experiment, the "evolution period" identified as the time between the preparation and mixing periods, is zero. A phase change, ϕ, is effected by physically rotating all excitation pulses during the preparation period, by ϕ. This means that a 180_x pulse, for example, becomes $180_{x+\phi}$, and a $180_{\bar{x}}$ pulse becomes a $180_{\bar{x}+\phi}$, etc. The operator form of U rotated by ϕ is just $U_\phi = \exp(-i\phi I_z)\cdot U\cdot \exp(i\phi I_z)$. The experimental arrangement is indicated in Figs. 5 and 6.

The expectation value of I_z detected at times $t = 2nt_c$ will be dependent upon ϕ, as follows:

$$\begin{aligned}\langle I_z(\phi, 2nt_c)\rangle &= \mathrm{Tr}\left[U(2nt_c,\ 0)\rho(0)U^{-1}(2nt_c,\ 0)T_z\right]\\ &= \mathrm{Tr}\left[U_{\phi=0}^{-1}(2nt_c,\ nt_c)U_\phi(nt_c,\ 0)\right.\end{aligned}$$

$$\begin{aligned}
&\times I_z U_\phi^{-1}(nt_c, 0) U_{\phi=0}(2nt_c, nt_c) I_z\big] \\
&\equiv \mathrm{Tr}\big(U_0^{-1} U_\phi I_z U_\phi^{-1} U_0 I_z\big) \\
&= \Sigma_{r,s}\langle r|\exp(-i\phi I_z)\cdot U\cdot\exp(i\phi I_z)\cdot I_z \\
&\quad\cdot\exp(-i\phi I_z)\cdot U^{-1}\cdot\exp(i\phi I_z)|s\rangle \\
&\quad\times\langle s|UI_zU^{-1}|r\rangle \\
&= \Sigma_{k=r-s}\,\mathrm{e}^{-ik\phi}|\langle r|UI_zU^{-1}|s\rangle|^2 \qquad (37)
\end{aligned}$$

We have noted that the quantity UI_zU^{-1} represents the time development of I_z under the propagator, U, in this case a propagator developing multiple quantum coherence. Non-zero values of $\langle r|UI_zU^{-1}|s\rangle$ indicate non-zero values of $r-s=k$Q-COH. $|\langle \mathrm{r}|UI_zU^{-1}|s\rangle|^2$ is the intensity of the kQ-COH.

The result,

$$\langle I_z(\phi, 2nt_c)\rangle = \sum_{k=-\infty}^{\infty} \mathrm{e}^{-ik\phi}|\langle r|UI_zU^{-1}|s\rangle|^2 \qquad (38)$$

may be compared to the value of the free precession decay of a system containing an ensemble of spin oscillating with intensities A_n at frequencies ω_n with some phase ϕ_n with respect to the phase of detection, chosen to be y for the present example;

$$G(t) = \langle I_y(t)\rangle = \Sigma_n A_n\cos(\omega_n t + \phi_n) \qquad (39)$$

The Fourier transform to the frequency domain reveals the frequency content of $G(t)$, which, with appropriate phase correction, becomes the frequency spectrum; $G(\omega) = F^- G(t)$. By direct analogy, the result Eqn. 38 is the superposition in the phase domain, $G(\phi)$, of oscillations with intensities $A_k = \langle r|UI_zU^{-1}|s\rangle^2$, and oscillations in the ϕ domain specified by k:

$$G(\phi) = \Sigma_k A_k\cos(k\phi + \delta_k) \qquad (40)$$

The ϕ dependence is experimentally mapped by incrementing the phase of all pulses during the preparation period by $\Delta\phi$, in a series of m experiments at fixed preparation and mixing periods nt_c, and observing the initial value of the FID following a 90° sampling pulse immediately after $t = 2nt_c$. In practice the signal-to-noise ratio is increased if the entire on-resonant decay is integrated from a period after the receiver has recovered from the overload of the 90° pulse until no further signal is present. For strongly dipolar coupled systems with a properly operating solid state spectrometer operating at, say 220 MHz for protons, this means a dead time of about 3 μs, and an integration period of less than 1 μs. Another means which has been used to increase the signal-to-noise ratio is the spin lock the magnetization along the y axis during the detection period, and detect stroboscopically in windows in the spin lock pulse until the magnetization is no longer visible.

The k dependence of $G(\phi)$ is determined from the ϕ Fourier transform. Though it is not obvious from the above discussion, $G(\phi)$ is symmetric in k, so only the cosine transform is needed;

$$G(k) = (1/\sqrt{2}\pi)\int_0^\infty \mathrm{d}\phi G(\phi)\cos k\phi \qquad (41)$$

Therefore, both positive and negative coherences are detected simultaneously. One needs to use $k_{\max}$ phase shifts, $\delta\phi_i$,

$$0 \le \delta\phi_i \le \pi \qquad (42)$$

in steps $\Delta\phi = \pi/k_{\max}$ to obtain all of the information necessary for the production of a multiple quantum spectrum, $G(k)$, vs. k, via Fourier transformation of the oscillatory signal, $G(\phi)$, collected from the initial values of the FIDs after the multiple quantum production and collection sequences (i.e., after the preparation and mixing periods). This is to say that to see a multiple quantum spectrum $G(k)$ vs. k with k extending to $k_{\max}$, one carries out $n = k_{\max} + 1$ experiments with phase shifts $\Delta\phi_1 = 0$, $\Delta\phi_2 = \pi/k_{\max}$, $\Delta\phi_3 = 2\pi/k_{\max}$ ... $\Delta\phi_n = \pi$. In the absence of irreversibility, the value of $\mathrm{G}(\phi)$ vs. ϕ is symmetric about $\phi = \pi$. Therefore the values of $G(\phi)$ in the range $\pi < \phi \le 2\pi$ are obtained from the data in the range $0 \le \phi \le \pi$. i.e., $G(2\pi) = G(0)$, $G(2\pi - \pi/k_{\max}) = G(\pi/k_{\max})$, etc. A suitably large number (e.g., 100) of periods of $G(\phi)$ vs. ϕ are then stored as an array which can be apodized by the function $\mathrm{e}^{-a\phi}$, and Fourier transformed on ϕ to produce the multiple quantum spectrum $G(k)$ vs. k. This spectrum will show peaks differing by

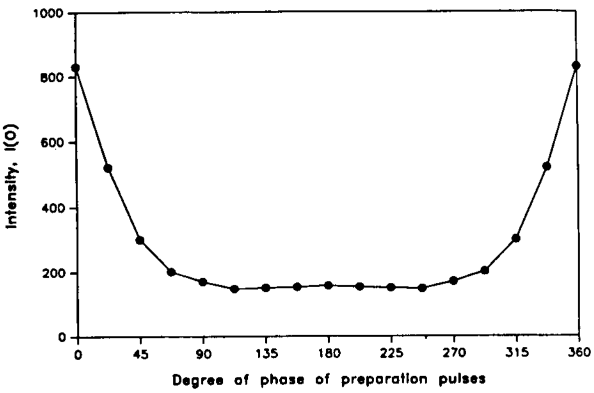

Fig. 7. The intensity changes with the phase increment ($\Delta\phi = 22.5°$) of the preparation pulses are plotted in the phase domain (adamantane). The FID of each phase is transformed to frequency domain, and each point on the plot is obtained by integrating the whole spectrum area, normally from −50 kHz to 50 kHz.

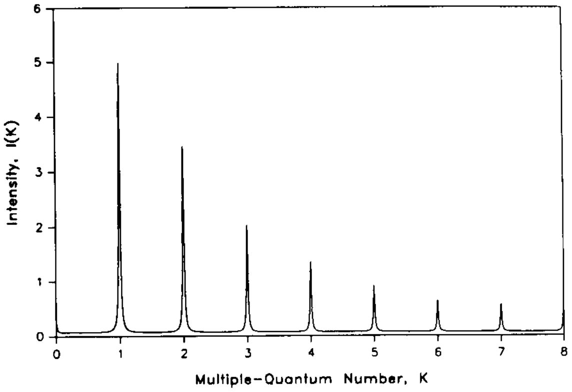

Fig. 9. The Fourier transformed spectrum, from phase domain to multiple-quantum number domain. We can see intensity distribution over the multiple-quantum number $k = 8$. The preparation time is 260 μs. The highest number of quanta, $k_{\max}$, is not seen due to the increment of the phase used.

units of 2 quanta each if a two quantum propagator is used or in steps of one quantum each if a single quantum propagator, as developed below, is used.

An example of experimental data obtained for $G(\phi)$, with $0 \leq \phi \leq 2\pi$, using a single quantum propagator on adamantane, with phase increments chosen so as to see $k_{\max} = 8$ and with 312 μs of excitation time, is shown in Fig. 7. These points repeated 128 times to fit to 2 K size, and tapered by an appropriate apodization function, are shown in Fig. 8. The baseline decay represents populations, so it may be subtracted from the oscillations shown in Figure 8 using a baseline adjustment technique before performing the transform on ϕ to yield the multiple quantum spectrum shown in Fig. 9. Note that the zero quantum peak is not present in this spectrum.

The development of multiple quantum coherence under pulse sequences resulting in a single quantum propagator for dipolar coupled spin 1/2 systems was first reported and discussed by Suter et al. in 1987 [21]. The sequence which we have used to produce the data shown in Fig. 9 was developed by Goldman [22] and essentially identical to that published in 1988 by Shykind et al. [23].

This sequence is shown in Fig. 10. Important to understanding how this sequence works is an understanding of the development of internal

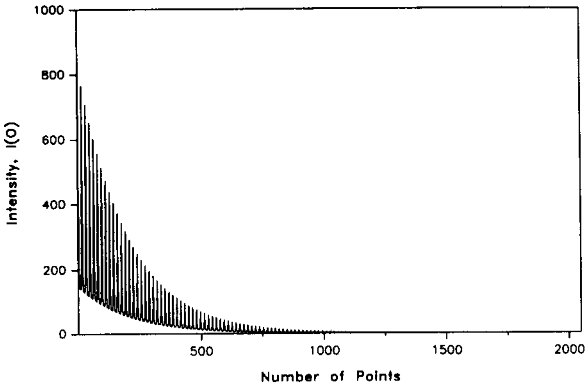

Fig. 8. An extension of data point and tapering are performed to generate a data set in the phase domain. Fig. 9 was repeated until the number of data points was to 2 K, and then tapered by an appropriate apodization function.

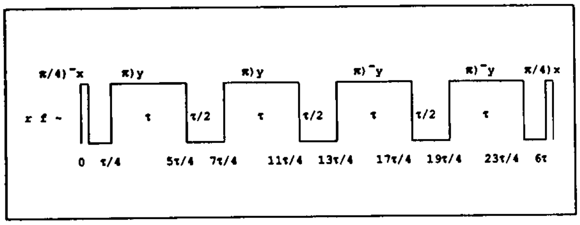

Fig. 10. Pulse sequence for the single quantum propagator used in this work.

Hamiltonians during finite pulses, an example of which is given in Section V, Chap. 5, of Ref. 10 for the case of the "flip-flop" phase tuning sequence (τ, 90_x, τ, $90_{\bar{x}}$, τ). Applied to the sequence of Fig. 10, the calculation proceeds as follows: consider the time interval $0 \le t < \tau/4$. Immediately after a perfect δ function rotation by 45^0_x at $t = 0$, the value of $\tilde{H}_{zz}$ will be

$$R_{45_x} H_{zz} = (H_{zz} + H_{yy})/2 - 3(I_{z1} I_{y2} + I_{y1} I_{z2})/2 \qquad (43)$$

The contribution of $\tilde{H}^{(0)}_{zz}$ for this period will then be

$$(1/t_c)\int_0^{\tau/4} \tilde{H}_{zz}\, dt = (1/t_c)\{(\tau/8)[H_{zz} + H_{yy} - 3(I_{z1} I_{y2} + I_{y1} I_{z2})]\} \qquad (44)$$

During the period $\tau/4 \le t < 5\tau/4$,

$$\begin{aligned}\tilde{H}_{zz}(t) &= R_{45x} R_{\xi\bar{y}} H_{zz} = R_{45x}\{\mathbf{I}_1 \cdot \mathbf{I}_2 - 3[I_{z1} I_{z2} \cos^2\xi + I_{x1} I_{x2} \sin^2\xi + (I_{z1} I_{x2} + I_{x1} I_{z2}) \sin\xi \cos\xi]\} \\ &= \mathbf{I}_1 \cdot \mathbf{I}_2 - 3/2\{(z_1 z_2 + y_1 y_2 + z_1 y_2 + y_1 z_2) \cos^2\xi + 2 x_1 x_2 \sin^2\xi \\ &\quad + \sqrt{2}\,[(z_1 + y_1) x_2 + x_1(z_2 + y_2)] \times \sin\xi \cos\xi\}\end{aligned} \qquad (45)$$

To ease the notation the symbol $z_1 z_2$ is now used to designate $I_{z1} I_{z2}$, etc. During the period $\tau/4 < t < 5\tau/4$, the flip angle ξ varies from zero to 180°. In the interval $\tau/4 < t < 5\tau/4$, the contribution of $\tilde{H}_{zz}$ to $H^{(0)}_{zz}$ can be calculated by assuming the flip angle, ξ, to be linear in t, so $\xi = \pi(t - \tau/4)/\tau$, and $dt = \tau\, d\xi/\pi$. Then in the period $\tau/4 < t < 5\,\tau/4$, or $0 \le \xi < \pi$, the contribution to $\bar{H}^{(0)}_{zz}$ is

$$\begin{aligned}\bar{H}^{(0)}_{zz} &= (1/t_c)\int \tilde{H}_{zz}(t)\, dt = (1/t_c)\Big[\tau \mathbf{I}_1 \cdot \mathbf{I}_2 - 3\Big\{(z_1 z_2 + y_1 y_2 + z_1 y_2 + y_1 z_2) \times (\tau/2\pi)\int_0^{\pi} \cos^2\xi\, d\xi \\ &\quad + x_1 x_2 (\tau/\pi)\int_0^{\pi} \sin^2\xi\, d\xi + [(z_1 + y_1) x_2 + x_1(z_2 + y_2)](\tau/\pi\sqrt{2})\int_0^{\pi} \sin\xi \cos\xi\, d\xi\Big\}\Big] \\ &= (\tau/2t_c)[(H_{zz} + H_{yy})/2 + H_{xx} - (3/2)(z_1 y_2 + y_1 z_2)]\end{aligned} \qquad (46)$$

In the period immediately following $t = 5\,\tau/4$, and before any other pulses are applied,

$$\tilde{H}_{zz} = 1/2[H_{zz} + H_{yy} - 3(y_1 z_2 + z_1 y_2)]$$

Proceeding in this manner, it may be verified that the sequence shown in Fig. 10, with cycle time $t_c = 6\tau$, yields the following values for the average Hamiltonian associated with the homonuclear dipolar coupling Hamiltonian, H_{zz}, and the chemical shift, $H_{cs} = \sigma_{zz} I_z$:

$$\begin{aligned}\bar{H}^{(0)}_{zz} &= -(I_{z1} I_{y2} + I_{y1} I_{z2}) \\ &= -(I_{z1} I^{+}_{2} - I_{z1} I^{-}_{2} + I^{+}_{1} I_{z2} - I^{-}_{1} I_{z2})/2i\end{aligned} \qquad (47)$$

a pure single quantum operator, and $\bar{H}^{(0)}_{cs} = 0$.

PROTON DENSITIES IN CAB-O-SIL SUPPORTS

Applications of multiple-quantum NMR have been extended to various problems in many different areas. The carbon skeleton or organic molecules and proteins in solution can be revealed under the multiple quantum filtering techniques [24,25], study of liquid crystal conformation [26], and a double quantum propagator has been applied to investigate the arrangement and the size of atoms in solids and liquid crystals [27,28]. In addition, it has been discussed and demonstrated that multiple-quantum NMR may be applied to the study of relaxation and motion in coupled spin systems [29,30]. By following the development of the highest order of multiple-quantum coherence produced as a function of preparation time, Ryoo et al. [31] have studied the distribution of hexamethylbenzene among the cavities of a Na–Y zeolite. The Reimer group [32,33] used the development of multiple-quantum coherence among protons in amorphous silicon hydride and amorphous silicon-carbide-hydride to probe cluster sizes of protons in these systems. In these studies, the development of multiple quantum coherence as a function of development time was used to infer the maximum number of relatively tightly coupled protons.

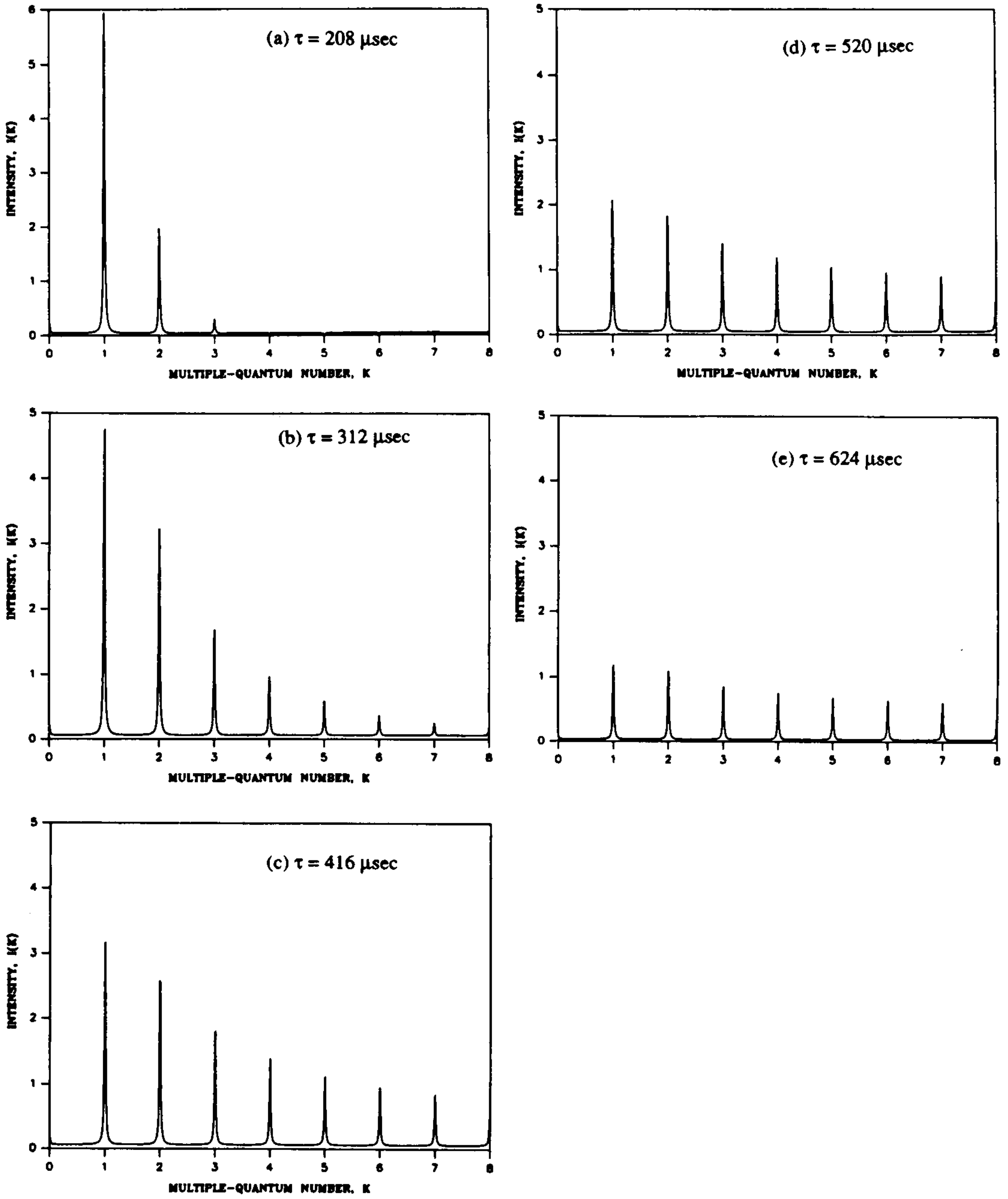

Fig. 11. The dependence of multiple-quantum spectra of adamantane with various preparation times was recorded. At short preparation times, the number of correlated protons are small: (a) $k_{\max} = 3$ for the preparation time, $\tau = 208$ μs. As the preparation time increases, $k_{\max}$ increases so rapidly that it is out of spectral range. Compared to (a), there is not much difference in $I(k)$ after the preparation time of 520 μs: See (d) and (e).

Wang and Slichter [34] used the relative intensities of 1, 2, and 3 quantum coherences to first probe possible identities of C_mH_n fragments resulting from the adsorption and reaction of acetylene on Pt.

The ability to count the number of atoms in a cluster is a powerful tool, when one considers that standard methods of structural characterization, such as x-ray crystallography, cannot be applied effectively to the studies of clusters of atoms that occur in materials such as semiconductors, polymers, liquid crystals, zeolites and heterogeneous catalysts.

As shown in Eqn. 32 and previously discussed [4,5] the intensities of the various orders of multiple quantum coherence of dipolar coupled spin systems depend on the details of the internuclear distances, and the excitation time or the cycles of the preparation pulse sequence; Fig. 11 shows the MQ-COH spectra of adamantane, obtained under the single quantum propagator discussed above. In this case, phase increments were chosen such that the highest order of MQ-COH detected was 8. The excitation time ranged from $\tau = 208$ μs to $\tau = 624$ μs. Adamantane molecules pack into a face centered cubic solid. Each adamantane molecule is surrounded by 12 nearest neighbors at a distance of 6.60 Å. While intramolecular dipolar interactions are severely attenuated by the rotation of the adamantane molecule in the solid, dipolar interactions between molecules remain, so adamantane represents a system in which there are basically an infinite number of dipolar coupled spins, albeit with dipolar couplings weaker than, e.g., those of protons in crystalline polyethylene. We therefore expect $k_{\max}$ to continuously grow as the number of MQ cycles increases. The experimental and theoretical investigation of the time evolution of MQ-COH with the excitation time provides a picture of the many-body interactions which develop the MQ-COH [35–38] and have been reviewed by Lacelle [39]. Shown in Fig. 12, to be compared with the result of the thought experiment shown in Fig. 1, are the development of multiple quantum coherences of order 1–8, with increase in time over which the coherences can develop. Similar results have been published for hexamethylbenzene [15] and a polycrystalline sample of 1,2,3,4-tetrachloronaphthalene-bis-(hexachlorocyclopentadiene) [26].

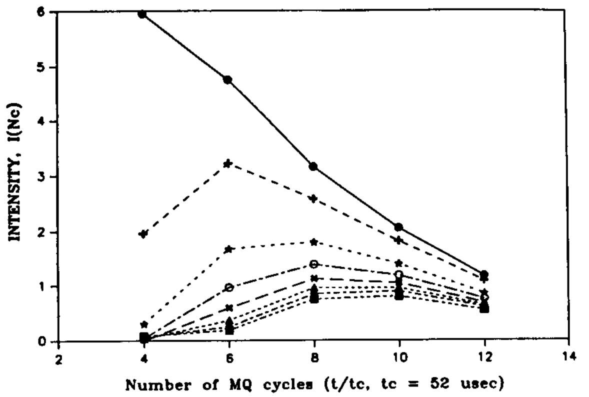

Fig. 12. Figure 11 is replotted as a function of the preparation time. Key to symbols: ●, 1Q-COH; +, 2Q-COH; ★, 3Q-COH; ○, 4Q-COH; ×, 5Q-COH; ▲, 6Q-COH; ◆, 7Q-COH; ■, 8Q-COH.

As an example of verification that the single quantum propagator discussed above provides multiple-quantum coherence in steps of single quanta, a model cluster system exhibiting long range order can be used [26]. The liquid crystal, *p*-hexyl-*p*′-cyanobiphenyl in the nematic phase, provides this system. Molecules in a nematic phase are sufficiently mobile to allow the intermolecular dipolar couplings to be averaged to zero, while the intramolecular dipolar couplings remain. Since there is no propagation of multiple quantum excitation between the molecules, the liquid crystal in the nematic phase which contains 21 protons is a nice example of a 21-spin cluster. The plot of the $k_{\max}$ vs. the preparation time is given in Fig. 13. At times long compared to the timescale shown in Fig. 13, the maximum order of multiple quantum coherence will begin to again rise, corresponding to the clusters of 21 protons coupling with each other. One notes that after $k_{\max} = 20$, the signal begins to oscillate to positive and negative values. These correspond to noise in the original data. Our experience with such systems is that the end of the maximum order of coherence observed corresponds to the onset of the appearance of negative intensities. The selection rules for production of multiple quantum

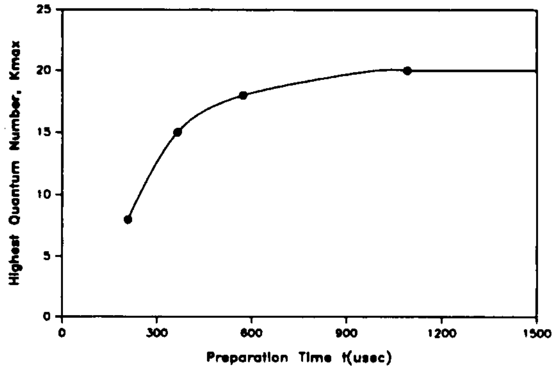

Fig. 13. $k_{\max}$ vs. preparation time for the liquid crystal, *p*-hexyl-*p*′-cyanobiphenyl in the nematic phase.

coherence under the single quantum propagator and preparation period used in the present experiment are shown in Fig. 14. The number of correlated spins or the number of the atoms in the individual molecule is equal to $k_{\max} + 1$. From the trend shown in Fig. 13, the limiting value for $k_{\max}$ is 20. This value is consistent with the number of protons in the liquid crystal molecule being 21. $k_{\max}$ increases as the preparation time increases from zero to 100 μs. For times greater than 1000 μs $k_{\max}$ remains constant, which confirms that there is no extension of the dipolar coupling network due to translational molecular motion. The multiple quantum spectrum shown in Fig. 15, obtained with the phase increment of 5.625° so as to develop a multiple quantum spectrum with $k_{\max} = 32$ and with the preparation time of 1092 μs, indicates that the highest MQ-COH is 20, i.e., $k_{\max} = 20$, with negligible intensities after $k = 20$.

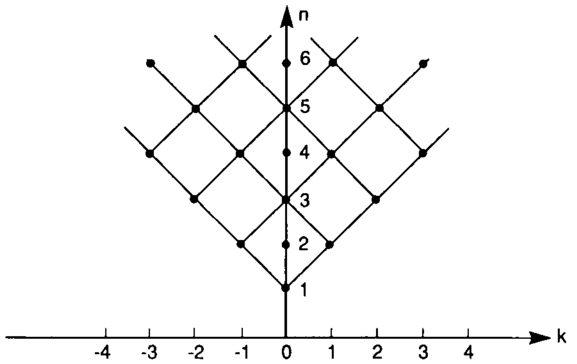

Fig. 14. Selection rules for the single quantum propagator used in this work.

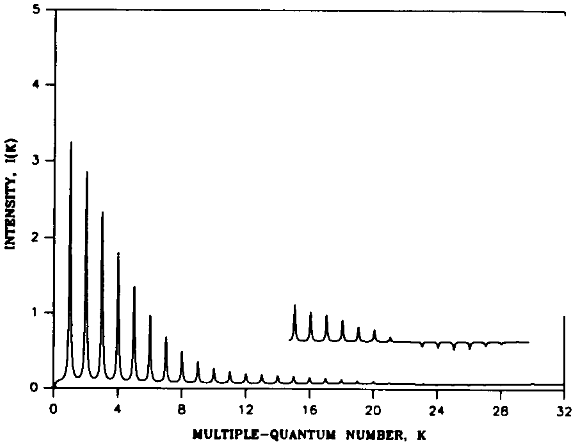

Fig. 15. Multiple-quantum NMR spectrum of the liquid crystal, *p*-hexyl-*p*′-cyanobiphenyl in the nematic phase (21 coupled protons) with preparation time 1096 μs. $k_{\max} = 20$ shows the full coupling of all spins. The small intensity after $k = 20$ is noise.

With the knowledge that the single quantum propagator does indeed produce multiple quantum spectra in units of single quanta, and that this propagator, acting for an excitation time of 310 μs on the relatively weakly coupled protons in adamantane results in the development of MQ-COH with $k > 8$, let us now consider the problem of providing possible identifications of differences in nominally inert supports used in catalysis of hydrocarbons to reform, or to expoxidize.

The subject of mechanisms of unsaturated hydrocarbons reacting with metallic catalyst surfaces has been of intense interest resulting in studies by single crystal techniques used in surface science [40,41] and in studies involving supported metal particles [42]. Studies of the epoxidation of ethylene over promoted and unpromoted single crystal silver surfaces have been reported as well [43–47].

Recent work in our laboratory has been devoted to studying the epoxidation of ethylene over promoted silver supported on Cab-O-Sil HS5 silica gel [48]. Initial results in studying the reaction of ethylene over promoted supported silver catalysts using high-resolution solid state ^{13}C

NMR has led us to question the nature of protons on the silica gel support itself. High-resolution NMR of protons in solids [49] have been used to probe identities of protonic species in zeolites and silicas [50–54] appropriate to determining isotropic chemical shifts in strongly homonuclear dipolar broadened systems. While these studies supply different identities of protonic species in these systems, e.g., single silanol protons, geminal silanol protons,..., they do not distinguish among possible differences in global densities of protons in these systems. In probing possible identities of C_mH_n fragments adsorbed upon supported Ru, we have used multiple quantum spin counting [55], with a single-quantum propagator as discussed above, to add a useful fingerprint to the study of such systems. In the present work we use this technique to probe possible differences in protons in Cab-O-Sil HS5 silica gel used as a support in a variety of catalytic reactions.

EXPERIMENTAL

The silica gels studied were amorphous fumed Cab-O-Sil HS5 (surface area 300 m^2 g^{-1} by BET determination). The "as received" sample was not "relaxed" by hydration with water, but was reduced under flowing hydrogen for 4 h at 673 K. All other samples were first hydrated in an aqueous slurry, impregnated with the metal where appropriate, dried for 24 h at room temperature, and reduced under flowing hydrogen for 4 h at 673 K. Ru loadings of 4 wt.% were achieved by impregnation with aqueous $Ru(NO)(NO_3)$ (AESAR) in distilled water. Silver loadings of 10 wt.% were achieved by impregnation in basic ammonium hydroxide solution (a mixture of solid silver oxide and ammonium hydroxide is explosive, so care must be exercised in the preparation). Pt loadings of 4 wt.% were obtained by ion exchange of $Pt(NH_3)_4^{2+}$ formed in an aqueous $Pt(NH_3)_4(NO_3)_2$ solution.

Transient NMR studies were performed in a home-built spectrometer operating at 220 MHz for protons previously described [56] with the exception that the four-phase switch was replaced by a digital phase shifter [57] capable of use in multiple pulse experiments on protons in solids [4] and necessary for the multiple quantum experiments used in this work. The absolute number of protons in each sample was determined for each sample using the initial value of the free induction decay under a single pulse excitation, with the standard being a spherical water sample [58]. The results are given in Table 1.

TABLE 1

Results of NMR spin counting on numbers of protons per gram of samples studied in this work

Sample	Protons ($g \times 10^{-21}$)	k_{max}
SiO_2, as received, dried and reduced	3.6	4
SiO_2, hydrated, dried, reduced	1.5	2
Ru/SiO_2, hydrated, dried, reduced	0.8	2
AgO_x/SiO_2, hydrated, dried, reduced	1.6	5–6
Pt/SiO_2, hydrated, dried, reduced	2.1	5

The pulse sequence used to produce a single quantum propagator was discussed above. A propagation time of 310 μs was used to develop multiple quantum coherence. The sequence producing the inverse of the propagation operator was used to collect the multiple quantum coherence into zero quantum coherence, and a single 90_x read-out pulse detected the resulting zero quantum coherence carrying the information resulting from the interference of the various orders of multiple quantum coherence developed during the propagation period. We note that as discussed above, this sequence for a propagation period of 310 μs resulted in detection of multiple quantum coherence to $k > 8$ for the relatively weakly coupled protons in solid adamantane. We note also that adamantane is a three dimensional system, whereas the systems under study here may be considered to be two dimensional [59] arrays of protons on a scale of 100 Å. We therefore expect that a time development which leads to observation of $k \geq 8$ for dipolar coupled protons in the relatively weakely coupled protons of the rotating adamantane molecule will be a lower limit for detection of this number of coupled protons in the present systems which experience conical motion reducing the observed shielding anisotropy and dipolar coupling. A recycle time of 60 s was used for signal averaging on all samples. This value was found to be longer than 5 T_1 for all samples studied.

RESULTS AND DISCUSSION

For each sample studied, two spectra are presented: (a) the multiple-quantum spectrum [$I(k)$ vs. multiple-quantum order of coherence k] obtained under the single-quantum propagator shown above with a propagation time of 310 μs; and (b) the single-quantum NMR spectrum [$I(\omega)$ vs. ($10^6[\omega - \omega_0]/\omega_0$], upfield (down frequency) being indicated by more negative shifts, taken under MAS at 5 KHz, under single pulse excitation.

Figures 16–19 show the multiple-quantum, and single-quantum MAS spectra of: (a) fumed Cab-O-Sil HS5, as received, and reduced under flowing hydrogen for 4 h at 673K; (b) fumed Cab-O-Sil HS5, hydrated in an aqueous slurry for 1 h at room temperature, dried at room temperature for 24 h, and reduced under flowing hydrogen for 4 h at 673 K. Exactly the same result is obtained for this sample as was obtained [55] for a sample loaded with 4 wt.% Ru. (c) fumed Cab-O-Sil HS5 impregnated with a 4 wt.% loading of Ru, dried at room temperature for 24 h, and reduced under flowing hydrogen for 4 h at 673 K; (d) fumed Cab-O-Sil HS5 impregnated with 10 wt.% loading of Ag, dried at room temperature for 24 h and reduced under flowing hydrogen for 4 h at 673 K, and (e) fumed Cab-O-Sil HS5 impregnated with 4 wt.% Pt, dried at room temperature for 24 h, and reduced under flowing hydrogen for 4 h at 673 K.

All samples exhibit sidebands in the single quantum MAS spectra. The spectral width of the sidebands is roughly 50 ppm, which is 11 kHz at a frequency of 220 MHz. The shielding anisotropy of hydroxyl protons is found to be $\leq$ 15 ppm, depending upon details of motion [60]. This means that sidebands due to shielding anisotropy would be $\leq$ 3 kHz, so the sideband structure seen in all samples must be associated with inhomogeneous dipolar interactions. The prime candidate for inhomogeneously broadened dipolar lines in the present system is the geminal pair of silanol protons mentioned above. In addition, all samples exhibit a sharp central line with a broadened base, again in agreement with identities previously established. The detail not found in previous work, exhibited by the multiple quantum spectra shown here is the local density of protons on different samples, as reflected in the long range homonuclear dipolar coupling leading to the development of multiple quantum coherence with time.

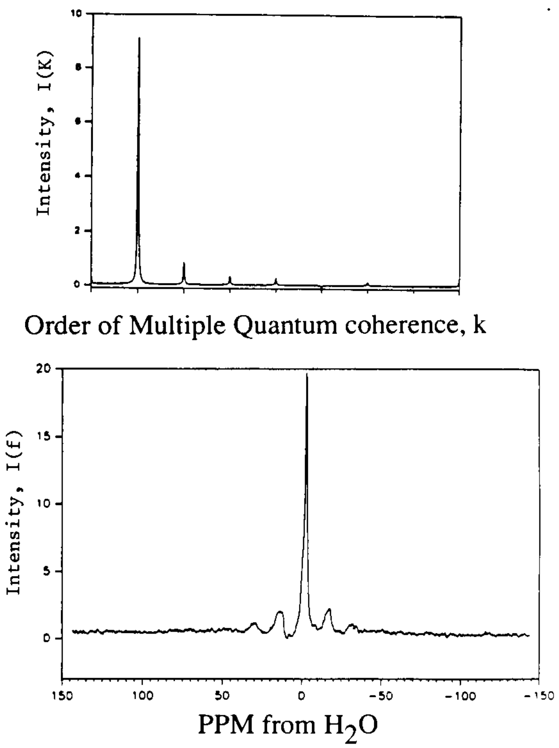

Fig. 16. Multiple-quantum spectrum $I(k)$ vs. k (top), and single-quantum spectrum (bottom), $I(\omega)$ vs. $10^6(\omega - \omega_0)/\omega_0$ of fumed Cab-O-Sil HS 5 silica gel, as received (without hydration), but reduced under flowing hydrogen at 673 K for 4 h. Negative numbers in the single quantum spectrum are upfield.

We see that the *unrelaxed* (non-hydrated) sample of fumed Cab-O-Sil HS5 silica gel which has been reduced under flowing hydrogen in exactly the same manner as all other samples exhibits a maximum value of multiple quantum coherence of $k_{\max} = 4$ (Fig. 18), meaning that under the selection rules extant in this experiment, there are five coupled protons being seen in a time development of 310 μs.

Figure 17 shows the result which we expected to find for all samples, namely that in a silica gel which has been hydrated and reduced, $k_{max} = 2$, the same result being obtained for the silica upon which Ru has been impregnated and reduced. The presence of Ru does not change the average density of dipolar coupled protons on the support.

However, the presence of Ag and Pt *does* change the average density of coupled protons as determined by the highest order of multiple quantum coherence observed, which is $k_{max} = 5$ for both samples (we feel that the $k = 6$ peak for the Ag/SiO_2 is in the noise). It is noted from Table 1 that the absolute numbers of protons per gram of sample bear no relation to the highest order of multiple quantum coherence observed. For example, SiO_2 hydrated, dried and reduced, and Ru/SiO_2 hydrated, dried and reduced differ by a factor of 2 in spins per gram, yet k_{max} is 2 for both. AgO_x/SiO_2 hydrated, dried, and reduced, and SiO_2 hydrated, dried and reduced, differ in protons per gram by 10%, yet k_{max} is 5 for the former, and 2 for the latter.

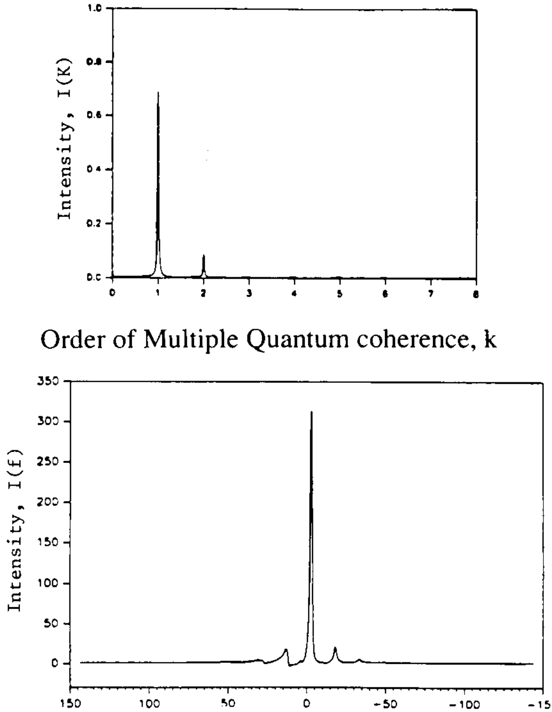

Fig. 17. Multiple-quantum spectrum $I(k)$ vs. k (top), and single-quantum spectrum (bottom), $I(\omega)$ vs. $10^6(\omega - \omega_0)/\omega_0$ of fumed Cab-O-Sil HS 5 silica gel, after hydration, drying for 4 h at room temperature, and reduction under flowing hydrogen at 673 K for 4 h. Negative numbers in the single quantum spectrum are upfield.

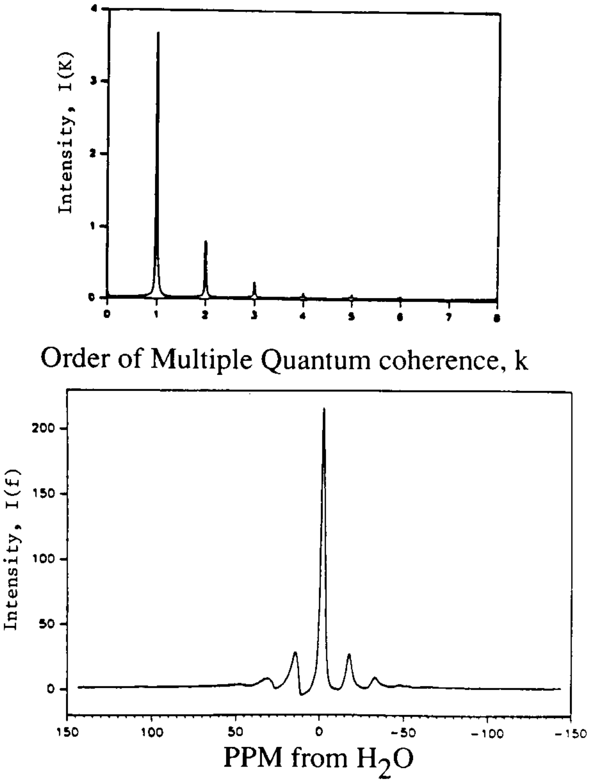

Fig. 18. Multiple-quantum spectrum $I(k)$ vs. k (top), and single quantum spectrum (bottom), $I(\omega)$ vs. $10^6(\omega - \omega_0)/\omega_0$ of fumed Cab-O-Sil HS 5 silica gel, after aqueous impregnation with Ag, drying for 4 h at room temperature, and reduction under flowing hydrogen at 673 K for 4 h. Negative numbers in the single quantum spectrum are upfield.

Strong precurser-support interactions have been studied in the preparation and characterization of Pt and Ru catalysts supported on silica gel by Alerasool and Gonzalez [61]. Ari et al. [62] have probed the effects of hydroxylation of a silica surface on metal dispersion in supported

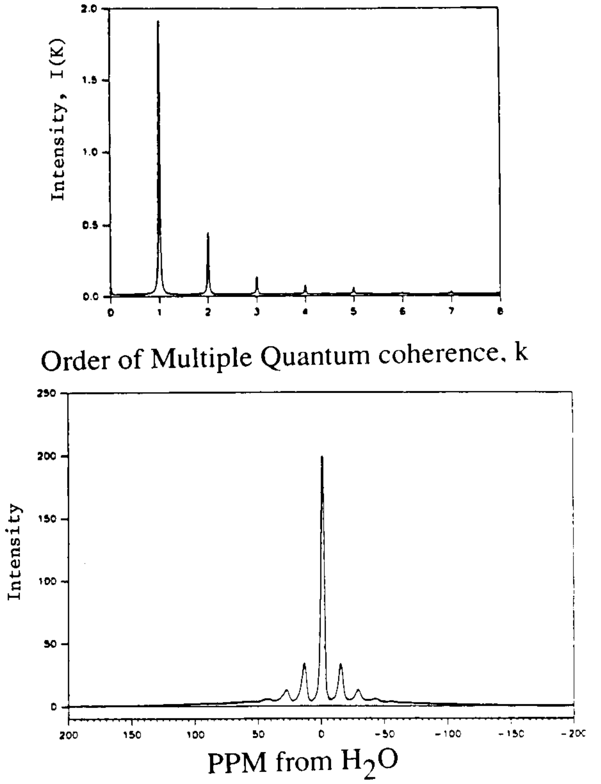

Fig. 19. Multiple-quantum spectrum $I(k)$ vs. k (top), and single-quantum spectrum (bottom), $I(\omega)$ vs. $10^6(\omega - \omega_0)/\omega_0$ of fumed Cab-O-Sil HS 5 silica gel, after aqueous impregnation with Pt, drying for 4 h at room temperature, and reduction under flowing hydrogen at 673 K for 4 h. Negative numbers in the single quantum spectrum are upfield.

platinum. Both of these studies indicate that the dispersion of the supported metal particles are dependent upon the chemistry taking place during the deposition and subsequent treatment to form the final catalyst, but do not seem to shed light upon the present results.

In summary, fumed Cab-O-Sil HS5 silica gel which has been unrelaxed by hydration, and which has been subsequently reduced under flowing hydrogen exhibits a more dense packing of protons than a sample relaxed by hydration followed by reduction. However, silica gels which *have* been relaxed by hydration, but on which have been deposited particles of Pt and Ag, (*unlike* the case for deposition of Ru, for which $k_{\max}$ is 2, the same found for silica gel relaxed by hydration with no deposition of Ru), show higher packing densities of protons than do the relaxed gel alone. The inference is that the presence of Pt and Ag particles, or the method of preparation, is responsible for different packing densities of protons on the support than found on the support alone, and on the support in the presence of Ru. We find this result to be surprising for metal-support interactions on this nominally "inactive" support. In view of our results on the interaction of silica gels with ethylene oxide (in preparation), these results raise a flag to those who expect that an "inert" support, SiO_2, is the same under all circumstances of sample preparation and/or deposition of catalytically active metal.

This work was supported by the Division of Basic Energy Sciences of the US Department of Energy under Contract No. W-7405-Eng-82. Our interest in this problem is the result of an extensive collaboration with Professor Terry King, whom we thank for advice and encouragement.

REFERENCES

1 F. Bloch, W.W. Hansen and M. Packard, Phys. Rev., 70 (1946) 474.
2 E.M. Purcell, H.C. Torrey and R.V. Pound, Phys. Rev., 69 (1946) 37.
3 W.G. Proctor and F.C. Yu, Phys. Rev., 81 (1951) 20.
4 B.C. Gerstein and C.R. Dybowski, Transient Techniques in NMR of Solids; An Introduction to the Theory and Practice, Academic Press, New York, 1985; and references cited therein.
5 B. Gerstein, M. Pruski, S.-J. Hwang, J. Solid State NMR, in preparation.
6 H. Tanaka, T. Terao and T. Hashi J. Phys. Soc. Jpn., 39 (1975) 378.
7 H. Tanaka and T. Hashi, J. Phys. Soc. Jpn., 39 (1974) 1139.
8 W.P. Aue, E. Bertholdi and R.R. Ernst, J. Chem. Phys., 64 (1976) 2229.
9 G. Bodenhausen, Prog. NMR Spectrosc., 14 (1983) 137.
10 D. Weitekamp, Adv. Magn. Reson., 11 (1983) 111.
11 M. Munowitz and A. Pines, Adv. Chem. Phys., 66 (1987) 1.
12 A. Pines, in B. Maraviglia (Ed.), Lectures on Pulsed NMR, in 100th Fermi School on Physics, Varenna, 1986, North-Holland, Amsterdam, 1988.
13 G. Drobny, Ann. Rev. Phys. Chem., 26 (1985) 451.
14 Y.S. Yen and A. Pines, J. Chem. Phys., 78 (1983) 3579.
15 J. Baum, M. Munowitz, A.N. Garroway and A. Pines, J. Chem. Phys., 83 (1983) 2015.

16 M. Goldman, Quantum Description of High Resolution NMR in Liquids, Oxford University Press, London, 1988, Section 2.5.
17 B.C. Gerstein and C.R. Dybowski, Transient Techniques in NMR of Solids; An Introduction to the Theory and Practice, Academic Press, New York, 1985, p. 141.
18 B.C. Gerstein and C.R. Dybowski, Transient Techniques in NMR of Solids; An Introduction to the Theory and Practice, Academic Press, New York, 1985, p. 70.
19 B.C. Gerstein and C.R. Dybowski, Transient Techniques in NMR of Solids; An Introduction to the Theory and Practice, Academic Press, New York, 1985, pp. 143–150.
20 S. Emid, Phys. B, 128 (1985) 79.
21 D. Suter, S.B. Liu, J. Baum and A. Pines, Chem. Phys., 114 (1987) 103.
22 M. Goldman, personal discussions during the RMN summer School organized by J. Virlet in September, 1987, Les Houches, France.
23 D.N. Shykind, J. Baum, S.-B. Liu and A. Pines, J. Magn. Reson., 76 (1988) 149.
24 M. Munowitz, Coherence and NMR, Wiley, New York, 1988, Chap. 6.
25 A. Bax, R. Freeman and T.A. Frenkiel, J. Am. Chem. Soc., 103 (1981) 2102.
26 S. Sinton and A. Pines, Chem. Phys. Lett., 76 (1980) 263.
27 J. Baum and A. Pines, J. Am. Chem. Soc., 108 (1986) 7447.
28 J. Baum, K.K. Gleason, A. Pines, A.N. Garroway and J.A. Reimer, Phys. Rev. Lett., 56 (1986) 1377.
29 A. Wokaun and R.R. Ernst, Molecular Phys., 36 (1978) 317.
30 J. Tang and A. Pines, J. Chem. Phys., 72 (1980) 3290.
31 R. Ryoo, S.-B. Liu, L.C. de Menorval, K. Takegoshi, B. Chemelka, M. Trecoske and A. Pines, J. Phys. Chem., 91 (1987) 6575.
32 M.A. Petrich, K.K. Gleason and J.A. Reimer, Phys. Rev. B, 36 (1987) 9722.
33 J.A. Reimer and M.A. Petrich, in H. Fritzsche (Ed.), Amorphous Silicon and Related Materials, World Scientific, Teaneck, NJ, 1988, pp. 3–27.
34 P.-K. Wang and C.P. Slichter, Phys. Rev. Lett., 53 (1984) 82.
35 M. Munowitz, A. Pines and M. Mehring, J. Chem. Phys., 86 (1987) 3172.
36 M. Munowitz and M. Mehring, Solid State Commun., 64 (1987) 605.
37 M. Munowitz, Molecular Phys., 71 (1990) 595.
38 W.V. Gerasimowicz, A.N. Garroway and J.B. Miller, J. Am. Chem. Soc., 112 (1990) 3726.
39 S. Lacelle, Adv. Mag. Opt. Reson., 16 (1991) 171.
40 J.E. Parmenter, M.M. Hills and W.H. Weinberg, J. Am. Chem. Soc., 108 (1986) 3563.
41 M.M. Hills, J.E. Parmenter, C.B. Mullins and W.H. Weinberg, J. Am. Chem. Soc., 110 (1988) 7952; and references cited therein.
42 S. Bhatia, X. Wu, D.K. Sanders, B.C. Gerstein, M. Pruski and T.S. King, Catal. Today, 12 (1992) 165; and references cited therein.
43 C.T. Campbell, J. Phys. Chem., 89 (1985) 5789.
44 C.T. Campbell, in L. Deviney and J.T. Gland, Catalyst Characterization Science, ACS Symposium Series No. 228, American Chemical Society, Washington, DC, 1985, pp. 210–221.
45 C.T. Campbell, J. Catal., 99 (1986) 28.
46 C.T. Campbell, J. Catal., 94 (1985) 436.
47 C.T. Campbell, J. Catal., 106 (1987) 301.
48 B.C. Gerstein, reported at the USDOE workshop, March 11–13, 1992 Santa Monica, CA.
49 B.C. Gerstein, R.G. Pembleton, R.C. Wilson and L.M. Ryan, J. Chem. Phys., 66 (1977) 361.
50 D. Freude, M. Hunger and H. Pfeifer, Chem. Phys. Lett., 91 (1982) 307.
51 M. Hunger, D. Freude, H. Pfeifer, H. Bremer, M. Jank and K.-P. Wendlandt, Chem. Phys. Lett., 100 (1983) 29.
52 J. Köhler, D.B. Chase, R.D. Farlee, A.J. Vega and J.J. Kirkland, J. Chromatogr., 352 (1986) 275.
53 H. Pfeifer, D. Freude, and M. Hunger, Zeolites, 5 (1985) 274.
54 C.E. Bronniman, R.C. Zeigler and G.E. Maciel, J. Am. Chem. Soc., 110 (1988) 1023.
55 S.-J. Hwang and B.C. Gerstein, Catal. Lett., 8 (1991) 367.
56 T.T.P. Cheung, L.E. Worthington, P.D. Murphy and B.C. Gerstein, J. Magn. Reson., 41 (1980) 158.
57 B.C. Gerstein, J.-W. Han, S.-J. Hwang, P-H. Jun and H. Skank, Rev. Sci. Instrum., 61 (1990) 2349.
58 B.C. Gerstein and R.G. Pembleton, Anal. Chem., 49 (1977) 75.
59 D.H. Levy and K.K. Gleason, J. Phys. Chem., 96 (1992) 1992.
60 H. Pfeifer, D. Freude and M. Hunger, Zeolites, 5 (1985) 274.
61 S. Alerasool and R.D. Gonzalez, J. Catal., 124 (1990) 204.
62 M. Ari, S.-L. Guao and Y. Nishiyama, Appl. Catal., 77 (1991) 141.

Analytica Chimica Acta, 283 (1993) 1081–1101
Elsevier Science Publishers B.V., Amsterdam

Nuclear magnetic resonance methods for measuring dipolar couplings in rotating solids

Janet M. Griffiths and Robert G. Griffin

Francis Bitter National Magnet Laboratory and Department of Chemistry, Massachusetts Institute of Technology, Cambridge, MA 02139 (USA)

(Received 4th June 1993; revised manuscript received 20th June 1993)

Abstract

The nuclear dipole–dipole coupling is a strong function of internuclear distance, and can therefore be used as a sensitive probe of local molecular structure. In most cases, however, the simultaneous presence of anisotropic chemical shielding and multiple dipolar interactions prevents isolation of the dipole coupling between individual spin pairs. Under these circumstances, it is customary to improve spectral resolution by employing magic angle spinning (MAS) which preserves the isotropic part of the chemical shift interaction but partially or fully averages the desired dipolar interactions. This article reviews NMR methods designed to selectively restore and measure dipolar couplings between like (homonuclear) spins and unlike (heteronuclear) spins in rotating solids. Applications of these methods – rotational resonance (R^2), rotational-echo double resonance (REDOR), transferred-echo double resonance (TEDOR), dipolar recovery at the magic angle (DRAMA), simple excitation for the dephasing of rotational-echo amplitudes (SEDRA), and rf-driven dipolar recoupling (RFDR) – to investigate the structure of biomolecules are presented.

Keywords: Nuclear magnetic resonance spectrometry; Dipolar coupling; Rotating solids; Solids; Review; Solid state NMR

Nuclear magnetic resonance (NMR) spectroscopy is a well-established method for determining the local structure and dynamics of a variety of amorphous and polycrystalline materials. In particular, the strong distance dependence of the nuclear magnetic dipole–dipole interaction makes this a valuable probe of local geometry, spatial connectivity, and order between molecules. Recently, two-dimensional (2D) solution-phase NMR experiments such as nuclear Overhauser effect spectroscopy (NOESY) have utilized indirect cross-relaxation effects to measure multiple $^1H-^1H$ internuclear distances, and hence, to determine the molecular structure of soluble macromolecules [1,2]. Analogous experiments in solids which utilize the direct through-space dipolar couplings are also possible, but are complicated by the simultaneous presence of the anisotropic chemical shift and dipolar interactions. Under these circumstances, it is customary to improve the resolution of solid state spectra by employing magic angle spinning (MAS) and to restore the dipolar couplings to the spectra using selective rotor-driven or rf-driven magnetization exchange, or rf-driven dephasing experiments.

The focus of this article is the expanding repertoire of NMR methods designed to recover dipolar couplings while maintaining conditions of high-resolution by MAS. These techniques can be separated into two general categories; techniques that measure dipolar couplings between "like"

Correspondence to: R.G. Griffin, Francis Bitter National Magnet Laboratory and Department of Chemistry, Massachusetts Institute of Technology, Cambridge, MA 02139 (USA).

0003-2670/93/$06.00

TABLE 1

Summary of MAS experiments designed to recover dipolar couplings in rotating solids

Common name	General pulse sequence	Application	Ref.
Dipolar chemical shift spectroscopy (DIPSHIFT)	2D Separation of dipolar and chemical shift tensors	Strong heteronuclear dipolar couplings, e.g., ^{13}C–^{1}H, ^{15}N–^{1}H	[33,34]
Rotational echo double resonance (REDOR)	2 π-Pulses per rotor period dephase rotational echoes	Weak heteronuclear dipolar couplings, e.g., ^{13}C–^{15}N, ^{31}P–^{13}C	[10,11]
Transferred echo double resonance (TEDOR)	2 π-Pulses per rotor period and coherence transfer	Weak heteronuclear dipolar couplings selective experiment, e.g., ^{13}C–^{19}F, ^{27}Al–^{31}P	[12,66]
Rotational resonance (R^2)	Rotor-driven magnetization exchange	Weak homonuclear dipolar couplings frequency selective, e.g., ^{13}C–^{13}C, ^{31}P–^{31}P	[3,37,40]
Dipolar recovery at the magic angle (DRAMA)	Combination of 2 $\pi/2$-pulses and one refocussing π-pulse per rotor period	Homonuclear couplings with small chemical shift differences, e.g., ^{1}H–^{1}H, ^{13}C–^{13}C	[4,5]
rf-Driven recoupling (RFDR)	Single π-pulses drive magnetization exchange between coupled spins	Broadband recoupling of homonuclear dipolar couplings, e.g., ^{13}C–^{13}C, ^{15}N–^{15}N	[8,9]
Simple excitation for the dephasing of rotational echo amplitudes (SEDRA)	Single π-pulse per rotor period dephases rotational echoes	Broadband dephasing of homonuclear dipolar couplings, e.g., ^{13}C–^{13}C, ^{15}N–^{15}N	[6,7]

spin pairs (^{13}C–^{13}C or ^{31}P–^{31}P) such as rotational resonance (R^2) [3], dipolar recovery at the magic angle (DRAMA) [4,5], simple excitation for the dephasing of rotational-echo amplitudes (SEDRA) [6,7], and rf-driven recoupling (RFDR) [8,9], and techniques that measure dipolar couplings between "unlike" spin pairs (^{13}C–^{15}N or ^{13}C–^{31}P) such as rotational-echo double resonance (REDOR) [10,11] and its cousin transferred-echo double resonance (TEDOR) [12]. These methods provide a route to structural information in a wide variety of materials including those not amenable to study by x-ray crystallography or solution NMR. Although a number of applications described here pertain to biological materials, such as membrane proteins, enzyme complexes, and crystalline and non-crystalline peptides, these techniques are equally applicable to problems in other areas, such as material science. Table 1 provides a summary of these techniques and selected applications.

BACKGROUND

The majority of spin systems considered here are comprised of pairs of "magnetically dilute" spin-1/2 nuclei introduced by deliberate spin labeling. This terminology refers to spins with intrinsically low natural abundance, or to situations where dipolar couplings are weak due to low γ-nuclei or large distance separations. Since a number of current applications pertain to biological materials, we will focus on dipolar couplings between spin-1/2 nuclei of interest in such systems, ^{13}C, ^{15}N and ^{31}P, although we note that ^{1}H, ^{19}F and ^{29}Si as well as some quadrupolar nuclei ^{2}H ($I = 1$), ^{17}O ($I = 5/2$) and ^{27}Al ($I = 5/2$) are becoming increasingly important in structural investigations of a broader range of materials. In most cases, dipolar recoupling techniques provide accurate distance measurements up to 0.5 nm for ^{13}C, ^{15}N or ^{31}P and longer distances for pairs containing high γ-nuclei such as ^{1}H or ^{19}F. Few other spectroscopic techniques provide such specific and accurate distance measurements.

The dipole–dipole interaction

The dipolar Hamiltonian describes the coupling of nuclear magnetic moments and can be expressed in a general form (Eqn. 1) where $\tilde{D}$ is a traceless second rank tensor

$$H_D = \sum_{j \neq k} I_j \tilde{D} I_k \quad (1)$$

In high magnetic fields H_D is truncated to the famous A and B terms [13], where A has a bilinear form, $I_{zj}I_{zk}$, and B is refered to as the dipolar "flip–flop" term

$$H_D = \sum_{j<k} \frac{\gamma_j \gamma_k \hbar}{r_{jk}^3} \frac{1}{2} \Big[(1 - 3\cos^2\Theta_{jk}) 2 I_{zj} I_{zk} - (1 - 3\cos^2\Theta_{jk}) \frac{1}{2} (I_{+j} I_{-k} + I_{-j} I_{+k}) \Big] \quad (2)$$

Here, r_{jk} is the internuclear distance, γ_j and γ_k are the gyromagnetic ratios of the two nuclei and Θ_{jk} is the angle between the internuclear vector and the external magnetic field direction.

For unlike spins, I and S, the flip–flop term does not conserve energy and the heteronuclear dipolar Hamiltonian reduces to the A term

$$H_D^{IS} = \frac{\gamma_I \gamma_S \hbar}{r^3} (1 - 3\cos^2\theta) I_z S_z \quad (3)$$

For an isolated pair of "like" spins, the same Hamiltonian is obtained for *weak* couplings, i.e. when $|H_D| \leq \Delta\omega_{iso}$, where $\Delta\omega_{iso}$ is the difference in isotropic chemical shifts of the relevant nuclei – a situation that is frequently encountered for magnetically dilute spins in solids. For ^1H couplings, the more usual situation is $|H_D| \gg \Delta\omega_{iso}$ and both A and B terms are significant in Eqn. 2.

Typical dipolar strengths for directly bonded spin pairs range from ~ 1 kHz for ^{13}C–^{15}N, ~ 2 kHz for ^{13}C–^{13}C bonds and ~ 30 kHz for ^1H pairs and decrease according to Eqn. 2 with internuclear distance. Although well-resolved dipolar splittings can be observed directly in powder pattern spectra [13,14], a more common situation arises for magnetically dilute spins, where chemical shift anisotropy obscures the dipolar splittings and deconvolution methods are needed to separate the various spectral features [15,16]. Furthermore, in the presence of long distances (~ 0.4–0.6 nm) which are important in many structural problems, dipolar couplings between magnetically dilute nuclei decrease to ~ 30–50 Hz. Under these circumstances, weak couplings are observed most effectively using a combination of magic angle spinning (MAS) and magnetization exchange or rf-driven dephasing experiments. Finally, if a large network of spins is present, the couplings are far more complex and the lineshape resembles a Gaussian function [17]. This situation is common for abundant spins, such as ^1H, and is not discussed further here.

Rapid sample rotation: magic angle spinning

Solution-phase NMR spectra exhibit narrow lines because rapid molecular motion averages the anisotropic chemical shift and dipolar interactions leaving the isotropic chemical shifts and spin–spin (J) couplings to dominate the spectra. In polycrystalline and powder samples, a similar spatial averaging is achieved by mechanically rotating the sample about an axis inclined at the "magic angle" ($\Theta_m = 54.7°$) relative to the external magnetic field [18,19]. The resulting magic angle spinning (MAS) spectra exhibit a centerband at the isotropic resonance frequency and a set of rotational sidebands spaced at the rotation frequency, $\omega_r/2\pi$. To clarify the effects of MAS on the various time-dependent spin interactions, it is helpful to categorize these as "inhomogeneous" or "homogeneous" according to whether the Hamiltonian commutes or does not commute with itself at all times, a definition due to Maricq and Waugh [20].

The chemical shift Hamiltonian, H_{CS}, is inhomogeneous and is therefore averaged by MAS even if the rotation frequency is less than the magnitude of $|H_{CS}|$. During each rotor period individual crystallites in the sample traverse a range of chemical shift frequencies with an average frequency equal to the isotropic chemical shift, ω_{iso}. At the completion of each rotor period, the magnetization evolution due to chemical shift anisotropy is completely recovered and appears as a train of "rotational echoes" in the time-domain signal. Fourier transformation of this echo train yields a MAS spectrum composed of a centerband at ω_{iso} flanked by a set of rotational sidebands spaced at integer multiples of ω_r. If $\omega_r \gg |H_{CS}|$, then the rotational echoes merge and Fourier transformation of the echo decay yields a single narrow resonance line. In the absence of other interactions, the rotational sideband intensities can be used to compute principal

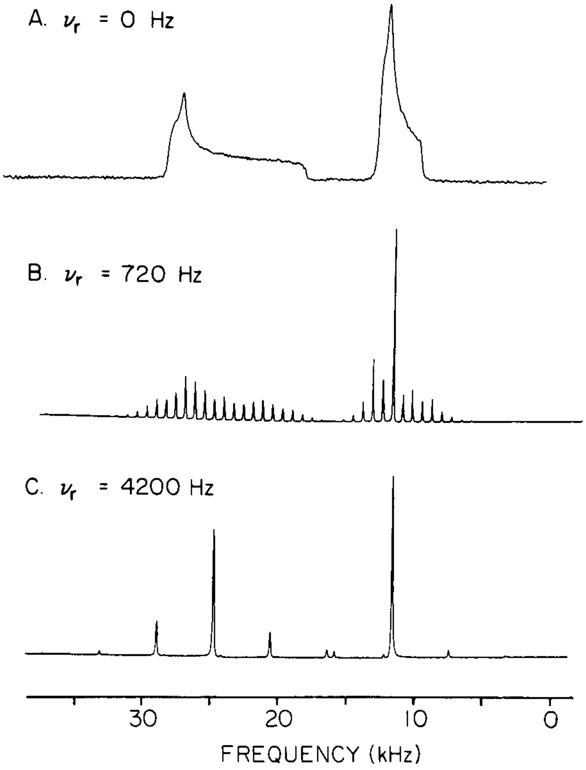

Fig. 1. Static and MAS ^{13}C spectra of zinc acetate $Zn^{2+}(CH_3COO^-)_2 \cdot 2H_2O$ recorded with cross-polarization and proton decoupling. (A) static powder pattern showing the difference in chemical shift anisotropy for the carboxyl and the methyl resonances. (B) and (C) were recorded with MAS rotation frequencies of 720 Hz and 4200 Hz, respectively. The methyl resonance chemical shift anisotropy is almost completely averaged at the faster spinning frequency. From [22]. Reproduced, with permission, from Annual Review of Physical Chemistry, Vol. 39, p. 519. Copyright 1988 by Annual Reviews, Inc.

values of the chemical shift tensor [20,21]. A demonstration of ^{13}C chemical shift sideband patterns for various MAS rotation rates is given for zinc acetate [22] in Fig. 1.

The heteronuclear dipolar interaction is inhomogeneous and therefore behaves in the same manner as chemical shift anisotropy during MAS. At slow spinning speeds, rotational echoes are modulated by the chemical shift and dipolar interactions concurrently and therefore sideband intensities depend on the magnitude and relative tensor orientations of both interactions. In practice, typical spinning speeds (5–10 kHz) exceed weak heteronuclear couplings, thereby effectively removing this interaction from MAS spectra. In contrast to the heteronuclear case, the homonuclear dipolar coupling is homogeneous and is not averaged by MAS unless the rotation rate exceeds the coupling strength, $\omega_r \gg |H_D^{II}|$, a condition frequently satisfied for magnetically dilute nuclei. For strongly coupled spins such as protons, however, MAS is combined with multiple pulse schemes to narrow resonance peaks [23,24]. A detailed review of the effect of MAS on the various spin interactions is given elsewhere [25].

A variety of experiments including separated local field spectroscopy [26–29], SEDOR [17,30,31], dipolar modulation techniques [29] and single crystal experiments [32] are used routinely for measuring dipolar couplings in static samples. Until quite recently, however, relatively few experiments have been developed for characterizing dipolar couplings in rotating solids. One such experiment, known as dipolar chemical shift spectroscopy (DIPSHIFT) [33,34], separates the chemical shift and dipolar tensors in two dimensions and therefore extracts dipolar coupling information in the presence of chemical shift anisotropy. DIPSHIFT is suitable for directly bonded ^{13}C–^1H and ^{15}N–^1H pairs where dipolar couplings are large and rotational sidebands are intense; however, this and similar approaches [35] are less effective for weak couplings. More contemporary experiments – including REDOR, TEDOR, RFDR, SEDRA and DRAMA – use rf pulses to interfere with the spatial averaging effects of MAS and therefore, to restore homonuclear or heteronuclear dipolar couplings to the spectrum. A different approach is employed by rotor-driven magnetization exchange experiments, such as rotational resonance (R^2), which rely on the mechanical motion of the sample rotor to recouple the spin system. In almost all experiments described herein, the coupling is detected through a change in spectral intensity rather than by a change in linewidth.

HOMONUCLEAR DIPOLAR COUPLINGS

Rotational resonance

The extent to which homonuclear dipolar couplings are averaged by MAS depends on the relative magnitude of the coupling strength and the spinning frequency. In addition, if the isotropic chemical shift difference, $\Delta\omega_{\mathrm{iso}}/2\pi$, exceeds the dipolar coupling strength, then the resulting energy mismatch further limits the efficiency of magnetization exchange via the dipolar flip–flop term. An exception occurs when the sample rotation frequency satisfies the rotational resonance (R^2) condition, $\Delta\omega_{\mathrm{iso}} = n\omega_r$, where n is a small integer [3,36]. At this condition, the energy difference between two chemically shifted spins is matched by the sample spinning frequency. As a consequence, the dipolar flip–flop term is reintroduced and energy is permitted to exchange at an enhanced rate governed by the coupling strength. This frequency selective reintroduction of the dipolar coupling leads to spectral line broadening and splittings that are particularly dramatic for directly bonded nuclei [3]. For a pair of spins it is possible to create a nonequilibrium population by inverting one of the resonance lines and monitoring the subsequent rate of magnetization exchange as a function of time [3,37]. This latter procedure serves as a basis for measuring *weak* homonuclear dipolar couplings in rotating solids.

Figure 2 shows the pulse sequence used for R^2 internuclear distance measurements. In this description, we refer to two chemically shifted ^{13}C nuclei, I and S, although this scheme is equally suitable for other types of like spin pairs. A cross-polarization pulse is used to create initial transverse ^{13}C magnetization and is followed immediately with a non-selective ($\pi/2$) pulse to restore this magnetization to the z-axis. A nonequilibrium population is created next by inverting one ^{13}C resonance peak with a weak, selective pulse or DANTE sequence [38,39]. If the sample rotation frequency is adjusted to the R^2 condition, then rotor-driven magnetization exchange takes place between coupled spins during the course of a mixing time, τ_m. Thereafter, a non-selective ($\pi/2$) pulse returns the magnetization to the transverse plane and the remaining difference in signal intensities, $I_z - S_z$, is recorded as a free-induction decay signal. A magnetization exchange curve is generated by recording this quantity for a number of discrete mixing times ranging from 0–30 ms. A comparison of the experimental magnetization exchange curve to numerical simulation is used to estimate dipolar coupling strength [40,41].

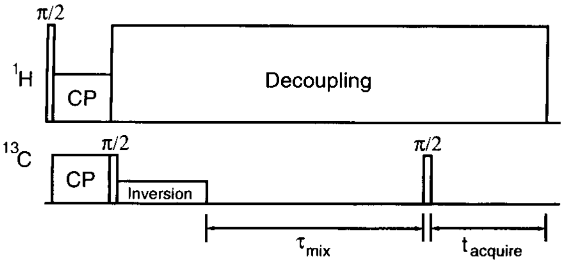

Fig. 2. Pulse sequence used for R^2 internuclear distance measurements. Cross-polarization is used to prepare the initial transverse magnetization and is followed by a $\pi/2$-pulse to restore magnetization to the z-axis. A population imbalance is created by inverting one resonance peak using a weak, selective pulse or DANTE sequence. If the R^2 condition ($\Delta\omega_{\mathrm{iso}} = n\omega_r$) is met, then rotor-driven magnetization exchange occurs between coupled spins during a variable mixing period, τ_m. The free-induction decay signal is recorded after applying a $\pi/2$-pulse to recover transverse magnetization. Strong proton decoupling is used to reduce dephasing by abundant protons and to maintain a sharp R^2 condition.

The exact time course of magnetization exchange at R^2 is determined by a number of parameters which can be measured or estimated: the homonuclear dipolar coupling strength (D), the principal values of the I and S chemical shift tensors, the relative orientations of chemical shift and dipolar tensors, the isotropic J-coupling between the two spins and the zero-quantum relaxation time (T_2^{ZQ}). The principal values of chemical shift tensors are usually measured from rotational sideband intensities [21] or from static NMR lineshapes [42], while J-couplings can be estimated from solution spectra or measured directly from solid state spectra, if resolution is adequate. The orientation of a large number of chemical shift tensors can be estimated from single crystal studies or model compounds [42,43]. In practice, however, the relative importance of this

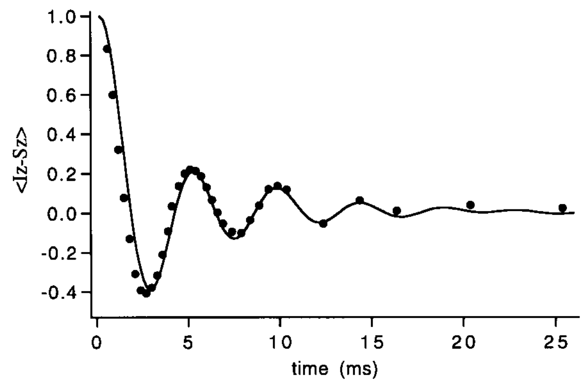

Fig. 3. Experimental (dots) and simulated (solid line) magnetization exchange curve for double-^{13}C labeled zinc acetate $Zn^{2+}(CH_3COO^-)_2 \cdot 2H_2O$ recorded at the $n = 3$ R^2 condition. Experimental points represent the difference magnetization $\langle I_z - S_z \rangle$ normalized to $\tau_m = 0$. Simulation parameters for zinc acetate can be found in [41]. These data were recorded at a spinning speed of $\omega_r / 2\pi = 5.50$ kHz.

geometric parameter depends on the order of the resonance condition [41]. Specifically, magnetization exchange rates are insensitive to molecular orientations for the $n = 1$ condition, but have a stronger dependence for higher resonance orders (i.e., when slower spinning speeds are used). In some circumstances, the orientation can be extracted from the curves and thus additional information is gleamed from the spectra [41,44]. Finally, the relative importance of the relaxation parameter, T_2^{ZQ}, depends on the specific system under study and has the most significance when distances are long or resonance peaks are broad.

Despite the number of parameters governing magnetization exchange, R^2 data can be analyzed to yield accurate internuclear distances as great as 0.5–0.6 ± 0.02 nm (corresponding to coupling strengths of ~ 30–50 Hz) [45]. A demonstration of magnetization exchange at the $n = 3$ condition is shown in Fig. 3 for 1,2-^{13}C labeled zinc acetate, where oscillations of the magnetization arise from exchange between these strongly coupled spins. A numerical simulation [40] of the magnetization curve is also shown and corresponds to a ^{13}C–^{13}C distance of 0.151 ± 0.002 nm.

In most practical applications, coupled spin pairs are separated by distances of 0.4–0.6 nm and the resulting couplings are weak. In such cases, no oscillations of the magnetization are observed, rather, the exchange process is damped by transverse relaxation between coupled spins and the exchange curve decays monotonically [37,46,47]. Transverse relaxation at R^2 is governed by zero-quantum relaxation, T_2^{ZQ}, which arises from dipolar interactions with natural abundance spins or distant spin pairs, incomplete proton decoupling and some types of molecular motion. Although this parameter is not readily accessible by experiment, its magnitude can be estimated by the sum of the individual single-quantum relaxation rates, T_2 [47]. In practice, T_2^{ZQ} is determined by summing the inverse linewidths of resonance peaks (measured off-R^2) which have been corrected for magnet inhomogeneity. The relationship between linewidth and estimated T_2^{ZQ} has been explored extensively with experimental standards [45].

The theoretical aspects of magnetization exchange at R^2 are presented in a number of recent works using coherent averaging theory and/or Floquet theory [37,40,47–50]. The analysis presented here draws from the fictitious field approach used by Levitt et al. [40] and Sodickson et al. [9] which provides a geometric description of magnetization exchange at R^2.

The relevant Hamiltonian for two chemically shifted spins, I and S, is given by

$$H(t) = \omega_I(t) I_z + \omega_s(t) S_z + \omega_A(t) 2 I_z S_z + \omega_B(t) \tfrac{1}{2}(I_+ S_- + I_- S_+) \qquad (4)$$

where the individual Zeeman terms are proportional to the resonance frequencies, $\omega_I(t)$ and $\omega_S(t)$ and the dipolar prefactors $\omega_A(t)$ and $\omega_B(t)$ can be expressed in terms of the dipolar Fourier components [20]. During MAS, their chemical shift of each spin has a time-independent isotropic contribution and oscillating terms due to its anisotropy, whereas the dipolar terms average to zero over a single rotor period.

As described earlier, if $\Delta\omega_{iso} \gg |H_D|$, then the dipolar flip–flop term is usually insignificant in Eqn. 4. Near the R^2 condition, however, quanta associated with the macroscopic sample rotation are at the right energy to reintroduce the flip–flop process between spins and both dipolar terms are

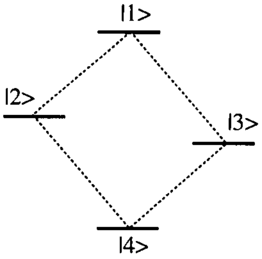

Fig. 4. Energy level diagram for two chemically shifted spin-1/2 nuclei. Single-quantum transitions are described by coherences between |2⟩ or |3⟩ and |1⟩ or |4⟩, while zero-quantum coherences are between |2⟩ and |3⟩. This figure is drawn to emphasize the difference in chemical shifts of the two spins.

significant. To understand the consequences of this idea in more detail, we consider the energy level diagram for two spins-1/2, given in Fig. 4, where the four eigenstates are expressed in the operator eigenbase $|m_I, m_S\rangle$,

$$|1\rangle = |+1/2,\ +1/2\rangle, \quad |2\rangle = |+1/2,\ -1/2\rangle$$
$$|3\rangle = |-1/2,\ +1/2\rangle, \quad |4\rangle = |-1/2,\ -1/2\rangle \tag{5}$$

To simplify the description of magnetization exchange, it is often possible to limit the discussion to the two central energy levels |2⟩ and |3⟩ and to describe the system in terms of a fictitious spin-1/2 [51,52], an approach that is valid if the spin-lattice relaxation time (T_1) is long relative to the exchange process. The time-development of the system and hence, the extent of magnetization exchange can then be traced geometrically.

A {|2⟩, |3⟩} subspace is constructed according to the standard definitions of single-transition spin-1/2 operators

$$I_z^{14} = \tfrac{1}{2}(\,|1\rangle\langle 1| - |4\rangle\langle 4|\,) = \tfrac{1}{2}(I_z + S_z)$$
$$I_z^{23} = \tfrac{1}{2}(\,|2\rangle\langle 2| - |3\rangle\langle 3|\,) = \tfrac{1}{2}(I_z - S_z) \tag{6}$$
$$I_x^{23} = \tfrac{1}{2}(\,|2\rangle\langle 3| - |3\rangle\langle 2|\,) = \tfrac{1}{2}(I_+S_- + I_-S_+)$$

where the unit operator is defined by

$$\mathbf{1} = \mathbf{1}^{14} + \mathbf{1}^{23} = |1\rangle\langle 1| + |4\rangle\langle 4| + |2\rangle\langle 2| + |3\rangle\langle 3| \tag{7}$$

Using these definitions, I-spin Zeeman magnetization is given by a superposition of $I_z^{14} + I_z^{23}$, and S-spin Zeeman magnetization is given by $I_z^{14} - I_z^{23}$. Selectively inverting I_z^{23}, while preserving I_z^{14}, allows magnetization exchange between I_z and S_z.

The Hamiltonian (Eqn. 4) can be separated into two commuting parts using the definitions, $\omega_\Sigma = \omega_I + \omega_S$ and $\omega_\Delta = \omega_I - \omega_S$, where H_0 is inhomogeneous and H_1 is homogeneous,

$$H = H_0 + H_1 \tag{8}$$

$$H_0 = \omega_\Sigma I_z^{14} + \omega_A(\mathbf{1}^{14} - \mathbf{1}^{23}) \tag{9}$$

$$H_1 = \omega_\Delta I_z^{23} + \omega_B I_x^{23} = \left(\omega_\Delta \hat{z} + \omega_B \hat{x}\right) \cdot \mathbf{1}^{23} \tag{10}$$

I_z^{14} commutes with Eqn. 8 in the absence of rf fields and is therefore a constant. Thus, the system can be described by analogy with a ficticious spin-1/2, I^{23}, and the Hamiltonian, H_1. Furthermore, H_1 defines an axis system in which the projection along the z-axis is given by the difference in I–S chemical shifts, $\omega_\Delta(t)$, and the projection along the x-axis is given by $\omega_B(t)$.

An interpretation of magnetization exchange at R^2 follows from this geometric description. The magnetization I^{23} in the {|2⟩, |3⟩} subspace is aligned initially along the $+z$-axis. If the sample rotation frequency is adjusted to match the R^2 condition, then one of the dipolar Fourier components ω_B of the x-component of the field matches in frequency the constant part of the chemical shift difference. The x-component of the field has a strong effect on I^{23} at this condition, and causes this vector to follow a complicated path reflecting the time course of magnetization exchange between coupled spins. In a z-axis rotating frame where the resonant Fourier component is stationary, I^{23} precesses about the x-axis from $+z$ to $-z$ with a rate proportional to the magnitude of this component. A representation of the I^{23} trajectory and the time development of the z-component, $I_z^{14} - I_z^{23}$, is given in Fig. 5. The extent of magnetization exchange recorded at time t reflects a change in population of |2⟩ and |3⟩ while the populations of |1⟩ and |4⟩ remain constant. Eventually, the length of I^{23} decreases to zero due to transverse (T_2^{ZQ}) and longitudinal relaxation (T_1). Away from R^2, the

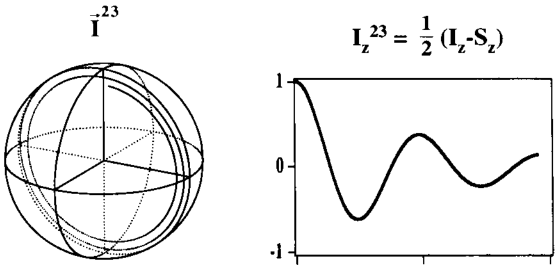

Fig. 5. The pathway traced by I^{23} in an interaction frame where the Fourier component, ω_B, is stationary. At R^2, the dynamic vector I^{23} follows a complex trajectory about the x-axis, tracing a path from $+z$ to $-z$. The diagram on the right shows the projection of I_z^{23} as a function of mixing time, τ_m. From [9]. Reprinted with permission from Journal of Chemical Physics, Vol. 98, p. 6747. Copyright 1993 American Institute of Physics.

dipolar Fourier components, ω_B, differ from ω_Δ and hence, these terms have little impact on the time development of the magnetization. This resonant picture bears close resemblance to the classical description of magnetic resonance where the constant z-direction is established by the external magnetic field, B_0, and the time-dependent x-component corresponds to the oscillating rf field, B_1.

Broadband dipolar recoupling

The rotational resonance (R^2) experiment provides one route to measuring homonuclear couplings that is highly frequency-selective and is presently one of the most accurate methods for measuring internuclear distances. A more flexible approach is offered by "broadband" experiments which reintroduce homonuclear dipolar couplings across a broad range of chemical shifts and MAS spinning speeds. In addition to placing less stringent requirements on the recoupling condition, broadband experiments may be used to generate correlation spectra in solid-state systems with more than two coupled spins in a manner akin to solution NOESY experiments. In this section, we describe three new experiments, DRAMA, SEDRA and RFDR, that facilitate broadband homonuclear recoupling in rotating solids.

Two related approaches for performing chemical shift correlation spectroscopy in dipole coupled systems have been presented by Ok et al. [53] and by Vega [6] and Gullion and Vega [7]. Ok used a mixing sequence of 8 π-pulses per rotor period in a transverse mixing sequence to promote polarization transfer among homonuclear coupled spins. Concurrently, Vega proposed the SEDRA (simple excitation for the dephasing of rotational-echo amplitudes) experiment which relies on one π-pulse per rotor period to dephase MAS rotational echoes. During the SEDRA pulse sequence, dephasing due to chemical shift anisotropy and heteronuclear interactions is refocussed after each pair of π-pulses, while a net dephasing arises from the homonuclear dipolar flip–flop term.

A different approach described by Bennett et al. [8] and Sodickson et al. [9] uses a single π-pulse per rotor period in a longitudinal mixing scheme to drive magnetization exchange among coupled spins. This experiment, known as rf-driven dipolar recoupling (RFDR), can be performed as a one-dimensional experiment where magnetization is recorded as function of mixing time, τ_m, in a manner similar to the R^2 experiment [9]. Alternatively, a 2D correlation experiment can be performed by incorporating an evolution period (t_1) in the pulse sequence [8]. The resulting 2D spectra show cross-peaks between shifted resonance lines that are correlated via their dipolar interaction. Furthermore, the t_m dependence of cross-peak intensity can be analyzed to yield quantitative distance information.

The 2D RFDR pulse scheme is shown in Fig. 6. Following a cross-polarization transfer from abundant protons, S-spins evolve under the influence of chemical shifts during the evolution time, t_1. A subsequent nonselective $\pi/2$ pulse restores the transverse S-spin magnetization to the z-axis. During a variable mixing time, τ_m, single π-pulses (one per rotor period) drive longitudinal magnetization exchange between coupled spins. A final non-selective $\pi/2$ pulse returns the S-spin magnetization to the transverse plane. S-spin magnetization is recorded for each t_1 and subjected to a 2D Fourier transformation.

The extent of magnetization exchange during RFDR (monitored by 2D cross-peak intensities or 1D exchange curves) is analyzed using a strategy similar to rotational resonance (R^2) since

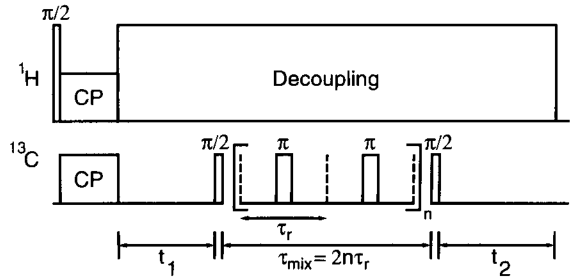

Fig. 6. RFDR pulse scheme for 2D homonuclear correlation. Following cross-polarization to create transverse S-spin magnetization, spins evolve according to their chemical shifts during t_1. A nonselective $\pi/2$-pulse places the S-spin magnetization along the z-axis. Rotor-synchronized π-pulses applied during a variable mixing time, τ_m, drive longitudinal magnetization exchange between coupled spins. A second non-selective $\pi/2$-pulse returns the magnetization to the transverse plane and S-spin magnetization is recorded. From [8]. Reprinted with permission from Journal of Chemical Physics, Vol. 96, p. 8626. Copyright 1992 American Institute of Physics.

both experiments depend on the same parameters: the principal components of the chemical shift tensor, the relative orientation of the chemical shift and dipolar tensors and the zero-quantum relaxation rate. RFDR is also sensitive to the sample rotation frequency, although, in contrast to R^2, dipolar recoupling is achieved over a broader range of rotation frequencies. Recent investigations of model compounds and an array of low molecular weight peptides suggest that distances as great as 0.50 nm are accessible with this technique [8]. A 2D RFDR spectrum of uniformly ^{13}C-labeled alanine is shown in Fig. 7. Rapid magnetization exchange among all coupled ^{13}C spins is evident by the appearance of cross-peaks after a mixing time of 8.6 ms.

The relevant Hamiltonian for a homonuclear spin pair includes chemical shift and dipolar coupling terms and a term describing the action of the rf π-pulses. These interactions can be partitioned into homogeneous and inhomogeneous terms that either commute or do not commute with themselves at all times. The homogeneous term, which contains the important dynamics of the spin system can be approximated with average Hamiltonian theory [23] and the zeroth order result for this spin system (neglecting chemical shift anisotropy) is given by

$$H_{D,1}^{(0)} = -\frac{\mathbf{d}}{2}(I_+S_- + I_-S_+) \tag{11}$$

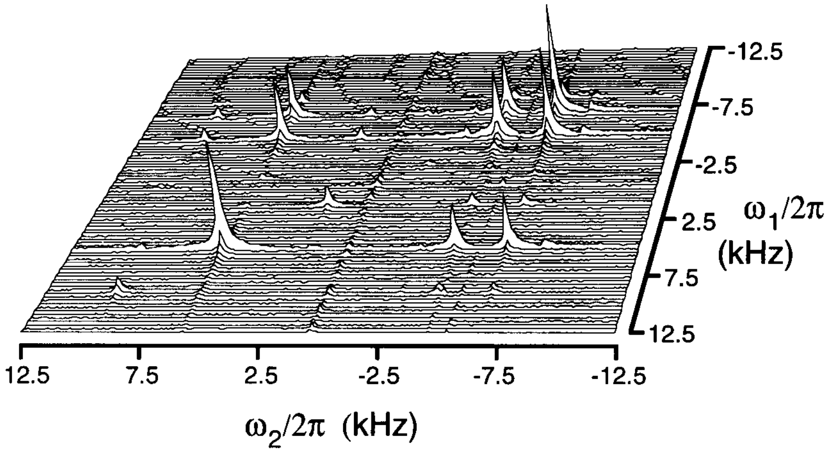

Fig. 7. A stack plot of the 2D RFDR magnitude spectrum of uniformly ^{13}C-labeled alanine recorded with 8.6 ms mixing and 3.72 kHz spinning frequency. Cross-peaks indicate connectivities between dipolar coupled spins. In this example, cross-peaks from directly bonded ^{13}C nuclei appear in ≤ 2 ms. From [8]. Reprinted with permission from Journal of Chemical Physics, Vol. 96, p. 8626. Copyright 1992 American Institute of Physics.

Here, **d** depends on the spinning speed, ω_r, and the isotropic chemical shift difference, $\Delta\omega_{iso}$, as follows:

$$\mathbf{d} = \frac{2}{\pi} \sum_{m=1,2} d_{12,|m|}(\beta) \cos(m\alpha) \frac{\dfrac{\Delta\omega_{iso}}{\omega_r}}{m^2 - \left(\dfrac{\Delta\omega_{iso}}{\omega_r}\right)^2} \times (-1)^{m-1} \sin\left(\pi \frac{\Delta\omega_{iso}}{\omega_r}\right) \qquad (12)$$

In Eqn. 12, d_{12} is the dipolar prefactor associated with the B term in Eqn. 2 and m is the index of dipolar Fourier components.

Computer simulations of Eqn. 12 for isolated spin pairs demonstrate that recoupling occurs across a broad range of chemical shift differences [8]. The RFDR technique may therefore provide an important advantage over R^2 for distance measurements between isolated spin pairs if spectral lines are inhomogeneously broadened, or when high spinning speeds are impractical. Furthermore, in some situations, RFDR may be used to map couplings between multiple spin sites, although this latter situation is complicated by the simultaneous exchange of magnetization between all coupled spins.

Tycko and Dabbagh [4] and Tycko and Smith [5] have used a pulse scheme consisting of rotor synchronized $\pi/2$ pulses to recover homonuclear dipolar couplings during MAS. This approach, named DRAMA (dipolar recovery at the magic angle), yields a partially-scaled dipolar lineshape for coupled spin pairs. Present versions of DRAMA are quite sensitive to chemical shift anisotropies and resonance offsets which are large in magnitude compared to ω_r, hence, this pulse scheme is best suited for like spin pairs with small chemical shift differences.

HETERONUCLEAR DIPOLAR COUPLINGS

Rotational-echo double resonance

High-resolution solid-state NMR spectra are insensitive to *weak* heteronuclear couplings due to the effective averaging of this interaction during MAS. The rotational-echo double resonance, (REDOR) experiment, introduced by Gullion and Schaefer [10,11], relies on rotor synchronized π-pulses to interupt the spatial averaging process of MAS and hence, to recover dipolar coupling information. REDOR was designed by analogy to SEDOR (spin-echo double resonance) [17,30,31], a static NMR experiment that uses a single π-pulse in the course of a Hahn spin-echo to quantify heteronuclear dipolar couplings. In both experiments, the action of each π-pulse is to change the sign of the dipolar interaction, thereby causing a net dephasing of the transverse magnetization.

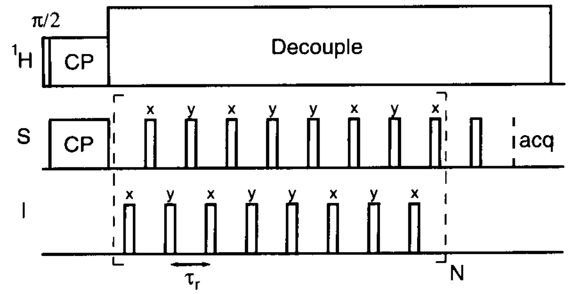

Fig. 8. REDOR pulse sequence used to measure I–S dipolar couplings. Transverse S-spin magnetization is created first by cross-polarization from abundant protons and followed with strong proton decoupling. Two π-pulses are applied each rotor period alternating between I and S channels. Two separate data arrays are collected, one *with* and one *without* I-spin π-pulses. In this diagram, dephasing of S-spin magnetization is accumulated for 8 N complete rotor cycles. The XY-8 phase-alternated scheme reduces errors due to pulse imperfections.

The REDOR pulse sequence is illustrated in Fig. 8. After cross-polarization (CP) from abundant protons, a train of rotor synchronized π-pulses are used to interrupt the formation of S-spin rotational echoes. A minimum of 2 π-pulses per rotor period are requisite for generating a nonzero dipolar interaction and can be applied solely to the I-spin channel [10] or alternated between I and S channels [54,55]. In either case, the first π-pulse is placed at one-half of the rotor period, while the second π-pulse is placed at the end of each rotor period. In circumstances where only I-spin π-pulses are applied, a single S-spin π-pulse is placed in the middle of the pulse sequence to refocus S-spin chemical shifts. REDOR data is usually sampled after N rotor periods of dephasing π-pulses. Phase cycling schemes are used to miminize errors due to resonance offset and pulse imperfections and are particularly important for weak couplings where dephasing is accumulated over a large number of rotor cycles (i.e., N is large) [56,57].

In common practice, the REDOR pulse sequence is applied *with* and *without* I-spin π-pulses on alternate scans; these data are collected and Fourier transformed separately. In the absence of π-pulses, the S-spin echo amplitude (S_0) decays according to inherent spin–spin relaxation (T_2) processes. In the presence of I-spin π-pulses, however, an additional decrease in the S-spin echo intensity (S) arises from I–S dipolar couplings. The echo intensity difference, $\Delta S = S_0 - S$, scaled by the full-echo intensity, S_0, therefore provides a measure of this interaction and hence, the corresponding internuclear distance. This quantity, called the REDOR difference signal, also depends on the placement of π-pulses (t_p) and the total number of rotor cycles, N, during which π-pulses are applied. A general strategy used in REDOR experiments is to optimize the difference signal for a given coupling strength by judicious choice of these parameters.

The Hamiltonian governing a coupled pair of unlike spins, I and S, is given by Eqn. 3 and is rewritten in Eqn. 13 to show the time-dependence of the dipolar frequencies:

$$H(t) = \omega_D(t) I_z S_z \tag{13}$$

where

$$\omega_D(\alpha, \beta; t) = \pm \tfrac{1}{2} D\left[\sin^2\beta \cos 2(\alpha + \omega_r t) - \sqrt{2} \sin 2\beta \cos(\alpha + \omega_r t)\right] \tag{14}$$

and the dipolar coupling constant is given by:

$$D = \gamma_I \gamma_S \hbar / r_{IS}^3 \tag{15}$$

In Eqn. 14, α and β are the azimuthal and polar angles which relate the I–S internuclear dipolar vector to the rotor coordinate system.

The time evolution of S-spin magnetization can be expressed in terms of an average Hamiltonian which evolves with an average dipolar frequency [58,59] defined over a rotor period, T_r,

$$\bar{\omega}_D = \frac{1}{T_r} \int_0^t \omega_D(t')\, dt' \tag{16}$$

In the absence of I-spin π-pulses $\bar{\omega}_D$ averages to zero and thus, full rotational echoes appear at the completion of each rotor cycle.

In the presence of I-spin π-pulses, the spin system evolves under the influence of $\bar{\omega}_D$ now determined by the placement of these pulses (t_p):

$$\bar{\omega}_D = \frac{1}{T_r}\left[\int_0^{t_p} \omega_D(t)\, dt - \int_{t_p}^{T_r} \omega_D(t)\, dt\right] \tag{17}$$

For $t_p = T_r/2$, the average dipolar frequency is

$$\bar{\omega}_D = 4\sqrt{2}\, D \sin\alpha \sin\beta \cos\beta \tag{18}$$

Equation 18 provides a measure of the phase, Φ, acquired during each rotor cycle due to the application of π-pulses and is manifest as a decrease in rotational echo intensity. For N rotor cycles of length T_r, the total phase accumulation is therefore, $\Delta\Phi = \bar{\omega}_D N T_r$.

The final REDOR difference signal, normalized to the full-echo intensity, S_0, is given by a powder average over all possible internuclear vector orientations:

$$\Delta S/S_0 = 1 - \frac{1}{2\pi} \times \int_0^{2\pi} \int_0^{\pi/2} \cos(\bar{\omega}_D N T_r) \sin\beta\, d\beta\, d\alpha \tag{19}$$

where the geometric factor, $\sin\beta$, accounts for the orientational distribution of spins about the rotor axis.

If the I–S coupling is weak, $(\bar{\omega}_D N T_r) \ll 1$, then the $\cos(\bar{\omega}_D N T_r)$ term in Eqn. 19 can be expanded to the following dimensionless quantity

$$\Delta S/S_0 = K(NDT_r)^2 \tag{20}$$

where K is a constant. The relationship between $\Delta S/S_0$ and the quantity $\lambda_D = NDT_r$ is illustrated in Fig. 9. The REDOR difference ratio is proportional to λ_D^2 for small λ_D, and oscillates as λ_D

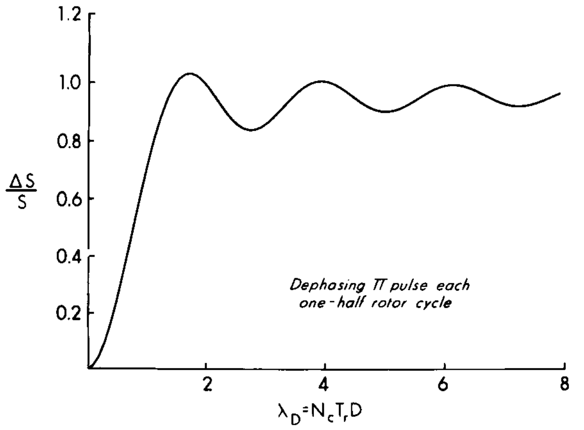

Fig. 9. The calculated REDOR difference signal, $\Delta S/S_0$, is shown as a function of the dimensionless parameter $\lambda_D = N_c D T_r$, where N_c is the number of rotor cycles, D is the direct dipolar coupling and T_r is the length of a rotor period. The REDOR difference ratio is quadratic at short times, but oscillates at longer times. From [11,60]. Reprinted with permission from Journal of Magnetic Resonance, Vol. 90, p. 334. Copyright 1990 Academic Press, Inc.

increases. Equation 20 therefore illustrates an important feature of REDOR; total dephasing is increased by longer accumulations, hence *weak* couplings are measured most effectively by chosing larger values of N. A practical limit to N is established by the various mechanisms contributing to transverse relaxation, T_2.

Samples for REDOR are prepared with selective labeling of unlike spin pairs – such as ^{13}C–^{15}N, or ^{13}C–^{31}P – in a manner analogous to samples prepared for R^2 and RFDR. An example of REDOR is given for a recrystallized mixture of L-[2-^{13}C,^{15}N]alanine and L-[1-^{13}C]alanine in Fig. 10 and which illustrates the evolution of the ^{13}C signal as a function of the number of dephasing rotor cycles [60]. In general, REDOR can measure internuclear distances as great as 0.4 ± 0.01 nm for ^{13}C–^{15}N spin pairs (corresponding to coupling strengths of about ~ 40 Hz) [61], and distances spanning 1.0 nm and greater for high γ-nuclei such as ^{31}P and ^{19}F.

Although magnetically dilute spins represent a small percentage of labeled sites (1.1% for ^{13}C and 0.33% for ^{15}N) these natural abundance spins are sometimes strongly coupled to intentionally labeled spins because of their proximity (i.e., directly bonded) and will therefore contribute to REDOR dephasing. In situations where the coupling between labeled spins is weak, the contribution of background spins to ΔS is sometimes comparable in magnitude to that of the targeted I–S pair [60] and an accurate estimate of this contribution is critical for obtaining distance information. In some cases, this contribution can be estimated from the sample composition, if the crystal structure is known, or can be reduced, in part, by choosing long REDOR cycles.

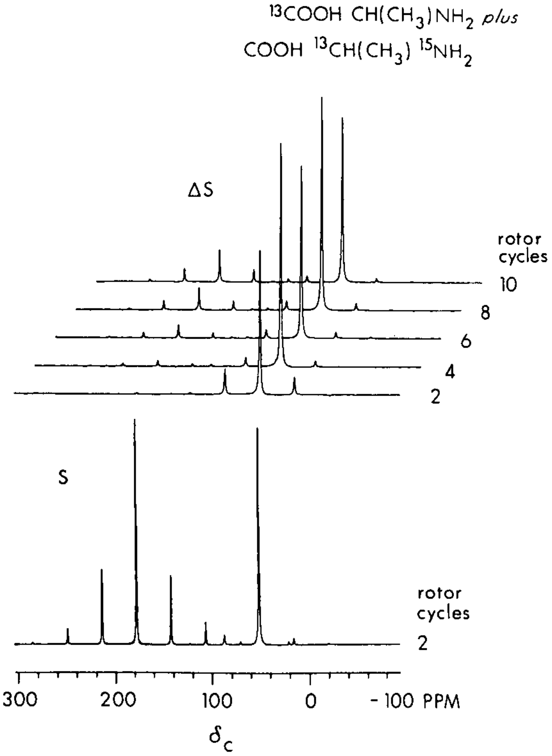

Fig. 10. Carbon-13 REDOR spectra of an equimolar recrystallized mixture of L-[2-^{13}C,^{15}N]alanine (99% ^{13}C and ^{15}N enrichment) and L-[1-^{13}C]alanine (90% ^{13}C enrichment). The full-echo spectrum is shown on the bottom and the REDOR difference spectrum, ΔS, is shown as a function of the number of rotor cycles (N) on the top. These spectra were recorded at 50.3 MHz using a MAS spinning rate of 2.7 kHz. From [60]. Reprinted with permission from Journal of Magnetic Resonance, Vol. 90, p. 335. Copyright 1990 Academic Press, Inc.

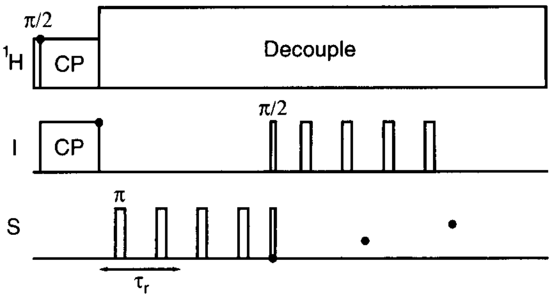

Fig. 11. The TEDOR pulse sequence uses cross-polarization to generate initial I-spin magnetization, followed by rotor-synchronized S-spin π-pulses to prevent refocusing of I–S dipolar interaction during the course of N rotor cycles. A coherence transfer is established via simultaneous application of I and S $\pi/2$ pulses. Subsequent I-spin π-pulses dephase magnetization of I–S pairs selected during the coherence transfer and permit measurement of their dipolar coupling. S-spin magnetization is recorded by synchronous sampling at rotational echo maxima.

As with R^2 experiments, natural abundance background signals also congest NMR spectra and therefore complicate measurement of the full echo intensity, S_0. In some cases, the natural abundance spectrum recorded under identical conditions, can be subtracted from the spectrum of the labeled sample. Alternatively, modifications [62,63] of the basic REDOR experiment can be used to eliminate or reduce the contribution of natural abundance background signal to the S-spin full-echo intensity – including synchronous sampling and two dimensional experiments [11]. Some limitations associated with extraneous background signals can be allayed, in part, by using transferred-echo double resonance spectroscopy (TEDOR) [12].

Transferred-echo double resonance

TEDOR utilizes a coherence transfer between heteronuclear spins pairs to select dipolar coupled I–S spin pairs from extraneous background spins. The TEDOR pulse scheme is diagrammed in Fig. 11. After cross-polarization from abundant protons, two S-spin π-pulses per rotor period prevent refocusing of the heteronuclear dipolar interaction during the course of N rotor cycles. A coherence transfer is accomplished with a pair of I, S $\pi/2$ pulses applied together at the end of a rotor period to ensure that magnetization is created solely by S-spins coupled to I-spins. A similar selection process is used routinely in the solution NMR experiment, INEPT [38] and has been utilized previously in 2D ^1H–^{13}C correlation experiments in solids [64,65]. Next, I-spin π-pulses create an observable S-spin signal which evolves during the course of M dephasing cycles. In common practice, the number of preparative rotor cycles, N and the number of evolution rotor cycles, M, are chosen to maximize the amplitude of the transferred magnetization during each portion of the experiment. Final S-spin magnetization is recorded by synchronous sampling at rotational echo maxima following the coherence transfer. Background signals are removed from the final TEDOR spectrum by alternating the phase of the $\pi/2$ I-spin transfer pulse which reverses the sign of the transferred signal but not the sign of the uncoupled S-spin background signal; subtraction of the two spectra yields an S-spin spectrum free of background resonances.

The time evolution of I and S magnetization during TEDOR can be analyzed in a manner similar to REDOR [10,60]. During the first stage of TEDOR, the density matrix evolves under the influence of an average Hamiltonian with an average dipolar frequency, $\bar{\omega}_D$, created by π-pulses. In TEDOR experiments, S-spin π-pulses are usually spaced at $1/4T_r$ and $3/4T_r$, hence, the average dipolar frequency is

$$\bar{\omega}_D = 4\sqrt{2}D \cos\alpha \sin\beta \cos\beta \tag{21}$$

Prior to the application of $\pi/2$ pulses, the density matrix is

$$\rho(t) = I_x \cos(\bar{\omega}_D NT_r) + 2I_yS_z \sin(\bar{\omega}_D NT_r) \tag{22}$$

Coherence transfer is achieved by application of two simultaneous $\pi/2$ pulses, one on the I-spin channel and one on the S-spin channel. This procedure converts the second term of Eqn. 22 to a coherence term and therefore permits the transfer of magnetization between I and S:

$$2I_yS_z \sin(\bar{\omega}_D NT_r) \rightarrow -I_zS_y \sin(\bar{\omega}_D NT_r) \tag{23}$$

Following this step, the density matrix evolves for M rotor cycles under the influence of an average frequency created by I-spin π-pulses as

$$\sin(\bar{\omega}_D N T_r)\left[-2I_z S_y \cos(\bar{\omega}_D M T_r) + S_x \sin(\bar{\omega}_D M T_r)\right] \qquad (24)$$

The final TEDOR signal is given by a powder average of the observable S-spin magnetization:

$$S = \frac{\pi}{2}\int_0^{2\pi}\int_0^{\pi/2} \sin(\bar{\omega}_D N T_r)\sin(\bar{\omega}_D M T_r) \times \sin\beta \, d\beta \, d\alpha \qquad (25)$$

The final S-spin magnetization, S, depends on the echo amplitude before and after the coherence transfer which in turn depends on the placement of π-pulses, the number of rotor cycles N and M and the rotor period length, T_R. The dipolar frequencies before and after the coherence transfer need not be same in the two different TEDOR dephasing cycles. The time dependence of the observed TEDOR signal is then compared to computer simulations [66].

The TEDOR experiment is used to measure I–S coupling strengths corresponding to distances of 0.3–0.4 nm for ^{13}C–^{15}N spin pairs, although this range can be extended by joining REDOR and TEDOR experiments and measuring a distance to a third spin [67]. A comparison of the TEDOR ^{13}C spectrum and a corresponding Hahn-echo spectrum recorded for a physical mixture of L-[4-^{13}C, amide-^{15}N]asparagine and [1-^{13}C]sodium propionate is shown in Fig. 12. Although the TEDOR pulse scheme is selective, there is nevertheless a sacrifice in signal amplitude when compared to a Hahn echo because of the random orientation in the sample. Calculations predict that the TEDOR signal should be 52% of the Hahn-echo intensity for these conditions, in practice however, TEDOR intensities are ~ 40% of the full signal [12].

Two-dimensional versions of TEDOR add another degree of flexibility to this experiment. For example, a correlation spectrum of dipolar coupled spins can be performed by inserting an evolution period (t_1) before the preparative S-spin π-pulses and allowing spins to evolve under the chemical shift Hamiltonian [68]. Alternatively, a two dimensional version of TEDOR can be designed to selectively examine weak couplings in the presence of strong couplings by choosing values of N and M that filter-out strong couplings [66].

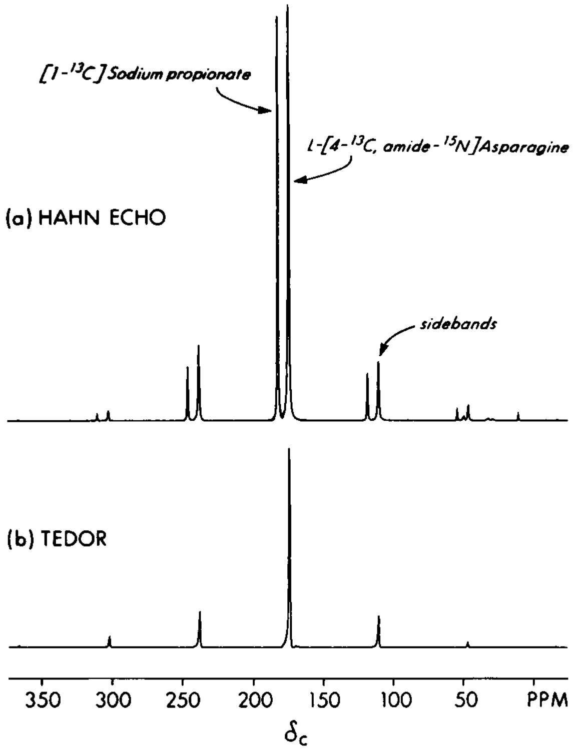

Fig. 12. A comparison of the TEDOR ^{13}C spectrum and the corresponding Hahn-echo spectrum recorded for a physical mixture of L-[4-^{13}C, amide-^{15}N]asparagine (90% ^{13}C, 98% ^{15}N) and [1-^{13}C]sodium propionate (90% ^{13}C). (a) Hahn-echo spectrum acquired with an interpulse spacing delay of $T = 2T_r$. (b) TEDOR ^{13}C spectrum acquired at $M = 2$ rotor periods after the coherence transfer and $N = 2$ rotor periods before the coherence transfer [66]. Reprinted with permission from Journal of Magnetic Resonance, Vol. 96, p. 206. Copyright 1992 Academic Press, Inc.

APPLICATIONS

Rotational resonance (R^2) NMR spectroscopy has been used to determine the conformation of the retinal [69,70] and most recently, to quantify retinal to protein distances [71,72] in the 26 kD light-driven membrane protein, bacteriorhodopsin (bR). Thompson et al. [44], for example, have used R^2 to determine the conformation about the Schiff base C=N bond at the retinal–protein linkage in dark-adapted bR. Knowledge of this conformation is important in deciphering the mechanism by which retinal isomerizations influence proton transport across the bR membrane. In this study, the conformation about the C=N bond was resolved by measuring the distance between two selectively enriched sites – retinal [14-^{13}C] and [ϵ-^{13}C]Lys216 – in each of the two molecules, bR$_{555}$ and bR$_{568}$, comprising dark-adapted bR.

Figure 13 [44] illustrates the proposed conformations of dark-adapted bR and several photointermediate states. Since the two selectively labeled ^{13}C sites are well-separated in their chemical shifts [73] in bR$_{555}$ and bR$_{568}$, two separate R^2 measurement were performed on the same sample (one for each molecule); these measurements differ only by adjustment of the sample rotation frequency. Figure 14 shows the CP/MAS spectra (after subtraction of natural-abundance bR), recorded as a function of mixing time, for these R^2 measurements. The integrated difference intensities of the two carbon resonance peaks, $\langle I_{14}-I_{\epsilon} \rangle$, are plotted in Fig. 15 along with computer simulations of the exchange process. These exchange plots are consistent with a C=N distance of 0.30 ± 0.02 nm for bR$_{555}$ and 0.41 ± 0.03 nm for bR$_{568}$, and are in agreement with C=N *syn* and C=N *anti* conformations, respectively. A similar strategy has been used to confirm the C=N anti conformation present in the *M* photointermediate of bR [71].

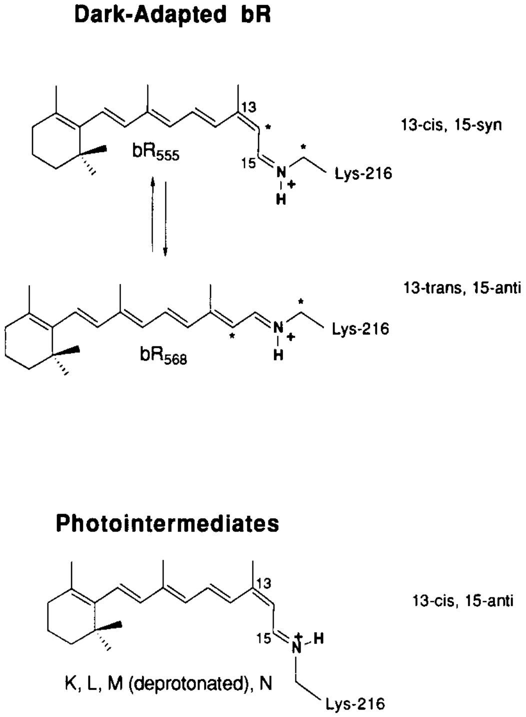

Fig. 13. Proposed structures of retinal in dark-adapted bR and several photocycle intermediates. The two selectively enriched ^{13}C sites, retinal [14-^{13}C] and [^{13}C-ϵLys] are indicated (*) in this figure. The distance between these two sites depends on the configuration of the C=N bond. bR$_{555}$ contains 13-*cis* retinal with a C=N *syn* bond, bR$_{568}$ is all *trans* with C=N *anti* and the *M*-state is 13-*cis* with C=N *anti*. From [44]. Reprinted with permission from Biochemistry, Vol. 31, p. 7932. Copyright 1992 American Chemical Society.

The opportunity to measure a single internuclear distance in a large protein like bR is attributed to the spectral selectivity of the R^2 condition. Several additional studies exemplify the wealth of information obtained by a single distance measurement. McDermott et al. [74], for example, used ^{31}P R^2 to demonstrate that the mechanism of inactivation in an enzyme bound inhibitor involves phosphorylation to form an adduct. In a separate study, Peerson et al. [75] measured a series of ^{13}C R^2 distances between adjacent helical turns of a hydrophobic α-helical peptide and concluded that its local secondary structure is maintained even after the peptide is embedded in a membrane.

Similar to R^2 experiments, single distance measurements obtained with REDOR can provide important geometric constraints in structural studies of individual molecules or molecular complexes. For example, two recent REDOR studies [61,67] have focussed on the 9-residue antibiotic peptide emerimicin Ac–Phe–MeA[1-^{13}C]–MeA(d$_6$)–MeA–Val–Gly[^{15}N]–Leu–MeA–MeA–OBzl (where MeA = α-methylalanine or aminoisobutyric acid). Although emerimicin is known to adopt an α-helical structure, a similar peptide, comprised of one less residue (2–9), adopts a 3$_{10}$-helix conformation, suggesting a relatively small energy difference between the two helical forms. A method for discerning between these two structures has been demonstrated by Marshall et al. [61] using a single $^{13}C-^{15}N$ REDOR distance measurement (0.40 ± 0.01 nm).

In a related study, Holl et al. [67] combined REDOR and TEDOR to measure a $^{19}F-^{13}C$ internuclear distance in a fluorinated analogue of emerimicin $^{19}FCH_2CO$-Phe-MeA-MeA-[1-^{13}C]MeA-[^{15}N]Val-Gly-Leu-MeA-MeA-OBzl. The TEDOR portion of the experiment was designed to target the $^{13}C-^{15}N$ pair in this triple-labeled peptide, thereby removing all other carbons from the experiment, and REDOR was used subsequently to quantify the $^{13}C-^{19}F$ coupling. This latter portion of the experiment yielded a distance of 0.78 nm, in close agreement with the predicted α-helical distance.

A recent $^{13}C-^{31}P$ REDOR study by Christensen and Schaefer [55] has focused on elucidating the geometry of shikimate 3-phosphate (S3P) and *N*-phosphonomethyl glycine (glyphosate) bound to a 46 kDa enzyme, EPSP synthase. EPSP is active in the catalytic synthesis of aromatic amino acids and is the primary site of action of the glyphosate herbicide. Although this enzyme system has been studied extensively for a number of years, the complex itself resists crystallization and is therefore not amenable to study by x-ray crystallography. The proposed S3P-glyphosate structure, shown in Fig. 16, results from two separate REDOR distance measurements used in conjunction with energetic considerations. First, an intermolecular REDOR measurement between [1-^{13}C]glyphosate and S3P bound to natural abundance EPSP determined a distance of 0.72 ± 0.04 nm, suggesting that S3P and glyphosate complex are near each other in the binding site of EPSP. Secondly, a $^{13}C-^{31}P$ in-

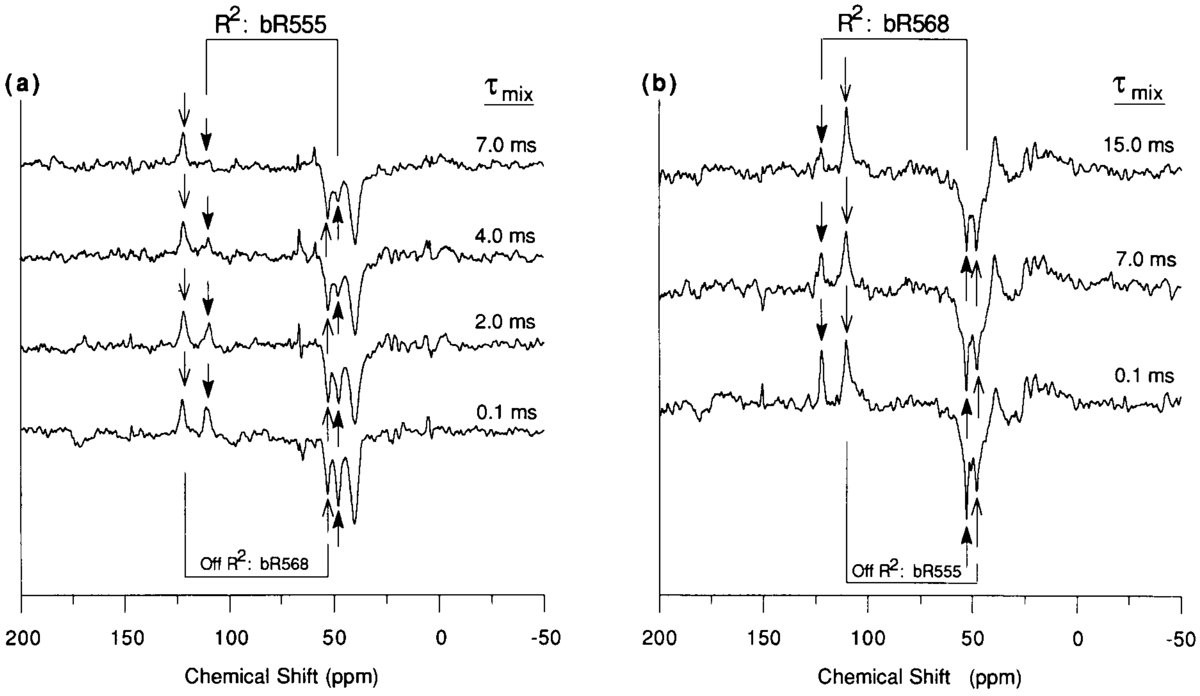

Fig. 14. CP MAS difference spectra of bR recorded with selective inversion of the [^{13}C-ϵLys] peak and after magnetization exchange at R^2 for various mixing times: (a) magnetization exchange spectra collected at $\omega_r/2\pi = 6240$ Hz, which facilitates magnetization exchange in bR_{555} and (b) spectra collected at $\omega_r/2\pi = 6910$ Hz which facilitates magnetization exchange in bR_{568}. The two peaks coupled by R^2 (filled arrows) decrease in intensity with mixing time. The off-R^2 peaks (open arrowheads) retain constant intensity with time. These spectra were recorded at −50°C and are displayed after subtraction of natural abundance ^{13}C. From [44]. Reprinted with permission from Biochemistry, Vol. 31, p. 7934. Copyright 1992 American Chemical Society.

tramolecular distance of 0.56 ± 0.02 nm established that glyphosate is fully extended when bound to the enzyme. Figure 17 shows the REDOR difference spectra recorded for these two measurements along with the corresponding REDOR difference spectra for unlabeled (natural-abundance) molecules. The REDOR difference signals for inter- and intramolecular distance measurements (after subtraction of natural abundance spectra), are plotted in Fig. 18 along with the theoretical dephasing curve. In both cases, REDOR data are consistent with a single, well-defined internuclear distance.

A different strategy is adopted if the goal is to elucidate the entire secondary structure of a molecule, such as a peptide fragment. Spencer et al. [76] used a series of R^2 measurements to study a 9-amino acid segment (residues 34–42) H_2N–Leu–Met–Val–Gly–Gly–Val–Val–Ile–Ala–CO_2H of the β-amyloid peptide found in the neuritic brain plaque of Alzheimer's disease victims. This study has identified an unusual *cis* conformation in the 37–38 Gly–Gly region of this 9 amino acid peptide. A similar strategy has been used by Garbow and McWherter [54] to investigate the solid-state structure of the neurohormone "melanostatin" (Pro–Leu–Gly–NH_2) using ^{13}C–^{15}N REDOR distances. From geometric considerations, two internuclear distances are sufficient to constrain the dihedral angles (ϕ, ψ and ω) of an amino acid to four possible values in dihedral space. Figure 19 illustrates a general strategy for determining dihedral angles through ^{13}C R^2 or ^{13}C–^{15}N REDOR measurements. In both studies, internuclear distance measurements were used together with energetic considerations to severely constrain the peptide structure. In general, however, elucidation of peptide and protein structures are complicated by the presence of strong intra- and intermolecular forces that govern the packing arrangement of molecules in the solid state.

Although this article concentrates on distance measurements between ^{13}C and ^{31}P or ^{15}N, the methods described here are generally applicable to a variety of other nuclei. Schmidt et al. [77], for example, have adapted REDOR for systems comprised of ^2H (spin-1) and ^{13}C nuclei, thereby

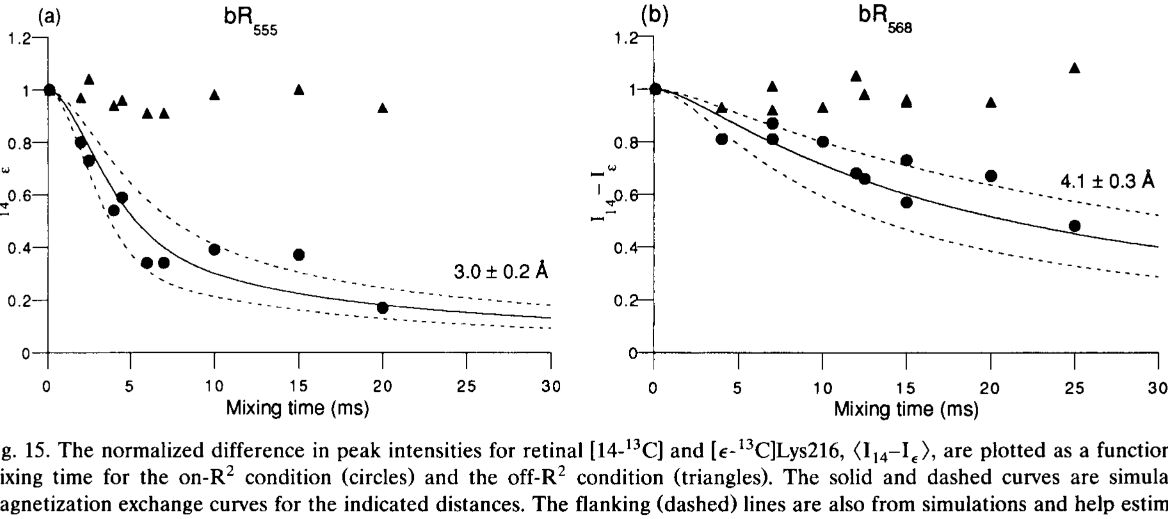

Fig. 15. The normalized difference in peak intensities for retinal [14-^{13}C] and [ϵ-^{13}C]Lys216, $\langle I_{14}-I_\epsilon \rangle$, are plotted as a function of mixing time for the on-R^2 condition (circles) and the off-R^2 condition (triangles). The solid and dashed curves are simulated magnetization exchange curves for the indicated distances. The flanking (dashed) lines are also from simulations and help estimate the uncertainty in the distance measurement. For bR_{568}, these data are consistent with a distance of 0.30 ± 0.02 nm and for bR_{568}, these data are consistent with a distance of 0.41 ± 0.03 nm. Parameters for simulations were obtained using methods detailed earlier in this review. From [44]. Reprinted with permission from Biochemistry, Vol. 31, p. 7935. Copyright 1992 American Chemical Society.

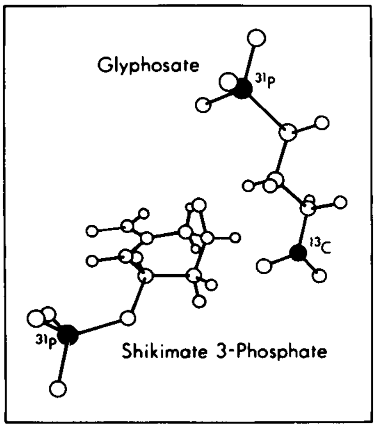

Fig. 16. Proposed structure of S3P–glyphosate complex bound to EPSP synthase [55]. A REDOR study has measured the intramolecular distance between ^{31}P–^{13}C sites on the glyphosate (0.56 nm) and the intermolecular distance between ^{31}P–^{13}C sites on the glyphosate and S3P molecule (0.72 nm). This structure assumes a hydrogen bond between the glyphosate NH proton and the C5 oxygen of S3P. Reprinted with permission from Biochemistry, Vol 32, p. 2871. Copyright 1993 American Chemical Society.

demonstrating the utility of this technique for combinations of spin-1/2 and quadrupolar nuclei. This approach offers the advantage that ^{2}H

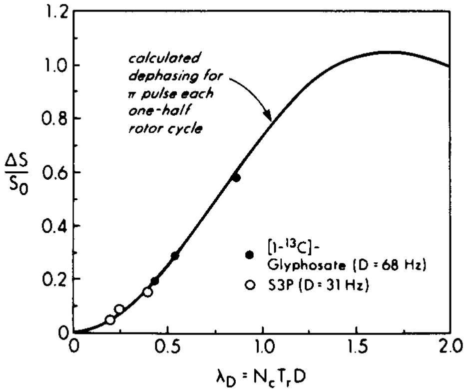

Fig. 18. The dependence of $\Delta S/S_0$ on the dimensionless quantity $\lambda_D = N_c D T_r$ for the S3P-glyphosate enzyme complex. The results for ^{31}P–^{13}C intramolecular coupling in labeled glyphosate is shown by the filled circles, while the intermolecular ^{31}P–^{13}C data are shown by open circles. The solid line shows the corresponding theoretical REDOR curve and is consistent with a single distance. From [55]. Reprinted with permission from Biochemistry, Vol. 32, p. 2872 Copyright 1993 American Chemical Society.

spectra are free of background interference problems because of the inherently low natural abundance of this isotope. In another recent example, Fyfe et al. [68] have used REDOR and 2D

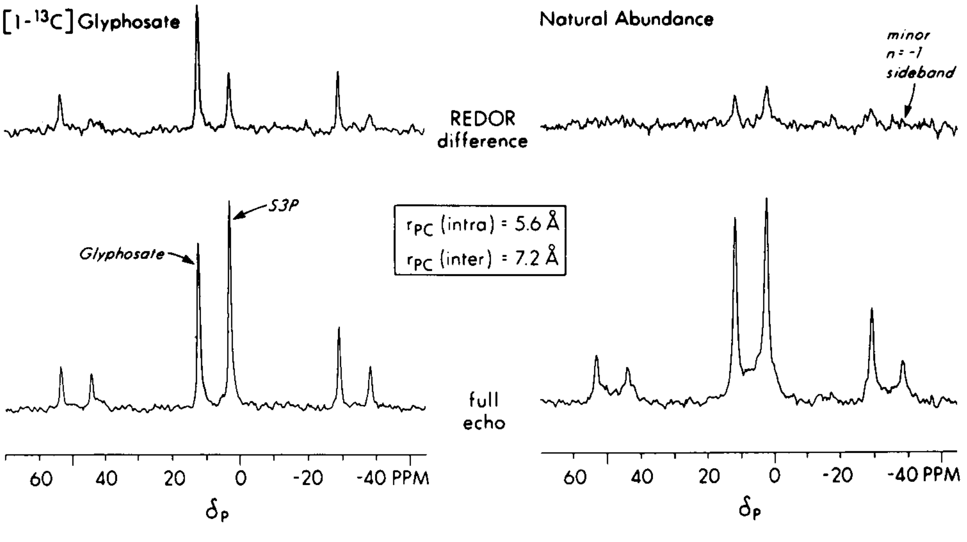

Fig. 17. Full-echo and ^{31}P REDOR difference spectra (left) were recorded for intermolecular and intramolecular measurements of S3P and [1-^{13}C]glyphosate bound to natural abundance EPSP. REDOR spectra on the right show the full-echo and REDOR difference spectra for S3P and natural abundance glyphosate bound to EPSP. These spectra were recorded after 64 rotor cycles and using a spinning frequency of 5 kHz. From [55]. Reprinted with permission from Biochemistry, Vol. 32, p. 2871. Copyright 1993 American Chemical Society.

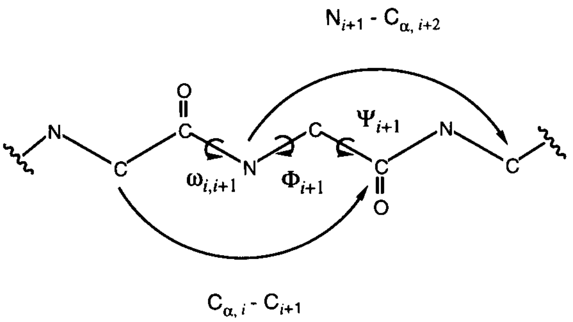

Fig. 19. A general strategy for mapping secondary structure of a peptide backbone using REDOR and R^2 distance measurements [54,76]. The distance between the C_α of amino acid i and the carbonyl carbon of amino acid $i+1$ ($C_{\alpha,i}$ to C_{i+1}) depends on the dihedral angle Φ_{i+1} and the intervening angle $\omega_{i,i+1}$. A second distance, from C_i to $C_{\alpha,i+1}$ depends on the dihedral angles Ψ_{i+1}, Φ_{i+1}, and $\omega_{i+1,i+2}$. In a similar fashion, N_{i+1} to $C_{\alpha,i+2}$ depends on the angle Ψ_{i+1}. These types of measurements are used to constrain each amino acid to one of four possible conformations.

TEDOR to study the ^{27}Al–O–^{31}P linkage in the very large pore aluminosilicate VPI-5.

Quantitative analysis of dipolar measurements may require consideration of parameters in addition to those described here. For example, some types of molecular motion will average dipolar couplings and hence, yield scaled coupling strengths [41,61]. In other circumstances, dipolar measurement might reflect an average internuclear distance between two rapidly interconverting conformations. Although the effects of molecular motion are sometimes difficult to estimate, temperature variable studies can often indicate whether molecular motion is an important factor in the system under study.

Conclusion

Solid-state MAS experiments that restore dipolar couplings are becoming increasingly important in studies of local molecular structure in a broad range of biological and inorganic materials. These techniques provide accurate determination of internuclear distances, due to the sensitivity of the dipolar coupling to internuclear distance, and are furthermore applicable to crystalline and non-crystalline materials alike. In comparison, solution NMR is generally unsuitable for insoluble macromolecules, while x-ray crystallography is restricted to materials that form crystals of adequate quality.

In many investigations, a number of questions related to structure and function can be answered with knowledge of a few accurate distance measurements in the range of 0.2–0.6 nm. Examples include distinguishing between various peptide conformations, elucidating the geometry of protein binding or folding, determining the geometry of molecules adsorbed on surfaces, and probing the interface between two materials or phases such as polymer blends, metal–polymer junctions, or enzyme–substrate linkages. R^2, REDOR and TEDOR experiments are well-suited to these types of applications and have been demonstrated for combinations of spins including ^{2}H, ^{13}C, ^{15}N, ^{19}F, ^{27}Al, and ^{31}P.

Future developments will undoubtably extend the flexibility of MAS experiments to provide accurate distances in situations where more than a single spin pair is present, in a manner akin to 2D solution NMR experiments. DRAMA, SEDRA, and RFDR experiments described here can, in principle, provide a broad mapping of dipolar coupled nuclei thereby establishing spatial connectivities and quantifying internuclear distances. These approaches will vastly improve the efficiency of gathering structural information. Furthermore, 2D dipolar correlation experiments may be extended in the future to include a third dimension – such as ^{15}N combined with ^{13}C–^{13}C – as a means to improve spectral resolution and to assist in assigning resonance peaks in complex molecules.

The authors acknowledge the support of the National Institutes of Health (GM-23403, GM-23289, GM-25505 and RR-00995). We express thanks to P.R. Costa, K.K. Gleason and D. Maus for critical comments and for assistance with several of the figures. We also thank Prof. J. Schaefer, of Washington University for several of the figures. Finally, we wish to acknowledge A.E. Bennett, F. Creuzet, M.H. Levitt, A.E. McDermott, D.P. Raleigh, D.K. Sodickson, L.K. Thompson, and S. Vega for stimulating discussions and for their contributions to the development of these NMR techniques. J.M.G. was the recipient of an American Cancer Society postdoctoral fellowship (PF-3875).

REFERENCES

1 K. Wuthrich, NMR of Proteins and Nucleic Acids, Wiley, New York, 1986. pp. 166.
2 G.M. Clore and A.M. Gronenborn, Science, 252 (1991) 1390.
3 D.P. Raleigh, M.H. Levitt and R.G. Griffin, Chem. Phys. Lett., 146 (1988) 71.
4 R. Tycko and G. Dabbagh, Chem. Phys. Lett., 173 (1990) 461.
5 R. Tycko and S.O. Smith, J. Chem. Phys, 98 (1993) 932.
6 S. Vega, talk entitled "Dressed States in Magic Angle Sample Spinning NMR" presented at the 32nd Experimental Nuclear Magnetic Resonance Spectroscopy Conference, St. Louis, Missouri, April, 1991.
7 T. Gullion and S. Vega, Chem. Phys. Lett., 194 (1992) 423.
8 A.E. Bennett, J.H. Ok, S Vega and R.U. Griffin, J. Chem. Phys, 96 (1992) 8634.
9 D.K. Sodickson, M.H. Levitt, S. Vega and R.G. Griffin, J. Chem. Phys., 98 (1993) 6742.
10 T. Gullion and J. Schaefer, J. Magn. Reson., 81 (1989) 196.
11 T. Gullion and J. Schaefer, in W.S. Warren (Ed.), Detection of Weak Heteronuclear Dipolar Coupling by Rotational-Echo Double-Resonance Nuclear Magnetic Resonance (Advances in Magnetic Resonance 13), Academic Press, New York, 1989, p. 57.
12 A.W. Hing, S. Vega and J. Schaefer, J. Magn. Reson., 96 (1992) 205.
13 A. Abragam, in W.C. Marshall and D.H. Wilkinson (Eds.), Principles of Nuclear Magnetism (The International Series of Mongraphs on Physics), Oxford University Press, New York, 1961, pp. 599.
14 G.E. Pake, J. Chem. Phys., 16 (1948) 327.
15 D.L. VanderHart and H.S. Gutowsky, J. Chem. Phys., 49 (1968) 261.
16 K.W. Zilm and D.M. Grant, J. Am. Chem. Soc., 103 (1981) 2913.
17 C.P. Slichter, in P. Fulde (Ed.), Principles of Magnetic Resonance (Springer Series in Solid-State Sciences 1), Springer Verlag, New York, 3rd end., 1990, pp. 655.
18 E.R. Andrew, A. Bradbury and R.G. Eades, Nature, 183 (1959) 1802.
19 J. Schaefer and E.O. Stejskal, J. Am. Chem. Soc., 98 (1976) 1031.
20 M.M. Maricq and J.S. Waugh, J. Chem. Phys., 70 (1979) 3300.
21 J. Herzfeld and A.E. Berger, J. Chem. Phys., 73 (1980) 6021.
22 S.O. Smith and R.G. Griffin, Ann. Rev. Phys. Chem., 39 (1988) 511.
23 U. Haeberlen, in J.S. Waugh (Ed.), High Resolution NMR in Solids (Advances in Magnetic Resonance), Academic Press, New York, 1976, pp. 190.
24 B.C. Gerstein and C.R. Dybowski, Transient Techniques in NMR of Solids, Academic Press, Orlando, FL, 1985, pp. 295.
25 R.G. Griffin, W.P. Aue, R.A. Haberkorn, G.S. Harbison, J. Herzfeld, E.M. Menger, M.G. Munowitz, E.T. Olejniczak, D.P. Raleigh, J.E. Roberts, D.J. Ruben, A. Schmidt, S.O. Smith and S. Vega, in B Maraviglia (Ed.), Physics of NMR Spectroscopy in Biology and Medicine, Course C, North-Holland, Amsterdam, 1988, p. 203.
26 M. Alla and E. Lippmaa, Chem. Phys. Lett., 37 (1976) 260.
27 J.S. Waugh, Proc. Natl. Acad. Sci., 73 (1976) 1394.
28 R.K. Hester, J.L. Ackerman, B.L. Neff and J.S. Waugh, Phys. Rev. Lett., 36 (1976) 1081.
29 M.E. Stoll, A.J. Vega and R.W. Vaughan, J. Chem. Phys., 65 (1976) 4093.
30 D.E. Kaplan and E.L. Hahn. J. Phys. Radium, 19 (1958) 821.
31 M. Emshwiller, E.L. Hahn and D. Kaplan, Phys. Rev., 118 (1960) 414.
32 R.G. Griffin, G. Bodenhausen, R.A. Haberkorn, T.H. Huang, M. Munowitz, R. Osredkar, D.J. Ruben, R.E. Stark and H.V. Willigen, Philos. Trans. Roy. Soc. London A, 299 (1981) 547.
33 M.G. Munowitz, R.G. Griffin, G. Bodenhausen and T. Huang, J. Am. Chem. Soc., 103 (1981) 2529.
34 J.E. Roberts, G.S. Harbison, M.G. Munowitz, J. Herzfeld and R.G. Griffin, J. Am. Chem. Soc., 109 (1987) 4163.
35 T. Gullion, M.D. Poliks and J. Schaefer, J. Magn. Reson., 80 (1988) 553.
36 E.R. Andrew, A. Bradbury, R.G. Eades and V.T. Wynn, Phys. Lett., 4 (1963) 99.
37 M.G. Colombo, B.H. Meier and R.R. Ernst, Chem. Phys. Lett., 146 (1988) 189.
38 G.A. Morris and R. Freeman, J. Magn. Reson., 29 (1978) 433.
39 P. Caravatti, G. Bodenhausen and R.R. Ernst, J. Magn. Reson., 55 (1983) 88.
40 M.H. Levitt, D.P. Raleigh, F. Creuzet and R.G. Griffin, J. Chem. Phys., 92 (1990) 6347.
41 F. Creuzet, D.P. Raleigh, M.H. Levitt and R.G. Griffin, J. Am. Chem. Soc., (1993) in press.
42 M. Mehring, Principles of High-Resolution NMR in Solids, Springer Verlag, New York, 1983, pp. 342.
43 W. Veeman, Philos. Trans. Roy. Soc. London, A299 (1981) 629.
44 L.K. Thompson, A.E. McDermott, J. Raap, C.M. van den Wielen, J. Lugtenburg, J. Herzfeld and R.G. Griffin, Biochemistry, 31 (1992) 7931.
45 D.P. Raleigh, F. Creuzet, S.K. das Gupta, M.H. Levitt and R.G. Griffin, J. Am. Chem. Soc., 111 (1989) 4502.
46 D. Suter and R.R. Ernst, Phys. Rev. Lett. B, 32 (1985) 5608.
47 A. Kubo and C.A. McDowell, J. Chem. Soc. Faraday Trans., 84 (1988) 3713.

48 B.H. Meier and W. Earl, J. Am. Chem. Soc., 109 (1987) 7937.
49 Z. Gan and D.M. Grant, Mol. Phys., 67 (1990) 1419.
50 A. Schmidt and S. Vega, J. Chem. Phys., 4 (1992) 2655.
51 A. Wokaun and R.R. Ernst, J. Chem. Phys., 67 (1977) 1752.
52 S. Vega, J. Chem. Phys., 68 (1978) 5518.
53 J.H. Ok, R.G.S. Spenser, A.E. Bennett and R.G. Griffin, Chem. Phys. Lett., 197 (1992) 389.
54 J.R. Garbow and C.A. McWherter, J. Am. Chem. Soc., 115 (1993) 238.
55 A.M. Christensen and J. Schaefer, Biochemistry, 32 (1993) 2868.
56 T. Gullion, D.B. Baker and M.S. Conradi, J. Magn. Reson., 89 (1990) 479.
57 T. Gullion and J. Schaefer, J. Magn. Reson., 92 (1991) 439.
58 M.G. Munowitz and R.G. Griffin, J. Chem. Phys., 76 (1982) 2848.
59 E.T. Olejniczak, S. Vega and R.G. Griffin, J. Chem. Phys., 81 (1984) 4804.
60 Y. Pan, T. Gullion and J. Schaefer, J. Magn. Reson., 90 (1990) 330.
61 G.R. Marshall, D.D. Beusen, K. Kociolek, A.S. Redlinski, M.T. Leplawy, Y. Pan and J. Schaefer, J. Am. Chem. Soc., 112 (1990) 963.
62 S.M. Holl, R.A. McKay, T. Gullion and J. Schaefer, J. Magn. Reson., 89 (1990) 620.
63 Y. Pan and J. Schaefer, J. Magn. Reson., 90 (1990) 341.
64 A. Bax, N.M. Szeverenyi and G.E. Maciel, J. Magn. Reson., 50 (1982) 227.
65 J.E. Roberts, S. Vega and R.G. Griffin, J. Am. Chem. Soc., (1984) 2506.
66 A.W. Hing, S. Vega and J. Schaefer, J. Magn. Reson., Series A, 103 (1993) 151.
67 S.M. Holl, G.R. Marshall, D.D. Beusen, K. Kociolek, A.S. Redlinski, M.T. Leplawy, R.A. McKay, S. Vega and J. Schaefer, J. Am. Chem. Soc., 114 (1992) 4830.
68 C.A. Fyfe, K.T. Meuller, H. Gondey and K.C. Wong-Moon, Chem. Phys. Lett., 199 (1992) 198.
69 F. Creuzet, A. McDermott, R. Gebhard, K. Van der Hoef, M.B. Spijker-Assink, J. Herzfeld, J. Lugtenburg, M.H. Levitt and R.G. Griffin, Science, 251 (1991) 783.
70 A.E. McDermott, F. Creuzet, R. Gebhard, K. Van der Hoef, J. Herzfeld, J. Lugtenburg and R.G. Griffin, Biochemistry, in press.
71 K.V. Lakshmi, M. Auger, J. Raap, J. Lugtenburg, R.G. Griffin and J. Herzfeld, JACS, submitted for publication.
72 M. Auger, K.V. Lakshmi, E.M.M. de Brabander-van den Berg, S.J. Rosselet, H.G. Khorana, S.K.D. Gupta, J. Raap, W.B.S. van Liemt, J. Lugtenburg, J. Herzfeld and R.G. Griffin, Biochemistry, submitted for publication.
73 M.R. Farrar, K.V. Lakshmi, S.O. Smith, R.S. Brown, J. Raap, J. Lugtenburg, R.G. Griffin and J. Herzfeld, Biophys. J., 65 (1993) 310.
74 A.E. McDermott, F. Creuzet, R.G. Griffin, L.E. Zawadzke, Q. Ye and C.T. Walsh, Biochemistry, 29 (1990) 5767.
75 O.B. Peerson, S. Yoshimura, H. Hojo, S. Aimoto and S.O. Smith, J. Am. Chem. Soc., 114 (1992) 4332.
76 R.G.S. Spencer, K.J. Halverson, M. Auger, A.E. McDermott, R.G. Griffin and P.T. Lansbury, Jr., Biochemistry, 30 (1991) 10382.
77 A. Schmidt, R.A. McKay and J. Schaefer, J. Magn. Reson., 96 (1992) 644.

Analytica Chimica Acta, 283 (1993) 1103–1112
Elsevier Science Publishers B.V., Amsterdam

^{129}Xe NMR spectroscopy in microporous solids: the effect of bulk properties

John A. Ripmeester and Christopher I. Ratcliffe
Steacie Institute for Molecular Sciences, National Research Council of Canada, Ottawa, Ontario K1A OR9 (Canada)

(Received 5th January 1993; Revised manuscript received 20th April 1993)

Abstract

In this contribution we point out a number of factors related to the bulk properties of microporous solids which must be taken into account in order first of all to obtain meaningful ^{129}Xe NMR spectral data, and secondly to interpret the data properly. This sensitivity to bulk properties is especially important for microporous solids where there is little or no barrier to xenon passage from inside the particle to the interparticle space. We examine the effect of particle size, powder bulk density and particle anisotropy, and also the effect of low thermal conductivity of low density powders.

Keywords: Nuclear magnetic resonance spectroscopy; Microporous solids; Solid state NMR; Xenon-129 NMR

In the last decade many papers have dealt with the various aspects of Xe nuclear magnetic resonance (NMR) spectroscopy [1–27], and the literature has recently been reviewed [28,29]. The fundamental concept, that the Xe chemical shift reflects the size and geometry of the trapping site, was recognized early for closed cage systems [4]. For open channel materials, matters are complicated by the loading dependence of the chemical shift [5,6], yet there have been many publications dealing with the use of Xe NMR chemical shifts as a probe of the void space in microporous solids [28,29]. However, the different approaches which have been suggested to account for chemical shift data quantitatively [7–9] have not been critically tested, and some clear disagreements between predictions and observations have been noted [21–24]. Some of the criticisms of the proposed models have been published [24], and as time progresses some of the fundamental aspects are being addressed [24,30–34].

One aspect of considerable concern is the observation that interparticle exchange of xenon that is fast on an NMR timescale may occur [11,12,14–19], thus further complicating the interpretation of Xe chemical shift data. This will also complicate the interpretation of other NMR parameters, such as linewidths and relaxation times, although these have as yet received little serious attention. In this contribution we examine the importance of some of the bulk properties of the powdered materials. The subject area is too complex to give a definitive treatment at this time, as the fundamental concepts which govern ^{129}Xe chemical shifts and relaxation for xenon trapped in solids are still unknown. Much of the theory developed for relaxation in heterogeneous systems [35,36] may well be appropriate for Xe–solid systems, yet study of the latter may provide additional insight as xenon NMR gives the additional dimension of chemical shift resolution. We use a strictly phenomenological approach to illustrate

Correspondence to: J.A. Ripmeester, Steacie Institute for Molecular Sciences, National Research Council of Canada, Ottawa, Ontario K1A OR9 (Canada).

the complexity of the subject, and to alert those interested in applications of the ^{129}Xe NMR technique to potential pitfalls in obtaining and interpreting data.

EXPERIMENTAL

Materials

A piece of Vycor controlled-pore glass rod with 40 Å pores, obtained from Dow-Corning, was cleaned first with a 10% hydrogen peroxide solution, then nitric acid before rinsing, drying and grinding the glass with a mortar and pestle. The powdered glass was then wet-screened through standard Tyler screens to give fractions of particles in different size ranges. NaY zeolite (LZY52) was obtained from Linde, silica gels of different pore sizes from Aldrich.

Samples were placed in 10 mm o.d. pyrex tubes, then dehydrated at 400°C before condensing a calibrated amount of xenon into the sample tube and flame-sealing. It was considered necessary to fill the empty space above the sample with a snugly fitting glass tube with a 1 mm diameter clear bore, both to confine the sample, and to fill dead space. For low temperature work on loose powders, it was also necessary to add a low pressure of helium gas to ensure adequate thermal contact between sample and the sample tube wall.

NMR experiments

^{129}Xe spectra were recorded at frequencies of 49.8, 55.3 and 83.0 MHz on Bruker CXP-180, MSL-200 and MSL-300 NMR spectrometers. Solid-state probes with horizontal solenoid geometry were used. The 90° pulse lengths used were between 5 and 7 μs. In addition to simple Bloch decay experiments, phase-cycled Hahn echo pulse sequences [37] were used to collect data for especially broad signals which were difficult to phase correctly when obtained from Bloch decays. Non-selective spin-lattice relaxation time measurements were made by means of inversion recovery experiments, and selective relaxation measurements were carried out with DANTE sequences [38].

RESULTS AND DISCUSSION

Particle size effects

The important consideration here is that if rapid interparticle exchange of Xe occurs for a powdered solid with internal pore space, then certainly rapid exchange will occur between intra and extra particle xenon. Then the diffusion pathlength of the xenon inside the particle as well as that outside the particle becomes important. First of all, we define a time characteristic of the lifetime of a xenon atom within a particle, t_1. This can be related to the diffusion pathlength r_1 through a diffusion equation such as the Einstein equation. Another parameter that is important is the time t_e which defines the criterion for fast and slow exchange for xenon between intraparticle and extraparticle space on the NMR chemical shift timescale. If d_s and d_g are the xenon chemical shifts in the solid and gas phases in absence of exchange, $t_e = [2\pi(\delta_s - \delta_g)]^{-1}$. The different situations that then come to mind are described below and illustrated in Fig. 1.

(i) Diffusion pathlength r_1 is much smaller than the particle size r_p, $t_1 > T_{1g}$, T_{1s}, t_e (Fig. 1a). This is the only case where the measured resonance parameters (chemical shift, linewidth and relaxation time) truly reflect the values for xenon in the two phases. In the complete absence of exchange or surface effects, a gas phase signal may be difficult to observe, as the relaxation time for the free gas is very long [39].

(ii) Diffusion pathlength is such that exchange is slow, but of the same order as the xenon T_1 in the gas or solid phases, T_{1g} or $T_{1s} > t_1 > t_e$ (Fig. 1a). Again the observed chemical shift values should be equal to the true values for the gas and solid phases. However, the observed spin-lattice relaxation times for xenon in the two phases will be complex, and may be non-exponential. The general problem of relaxation of two coupled spin systems was treated in detail many years ago [40]. One may expect exchange broadening of the resonance lines as well.

(iii) Diffusion pathlength much greater than particle size, exchange is fast T_1, $t_e > t_1$ (Fig. 1b). In this case, a single line is seen at a chemical shift value which is a weighted average for the two phases. Similarly, the spin-lattice relaxation can be expected to be single-exponential, and the linewidth may again show exchange broadening.

Since it is difficult to obtain samples with well-defined, uniform particle size ranges for crystalline materials such as zeolites, we have used a Vycor 40 Å controlled pore glass. Samples in different particle size ranges were prepared as described above. ^{129}Xe NMR spectra for four samples with different particle sizes are shown in Fig. 2.

It can be seen that a two-phase picture really is never valid, but it seems a reasonable approximation for the largest size fraction (Fig. 2a). For the next two smaller size ranges, three distinguishable xenon populations can be seen quite clearly (Fig. 2b and c). For both samples, the xenon signal near 0 ppm shows two populations. There is a population for which exchange is in the slow limit, and is coupled to the internal xenon only on the scale of T_1. A second population shows considerable line broadening, and is shifted towards the trapped xenon line at lower field. This second population must be considered as a distinct surface phase. As the internal xenon line also becomes broader with decreasing particle size, this suggests that exchange between internal and surface xenon is significant. Finally, for the smallest particle size fraction, exchange is sufficiently fast to give a single line at an intermediate chemical shift, although there is some residual intensity at the pure phase positions. The width of the line can be attributed to exchange broadening. Since there is a distribution in particle sizes there must be a distribution in exchange broadening parameters, and perhaps also, chemical shifts. It appears that the broad, fast-exchange signal for the smallest size fraction can still be identified with the "surface phase" line seen for the next two larger size fractions.

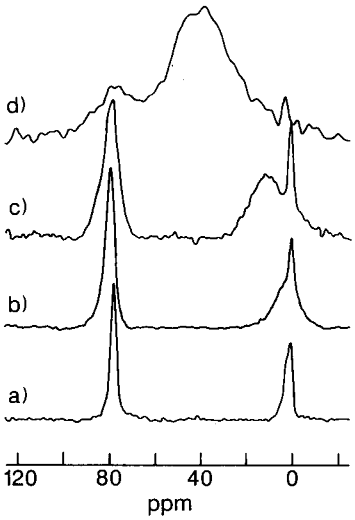

Fig. 2. ^{129}Xe NMR spectra for xenon sorbed in 40 Å Vycor glass of different particle sizes at a loading of 9×10^{19} Xe atoms per gram; (a) $d > 250$; (b) $250 > d > 75$; (c) $53 > d > 38$; (d) $38 > d$, diameters all in μm.

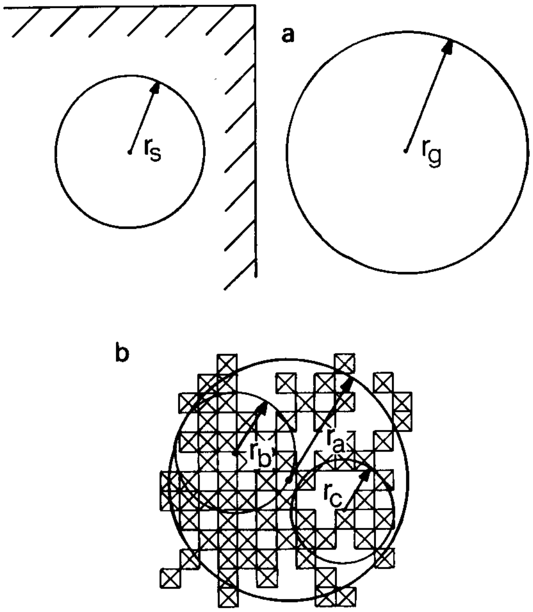

Fig. 1. Illustration of the importance of xenon diffusion path length and particle size; (a) r_s and r_g, the diffusion path lengths in solid and gas in time t much less than particle size; (b) r_a, r_b, r_c diffusion pathlengths in the powder in time t much greater than the particle size. The figure also illustrates that even if sample packing appears homogeneous in a volume set by r_a, it may be quite different in the smaller volumes set by r_b and r_c.

We did not show explicitly that the xenon populations for the largest size fraction (Fig. 2a) were coupled on a T_1 timescale, however, we do show this for a similar system, silica gel beads with 60 Å pores. Figure 3b shows the data obtained in a T_1 inversion recovery experiment for a broad signal due to xenon associated with silica gel pores, and a gas signal near 0 ppm. When the experiment is repeated, inverting the gas line selectively with a DANTE sequence (Fig. 3a), it can be seen that the null time is considerably smaller than for the non-selective experiment, and the magnetization recovery is distinctly non-exponential. Clearly, the two xenon populations are coupled.

For all of the spectra shown in Fig. 2, the only parameter changed is the particle size, so that it is very clear that this must be taken into account when analyzing xenon chemical shift data. This will be true for all materials where there is little restriction to passage from the internal to the external void space. There will be many materials for which the particle size may not be a problem. For instance, for A zeolites with singly charged cations exchange between internal and external void space is slow due to the small openings (~ 4.4 Å) between cages. On the other hand, zeolite Y represents another large-pore case with fast exchange between intra and inter particle xenon, as already illustrated in a number of pub-

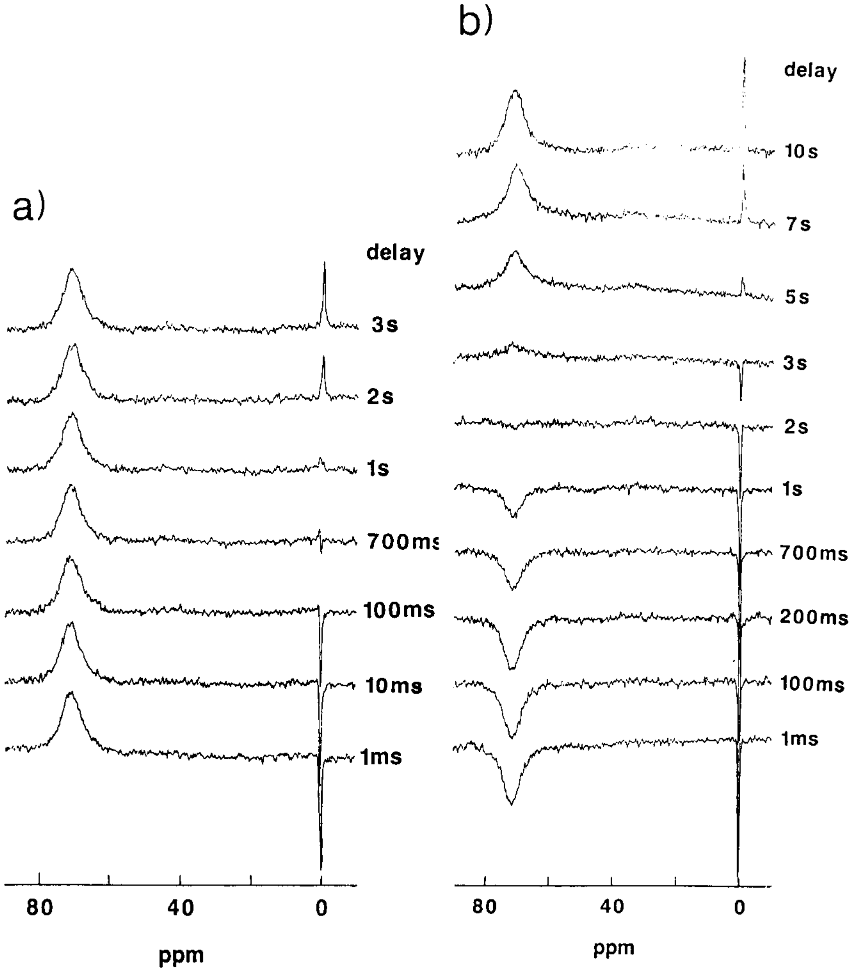

Fig. 3. ^{129}Xe spin-lattice relaxation of xenon sorbed in 60 Å silica gel beads; (a) selective inversion of xenon gas line; (b) non-selective inversion recovery experiment.

lications [12,19,41–43]. We consider the case of NaY zeolite in some more detail in the next section.

The effect of powder bulk density

If we look at case (iii) in some more detail, we have seen that rapid exchange for intra- and interparticle xenon predicts observation of a single line (Fig. 2), however, its exact chemical shift will depend on the relative amounts of xenon inside and outside the particles. (Related results [19] and a preliminary report [18] have been published previously.) This depends on the loading characteristics of the solid, which in turn depends on the number and strength of the sorption sites, and the interparticle volume V_i. For specific cases a quantitative estimate can be made. The interparticle volume is given by $V_i = V_p - V_f$, where V_p and V_f are the total apparent volume of the powder and the true volume of the solid phase, respectively. These quantities are related to the bulk density of the solid, $d_b = W_p/V_p$, and the true framework density of the solid, $d_f = W_p/V_f$, where W_p is the weight of the solid. The number of Xe atoms in the gas phase at a pressure P and temperature T is given by $n_g = NPV_i/RT$, where N is Avogadro's number. We have neglected the small amount of xenon adsorbed on the external surface of the crystallites. This is reasonable, as we have measured the shift for the interparticle xenon to be very close to 0 ppm at low Xe pressure. The number of Xe atoms in a weight of solid W_p contained in a volume V_f is $n_s = g(P)W_p$, where $g(P)$ describes the sorption characteristics, and in its simplest form becomes Henry's law, $g(P) = KP$.

In the fast exchange limit, the chemical shift observed is $\delta_o = f_s\delta_s(P) + f_g\delta_g(P)$, where f_s and f_g are the fractions of Xe atoms in the solid and gas phases respectively. The chemical shifts in the gas and solid phases, $\delta_g(P)$ and $\delta_s(P)$ respectively, are both functions of pressure.

$$\delta_o = \frac{g(P)d_b\delta_s(P) + (NP/RT)(1 - d_b/d_f)\delta_g(P)}{g(P)d_b + (NP/RT)(1 - d_b/d_f)} \tag{1}$$

We evaluate this expression for an average loading of one Xe atom per cage from published sorption data [5], the framework density of NaY zeolite, 1.27 g cm^{-3}, and the bulk density of the powdered sample from its weight and geometry. In Fig. 4 we show results obtained for a loosely powdered sample with a bulk density of 0.3 g cm^{-3} and a die-compressed sample with a bulk density of 1.08 g cm^{-3}. From sorption data [6] and the expressions above, we estimate $f_g = 0.07$, $f_s = 0.93$ for the loosely powdered sample. $\delta_s = 70$ ppm (the chemical shift of Xe on NaY at a loading of about one Xe atom per cage), and the interparticle xenon will have a chemical shift close to the dilute gas value, 0 ppm. From these values

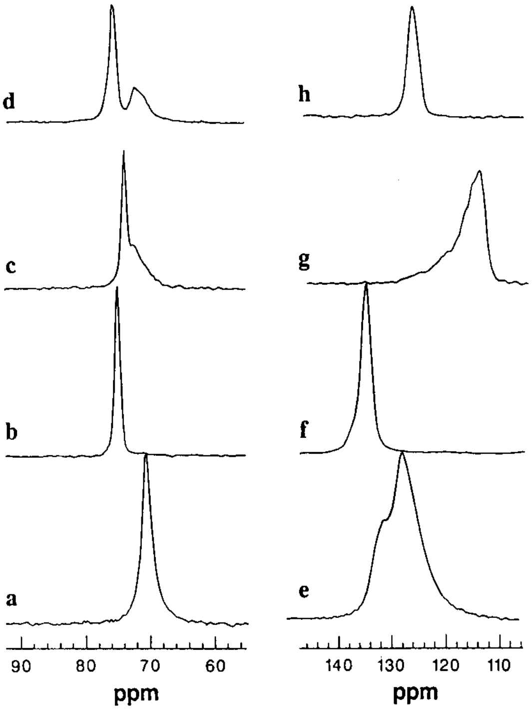

Fig. 4. ^{129}Xe NMR spectra for xenon sorbed in NaY zeolite; a–d average loading of one Xe atom per cage. (a) Loose powder of bulk density 0.3 g cm^{-3}; (b) pressed pellet of bulk density 1.06 g cm^{-3}; (c) loose powder and hand-packed powder; (d) loose powder and die-pressed pellet; (e) average loading 6 Xe atoms per cage, loose powder; (f) average loading 6 Xe atoms per cage, hand-packed powder; (g) average loading 4 Xe atoms per cage, loose powder at 233 K; (h) average loading 4 Xe atoms per cage, hand-packed powder at 233 K.

we calculate an observed chemical shift of 65.8 ppm, 4.2 ppm lower than that of xenon in the zeolite pores. This compares with a measured difference of 4.7 ppm for the loose powder and the die compressed sample (Fig. 4). Clearly, a marked bulk density dependence of the xenon chemical shift can be used as a test for rapid exchange of inter- and extraparticle xenon. The chemical shift values for the densest compressed samples are then actually more characteristic of the true solid phase, whereas the measured chemical shift for the loose powder is characteristic of the combined internal–external pore system.

There also is a remarkable dependence of the linewidth on powder bulk density. For instance, on going from the loosely packed to the die compressed sample, the linewidth decreases from 170 to 70 Hz. We suggest that this observation also can be attributed, at least in part, to the fast exchange of inter- and extraparticle xenon. In a loosely packed sample of NaY with a bulk density of 0.3, most of the sample is essentially empty space, where, once in the interparticle gas phase, a xenon atom may have a mean free path which approaches that of a xenon atom in pure xenon gas under similar conditions of temperature and pressure. Therefore, each xenon atom couples together a limited number of zeolite particles and the surrounding gas volume in a time determined by the fast exchange limit. The size of this volume (cell) is determined by the mean free path of a xenon atom, i.e., the diffusion constant. The macroscopic solid is then made up of a large number of such cells which are not coupled by fast exchange and in each cell the chemical shift is determined by an expression such as given in Eqn. 1. Inhomogeneities in packing of the solid particles then can be described in terms of a distribution of local bulk densities, which results in a distribution of chemical shifts. We note that as the xenon mean free path changes with temperature and pressure, the cell volume sampled by a xenon atom also changes. With decreasing temperature or increasing pressure, the xenon linewidth samples variations in packing density on a decreasing scale. The increasing linewidth and emerging fine structure at higher sample loading therefore reflects small scale packing inhomogeneities. The maximum size of a cell volume coupled by fast exchange can be estimated assuming that in samples of low bulk density the diffusion rate is the same as in the free gas phase. For fast exchange to hold, the characteristic maximum time is 1.8×10^{-4} s for an average loading of one Xe atom per cage in NaY zeolite at an NMR frequency of 83 MHz. At 1 atm, the diffusion constant for Xe gas is 5.71×10^{-2} cm^2 s^{-1} [44], and from Einstein's relation $\langle r(t)^2 \rangle = 6Dt$, the root mean square displacement of a diffusing Xe atom is 7.8×10^{-3} cm. There is some justification for the assumption that the interparticle gas is much like the free gas. If we examine a sample of NaY zeolite that has not been dehydrated so that xenon is prevented from entering the internal pores, the ^{129}Xe spectral line at low loading occurs within a few ppm of the free gas line.

A third parameter of importance is the spin-lattice relaxation time (T_1). Figure 5 shows results of an inversion recovery experiment on a NaY sample with two regions of quite distinct bulk density. It can be seen that the sample of higher bulk density has a much shorter T_1 than the loose powder, 200 ms vs. 440 ms. One way of analyzing these data is in terms of a fluid in a microporous material where the atoms or molecules sample all the parts of the pore volume inside and between the NaY particles in a time short compared to the observed T_1 [45]. This approach leaves the actual relaxation mechanism unspecified.

$$\frac{1}{T_1} = \frac{1}{T_{1i}} + \frac{\lambda}{T_{1e}(S/V)} \tag{2}$$

The surface relaxation time T_{1e} is characteristic of atoms in a region of thickness λ from the surface, and T_{1i} is the relaxation time characteristic of Xe atoms inside the NaY pores. The latter term is independent of bulk density, whereas the surface to volume ratio (S/V) scales linearly with bulk density to a first approximation. Analysis of the relaxation time data in terms of the above equation yields a T_{1i} value of 1 s, with the major contribution to relaxation contributed by extraparticle interactions. The relatively long T_1 for xenon atoms inside the pore system is supported by recent measurement of the Xe T_1 in NaA and AgA zeolite, where T_1 values of 40 and 22 s were measured [46]. In any case, it is important to recognize that in order to obtain reliable intensities in multicomponent spectra, the longest relaxation time must be taken into account to set relaxation delays. There is little precedent for the short relaxation delays reportedly used in many studies.

Temperature effects

Variable temperature studies are of considerable importance in sorting out the fundamental aspects of the ^{129}Xe chemical shift, as pointed out previously [24]. However, in microporous solids with little restriction to passage from internal to external pore space, there are some special problems. It is clear that with decreasing temperature, increasing amounts of xenon will condense in the internal pore system. Below specific temperatures which depend on the xenon loading of the system, there will be almost no free gas xenon left. This will have rather profound effects on the thermal conductivity of loose powders of bulk density 0.3 g cm^{-3} or so, e.g., as observed for some of the NaY samples, and on the way experiments should be conducted to give meaningful results. Figure 6 shows a set of data for two NaY samples loaded to an average value of 7.4 Xe atoms per cage. To one of these a small quantity of He gas was added to promote efficient thermal contact between the glass walls of the tube and the powder particles. Down to 230 K the two samples behave in very similar ways. Below that, the spectra are entirely different. For the He-free sample it is clear that there is considerable thermal lag between the walls of the tube and the interior of the sample. The temperature gradients in turn cause Xe density gradients, which give rise to the rather complex spectra. At 143 K, Xe

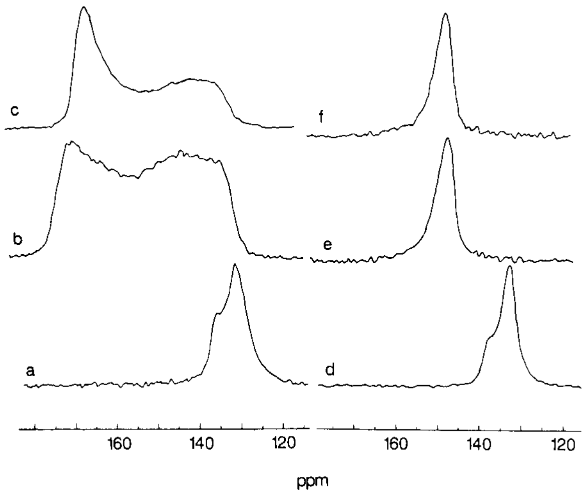

Fig. 6. ^{129}Xe NMR spectra of xenon in NaY at an average loading of 7.4 Xe atoms per cage; (a–c) sample without He gas, (d–f) sample with He gas; (a and d) room temperature; (b and e) sample cooled at 2°C every 5 min from 230 K down to 143 K; (c and f) samples b and e 10 min after reaching 143 K.

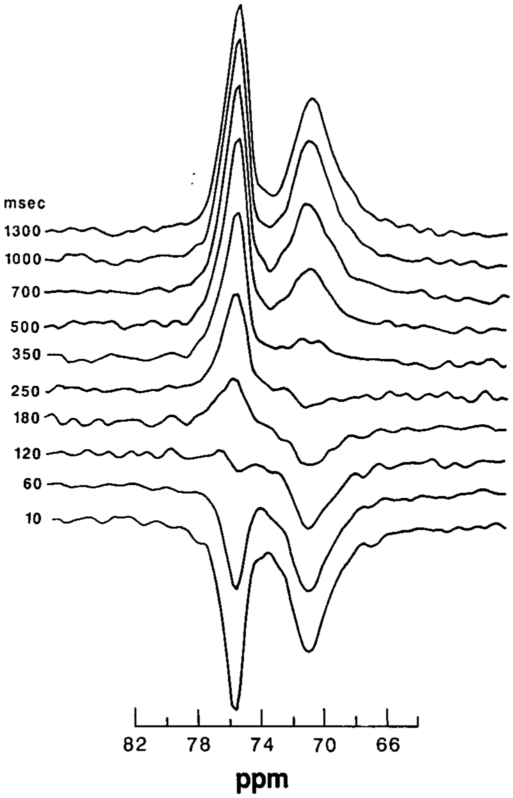

Fig. 5. ^{129}Xe spin-lattice relaxation time experiment on a sample of NaY zeolite with an average loading of one Xe atom per cage. The sample tube contains both a die-pressed pellet of bulk density 1.06 g cm^{-3} and a loose powder of bulk density 0.3 g cm^{-3}.

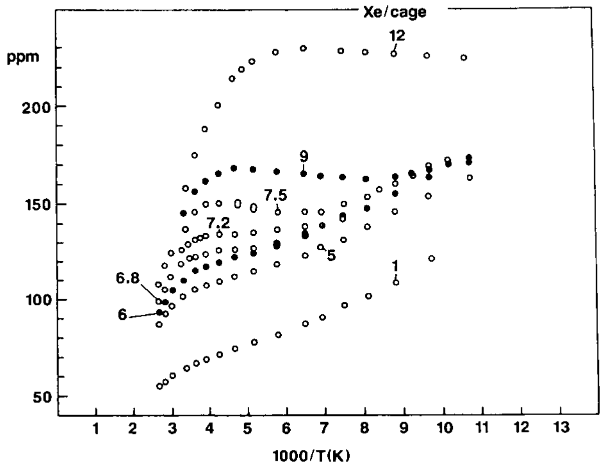

Fig. 7. ^{129}Xe chemical shifts for xenon in NaY zeolite at different average xenon loadings plotted as a function of inverse temperature.

transport clearly is quite slow, and it takes several hours before the density gradients disappear completely. Some experiments carried out on a He-free sample quenched in liquid nitrogen gave a spectrum that continued to change a year later, although it did become similar in appearance to a sample which contained He gas. Xe transport in these samples may take place by movement from inside the particles to the external surface, and where particles make contact, Xe atoms then can travel from particle to particle.

The temperature at which Xe transport changes from gas phase mediated transfer to surface diffusion should also correspond to the temperature at which the thermal conductivity changes rather suddenly. A hint where this occurs comes from the examination of Xe spectra as a function of loading for a number of samples (Fig. 7). We note that there is a region at relatively high temperatures where the Xe chemical shift changes rapidly with temperature, especially for higher loadings. If we associate the Xe shift variation with density changes, this regime we take to correspond to the temperature region where xenon continues to condense inside the internal pore space, that is, the Xe in the internal pore space becomes much more dense. Once all of the xenon is inside the particles, the Xe chemical shift shows very little temperature dependence. The flat temperature dependence disappears again at lower temperature for the higher loadings, the shift again increasing with temperature. For the lower loadings, the temperature independent shift region does not exist. The "knee" in the shift vs. inverse temperature plots then simply corresponds to the point where the internal xenon reaches constant density, and there is no extraparticle xenon left. The proper description of this phase is not completely clear, and there seems to be a minimum loading for the appearance of this phase at an average loading of ca. 7 xenon atoms per cage. We then interpret the change in slope at lower temperature to some kind of phase transition phenomenon where again the description of the new phase is not clear. Evidently additional work needs to be done.

A study by Chen and Fraissard [47] for Xe loading levels up to 2 Xe atoms per cage in the temperature range −100 to 100°C was in qualitative agreement with the results reported here. We have not been able to duplicate the results of Cheung et al. who observed extremely broad Xe resonances in Y zeolites [13]. We, and others [32], speculate that the results in question were indeed affected by the lack of thermal equilibrium in the samples studied.

Effects of anisotropy

There are two different anisotropic effects to be considered here, one at the molecular level, the other macroscopic. First of all, it is necessary to recognize that when a xenon atom interacts with a surface, the chemical shift is a tensor interaction. A ^{129}Xe chemical shift ab initio calculation for a Xe–H_2O pair, with the Xe atom approaching the oxygen atom along the symmetry axis, shows the short range and anisotropic nature of the interaction [48]. The calculated shielding tensor components δ_{zz}, δ_{yy} and δ_{xx} were −0.68, 53.84, 48.24 ppm and −0.55, 4.21, 2.59 ppm for internuclear distances of 3 and 4 Å respectively. Experimental observation of ^{129}Xe chemical shift tensors is limited to a few cases [4,10,34,49–52], although several reported broad lines could easily have an anisotropic component [23,27]. In many other cases, the tensor has been averaged to its isotropic value by molecular mo-

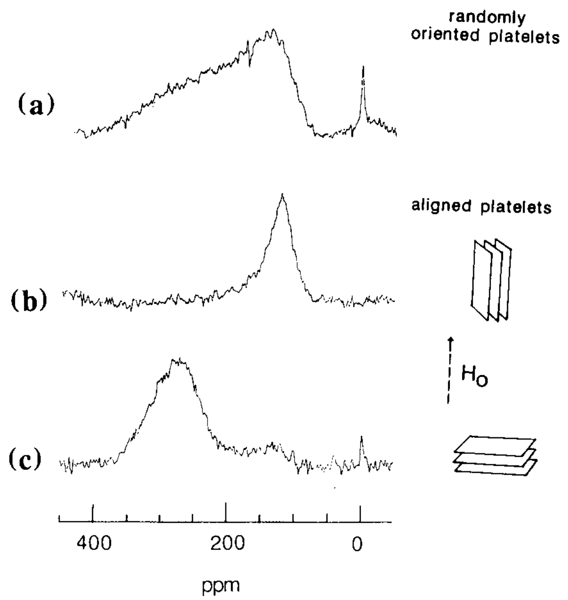

Fig. 8. ^{129}Xe NMR spectra of xenon sorbed in tetramethylammonium exchanged montmorillonite; (a) powder spectrum; (b and c) spectra for platelets aligned parallel and perpendicular to the magnetic field.

tion. Nevertheless, it should be recognized that anisotropic interactions are possible, and indeed should be expected in asymmetric small-pore systems.

The most serious manifestation of anisotropy occurs when an anisotropic chemical shift is present in samples consisting of anisotropic particles. For instance, when xenon is trapped between the layers of a pillared smectite clay such as tetramethylammonium (TMA) montmorillonite, the ^{129}Xe spectrum obtained can be changed by tapping the tube in different directions so that the plate-like clay particles are oriented in different ways. Oriented samples can be produced intentionally by pressing plate-like particles in a die to produce a pellet. ^{129}Xe NMR spectra for different orientations of the pellet in the magnetic field are shown in Fig. 8, along with a proper powder spectrum. A chemical shift anisotropy of 155 ppm is indicated, one of the largest values observed for atomic xenon so far.

Therefore, first of all one must guard against unwanted macroscopic particle orientation effects, and secondly, one must be aware of the possibility of significant anisotropy of the chemical shift.

Conclusions

It is clear that considerable caution must be exercised both in the aquisition of xenon NMR data, and in its interpretation. In previous work, we have pointed out that overly simplistic models must lead to incorrect interpretations of chemical shift–pore space correlations. In this work we have pointed out some of the factors related to the macroscopic nature of powdered samples which must be considered in order to obtain reliable data, especially if there is relatively free passage of xenon atoms from particle to particle. We note that although these factors complicate the interpretation of chemical shift data in terms of internal pore space, there is some hope that Xe NMR may actually be useful in the study of packing density and gas transport in beds of powdered solids.

Issued as NRCC No. 3527.

REFERENCES

1 T. Ito and J. Fraissard, in L.V.C. Rees (Ed.), Proc. 5th Int. Conf. on Zeolites, Naples, 1980, Heyden, London, 1980, p.150.
2 J.A. Ripmeester and D.W. Davidson, Bull. Magn. Reson., 2 (1981) 139.
3 J.A. Ripmeester and D.W. Davidson, J. Mol. Struct., 75 (1981) 67.
4 J.A. Ripmeester, J. Am. Chem. Soc., 104 (1982) 209.
5 T. Ito and J. Fraissard, J. Chem. Phys., 76 (1982) 5225.
6 J.A. Ripmeester, J. Magn. Reson., 56 (1984) 247.
7 D.W. Johnson and L. Griffiths, Zeolites, 7 (1987) 484.
8 J. Demarquay and J. Fraissard, Chem. Phys. Lett., 136 (1987) 314.
9 E.G. Derouane and J.B. Nagy, Chem. Phys. Lett., 137 (1987) 341.
10 J.A. Ripmeester, C.I. Ratcliffe and J.S. Tse, J. Chem. Soc. Faraday Trans. 1, 84 (1988) 3731.
11 W.C. Conner, E.L. Weist, T. Ito and J. Fraisard, J. Phys. Chem., 93 (1989) 4138.
12 R. Shoemaker and T. Apple, J. Phys. Chem., 91 (1987) 4024.
13 T.P.P. Cheung, C.M. Fu and S. Wharry, J. Phys. Chem., 92 (1988) 5178.

14 L.C. de Menorval, D. Raftery, S.B. Liu, K. Takegoshi, R. Ryoo and A. Pines, J. Phys. Chem., 94 (1990) 27.
15 Q.J. Chen and J. Fraissard, Chem. Phys. Lett., 169 (1990) 595.
16 B.F. Chmelka, J.G. Pearson, S.B. Liu, L.C. de Menorval and A. Pines, J. Phys. Chem., 95 (1991) 303.
17 R. Ryoo, C. Pak and B.F. Chmelka, Zeolites, 10 (1990) 790.
18 J.A. Ripmeester and C.I. Ratcliffe, Mat. Res. Soc. Symp. Proc., 233 (1991) 281.
19 Q.J. Chen and J. Fraissard, J. Phys. Chem., 96 (1992) 1814.
20 N. Bansal and C. Dybowski, J. Magn. Reson., 89 (1990) 21.
21 C. Tsiao, D.R. Corbin, V. Durante, D. Walker and C. Dybowski, J. Phys. Chem., 94 (1990) 4195.
22 M.J. Annen, M.E. Davis and B.C. Hanson, Catal. Lett., 6 (1990) 331.
23 P.J. Barrie, G.F. McCann, I. Gameson, T. Rayment and J. Klinowski, J. Phys. Chem., 95 (1991) 9416.
24 J.A. Ripmeester and C.I. Ratcliffe, J. Phys. Chem., 94 (1990) 7652.
25 T.R. Stengle and K.L. Wiliamson, Macromolecules, 20 (1987) 1428.
26 A.P. Kentgens, H.A. van Boxtel, R.-J. Verweel and W.S. Veeman, Macromolecules, 24 (1991) 3713.
27 P.C. Wernett, J.W. Larson, O. Yamada and H.J. Yue, Energy Fuels, 4 (1990) 413.
28 N. Bansal and C. Dybowski, Ann. Rev. Phys. Chem., 42 (1991) 433.
29 P.J. Barrie and J. Klinowski, Prog. NMR Spectrosc., 24 (1992) 91.
30 B.F. Chmelka, D. Raftery, A.V. McCormick, L.C. de Menorval, R.D. Levine and A. Pines, Phys. Rev. Lett., 66 (1991) 931.
31 C.J. Jameson, A.K. Jameson, R. Gerald and A.C. de Dios, J. Chem. Phys., 96 (1992) 1676.
32 C.J. Jameson, A.K. Jameson, R. Gerald and A.C. de Dios, J. Chem. Phys., 96 (1992) 1690.
33 C.J. Jameson and A.C. de Dios, J. Chem. Phys., 97 (1992) 417.
34 J.A. Ripmeester and C.I. Ratcliffe, R. von Ballmoos et al. (Eds.), Proc. 9th Int. Zeolite Conf., Montreal, July 1992, Butterworth-Heinemann, 1993, p. 571.
35 D.E. Woessner, Mol. Phys., 34 (1977) 899.
36 B. Halle and H. Wennerstrom, J. Chem. Phys., 75 (1981) 1928.
37 M. Rance and R.A. Byrd, J. Magn. Reson., 52 (1983) 221.
38 P. Caravatti, G. Bodenhausen and R.R. Ernst, J. Magn. Reson., 55 (1983) 88.
39 E.R. Hunt and H.Y. Carr, Phys. Rev., 130 (1963) 2302.
40 N. Bloembergen, S. Shapiro, P.S. Pershan and J.O. Artman, Phys. Rev., 114 (1959) 445.
41 J. Karger, H. Pfeifer, F. Stallmach and H. Spindler, Zeolites, 10 (1990) 288.
42 W. Heink, J. Karger, H. Pfeifer and F. Stallmach, J. Am. Chem. Soc., 112 (1990) 2175.
43 J. Karger, H. Pfeifer, T. Wutscherk, S. Ernst, J. Weitkamp and J. Fraissard, J. Phys. Chem., 96 (1992) 5059.
44 S. Visnew, in J.O. Hirschfelder, C.F. Curtis and R.B. Bird (Eds.), Molecular Theory of Gases and Liquids, Wiley, New York, 1954, p. 581.
45 K.R. Brownstein and C.E. Tarr, Phys. Rev., A19 (1979) 2446.
46 J.A. Ripmeester and C.I. Ratcliffe, unpublished results.
47 Q.J. Chen and J. Fraissard, J. Phys. Chem., 96 (1992) 1809.
48 J.S. Tse, private communication.
49 F. Lee, E. Gabe, J.S. Tse and J.A. Ripmeester, J. Am. Chem. Soc., 110 (1988) 6014.
50 M.A. Springuel-Huet and J. Fraissard, Chem. Phys. Lett., 154 (1989) 299.
51 P.J. Barrie, Ph.D. Thesis, Cambridge University, 1990, and Ref. 29.
52 C. Pellegrino, T. Ito, Z. Gabelica, J.B. Nagy and E.G. Derouane, Appl. Catal., 61 (1990) L1.

ANALYTICA CHIMICA ACTA, VOL. 283 (1993)

AUTHOR INDEX

Adams, F.
—, Adriaens, A., Berghmans, P. and Janssens, K.
Surface microanalysis 19
Adams, F., see Janssens, K. 98
Adriaens, A., see Adams, F. 19
Adriaensens, P., see Hoogmartens, I. 1025
Agraz, R.
—, Sevilla, M.T. and Hernández, L.
Copper speciation analysis using a chemically modified electrode 650
Aizpún Fernández, B., see Valdés-Hevia y Temprano, M.C. 175
Albertí, J., see Rubio, R. 160
Alçada, M.N.M.P.
—, Lima, J.L.F.C. and Montenegro, M.C.B.S.M.
Quinidine ion-selective electrode for potentiometric determinations in pharmaceutical preparations 657
Alés Barrero, F., see Cruces Blanco, C. 213
Arnold, M.A., see Pań, S. 663
Arroyo Cortéz, J., see López García, I. 167
Arruda, M.A.Z.
—, Zagatto, E.A.G. and Maniasso, N.
Kinetic determination of cobalt and nickel by flow-injection spectrophotometry 476

Backbier, L.
—, Rousseau, J. and Bart, J.C.J.
Analytical study of salt migration and efflorescence in a mediaeval cathedral 855
Baeza Baeza, J.J.
—, Matsumoto, K. and Mottola, H.A.
Comparative studies on data collection and data treatment in kinetic-based determinations with two rotating bioreactor/amperometric detection systems 785
Baltensperger, U., see Seefeld, S. 246
Barbosa, J.
— and Sanz-Nebot, V.
Standard pH values in non-aqueous mobile phases used in reversed-phase liquid chromatography 320
Barendswaard, W.
—, Moonen, J. and Neilen, M.
Analysis of polymer stabilizers by means of solid state NMR: some case studies 1007
Barnes, R.M.
Advances in inductively coupled plasma mass spectrometry: human nutrition and toxicology 115
Bart, J.C.J., see Backbier, L. 855
Beltran, J.
—, López, F.J. and Hernández, F.
Solid-phase extraction of pesticide residues from ground water: comparison between extraction cartridges and extraction discs 297
Berghmans, P., see Adams, F. 19
Borguet, F., see Cornelis, R. 183
Bos, M., see Pałys, M.J. 811
Bosch-Reig, F.
—, Campíns-Falcó, P. and Verdú-Andrés, J.
Development of the H-point standard additions method for analyte determinations in unknown matrix. Location of linear matrix spectral interval 831
Brázdová, D., see Kalous, J. 645
Bruchmann, A.
—, Zinn, P. and Haffer, Chr.M.
Prediction of gas chromatographic retention index data by neural networks 869

Cámara, C., see Marco, V. 489
Camara, C., see Cobo Fernandez, M.G. 386
Campillo, N., see Viñas, P. 393
Campíns-Falcó, P., see Bosch-Reig, F. 831
Campíns Falcó, P., see Molins Legua, C. 635
Cano Pavon, J.M., see Vereda Alonso, E. 224
Caravatti, P., see Struyf, H. 139
Caroli, S.
Certified reference materials: use, manufacture and certification 573
Carrillo, F., see Marco, V. 489
Casamayor, F., see Maquieira, A. 401
Casassas, E.
—, Domínguez, N., Fonrodona, G. and De Juan, A.
Factor analysis applied to the study of the effects of solvent composition and nature of the inert electrolyte on the protonation constants in dioxane–water mixtures 548
—, Gargallo, R., Giménez, I., Izquierdo-Ridorsa, A. and Tauler, R.
Application of an evolving factor analysis-based procedure to speciation analysis in the copper(II)–polyuridylic acid system 538
Cerezo Galan, A., see Ismail Salem, I. 334
Cholewa, N., see Legge, G.J.F. 62
Ciocan, A., see Hiddemann, L. 152
Cobo Fernandez, M.G.
—, Palacios, M.A. and Camara, C.

Flow-injection and continuous-flow systems for the determination of Se(IV) and Se(VI) by hydride generation atomic absorption spectrometry with on-line prereduction of Se(VI) to Se(IV) 386
Compañó, R.
—, Granados, M., Leal, C. and Prat, M.D.
Solid-phase extraction and spectrofluorimetric determination of triphenyltin in environmental samples 272
Cornelis, R.
—, Borguet, F. and De Kimpe, J.
Trace elements in medicine. Speciation: the new frontier 183
Cosano, J., see Quevauviller, Ph. 600
Crouch, S.R.
Trends in kinetic methods of analysis 453
Cruces Blanco, C.
—, García Campaña, A., Alés Barrero, F. and Román Ceba, M.
Simultaneous spectrofluorimetric determination of traces of molybdenum and boron in plant leaves 213
Cruz, I.
—, Wells, D.E. and Marr, I.L.
Determination of organochlorines in sea water: an assessment 280

Dasgupta, P.K., see Liu, S. 739, 747
De Juan, A., see Casassas, E. 548
De Kimpe, J., see Cornelis, R. 183
De la Peña, L.
—, Gómez-Hens, A. and Pérez-Bendito, D.
Simultaneous kinetic-photometric determination of imipramine and desipramine by stopped-flow mixing technique 471
De la Rosa, F.F., see Lin, Q. 379
Dessenne, O., see Hiddemann, L. 152
Díaz-García, M.E., see Valencia-González, M.J. 439
Dombek, V., see Praus, P. 917
Domínguez, N., see Casassas, E. 548
Do Nascimento, D.B.
— and Schwedt, G.
Off-line and on-line preconcentration of trace levels of beryllium using complexing agents with atomic spectrometric and fluorimetric detection 909
Do Nascimento, P.C.
— and Schwedt, G.
Comparative studies of the determination of cyanide at low concentration levels in waste waters 755
Dunemann, L.
— and Hajimiragha, H.
Development of a screening method for the determination of volatile organic compounds in body fluids and environmental samples using purge and trap gas chromatography–mass spectrometry 199
Dybowski, C.R., see Rethwisch, D.G. 1033

Eagles, J., see Mellon, F.A. 190
Ebdon, L., see Garcia-Alonso, J.I. 261
Eckert, H., see Franke, D. 987
Ellis, P.D., see Koons, J.M. 1045
El'skaya, A.V., see Soldatkin, A.P. 695
Elswijk, H.B.
Scanning tunnelling microscopy of silicon surfaces 35
Engelhardt, G.
—, Sieger, P. and Felsche, J.
Multinuclear solid state NMR of host–guest systems with TO_2 ($T = Si$, Al) host-frameworks. A case study on sodalites 967
Escobar, R., see Lin, Q. 379

Fairweather-Tait, S.J., see Mellon, F.A. 190
Fan, Z., see Harrison, D.J. 361
Felsche, J., see Engelhardt, G. 967
Fernández-Romero, J.M.
—, Luque de Castro, M.D., Valcárcel, M. and Quiles-Zafra, R.
Spectrophotometric determination of magnesium in serum by using a flow-injection system with an immobilized enzyme reactor 447
Fernández de la Campa, M.R., see Valdés-Hevia y Temprano, M.C. 175
Fiedor, J.N., see Hercules, D.M. 42
Fonrodona, G., see Casassas, E. 548
Fox, T.E., see Mellon, F.A. 190
Franke, D.
—, Eckert, H., Kaner, R.B. and Treece, R.E.
Quantitative evaluation of gallium phosphide samples prepared from rapid solid state metathesis. Solid state ^{31}P and ^{69}Ga magic angle spinning NMR strategies 987
Frimmel, F.H., see Schullerer, S. 251

Garcia-Alonso, J.I.
—, Sanz-Medel, A. and Ebdon, L.
Determination of butyltin ion species by ion-exchange chromatography with inductively coupled plasma mass spectrometric and spectrofluorimetric detection 261
Garcia Beltran, L., see Rubio, R. 207
García Campaña, A., see Cruces Blanco, C. 213
Garcia de Torres, A., see Vereda Alonso, E. 224
Gargallo, R., see Casassas, E. 538
Gautier, E.A.
—, Gettar, R.T. and Servant, R.E.
Simultaneous determination of lanthanum, strontium and copper in superconductor materials by ion chromatography 350
Gelan, J., see Hoogmartens, I. 1025
Gerstein, B.C.
—, Pruski, M. and Hwang, S.-J.
Determination of proton densities on silica gel catalyst supports by n-quantum coherence in NMR 1059
Gettar, R.T., see Gautier, E.A. 350
Gijbels, R., see Struyf, H. 139
Giménez, I., see Casassas, E. 538
Glennon, J.D., see Ryan, N. 344
Gómez-Hens, A., see De la Peña, L. 471
Granados, M., see Compañó, R. 272
Griepink, B., see Maier, E.A. 590

Griepink, B., see Quevauviller, Ph. 583, 600
Griffin, R.G., see Griffiths, J.M. 1081
Griffiths, J.M.
  — and Griffin, R.G.
  Nuclear magnetic resonance methods for measuring dipolar couplings in rotating solids 1081
Gübitz, G.
  — and Shellum, C.
  Flow-injection immunoassays. Review 421
Guiochon, G.A.
  Chromatography, today and tomorrow 309
Guiraûm, A., see Lin, Q. 379
Gutzman, D.W.
  — and Langford, C.H.
  Application of thermal lens spectrometry to kinetic speciation studies of metal ions in natural water models with colloidal ligands 773

Haffer, Chr.M., see Bruchmann, A. 869
Hajimiragha, H., see Dunemann, L. 199
Håkanson, H., see Shu, H.-C. 727
Hamplová, V., see Novák, J. 923
Harrison, D.J.
  —, Fan, Z., Seiler, K., Manz, A. and Widmer, H.M.
  Rapid separation of fluorescein derivatives using a micromachined capillary electrophoresis system 361
Hercules, D.M.
  —, Houalla, M., Proctor, A. and Fiedor, J.N.
  Quantitation of species on catalyst surfaces 42
Hernández-Cassou, S., see Saurina, J. 414
Hernández, F., see Beltran, J. 297
Hernández-Hernández, F., see Sancho-Llopis, J.V. 287
Hernández, L., see Agraz, R. 650
Hernández, L., see Pilar da Silva, M. 326
Hernández Córdoba, M., see López García, I. 167
Hernández Córdoba, M., see Viñas, P. 393
Heumann, K.G.
  Determination of inorganic and organic traces in the clean room compartment of Antarctica 230
Heydorn, K.
  Detecting errors in micro and trace analysis by using statistics 494
Hiddemann, L.
  —, Uebbing, J., Ciocan, A., Dessenne, O. and Niemax, K.
  Simultaneous multi-element analysis of solid samples by laser ablation–microwave-induced plasma optical emission spectrometry 152
Hogendoorn, E.A., see Sancho-Llopis, J.V. 287
Hoogmartens, I.
  —, Adriaensens, P., Vanderzande, D. and Gelan, J.
  Improving selectivity by using a multipurpose cross polarization magic angle spinning NMR pulse sequence. Characterization of π-conjugated compounds 1025
Houalla, M., see Hercules, D.M. 42
Huang, X.Z., see Li, Y.Q. 903
Huang, Y.L.
  —, Khoo, S.B. and Yap, M.G.S.
  Flow-injection analysis–wall-jet electrode system for monitoring glucose and lactate in fermentation broths 763
Hughes, E., see Koons, J.M. 1045
Hwang, S.-J., see Gerstein, B.C. 1059

Imasaka, T., see Kawabata, Y. 689
Ismail Salem, I.
  — and Cerezo Galan, A.
  Determination of the stability of morphine tablets by ion-pair reversed-phase liquid chromatography 334
Isoyama, H., see Uchida, T. 881
Izquierdo-Ridorsa, A., see Casassas, E. 538

Jacintha, M.A., see Rethwisch, D.G. 1033
Jaffrezic-Renault, N., see Soldatkin, A.P. 695
Janssens, K.
  —, Vincze, L., Adams, F. and Jones, K.W.
  Synchrotron radiation-induced x-ray microanalysis 98
Janssens, K., see Adams, F. 19
Jiang, Z., see Peng, X. 887
Jones, K.W., see Janssens, K. 98

Kalous, J.
  —, Brázdová, D. and Vytřas, K.
  Microdetermination of sulphate and organic sulphur: potentiometric back-titration using simple coated-wire electrodes 645
Kaner, R.B., see Franke, D. 987
Kawabata, Y.
  —, Sugamoto, H. and Imasaka, T.
  Micro-optrode for urea using an ammonium ion-sensitive membrane covered with a urease-immobilized membrane 689
Kawazumi, H.
  —, Yasuda, T.-o. and Ogawa, T.
  Two-photon ionization detection of adsorbed molecules on a metal surface at atmospheric pressure by 355-nm laser irradiation 111
Kayali, M.N., see Rubio-Barroso, S. 304
Khoo, S.B., see Huang, Y.L. 763
Kikuchi, N.
  —, Matsuno, K. and Miki, T.
  Separation and determination of betaine in an oriental medicine by liquid chromatography 338
Klinowski, J.
  Applications of solid-state NMR for the study of molecular sieves. Review 929
Koenig, J.L., see Silvestri, R.L. 997
Koons, J.M.
  —, Hughes, E. and Ellis, P.D.
  Non-linear least squares procedure for the extraction of NMR parameters from multi-tensor solid state line shapes 1045

Langford, C.H., see Gutzman, D.W. 773
Laserna, J.J.
  Combining fingerprinting capability with trace analytical detection: surface-enhanced Raman spectrometry 607

Leal, C., see Compañó, R. 272
Legge, G.J.F.
—, Saint, A. and Cholewa, N.
Non-destructive 2- and 3-dimensional microanalysis with (high energy) ion microprobes 62
Li, Y.Q.
—, Huang, X.Z. and Xu, J.G.
Raman scattering interference in constant-wavelength synchronous spectrofluorimetry 903
Liapis, K.S., see Miliadis, G.E. 258
Lima, J.L.F.C., see Alçada, M.N.M.P. 657
Lin, Q.
—, Guiraúm, A., Escobar, R. and De la Rosa, F.F.
Flow-injection chemiluminescence determination of cobalt(II) and manganese(II) 379
Liu, S.
— and Dasgupta, P.K.
A simple means to increase absorbance detection sensitivity in capillary zone electrophoresis 747
— and Dasgupta, P.K.
Electroosmotically pumped capillary flow-injection analysis. Valve-based injection systems and sample throughput 739
Liu, Y.M., see Valencia-González, M.J. 439
López, F.J., see Beltran, J. 297
López Carreto, M.
—, Sicilia, D., Rubio, S. and Pérez-Bendito, D.
Simultaneous determination of arsenate and phosphate by use of the kinetic wavelength-pair method 481
López García, I.
—, Arroyo Cortéz, J. and Hernández Córdoba, M.
Slurry-electrothermal atomic absorption spectrometry of samples with large amounts of silica. Determination of cadmium, zinc and manganese using fast temperature programmes 167
López García, I., see Viñas, P. 393
Luque de Castro, M.D., see Fernández-Romero, J.M. 447
Luque de Castro, M.D., see Quevauviller, Ph. 600
Luque de Castro, M.D., see Richter, P. 408

Maier, E.A.
—, Quevauviller, Ph. and Griepink, B.
Interlaboratory studies as a tool for many purposes: proficiency testing, learning exercises, quality control and certification of matrix materials 590
Maier, E.A., see Quevauviller, Ph. 583
Málková, Z., see Novák, J. 923
Maniasso, N., see Arruda, M.A.Z. 476
Manz, A., see Harrison, D.J. 361
Maquieira, A.
—, Casamayor, F., Puchades, R. and Sagrado, S.
Determination of total and free sulphur dioxide in wine with a continuous-flow microdistillation system 401
Marco, V.
—, Carrillo, F., Pérez-Conde, C. and Cámara, C.
Kinetic flow-injection spectrofluorimetric method for the determination of fluoride 489
Marcos, J.
—, Ríos, A. and Valcárcel, M.
Automatic determination of Michaelis–Menten constants by the variable flow-rate technique 429
Marr, I.L., see Cruz, I. 280
Martelet, C., see Soldatkin, A.P. 695
Masini, J.C.
Evaluation of neglecting electrostatic interactions on the determination and characterization of the ionizable sites in humic substances 803
Matsumoto, K., see Baeza Baeza, J.J. 785
Matsuno, K., see Kikuchi, N. 338
Mattiasson, B., see Shu, H.-C. 727
Mellon, F.A.
—, Eagles, J., Fox, T.E. and Fairweather-Tait, S.J.
Absorption and bioavailability studies of mineral nutrients by mass spectrometry 190
Méndez, J.
—, Quejido, A.J., Pérez-Pastor, R. and Pérez-García, M.
Chemometric study of organic pollution in the aerosol of Madrid 528
Meyerhoff, M.E., see Wang, E. 673
Miki, T., see Kikuchi, N. 338
Miliadis, G.E.
— and Liapis, K.S.
Determination of arsenic residues in agricultural products of Milos island 258
Molins Legua, C.
—, Campíns Falcó, P. and Sevillano Cabeza, A.
Extractive–spectrophotometric determination of amphetamine in urine samples with sodium 1,2-naphthoquinone 4-sulphonate 635
Montenegro, M.C.B.S.M., see Alçada, M.N.M.P. 657
Moonen, J., see Barendswaard, W. 1007
Mottola, H.A., see Baeza Baeza, J.J. 785
Muller, D., see Ryan, N. 344

Nagy, A.
— and Nagy, G.
Amperometric air gap cell for the measurement of free cyanide 795
Nagy, G., see Nagy, A. 795
Neilen, M., see Barendswaard, W. 1007
Netchiporouk, L.I., see Soldatkin, A.P. 695
Niemax, K., see Hiddemann, L. 152
Nigretto, J.-M., see Randriamahazaka, H. 719
Novák, J.
—, Málková, Z., Pokorná, Z. and Hamplová, V.
Cerimetric determination of oxygen balance in oxide superconductors 923
Nyamsi Hendji, A.M., see Soldatkin, A.P. 695

Oda, H., see Uchida, T. 881
Oechsner, H.
Inorganic mass spectrometry for surface and thin film analysis 131
Ogawa, T., see Kawazumi, H. 111

Olson, D.L.
— and Scheeline, A.
The peroxidase–NADH biochemical oscillator: experimental system, control variables, and oxygen mass transport 703
Otto, M.
Fuzzy logic for spectra interpretation 500

Padró, A., see Rubio, R. 160
Palacios, M.A., see Cobo Fernandez, M.G. 386
Pałys, M.J.
—, Bos, M. and Van der Linden, W.E.
Automatic polarographic elucidation of electrode mechanisms by means of a knowledge-based system. Part 3. Mechanisms ECE, EE and mechanisms involving adsorption 811
Pan, S.
— and Arnold, M.A.
Amperometric internal enzyme gas-sensing probe for hydrogen peroxide 663
Peng, X.
—, Jiang, Z. and Zen, Y.
On-line microcolumn preconcentration with desolvation and determination of trace elements by flow-injection inductively coupled plasma atomic emission spectrometry 887
Pérez-Bendito, D., see De la Peña, L. 471
Pérez-Bendito, D., see López Carreto, M. 481
Pérez-Conde, C., see Marco, V. 489
Pérez-García, M., see Méndez, J. 528
Pérez-Pastor, R., see Méndez, J. 528
Pilar da Silva, M.
—, Procopio, J.R. and Hernández, L.
Liquid chromatographic study of the photochemical decomposition of sodium ethylmercurithiosalicylate 326
Poe, R.B.
— and Rutan, S.C.
Effects of resolution, peak ratio and sampling frequency in diode-array fluorescence detection in liquid chromatography 845
Pokorná, Z., see Novák, J. 923
Polo-Díez, L.M., see Rubio-Barroso, S. 304
Pouchou, J.-L.
X-Ray microanalysis of stratified specimens 81
Prat, M.D., see Compañó, R. 272
Praus, P.
— and Dombek, V.
Utilization of polyethylene glycol for the separation of chlorophenols by capillary isotachophoresis 917
Procopio, J.R., see Pilar da Silva, M. 326
Proctor, A., see Hercules, D.M. 42
Pruski, M., see Gerstein, B.C. 1059
Puchades, R., see Maquieira, A. 401

Quejido, A.J., see Méndez, J. 528
Quevauviller, Ph.
—, Maier, E.A. and Griepink, B.
Projects for the improvement and quality control of inorganic and organic analysis in environmental matrices 583
—, Van Renterghem, D., Griepink, B., Valcarcel, M., Luque de Castro, M.D. and Cosano, J.
Interlaboratory programme for the quality control of nitrate determination in freshwater 600
Quevauviller, Ph., see Maier, E.A. 590
Quevauviller, Ph., see Rubio, R. 207
Quiles-Zafra, R., see Fernández-Romero, J.M. 447

Ramis-Ramos, G.
Analytical characteristics, applications and perspectives in thermal lens spectrometry 623
Randriamahazaka, H.
— and Nigretto, J.-M.
Electrochemical activation of human factor XII (Hageman factor) immobilized on carbon electrodes 719
Ratcliffe, C.I., see Ripmeester, J.A. 1103
Rauret, G., see Rubio, R. 160, 207
Rethwisch, D.G.
—, Jacintha, M.A. and Dybowski, C.R.
Quantification of ^{13}C in solids using CPMAS-DD-NMR spectroscopy 1033
Richter, P.
—, Luque de Castro, M.D. and Valcárcel, M.
Spectrophotometric flow-through sensor for the determination of sulphur dioxide 408
Rigin, V.
Simultaneous atomic fluorescence spectrometric determination of traces of iron, cobalt and nickel after conversion to their carbonyls and gas-phase atomization by microwave-induced plasma 895
Ríos, A., see Marcos, J. 429
Ripmeester, J.A.
— and Ratcliffe, C.I.
^{129}Xe NMR spectroscopy in microporous solids: the effect of bulk properties 1103
Rius, F.X.
Expert systems in trace analysis 518
Román Ceba, M., see Cruces Blanco, C. 213
Rousseau, J., see Backbier, L. 855
Rubio-Barroso, S.
—, Kayali, M.N. and Polo-Díez, L.M.
Fluorimetric study of polycyclic aromatic hydrocarbons in Brij-35 micellar solution. Evaluation of polycyclic aromatic hydrocarbons in air samples 304
Rubio, R.
—, Padró, A., Albertí, J. and Rauret, G.
Determination of arsenic speciation by liquid chromatography–hydride generation inductively coupled plasma atomic emission spectrometry with on-line UV photooxidation 160
—, Sahuquillo, A., Rauret, G., Garcia Beltran, L. and Quevauviller, Ph.
Systematic study of chromium determination in urine by graphite furnace atomic absorption spectrometry 207
Rubio, S., see López Carreto, M. 481
Rutan, S.C., see Poe, R.B. 845

Ryan, N.
—, Glennon, J.D. and Muller, D.
On-line trace metal ion preconcentration in ion chromatography using carboxymethyl and hydroxamate dextran-coated silicas 344

Sagrado, S., see Maquieira, A. 401
Sahuquillo, A., see Rubio, R. 207
Saint, A., see Legge, G.J.F. 62
Sancho-Llopis, J.V.
—, Hernández-Hernández, F., Hogendoorn, E.A. and Van Zoonen, P.
Rapid method for the determination of eight chlorophenoxy acid residues in environmental water samples using off-line solid-phase extraction and on-line selective precolumn switching 287
Sanz-Medel, A.
Solid surface photoluminescence and flow analysis: a happy marriage 367
Sanz-Medel, A., see Garcia-Alonso, J.I. 261
Sanz-Medel, A., see Valdés-Hevia y Temprano, M.C. 175
Sanz-Medel, A., see Valencia-González, M.J. 439
Sanz-Nebot, V., see Barbosa, J. 320
Saurina, J.
— and Hernández-Cassou, S.
Continuous-flow spectrophotometric determination of amino acids with 1,2-naphthoquinone-4-sulphonate reagent 414
Scheeline, A., see Olson, D.L. 703
Schullerer, S.
— and Frimmel, F.H.
Characterization of organic sulphur compounds in surface water by ion-pair adsorption under different conditions 251
Schwedt, G., see Do Nascimento, D.B. 909
Schwedt, G., see Do Nascimento, P.C. 755
Seefeld, S.
— and Baltensperger, U.
Determination of bromide in snow samples by ion chromatography with electrochemical detection 246
Seiler, K., see Harrison, D.J. 361
Servant, R.E., see Gautier, E.A. 350
Sevilla, M.T., see Agraz, R. 650
Sevillano Cabeza, A., see Molins Legua, C. 635
Shellum, C., see Gübitz, G. 421
Sherwood, P.M.A.
Surface analysis for the investigation of electrochemical and corrosion systems 52
Shu, H.-C.
—, Håkanson, H. and Mattiasson, B.
D-Lactic acid in pork as a freshness indicator monitored by immobilized D-lactate dehydrogenase using sequential injection analysis 727
Shul'ga, A.A., see Soldatkin, A.P. 695
Sicilia, D., see López Carreto, M. 481
Sieger, P., see Engelhardt, G. 967
Siles Cordero, M.T., see Vereda Alonso, E. 224
Silvestri, R.L.
— and Koenig, J.L.
Applications of nuclear magnetic resonance spectrometry to solid polymers. Review 997
Soldatkin, A.P.
—, El'skaya, A.V., Shul'ga, A.A., Netchiporouk, L.I., Nyamsi Hendji, A.M., Jaffrezic-Renault, N. and Martelet, C.
Glucose-sensitive field-effect transistor with additional Nafion membrane. Reduction of influence of buffer capacity on the sensor response and extension of its dynamic range 695
Struyf, H.
—, Van Roy, W., Van Vaeck, L., Van Grieken, R., Gijbels, R. and Caravatti, P.
Laser microprobe Fourier transform mass spectrometer with external ion source for organic and inorganic microanalysis 139
Sugamoto, H., see Kawabata, Y. 689

Tauler, R., see Casassas, E. 538
Tölg, G.
Problems and trends in extreme trace analysis for the elements 3
Treece, R.E., see Franke, D. 987

Uchida, T.
—, Isoyama, H., Oda, H., Wada, H. and Uenoyama, H.
Determination of ultratrace metals in biological standards by inductively coupled plasma atomic emission spectrometry with ultrasonic nebulisation 881
Uebbing, J., see Hiddemann, L. 152
Uenoyama, H., see Uchida, T. 881

Valcárcel, M., see Fernández-Romero, J.M. 447
Valcárcel, M., see Marcos, J. 429
Valcárcel, M., see Richter, P. 408
Valcarcel, M., see Quevauviller, Ph. 600
Valdés-Hevia y Temprano, M.C.
—, Aizpún Fernández, B., Fernández de la Campa, M.R. and Sanz-Medel, A.
Study of the influence of ordered media on the determination of lead by hydride generation inductively coupled plasma atomic emission spectrometry 175
Valencia-González, M.J.
—, Liu, Y.M., Díaz-García, M.E. and Sanz-Medel, A.
Optosensing of D-glucose with an immobilized glucose oxidase minireactor and an oxygen room-temperature phosphorescence transducer 439
Van der Linden, W.E., see Pałys, M.J. 811
Vanderzande, D., see Hoogmartens, I. 1025
Van Grieken, R., see Struyf, H. 139
Van Renterghem, D., see Quevauviller, Ph. 600
Van Roy, W., see Struyf, H. 139
Van Vaeck, L., see Struyf, H. 139
Van Zoonen, P., see Sancho-Llopis, J.V. 287
Verdú-Andrés, J., see Bosch-Reig, F. 831

Vereda Alonso, E.
—, Cano Pavon, J.M., Garcia de Torres, A. and Siles Cordero, M.T.
Determination of nickel in biological samples prepared by microwave dissolution using electrothermal atomic absorption spectrometry after extraction with 1,5-bis[phenyl-(2-pyridyl)methylene] thiocarbonhydrazide 224
Viñas, P.
—, Campillo, N., López García, I. and Hernández Córdoba, M.
Flow-injection flame atomic absorption spectrometry for slurry atomization. Determination of calcium, magnesium, iron, zinc and manganese in vegetables 393
Vincze, L., see Janssens, K. 98
Voigtman, E.
Computer experimentation in and teaching of modern instrumental techniques using circular dichroism measurement as an example 559
Vytřas, K., see Kalous, J. 645

Wada, H., see Uchida, T. 881
Walczak, B.
— and Wegscheider, W.
Non-linear modelling of chemical data by combinations of linear and neural net methods 508
Wang, E.
— and Meyerhoff, M.E.
Anion selective optical sensing with metalloporphyrin-doped polymeric films 673
Wang, J.
— and Wu, H.
Permselective lipid–poly(*o*-phenylenediamine) coatings for amperometric biosensing of glucose 683
Weber, G.
Measurement of the speciation of iron in the nanogram range: investigation of chromatographic peaks induced by iron blanks 354
Wegscheider, W., see Walczak, B. 508
Wells, D.E., see Cruz, I. 280
Widmer, H.M., see Harrison, D.J. 361
Wu, H., see Wang, J. 683

Xu, J.G., see Li, Y.Q. 903

Yap, M.G.S., see Huang, Y.L. 763
Yasuda, T.-o., see Kawazumi, H. 111

Zagatto, E.A.G., see Arruda, M.A.Z. 476
Zen, Y., see Peng, X. 887
Zinn, P., see Bruchmann, A. 869

Environmental Analysis

Techniques, Applications and Quality Assurance

Edited by **D. Barceló**

Techniques and Instrumentation in Analytical Chemistry Volume 13

Three aspects of environmental analysis are treated in this book:

- the use of various analytical techniques
- their applications to trace analysis of pollutants, mainly organic compounds
- quality assurance aspects, including the use of certified reference materials for quality control of the entire analytical process.

The book will serve as a general reference for post-graduate students as well as a practical reference for environmental chemists who need to use the analytical techniques for environmental studies. Analytical chemists needing information on the complexity of environmental sample matrices and interferences will also find this an invaluable reference.

Contents: Part 1. Field Sampling Techniques and Sample Preparation. 1. Sampling techniques for air pollutants (R. Niessner). 2. Sample handling strategies for the analysis of organic contaminants from environmental samples (M.-C. Hennion, P. Scribe). 3. Extraction, clean-up and recoveries of persistent trace organic contaminants from sediment and biota samples (D.E. Wells).
Part 2. Application Areas.
4. Current developments in the analysis of polychlorinated biphenyls (PCBs) including planar and other toxic metabolites in environmental matrices (D.E. Wells). 5. Official methods of analysis of priority pesticides in water using gas chromatographic techniques (D. Barceló).
6. Coupled-column reversed phase liquid chromatography as a versatile technique for the determination of polar pesticides (E.A. Hogendoorn, P. van Zoonen).
7. Liquid chromatographic determination of phenols and substituted derivatives in water samples (G. Marko-Varga).
8. HPLC methods for the determination of mycotoxins and phycotoxins (J.F. Lawrence, P.M. Scott). 9. Determination of radionuclides in environmental samples (V. Valkovic).
Part 3. Quality Assurance and Reference Materials. 10. Quality assurance in environmental analysis (W.P. Cofino).
11. Certified reference materials for the quality control of measurements in environmental monitoring (E.A. Maier).
12. Standard reference materials for the determination of trace organic constituents in environmental samples (S.A. Wise).
Part 4. Emerging Techniques.
13. Application of fluorescence spectroscopic techniques in the determination of PAHs and PAH metabolites (F. Ariese, C. Gooijer, N.H. Velthorst).
14. Characterization of surfactants in water by desorption ionization methods (F. Ventura).
15. Utilization of various LC-MS interfacing systems in environmental analysis; application to polar pesticides (M.H. Lamoree, R.T. Ghijsen, U.A.Th. Brinkman).
16. Hyphenated techniques applied to the speciation of organometallic compounds in the environment (O.F.X. Donard, R. Ritsema).
17. The potential of capillary electrophoresis in environmental analysis (M.W.F. Nielen).
Subject index.

©1993 660 pages Hardbound
Price: Dfl. 465.00 (US $ 265.75)
ISBN 0-444-89648-1

ELSEVIER
SCIENCE PUBLISHERS

ORDER INFORMATION
For USA and Canada
ELSEVIER SCIENCE PUBLISHERS
P.O. Box 945
Madison Square Station
New York, NY 10160-0757
Fax: (212) 633 3880
In all other countries
ELSEVIER SCIENCE PUBLISHERS
P.O. Box 330
1000 AH Amsterdam
The Netherlands
Fax: (+31-20) 5862 845

US$ prices are valid only for the USA & Canada and are subject to exchange rate fluctuations; in all other countries the Dutch guilder price (Dfl.) is definitive. Customers in the European Community should add the appropriate VAT rate applicable in their country to the price(s). Books are sent postfree if prepaid.

ANALYTICAL BIOTECHNOLOGY

Proceedings of the 4th International Symposium on Analytical Methods, Systems and Strategies in Biotechnology (ANABIOTEC '92), Noordwijkerhout, The Netherlands, 21-23 September 1992

Edited by **C. van Dijk**

Previously published as part of the 1993 subscription to the journals *Analytica Chimica Acta* and *Journal of Biotechnology*

ANABIOTEC '92 focused on the further integration of biotechnology and analytical chemistry. The results of this symposium clearly demonstrated that a substantial progress could be reported in the application of both conventional and new analytical techniques, the latter essentially based on natural analytical tools such as biomolecules. The main themes covered during this meeting are fermentation monitoring, chromatography, instrumental analysis, biosensors and bioanalysis.

A selection of the contents. Preface. **Process Control.** Monitoring and control of recombinant protein production (K. Schügerl *et al.*). Rapid and quantitative analysis of bioprocesses using pyrolysis mass spectrometry and neural networks: application to indole production (R. Goodacre, D.B. Kell). Characterization of a sampling unit based on tangential flow filtration for on-line bioprocess monitoring (T. Buttler, L. Gorton, G. Marko-Varga). Automated monitoring of biotechnological processes using on-line ultrafiltration and column liquid chromatography (N.C. Van de Merbel *et al.*). On-line monitoring of penicillin V during penicillin fermentations: a comparison of two different methods based on flow-injection analysis (M. Carlsen *et al.*). Development of an on-line method for the monitoring of vicinal diketones and their precursors in beer fermentation (C. Mathis *et al.*). Monitoring of fermentation by infrared spectrometry. Alcoholic and lactic fermentations (D. Picque *et al.*). **Chromatography and other Separation Techniques.** Chromatographic analysis of biopolymers distribution in "poly-hemoglobin", an intermolecularly crosslinked hemoglobin solution (J. Simoni, G. Simoni, M. Feola). Application of multivariate mathematical-statistical methods for the comparison of the retention behaviour of porous graphitized carbon and octadecylsilica columns (E. Forgács, T. Cserháti, B. Bordás). **Antibodies.** Catalytic antibodies: new developments (R. Hilhorst). **Biosensors.** Measurements of nitric oxide in biological materials using a porphyrinic microsensor (T. Malinski *et al.*). Reusable fiber-optic-based immunosensor for rapid detection of imazethapyr herbicide (R.B. Wong, N. Anis, M.E. Eldefrawi). Biosensor monitoring of blood lactate during open-heart surgery (M. Kyröläinen *et al.*). **Instrumental Techniques.** Introduction to the dielectric estimation of cellular biomass in real time, with special emphasis on measurements at high volume fractions (C.L. Davey *et al.*). Spectral analysis of interactions between proteins and dye ligands (J. Hubble, A.G. Mayes, R. Eisenthal). **Enzymatic Analysis.** Preservation of shelf life of enzyme based analytical systems using a combination of sugars, sugar alcohols and cationic polymers or zinc ions (T.D. Gibson, J.N. Hulbert, J.R. Woodward). **Colloidal Carbon Particles.** Colloidal carbon particles as a new label for rapid immunochemical test methods: Quantitative computer image analysis of results (A. van Amerongen *et al.*). Author Index.

© 1993 208 pages Hardbound
Price: Dfl. 265.00 (US $ 151.50)
ISBN 0-444-81640-2

ORDER INFORMATION
For USA and Canada
ELSEVIER SCIENCE INC.
P.O. Box 945
Madison Square Station
New York, NY 10160-0757
Fax: (212) 633 3880
In all other countries
ELSEVIER SCIENCE B.V.
P.O. Box 330
1000 AH Amsterdam
The Netherlands
Fax: (+31-20) 5862 845

US$ prices are valid only for the USA & Canada and are subject to exchange rate fluctuations; in all other countries the Dutch guilder price (Dfl.) is definitive. Customers in the European Community should add the appropriate VAT rate applicable in their country to the price(s). Books are sent postfree if prepaid.

ELSEVIER
SCIENCE B.V.

PUBLICATION SCHEDULE FOR 1994

	S'93	O'93	N'93	D'93	J	F						
Analytica Chimica Acta	281/1 281/2 281/3	282/1 282/2 282/3	283/1 283/2	283/3 284/1 284/2	284/3 285/1 285/2	285/3 286/1 286/2						
Vibrational Spectroscopy		6/1			6/2							

INFORMATION FOR AUTHORS

Detailed "Instructions to Authors" for *Analytica Chimica Acta* was published in Volume 256, No. 2, pp. 373–376. Free reprints of the "Instructions to Authors" of *Analytica Chimica Acta* and *Vibrational Spectroscopy* are available from the Editors or from: Elsevier Science Publishers B.V., P.O. Box 330, 1000 AH Amsterdam, The Netherlands. Telefax: (+31-20) 5862845.

Manuscripts. The language of the journal is English. English linguistic improvement is provided as part of the normal editorial processing. Authors should submit three copies of the manuscript in clear double-spaced typing on one side of the paper only. *Vibrational Spectroscopy* also accepts papers in English only.

Abstract. All papers and reviews begin with an Abstract (50–250 words) which should comprise a factual account of the contents of the paper, with emphasis on new information.

Figures. Figures should be prepared in black waterproof drawing ink on drawing or tracing paper of the same size as that on which the manuscript is typed. One original (or sharp glossy print) and two photostat (or other) copies are required. Attention should be given to line thickness, lettering (which should be kept to a minimum) and spacing on axes of graphs, to ensure suitability for reduction in size on printing. Axes of a graph should be clearly labelled, along the axes, outside the graph itself. All figures should be numbered with Arabic numerals, and require descriptive legends which should be typed on a separate sheet of paper. Simple straight-line graphs are not acceptable, because they can readily be described in the text by means of an equation or a sentence. Claims of linearity should be supported by regression data that include slope, intercept, standard deviations of the slope and intercept, standard error and the number of data points; correlation coefficients are optional.

Photographs should be glossy prints and be as rich in contrast as possible; colour photographs cannot be accepted. Line diagrams are generally preferred to photographs of equipment.

Computer outputs for reproduction as figures must be good quality on blank paper, and should preferably be submitted as glossy prints.

Nomenclature, abbreviations and symbols. In general, the recommendations of the International Union of Pure and Applied Chemistry (IUPAC) should be followed, and attention should be given to the recommendations of the Analytical Chemistry Division in the journal *Pure and Applied Chemistry* (see also *IUPAC Compendium of Analytical Nomenclature, Definitive Rules*, 1987).

References. The references should be collected at the end of the paper, numbered in the order of their appearance in the text (*not* alphabetically) and typed on a separate sheet.

Reprints. Fifty reprints will be supplied free of charge. Additional reprints (minimum 100) can be ordered. An order form containing price quotations will be sent to the authors together with the proofs of their article.

Papers dealing with vibrational spectroscopy should be sent to: Dr J.G. Grasselli, 150 Greentree Road, Chagrin Falls, OH 44022, U.S.A. Telefax: (+1-216) 2473360 (Americas, Canada, Australia and New Zealand) or Dr J.H. van der Maas, Department of Analytical Molecule Spectrometry, Faculty of Chemistry, University of Utrecht, P.O. Box 80083, 3508 TB Utrecht, The Netherlands. Telefax: (+31-30) 518219 (all other countries).

0003-2670/93/$06.00

This issue is printed on acid-free paper.

PRINTED IN THE NETHERLANDS

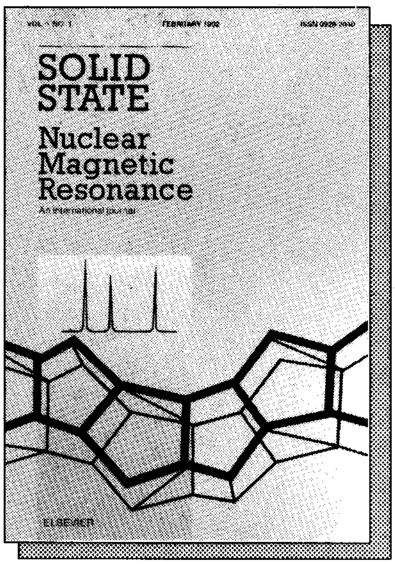

SOLID STATE NUCLEAR MAGNETIC RESONANCE

Editor-in-Chief
J. Klinowski, University of Cambridge, Department of Chemistry, Lensfield Road, Cambridge CB2 1EW, UK
Fax: (+44-223) 33-6362

Regional Editors
H. Eckert, University of California, Department of Chemistry, Santa Barbara, CA 93106, USA
Fax: (+1-805) 893-4120
D. Müller, Bruker Analytische Messtechnik GmbH, Silberstreifen, 7512 Rheinstetten 4, Germany
Fax: (+49-721) 51-7101

Audience
Industrial and academic researchers engaged in the development of new NMR techniques and their application to structural analysis.

"...papers published in Solid State Nuclear Magnetic Resonance have been of uniformly excellent quality and of importance to practising solid-state NMR spectroscopists All indications are that this trend will continue."
From Nature, Oct.7, 1993; p.581

The Journal **Solid State Nuclear Magnetic Resonance** publishes original manuscripts dealing with all experimental and theoretical aspects of solid state NMR.

This includes advances in instrumentation, development of new experimental techniques and methodology, new theoretical insights, new data processing and simulation methods, and original applications of established or novel methods to scientific problems of product and procedure developments. Typical areas for such applications include:

- **Solid State Chemistry / Materials Science**
- **Surface Chemistry / Catalysis**
- **Polymer Science and Characterization**
- **Geology / Mineralogy**
- **Biochemistry / Biology / Medicine**
- **Physics**

Subscription Information

© 1994 Subscription Information: Volume 3 (in 6 issues)
Subscription price: Dfl. 446.00 (US $ 241.00) incl. postage
ISSN 0926-2040

SOLID STATE NUCLEAR MAGNETIC RESONANCE
I would like ☐ a free sample of the above journal
☐ Instructions to Authors
☐ to enter a subscription for 1994
Please send me a Proforma Invoice

Name ______________________________
Address ______________________________
____
____

The Dutch Guilder price(s) (Dfl.) applies worldwide, except in the Americas (North, Central & South America). US $ price(s) quoted applies in the Americas only. Customers in the European Community should add the appropriate VAT rate applicable in their country to the price(s).

Elsevier Science Publishers
Attn. Eugene P.M. Wijnhoven
P.O. Box 330, 1000 AH Amsterdam
The Netherlands
Fax: (+31-20) 5862 845

<u>In the USA & Canada</u>
Attn. Judy Weislogel
P.O. Box 945, Madison Square Station
New York, NY 10160-0757, USA
Fax: (212) 633 3880

0003-2670(19931215)283:3;1-9